

## Library Declaration Form



University of Otago Library

Author's full name and year of birth: Francesco Turco,  
(for cataloguing purposes) 25 March 1992

Title of thesis: Geophysical characterisation of gas hydrate systems on the southern Hikurangi Margin of New Zealand

Degree: Doctor of Philosophy

Department: Department of Geology

Permanent Address: 66 Forbury Road, Dunedin, NZ

I agree that this thesis may be consulted for research and study purposes and that reasonable quotation may be made from it, provided that proper acknowledgement of its use is made.

I consent to this thesis being copied in part or in whole for

- i) a library
- ii) an individual

at the discretion of the University of Otago.

Signature:



Date: 11/11/2021

Geophysical characterisation of  
gas hydrate systems on the  
southern Hikurangi Margin of  
New Zealand

Francesco Turco

a thesis submitted for the degree of  
Doctor of Philosophy  
at the University of Otago, Dunedin,  
New Zealand.

11 August 2021

## **Abstract**

Gas hydrates act as an efficient natural sequester of large amounts of carbon, and it is estimated that  $\sim 15\%$  of Earth's total mobile carbon could be stored in gas hydrate provinces. They form complex systems in the shallow sediments of deep-sea regions, where there is sufficient supply of natural gas along with the stability conditions of moderately low temperatures and high pressures. Most gas hydrate provinces are found on continental margins. The southern Hikurangi subduction margin, off Wairarapa (New Zealand), contains a large gas hydrate province, inferred by the presence of widespread bottom simulating reflections (BSR) in shallow sediments. Locally intense fluid seepage at the seafloor associated with methane hydrate has also been observed and documented. Understanding the complexity of hydrate systems is valuable for a range of scientific issues related to climate change and ocean chemistry, geological hazards, deep-sea ecology, and energy supply. A quantitative approach to the characterisation of gas hydrate systems in the region is an essential step towards the estimation of the local carbon budget, especially in terms of the total volume of gas hydrate in the region and estimation of gas fluxes through the seafloor at cold seep locations.

In this thesis, I combine a range of geophysical data and theoretical models to identify, map and quantitatively characterise gas hydrate deposits and cold seeps on the southern Hikurangi Margin. Multi-channel seismic (MCS) data and methods form a large part of the basis of the studies presented in this thesis. Two MCS datasets were used: long-offset, lower resolution petroleum industry data APB13 (R/V Duke, 2013) and higher resolution, short-offset academic data TAN1808 (R/V Tangaroa, 2018), acquired as a

densely spaced grid of lines over five target sites. The synthesis of these datasets provides a complementary basis for characterising concentrated gas hydrate deposits. The long-offset data allow retrieval of P-wave velocity information of the subsurface, whereas the higher resolution data enable detailed imaging of geologic features associated with gas hydrates and fluid flow. Hydroacoustic data were used to characterise the water column and to estimate methane fluxes from gas seeps related to the gas hydrate systems.

Chapter 3 focuses on two elongated four-way closures systems at the toe of the Hikurangi accretionary wedge - Glendhu and Honeycomb ridges, which host gas hydrate deposits in high concentration. I found that the mechanism for concentrated hydrate accumulation is along-strata gas migration, and that the vertical extent of these accumulations is a function of the steepness of the strata crossing the base of the gas hydrate stability zone and of the volume of sediments from which fluid flows into each structure.

In Chapter 4, I present a quantitative assessment of the total gas hydrate in place in these deposits, by carrying out a two-step inversion of long-offset seismic profiles that cross areas of concentrated hydrate deposits at Glendhu and Honeycomb ridges. First, the elastic properties of the subsurface were estimated through geostatistical amplitude-versus-angle (AVA) seismic inversion. Second, these properties were inverted for porosity and gas hydrate saturation through a Bayesian framed petrophysical inversion built on a rock physics model for hydrate-bearing marine sediments. This geological modelling workflow enabled the spatial distribution of gas hydrate saturation and porosity in the gas hydrate stability zone to be retrieved. Among the advantages of combining geostatistical AVA seismic inversion with a Bayesian rock physics inversion is the possibility to determine the variability associated with the results. Estimates of the total gas hydrate volume in place at these two reservoirs are between  $2.45 \times 10^5 \text{ m}^3$  and  $1.72 \times 10^6 \text{ m}^3$ , with the best estimate at  $9.68 \times 10^5 \text{ m}^3$ .

A more detailed characterisation of the gas hydrate stability zone was

achieved through 1D full-waveform inversion. The goal of this study, presented in Chapter 5, was to retrieve fine-scale P-wave velocity profiles at selected locations corresponding to specific structures related to gas hydrates and fluid flow observed in the seismic data. The results show high velocity anomalies associated with high reflectivity with positive polarity, interpreted as porous units bearing gas hydrate in high concentration. Lower velocities are predicted in correspondence to chimney-like structures, which could be associated with focused fluid flow. However, the resolution of the inverted velocity models depends on the vertical resolution of the seismic data, which could be at least an order of magnitude larger than the thickness of interbedded sandy and silty layers of typical lower wedge sedimentary units.

Finally, in Chapter 6, I integrate the seismic data with hydroacoustic data from both multibeam and split-beam echo sounders to investigate the large-scale methane seepage from five known sites of gas venting over a three year period. Qualitative analysis of multibeam data, which enabled mapping of the backscatter anomalies near the seafloor at the sites of seepage, suggests that there is no substantial difference in the activity of the main seeps between 2018 and 2020. I then made estimates of gas flux at the five target sites using multi-frequency split-beam echo sounder data. Results of this analysis indicate that the cold seeps in water depths ranging from 1110 to 2060 m emit between 9.52 and  $27.52 \times 10^6$  kg of methane gas per year, collectively.

Through diverse geophysical analyses, this thesis has provided a detailed investigation of gas hydrate formation styles (Chapter 3), concentrations (Chapters 4 and 5) and methane seepage (Chapter 6) related to the hydrate system. This integrated approach has led to a thorough understanding of the entire gas hydrate system, from gas charge beneath the stability zone, through hydrate formation within the stability zone, to methane release into the water column. The estimates of gas hydrate saturation and methane flux into the ocean provide the most quantitative assessments to date of methane budgets on the southern Hikurangi Margin. The results will be crucial for understanding the role of gas hydrate systems in supporting

seafloor biological communities and in altering ocean chemistry, which are the focus of ongoing research on the Hikurangi Margin.

## Acknowledgements

My Ph.D. experience has been a three years-long journey of professional and personal growth. I have been very fortunate to be surrounded by supporting and loving people, to whom I want to express my full gratitude.

Above all, I am most grateful to my family, whom I was not expecting to miss this much. Even from the other side of the world, you have managed to send the love and moral support that I most needed during hardest times. The downside of living the pandemic in a covid-free New Zealand has been the impossibility to see you all, and the uncertainty of how much longer we will have to wait to hug each other again.

I want to especially thank my two supervisors, Prof. Andrew Gorman and Dr. Gareth Crutchley. During the past three years, your supervision has been much more than merely professional. With your kindness, patience and general support, you made this journey of research enjoyable, and I hope that our professional paths will cross again in the future.

Being part of the HYDEE programme has been a great experience, especially because I was lucky to travel often and get to know and work with wonderful people from NIWA and GNS Science. Sally Watson, Jess Hillman, Joshu Mountjoy, Susi Woelz, Sarah Seabrook, Tayla Hill and the TAN1808 and TAN2012 crews: research voyages are more fun when shared with positive and easy-going colleagues like you. I would also like to acknowledge Prof. Ingo Pecher for his patience and professionalism during the time spent at the University of Auckland in 2019 working on the 1D full-waveform inversion code. A special thank you to Yoann Ldroit for

introducing me to the world of fisheries acoustics and its applications to methane seeps studies.

I was also lucky to work with IT *angel* Hamish Bowman in the Department of Geology. He helped me during countless afternoons spent at trying to get old (and new) codes up and running. Half of my thesis would not exist without his support. I should also acknowledge Jasper Hoffman, who taught me many Kingdom tricks.

I wish to thank Leonardo Azevedo and Dario Grana, who patiently supervised my the work on quantitative assessment of hydrate in place. This collaboration has been facilitated by Leonardo, whom I want to thank once more not only for all the technical support he gave me during the months spent at Instituto Superior Tecnico of Lisbon in 2019, but also for being a good 'old' friend and colleague.

There are many friends with whom I shared unforgettable moments in the past three years. The time spent in Dunedin has been memorable, in many ways. After one and a half year since I moved away, some of the strongest friendships I have made in New Zealand remain those from the Dunedin whānau: Massi, Carmen, Paula, Helo, Carol, Tom, and all the rest of the *gang* have been (and still are) my family far from home, and I cannot thank you enough for the help and support you keep giving me.

When I moved to Wellington in February 2020, the world as we knew it decided to change. Since then, I have been so lucky to get to know another group of beautiful humans - the NIWA whānau. Together, we have managed to turn our "new normal" into a safe, funny, relaxed and loving environment. Antonia, Chris, Khush, Kate, Rafa, Savannah, Valeria, Alexia, Arnaud, Frankie, Jon, Ashley, Katie, Alex: thanks to you, being stuck 18000 km far from my family felt a little bit easier.

A big hug of gratitude goes to my Wellington neighbours, Pablo, Sergi and Alfonzo. You guys have lifted my spirit so many times when things were looking grim, and I feel very lucky to have shared with you a part of my journey.

A special thank you to my closest friends back "home" (whatever *home* means), who gave me strength when I needed it, in particular Bea, Rebe, Giulia, Maraia, Floria, my old friends "Italians from Lisbon" (Caco, Alex,



Chiara), Fede, Marghe, and all the rest. You have always been there, and I can't wait to thank you in person with the warmest hug that you all deserve.

Finally, the most important thought is for Julio: thanks for teaching me so much. Your unconditional love is the power that fuelled this whole adventure, and I am grateful that I could share most of it with you.

# Contents

<b>1</b>	<b>Introduction</b>	<b>3</b>
1.1	Natural gas hydrates . . . . .	3
1.1.1	Structure and distribution . . . . .	3
1.1.2	Global importance . . . . .	6
1.2	Gas hydrate research in Aotearoa/New Zealand . . . . .	11
1.2.1	The Hikurangi Margin . . . . .	11
1.2.2	The HYDEE programme . . . . .	12
1.3	Thesis outline . . . . .	13
<b>2</b>	<b>Geophysical methods for the study of gas hydrate systems</b>	<b>17</b>
2.1	Seismic imaging of gas hydrate systems . . . . .	17
2.2	Seismic velocities . . . . .	20
2.2.1	Semblance-based velocity analysis . . . . .	20
2.2.2	Traveltime tomography . . . . .	23
2.2.3	Full-waveform inversion . . . . .	24
2.3	Rock physics modelling . . . . .	26
2.3.1	Effective medium theory . . . . .	27
2.4	Hydroacoustic characterisation of gas seeps . . . . .	31
2.4.1	Acoustic imaging of gas flares . . . . .	32
2.4.2	Bubble backscatter theory and modelling . . . . .	35
2.5	Controlled-source electromagnetic methods . . . . .	36
<b>3</b>	<b>Seismic velocity and reflectivity analysis of concentrated gas hydrate deposits on the southern Hikurangi Margin</b>	<b>38</b>
3.1	Introduction . . . . .	39
3.2	Seismic data processing . . . . .	41
3.3	Reflectivity and velocity analysis . . . . .	43
3.3.1	Three-phase weighted equation . . . . .	44
3.3.2	Effective medium model . . . . .	46
3.4	Results . . . . .	46
3.4.1	Concentrated hydrate zones (CHZ) . . . . .	46
3.4.2	Structural analysis of Glendhu and Honeycomb ridges . . . . .	51
3.4.3	Reflectivity analysis and hydrate saturation . . . . .	53
3.5	Discussion . . . . .	54
3.5.1	Evolution of thrust ridges at the deformation front . . . . .	54
3.5.2	Stratigraphic versus structural control on fluid flow . . . . .	56

3.5.3	Comparison of Glendhu and Honeycomb ridges . . . . .	58
3.5.4	Seismic resolution and tuning effects . . . . .	60
3.5.5	Sensitivity of hydrate saturation estimates . . . . .	60
3.6	Conclusions . . . . .	62
<b>4</b>	<b>Characterisation of gas hydrates systems through geostatistical seismic and petrophysical inversion</b>	<b>63</b>
4.1	Introduction . . . . .	64
4.2	Two step inversion . . . . .	67
4.2.1	Rock physics model calibration . . . . .	67
4.2.2	Geostatistical seismic AVA inversion . . . . .	68
4.2.3	Bayesian petrophysical inversion . . . . .	71
4.3	Geophysical data . . . . .	73
4.4	Results . . . . .	75
4.4.1	Prediction of elastic properties . . . . .	75
4.4.2	Prediction of petrophysical properties . . . . .	78
4.4.3	Local gas hydrate volume assessment . . . . .	81
4.5	Discussion . . . . .	82
4.5.1	Comparison with previous studies . . . . .	82
4.5.2	Limitations of the method . . . . .	84
4.6	Conclusions . . . . .	86
<b>5</b>	<b>1D full-waveform inversion studies of the gas hydrate stability zone</b>	<b>89</b>
5.1	Motivation . . . . .	89
5.2	Methodology . . . . .	90
5.2.1	Seismic processing . . . . .	90
5.2.2	Wavelet estimation . . . . .	91
5.2.3	Definition of the background Earth model . . . . .	91
5.2.4	Inversion procedure . . . . .	93
5.3	Seismic observations and inversion results . . . . .	94
5.3.1	APB13-21 - Glendhu Ridge . . . . .	95
5.3.2	APB13-58 - Honeycomb Ridge . . . . .	96
5.4	Discussion and conclusions . . . . .	97
<b>6</b>	<b>Quantitative analysis of gas seeps and methane fluxes</b>	<b>102</b>
6.1	Introduction . . . . .	102
6.2	Data and methods . . . . .	104
6.2.1	Acoustic data processing . . . . .	104
6.2.2	Estimation of gas fluxes . . . . .	106
6.3	Results . . . . .	108
6.3.1	Identification of gas seeps . . . . .	108
6.3.2	Gas fluxes and seismic observations . . . . .	111
6.4	Discussion . . . . .	119
6.4.1	Acoustic data resolution . . . . .	119
6.4.2	Constraints on bubble size distributions . . . . .	121
6.4.3	Source of gas and seismic manifestation of fluid flow . . . . .	123

6.4.4	Temporal variability of the seeps . . . . .	125
6.4.5	Global implications for ocean acidification . . . . .	126
6.5	Conclusions . . . . .	127
<b>7</b>	<b>Conclusions</b>	<b>129</b>
7.1	Future work . . . . .	131
	<b>References</b>	<b>135</b>

# List of Tables

2.1	Examples of rock physics model parameters. . . . .	31
3.1	Seismic acquisition parameters. . . . .	42
4.1	Low (P25), best (P50) and high (P75) estimates of petrophysical properties for the two reservoirs and total gas hydrate volume assessment. . . . .	82
6.1	Bubble size parameters and fluxes. (1): linear inversion with Weibull distribution; (2): linear inversion with log-normal distribution; (3): manual curve fitting with Weibull distribution. All values are calculated at the seafloor. . . . .	119

# List of Figures

1.1	Gas hydrate structures (Sloan, 1998) . . . . .	4
1.2	Gas hydrate stability zone in marine environments . . . . .	4
1.3	Thickness of the theoretical gas hydrate stability zone (GHSZ) in the world's oceans calculated by Kretschmer <i>et al.</i> (2015). . . . .	5
1.4	Crater-like feature associated with gas release from gas permafrost regions. . . . .	7
1.5	Map showing the location of field tests performed on gas hydrates resources . . . . .	9
1.6	Aotearoa's gas hydrate provinces, modified after Pecher (2011). . . . .	10
1.7	a) Overview of the geographic and tectonic setting of the Hikurangi Margin in Aotearoa; b) Setting of the southern Hikurangi Margin and one of the available seismic reflection profiles. . . . .	15
1.8	Map showing the target locations of HYDEE voyages offshore Wairarapa, on the southern Hikurangi Margin . . . . .	16
2.1	Examples of evidence of gas hydrates and free gas in seismic data . . . . .	18
2.2	Comparison between profiles of interval velocities for CDP 5031 of Line APB13-21 estimated using different methodologies . . . . .	21
2.3	Example of the semblance spectrum of CDP 5031 . . . . .	22
2.4	Results of raytracing for CDP 5031 of Line APB13-21. . . . .	24
2.5	1D full-waveform inversion results for CDP 5031 of Line APB13-21. . . . .	26
2.6	Different types of hydrate morphologies, after Fang <i>et al.</i> (2020) . . . . .	28
2.7	Schematic 3D view of a typical Hikurangi Margin seep site. Image after Barnes <i>et al.</i> (2010). . . . .	32
2.8	Example of the use of hydroacoustic data to image water column features such as gas flares. . . . .	34
2.9	Example of two marine CSEM experiments . . . . .	37
3.1	Overview of the geographic and tectonic setting of the Hikurangi Margin in New Zealand, and location of the available seismic reflection profiles . . . . .	40
3.2	P-wave interval velocities at Glendhu and Honeycomb ridges, overlying the pre-stack time migrated seismic sections. . . . .	47
3.3	Glendhu Ridge overview (see Fig. 3.1c for profile locations) . . . . .	49
3.4	Honeycomb Ridge overview (see Fig. 3.1c for profile locations) . . . . .	50
3.5	Structural map of the geology underlying Glendhu and Honeycomb ridges and thickness and spatial extend of the relative CHZs . . . . .	51
3.6	Deformation processes at Glendhu Ridge. . . . .	52
3.7	Reflectivity analysis and gas hydrate saturation estimates for selected seismic reflections. . . . .	55

3.8	Schematic representation of the evolution of a CHZ in a thrust ridge at the southern Hikurangi Margin . . . . .	57
4.1	Flow chart representation of the geological modelling workflow used to predict the spatial distribution of gas hydrate saturation and porosity. . . . .	65
4.2	Location of the Hikurangi Margin of New Zealand. . . . .	66
4.3	Graphical illustration of the calibration of the rock physics model. . . . .	74
4.4	Examples of starting models of $V_P$ and $V_S$ for Line APB13-17 (Honeycomb Ridge). . . . .	75
4.5	Mean model of the elastic realizations generated at the last iteration of the geostatistical inversion for Glendhu and Honeycomb ridges. . . . .	76
4.6	Near-stack sections of APB13-21 and APB13-17 at Glendhu and Honeycomb ridges. . . . .	77
4.7	Inverted models of hydrate saturation and porosity for profile APB13-21 at Glendhu Ridge, for profile APB13-17 at Honeycomb Ridge, calculated from the mean models. . . . .	80
4.8	Graphs illustrating the variability of the results. . . . .	87
4.9	Percentiles (P25 and P75) sections of all predicted petro-elastic properties. . . . .	88
5.1	Examples of pre-stack time migrated gather (CDP 5031, line APB13-21). NMO corrections were removed prior to $\tau$ - $p$ transformation. . . . .	92
5.2	Example of seafloor reflection for wavelet estimation. . . . .	93
5.3	Near-trace (up to 700 m offset), pre-stack time migrated data of line APB13-21, spanning longitudinally across Glendhu Ridge with fine-scale $V_P$ inversion results overlain in red. . . . .	97
5.4	Near-trace (up to 700 m offset), pre-stack time migrated data of line APB13-58 crossing Honeycomb Ridge with fine-scale $V_P$ inversion results overlain in red. . . . .	98
5.5	Examples of wiggle plots of inverted waveforms displayed in the $\tau$ - $p$ domain (red lines), overlying the $\tau$ - $p$ real seismograms (black lines). . . . .	101
6.1	Illustration of the workflow to estimate gas fluxes from MBES and single-beam backscatter data. . . . .	106
6.2	Southern Hikurangi Margin: gas flares identified from the MBES data from the three HYDEE voyages. . . . .	109
6.3	Backscatter intensity images of the Glendhu seep field from multibeam data. . . . .	110
6.4	Distribution of the acoustic seeps identified in the five target areas. . . . .	111
6.5	Graphical illustration of the lateral resolution of the acoustic images of the single-beam (EK60) data. . . . .	112
6.6	Overview of the Urutī Ridge seep site. . . . .	114
6.7	Overview of the Glendhu Ridge seep site. . . . .	115
6.8	Overview of the Pahaua Bank seep site. . . . .	117
6.9	Overview of the Tokorakau Ridge seep site. . . . .	118
6.10	Overview of the Mungaroa Ridge seep site. . . . .	120
6.11	Results of methane flux estimations for the five seep locations. . . . .	121

6.12	Bubble size distributions estimated from linear inversion of the split-beam data at the Glendhu Ridge gas flare. . . . .	123
6.13	Evolution of the Glendhu Ridge seep site over the years, from MBES data.	128
7.1	Crew and scientific party of the TAN1808 research voyage (HYDEE I).	133
7.2	Scientific party of the TAN2012 research voyage (HYDEE III). . . . .	134



# Place Names

Some of the names adopted in this thesis to refer to submarine regions and features are informal, and have not been officially approved and gazetted by the New Zealand Geographic Board - Ngā Pou Taunaha o Aotearoa. For more information, the reader is referred to the Toitū Te Whenua - Land Information New Zealand website.

# Glossary

BGHS: base of gas hydrate stability;  
BSD: bubble size distribution;  
BSR: bottom simulating reflection;  
CDP: common depth-point;  
CHZ: concentrated hydrate zone;  
CIG: common image gather;  
CMP: common mid-point;  
FWI: full-waveform inversion;  
GHSZ: gas hydrate stability zone;  
LWD: logging-while-drilling;  
MCS: multi-channel seismic;  
MBES: multibeam echosounder;  
PDF: probability density function;  
PSTM: pre-stack time migration;  
RPM: rock physics model;  
SBES: split-beam echosounder;  
 $S_v$ : volume backscattering strength;  
 $S_H$ : hydrate saturation;  
 $V_P$ : P-wave velocity;  
 $V_S$ : S-wave velocity;  
TS: target strength;

# Chapter 1

## Introduction

The objective of this thesis is to characterise gas hydrate systems on the southernmost region of the Hikurangi subduction margin. This work builds upon more than a decade of scientific investigation that has identified and described gas hydrate occurrences in the region. The quantitative approach carried out in the studies presented herein provides a novel and significant contribution to the existing literature by presenting first-order estimates of the amount of gas hydrate stored in concentrated hydrate accumulations, and by constraining the fluxes at which greenhouse gases are venting out of the seabed in this region.

### 1.1 Natural gas hydrates

#### 1.1.1 Structure and distribution

Gas hydrate is an ice-like crystalline substance that forms under low temperature and high-pressure conditions when pore water is saturated with low molecular weight gases such as methane, ethane or carbon dioxide (Kvenvolden, 1993).

Under such conditions, water forms a crystalline clathrate structure that encages the gas molecules. The crystalline structure of gas hydrates is controlled by the gas composition; there are three known types of gas hydrate structures (Figure 1.1; Milkov, 2005; Sloan, 1998). Structure I ( $S_I$ ) is a body-centred cubic structure that hosts almost pure  $\text{CH}_4$  and is commonly found in deep ocean sediments. Structure II ( $S_{II}$ ) and structure H ( $S_H$ ) are characterised by a cubic and an hexagonal lattice, respectively, that can incorporate heavier hydrocarbon molecules ( $\text{C}_{2+}$ ) and that have a wider range of stability conditions than  $S_I$  gas hydrates (Sloan, 1998).

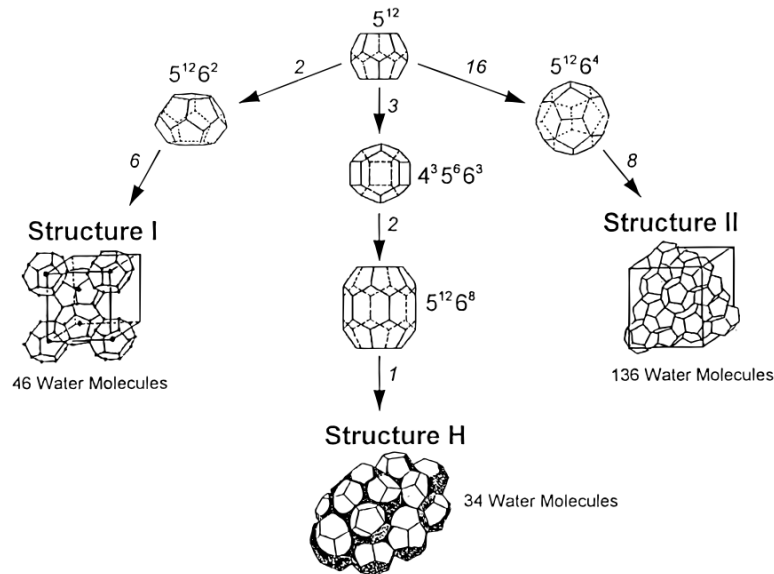


**Figure 1.1:** Gas hydrate structures: three hydrate unit crystals and constituent cavities. Image after Sloan (1998).

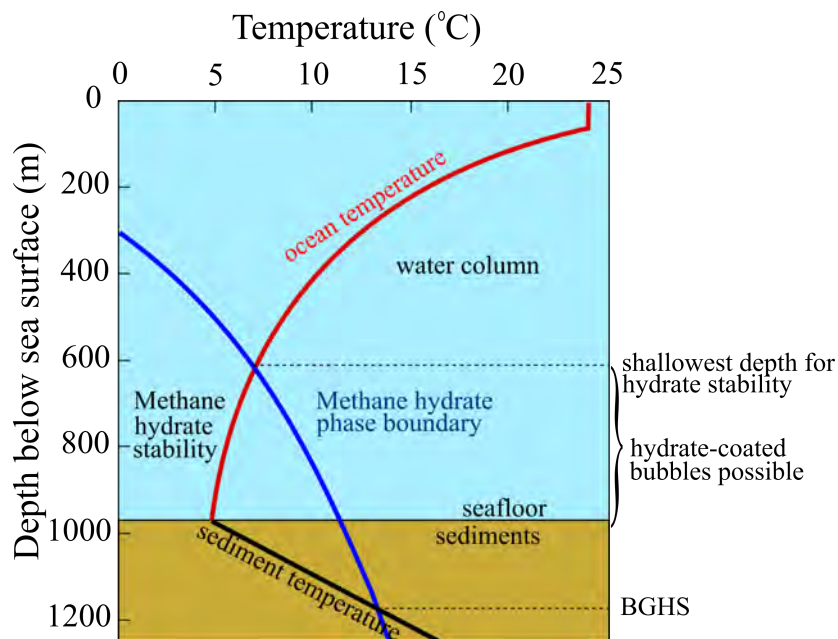


**Figure 1.2:** Gas hydrate stability zone in marine environments (modified after C. Ruppel, U.S. Geological Survey).

In nature, the occurrence of gas hydrates requires sufficient supply of natural gas and pore water and is governed by the conditions of low temperatures and high pressure at which gas hydrates are stable (Figure 1.2). These conditions are met in some natural environments such as in permafrost regions and in sedimentary basins below cold lakes

and in deep seas (Granin *et al.*, 2019; Rivkina *et al.*, 2001). In these regions, the spatial extent of the gas hydrate stability zone (GHSZ, shown in Figure 1.3) is controlled by the gas hydrate phase boundary and the in situ geothermal and pressure gradient. The base of the gas hydrate stability zone (BGHS) is marked by the intersection of the geothermal gradient with the gas hydrate phase boundary.

Natural gas can form in sediments that are rich in organic matter either through microbial methanogenesis or through thermogenic processes (Schoell, 1988). Although several onshore permafrost regions have been documented to contain large gas hydrate provinces (Bellefleur *et al.*, 2012; Lu *et al.*, 2011; Makogon and Omelchenko, 2013), modern conservative estimates show that only slightly more than 1% of the global in-place methane hydrates is found in permafrost regions (Ruppel, 2015), and the largest

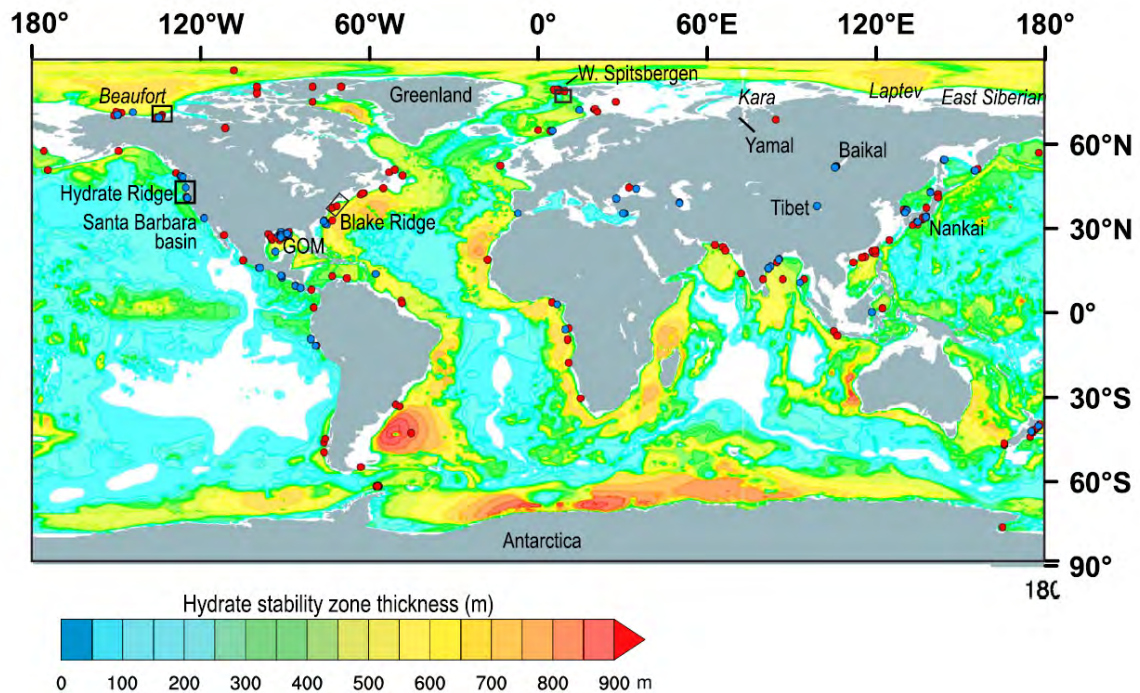


**Figure 1.3:** Thickness of the theoretical gas hydrate stability zone (GHSZ) in the world's oceans calculated by Kretschmer *et al.* (2015). The blue dots represent location of known gas hydrate occurrence, while the red dots are areas where gas hydrate is inferred based on well logs or geophysical markers like BSR. Boxes show locations where upper continental slope methane seeps may be linked to gas hydrate dissociation processes (Johnson *et al.*, 2015; Paull *et al.*, 2015; Skarke *et al.*, 2014; Westbrook *et al.*, 2009). (Image after Ruppel and Kessler, 2017).

accumulations of natural gas hydrates are inferred to occur in marine environments. In fact, the upper few tens to hundreds of metres of marine sediment on many of the world's continental margins, typically below water depths of about 500 m, are partially saturated with natural gas hydrate (Collett *et al.*, 2010).

Deposits of gas hydrates can occur in several forms, but they are usually concentrated within the pore spaces of coarse-grained strata, or they occur in lenses, fractures or nodules in less porous, fine-grained sediments (Holland *et al.*, 2008; Yun *et al.*, 2005). The type of occurrence of gas hydrate accumulations is a key factor for the identification and the characterisation of these systems through indirect geophysical methods, as explained in Chapter 2.

The effect of hydrates on the physical properties of the host sediments is not only dependent on the amount of hydrate present (saturation), but also on the microstructural distribution of hydrate grains within host sediments, which may include morphologies such as contact-cementing, grain-coating, pore-filling, matrix-supporting, matrix-inclusion and fracture-filling (Dai *et al.*, 2004a; Ecker *et al.*, 2005; Helgerud *et al.*, 1999). These morphologies frequently coexist in nature. For example, occurrence of gas hydrates occupying the pore space or the fractures of the host rock (pore-filling and fracture-filling) with possible matrix-supporting or grain-coating hydrate morphologies have been reported in the Krishna-Godavari Basin (Yoneda *et al.*, 2019) and in the South China Sea (Qian *et al.*, 2018).

### **1.1.2 Global importance**

Gas hydrates form complex systems in the shallow tens to few hundred meters of deep-sea regions, especially on continental margins. Understanding these system is valuable for a range of scientific issues related to climate change and ocean chemistry (Buffett and Archer, 2004; Ruppel and Kessler, 2017), geological hazards (Mienert *et al.*, 2005), deep-sea ecology (Turner *et al.*, 2019) and energy supply (Johnson and Max, 2006; Makogon *et al.*, 2007).

#### **Role of hydrates in climate change**

Gas hydrates efficiently sequester large amounts of carbon: between half (Kvenvolden, 1988) and  $\sim 15\%$  (Boswell and Collett, 2011) of Earth's total mobile carbon is estimated to be stored in gas hydrate provinces.



**Figure 1.4:** Crater-like feature associated with gas release from gas hydrate in Arctic regions. Scientists at the Russian Academy of Sciences' Institute of Oil and Gas Problems visited the newest crater during an expedition to Yamal in August 2020 (Credit: Evgeny Chuvilin) <https://www.bbc.com/future/article/20201130-climate-change-the-mystery-of-siberias-explosive-craters>.

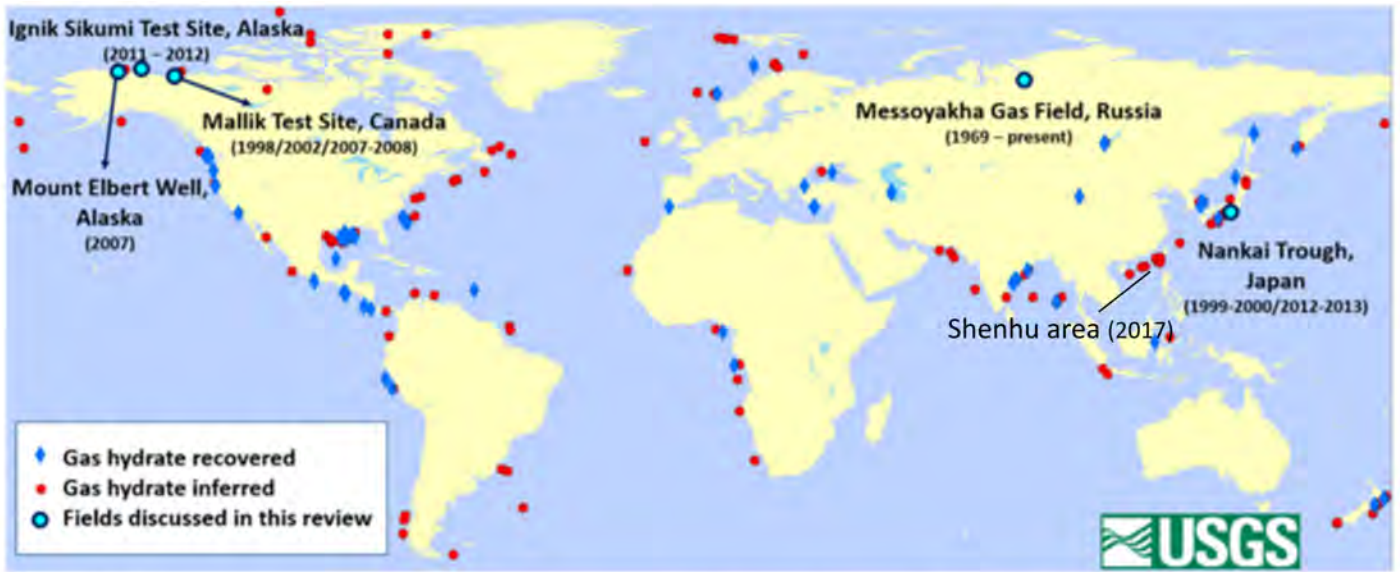
Onshore hydrate provinces are located in permafrost regions, where global warming is more likely to perturb the hydrate stability field, leading to hydrate dissociation and release of methane and other greenhouse gases into the overlying sediments, soils and, eventually, into the atmosphere. The fact that hydrate dissociation represents both an effect of and a probable contributor to global warming, has sometimes led to interpretations of catastrophic scenarios on the relationship between gas hydrate dissociation and climate change - e.g., the so-called clathrate gun hypothesis (Gail *et al.*, 2013; Kennett *et al.*, 2003; Mascarelli, 2009; O'Connor *et al.*, 2010). However, most of the largest hydrate regions are found offshore, on continental margins. Here, the effect of ocean warming on reducing the hydrate stability field is not instantaneous, as the time response of the heat propagation through the water column and into the subsurface is governed by the equations of heat transfer. The increase in pressure at the seafloor caused by sea-level rise, on the other hand, is nearly immediate, and shifts the base of gas hydrate stability downwards, resulting in a potential increase of methane hydrate formation (Maslin *et al.*, 2004). The interaction of global warming and sea level rise caused by melting glaciers and sea-ice is an example of the complexity of the effect of climate change on marine gas hydrate systems.

There is extensive evidence of methane being released from the subsurface into the atmosphere, especially in high-latitude regions. Warmer climate in the Arctic regions has been shown to lead to exceeding the threshold temperature for the dissociation of shallow methane hydrates on continental permafrost (Arzhanov *et al.*, 2020). At these latitudes, gas emissions can also manifest themselves in explosive events that leave crater-like features on the surface (Figure 1.4; Arzhanov *et al.*, 2020; Laurion *et al.*, 2010; Turetsky *et al.*, 2019). Similar geomorphological features (referred to as pockmarks) are also observed in the marine environment (Riboulot *et al.*, 2016), and are sometimes associated with gas hydrate systems and fluid flow. In marine environments, however, there are additional factors that mitigate the effect of gas emissions on climate change. For instance, the methane contained in gas bubbles rising from the seafloor diffuses rapidly into the seawater, and gets oxidised to CO<sub>2</sub>, increasing ocean acidification though preventing CH<sub>4</sub> release into the atmosphere (Vielstädte *et al.*, 2015; Wang *et al.*, 2016). Marine hydrates on continental margins are likely undergoing the same dissociation processes as on-shore permafrost hydrates (Ruppel and Kessler, 2017). However, the synergy between gas hydrate dissociation and warming climate is a complex system that is the topic of current research (e.g., Farahani *et al.*, 2021; Ketzer *et al.*, 2020; Mestdagh *et al.*, 2017), and there is no conclusive proof that large amounts of methane coming from dissociating marine hydrates are reaching the atmosphere at this stage (August 2021). For this reason, a detailed knowledge of the sources of greenhouse gas emissions both on- and offshore is necessary.

### **Role of hydrates as an energy resource**

A slightly different perspective on gas hydrates research comes from the hydrocarbon industry. As the world tries to tackle climate change, natural gas from gas hydrates is sometimes considered a "bridging" energy resource that could assist us in the transition towards a renewable energy system (Krey *et al.*, 2009; Nakicenovic *et al.*, 2000), as methane is the cleanest burning fossil fuel. Despite their vast global volume, marine gas hydrates mainly occur diffused in the sediments and in low saturation (Milkov, 2004). However, localised accumulations of gas hydrate in high concentrations have been discovered in several locations worldwide, which have much greater potential as an energy resource (e.g., Berndt *et al.*, 2019; Crutchley *et al.*, 2018; Frye *et al.*, 2012a; Ryu *et al.*, 2013).





Year of production test	Location for production test	Method used in production test	Duration	Total yield /m <sup>3</sup>
2002	Mackenzie Delta, Canada	Heating	5d	516
2007	Mackenzie Delta, Canada	Depressurization	12.5h	830
2008	Mackenzie Delta, Canada	Depressurization	6d	13000
2012	North slope of Alaska, USA	CO <sub>2</sub> replacement and depressurization	30d	24000
2013	Nankai trough, Japan	Depressurization	6d	119000
2017	Nankai trough, Japan	Depressurization	12d	35000
2017	Nankai trough, Japan	Depressurization	24d	200000
2011	Permafrost area of the Qilian Mountains, Qinghai, China	Depressurization and heating	101h	95
2016	Permafrost area of the Qilian Mountains, Qinghai, China	Depressurization	23d	1078
2017	Shenhu area of SCS, China	Formation fluid extraction	60d	309000

**Figure 1.5:** Map showing the location of field tests performed on gas hydrates resources (Chong *et al.*, 2016). The lower table is a summary of methane production tests from gas hydrate reservoirs after Li *et al.* (2018)

Production of natural gas from hydrates is not commercially viable yet, as it is much more technologically challenging than standard hydrocarbon production (Chong *et al.*, 2016). A typical issue to be overcome is that the hydrate needs to be dissociated in situ in order to separate the gas molecules from their cages, prior to extraction. Dissociation can be achieved in several ways, for instance by increasing the in situ temperature (thermal stimulation), decreasing the pressure (depressurisation) or through the injection of chemical inhibitors. The thermal stimulation method has been used in the 2002 production test to recover gas from permafrost hydrate on the MacKenzie Delta, Canada (Dallimore and Collett, 2005). In 2013, depressurization was used during the world’s first methane hydrate production test on the Nankai Trough (Konno *et al.*,

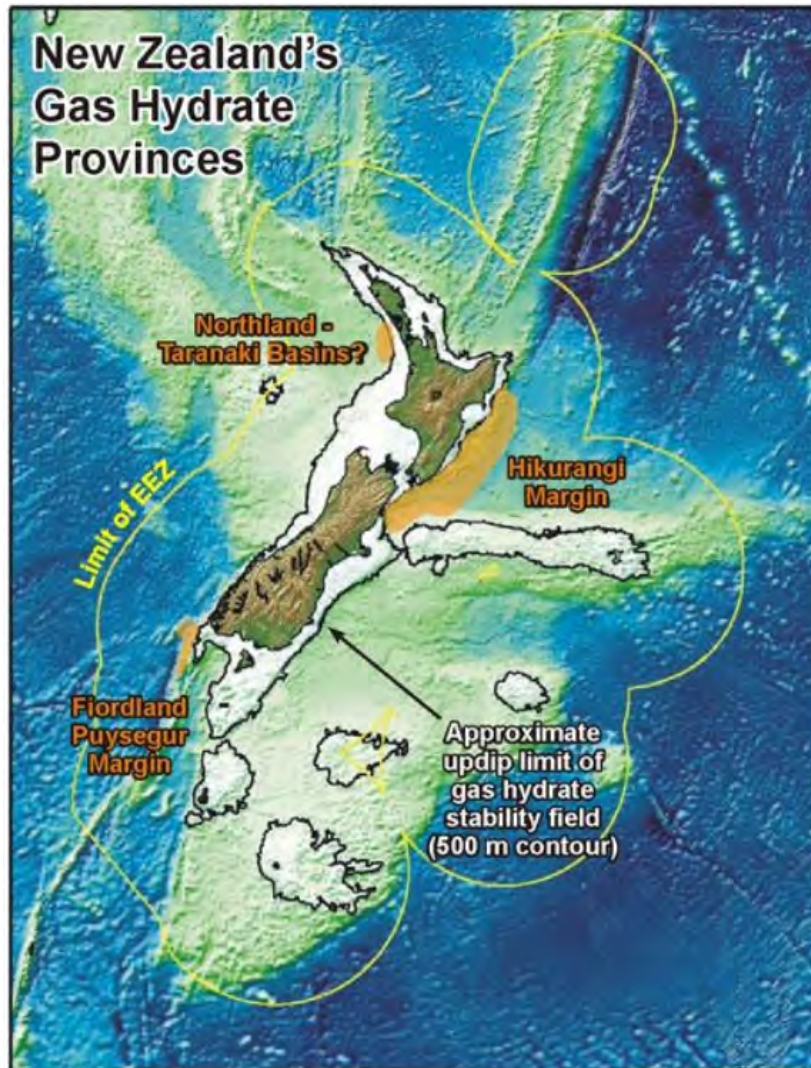


**Figure 1.6:** Aotearoa's gas hydrate provinces, modified after Pecher (2011).

2017; Yu *et al.*, 2019) and in the China Sea (Zhao *et al.*, 2020). Another method for methane extraction from hydrates is through injection of  $\text{CO}_2$ , another gas that forms clathrates, into the reservoir, to allow the replacement of  $\text{CH}_4$ . This method, known as  $\text{CO}_2$ - $\text{CH}_4$  exchange, is theoretically carbon neutral, and has been used in the Ignik-Sikumi field experiment on the North Alaska slope (Boswell *et al.*, 2017). As of 2021, global research continues towards the commercial viability of methane production from gas hydrates, especially in regions where hydrates accumulate in high-saturations (Boswell *et al.*, 2020).

## 1.2 Gas hydrate research in Aotearoa/New Zealand

During the last decades, gas hydrate-related research has experienced a steady increase in Aotearoa/New Zealand, as it has worldwide. There are three main gas hydrate provinces on the continental margins around Aotearoa (Fig. 1.6): the Fiordland-Puysegur subduction margin (Crutchley *et al.*, 2007), southwest of Te Waipounamu (South Island), the Northland-Taranaki Basin, west of Auckland (Kroeger *et al.*, 2017; Pecher *et al.*, 2011) and the Hikurangi Margin, east of Te Ika-a-Māui (North Island). While much of the research has been focused on the geological processes that lead to the formation of concentrated hydrate deposits (e.g., Barnes *et al.*, 2010), great interest has also been addressed to identify and characterise sites of methane seepage out of the seabed (e.g., Naudts *et al.*, 2010; Watson *et al.*, 2020). Several international research voyages have taken place in the last few years to investigate gas hydrate systems along New Zealand's continental margins; amongst these, IODP Expedition 372 took place in 2018 onboard the R/V Joides Resolution and successfully drilled through the GHSZ on the northern Hikurangi Margin (Pecher *et al.*, 2018).

### 1.2.1 The Hikurangi Margin

Along the Hikurangi Margin, east of New Zealand's North Island, the Pacific Plate subducts obliquely underneath the Australian Plate. The convergence obliquity increases towards the south, finally transitioning into dextral strike-slip tectonics to the south-east of the Cook Strait, in the Marlborough region (Wallace *et al.*, 2012). The frontal accretionary prism in the southern Hikurangi Margin is characterised by an imbricated thrust wedge that builds against a Mesozoic basement backstop (Barnes *et al.*, 2010). The ridge and basin morphology typical of this part of the margin is shown in the representative seismic line APB13-58 in Figure 1.7c, where an example of the BSR can also be observed. The thick sediment sequence is likely composed of accreted and imbricated turbidites (Lewis *et al.*, 1998).

Evidence of fluid flow within the margin has been widely documented: multi-channel seismic (MCS) data reveal widespread bottom simulating reflections (BSR) in shallow sediments across the Hikurangi subduction margin (Henry *et al.*, 2003; Katz, 1981). Moreover, locally intense fluid seepage associated with methane hydrate has been observed across the margin (Greinert *et al.*, 2010; Watson *et al.*, 2020).

The Hikurangi Margin is Aotearoa's principal gas hydrate province, covering an area of over 50 000 km<sup>2</sup>. While most of the gas hydrate may be distributed in low concentrations, several regions along the margin have been interpreted as hosting localised high concentrations (e.g., Fohrmann and Pecher, 2012; Wang *et al.*, 2017b). First estimates based on regional BSR analysis suggest that the volume of gas in all concentrated hydrate deposits combined is on the order of  $\sim 5.66 \times 10^{11}$  m<sup>3</sup> (Pecher and Henrys, 2003).

### 1.2.2 The HYDEE programme

In 2017, the New Zealand Ministry for Business, Innovation and Employment funded the HYDEE research programme (acronym for "Economic Opportunities and Environmental Implications of Energy Extraction from Gas Hydrates"). By undertaking marine, economic and social science research, the programme has been investigating the balance between economic opportunities, cultural values and environmental risks associated with potential extraction of gas from hydrates. The overarching goal is to determine where and how gas hydrates could be produced economically, while also investigating whether production would be socially and environmentally acceptable. The two main questions that this programme aims to tackle are:

- 1 Will feasible hydrocarbon production scenarios, either directly from gas hydrates or through gas hydrates, significantly impact seafloor stability, ecology or ocean biogeochemistry?
- 2 What are the likely socioeconomic implications of gas hydrate production in New Zealand

From 2018 to 2020, three research voyages were funded or co-funded by the HYDEE programme (Figure 1.8). The data collected during these voyages allowed addressing several research aims of the programme such as: determine New Zealand-specific frameworks (geological and economic) for energy production from and through gas hydrates, investigate the potential impacts of gas extraction on deep marine ecosystems, provide new constraints on the relative volumes of sediment hosting low (<10% of pore space) and high (>40% of pore space) gas hydrate saturations and determine how sensitive these gas hydrate deposits are to dissociation caused by ocean warming. The primary aim of the HYDEE I (TAN1808) voyage in September/October 2018 was to collect geophysical and geological data to identify and characterise areas of concentrated gas

hydrate accumulations and gas seepage at the seafloor. Based on the analysis of these data, the HYDEE II research voyage (TAN1904) in July 2019 focused on gathering biological and biogeochemical data to investigate the impact that changes in seafloor stability and/or methane flux could have on marine ecosystems. Finally, the main aim of the HYDEE III voyage (TAN2012) in November 2020 was to characterise and quantify gas and gas hydrate accumulations in the sub-seafloor, by collecting controlled source electromagnetic (CSEM) data along collocated seismic profiles. Hydro-acoustic data from these voyages supplement the study of gas hydrate systems by allowing a quantitative characterisation of the water column and the shallow subsurface.

### 1.3 Thesis outline

The broad objective of this thesis is to study the interaction between tectonic processes, focused fluid migration, hydrate formation and seafloor gas seepage at the southern end of the Hikurangi Margin. The novelty of this thesis is to provide a quantitative assessment of methane budget in terms of: 1) the volumes of gas hydrate stored in concentrated accumulations within the thrust-ridges and 2) the volumes of methane emitted at the seafloor at known cold seepage locations.

**Chapter 1** The introductory section explains background and scientific relevance of the studies presented in this thesis.

**Chapter 2** This chapter introduces the geophysical methods and theoretical models that are used in this thesis.

**Chapter 3** This chapter presents a detailed analysis of high- and medium-resolution seismic reflection data across Glendhu and Honeycomb ridges, two elongated four-way closure systems at the toe of the deformation wedge that host highly concentrated gas hydrate accumulations. A novel method involving combined seismic velocity and reflectivity analysis and rock physics modelling is used to calculate hydrate saturation values in localised areas. This work has been published as *Seismic velocity and reflectivity analysis of concentrated gas hydrate deposits on the southern Hikurangi Margin (New Zealand)* by Turco F., Crutchley G.J., Gorman A.R., Mountjoy J.J., Hillman J.I.T. and Woelz S. in the journal *Marine and*

- Chapter 4** This chapter introduces the results of the quantitative characterisation of the gas hydrate stability zone at the location of two highly concentrated hydrate deposits - Glendhu and Honeycomb ridges, presenting first-order estimates of the total gas hydrate volumes in place. This work has been published under the title *Characterisation of gas hydrate systems on the Hikurangi Margin (New Zealand) through geostatistical seismic and petrophysical inversion* by Turco F., Azevedo L., Grana D., Crutchley G.J., Gorman A.R., in the journal *GEOPHYSICS*.
- Chapter 5** This chapter presents the results of 1-D full-waveform inversion studies to characterise the small-scale variability of seismic velocities within the GHSZ at selected locations.
- Chapter 6** This chapter presents the results of a study conducted at five cold seep locations, coupling subsurface and water column acoustic imaging to describe the geologic expression of subsurface gas flow and to constrain the methane fluxes at the seabed.
- Chapter 7** This chapter outlines the main conclusions of the studies presented in Chapters 3, 4, 5 and 6, and provides suggestions for future research.



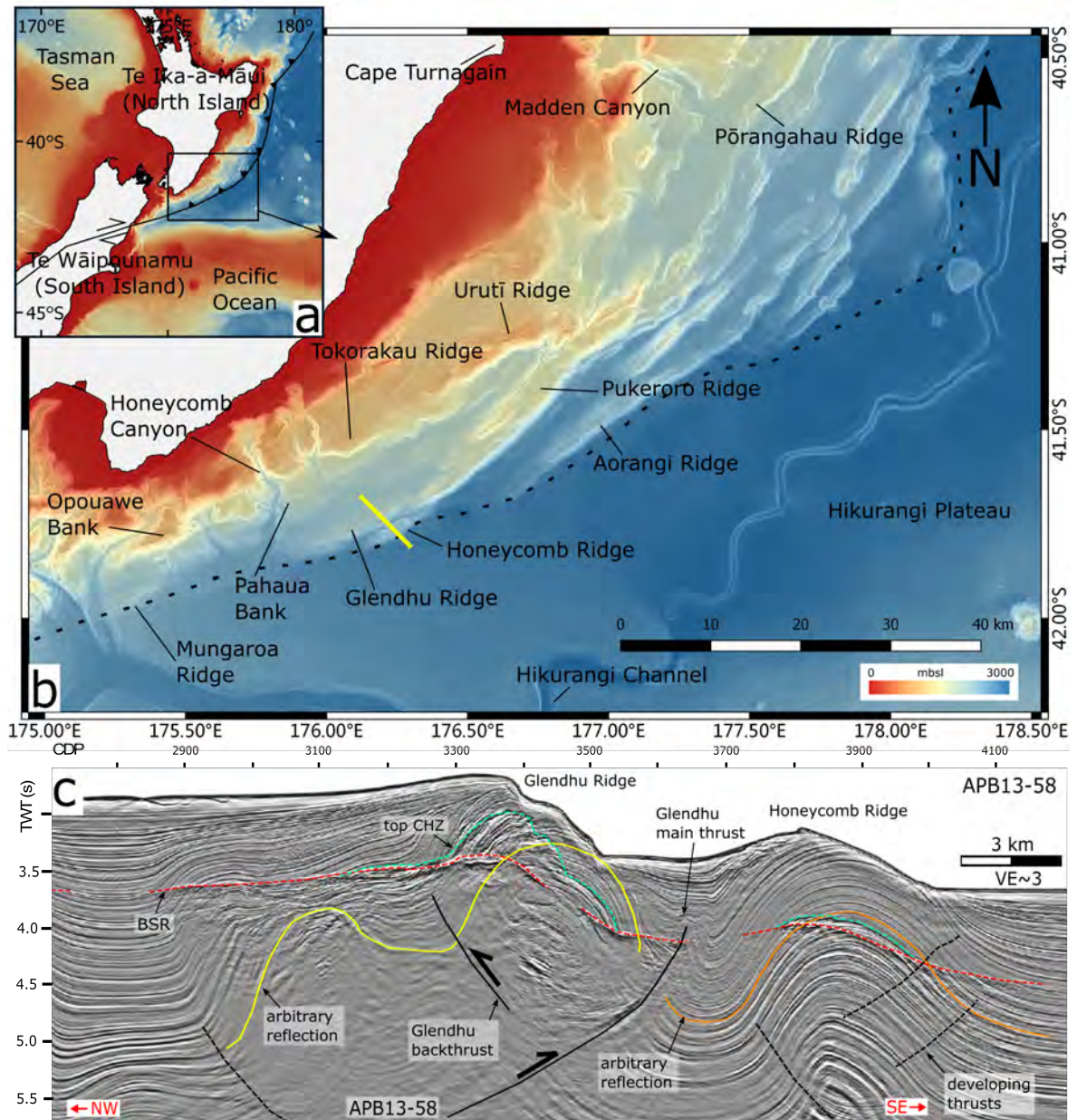


**Figure 1.7:** a) Overview of the geographic and tectonic setting of the Hikurangi Margin in Aotearoa; b) Setting of the southern Hikurangi Margin and one of the available seismic reflection profiles. The dashed black line represents the approximate seafloor location of the deformation front. In yellow is the seismic section APB13-58 shown in c). Map coordinates are in latitude/longitude (WGS84 datum). c) Overview of large-scale structural features across Glendhu and Honeycomb ridges; BSR: bottom simulating reflection; CHZ: concentrated hydrate zone; the yellow and orange reflections labelled “arbitrary reflection” highlight folding of strata within the anticlines. VE: vertical exaggeration at the seafloor. These same reflections are presented in Fig. 3.1 to show the spatial character of folding beneath Glendhu and Honeycomb ridges.

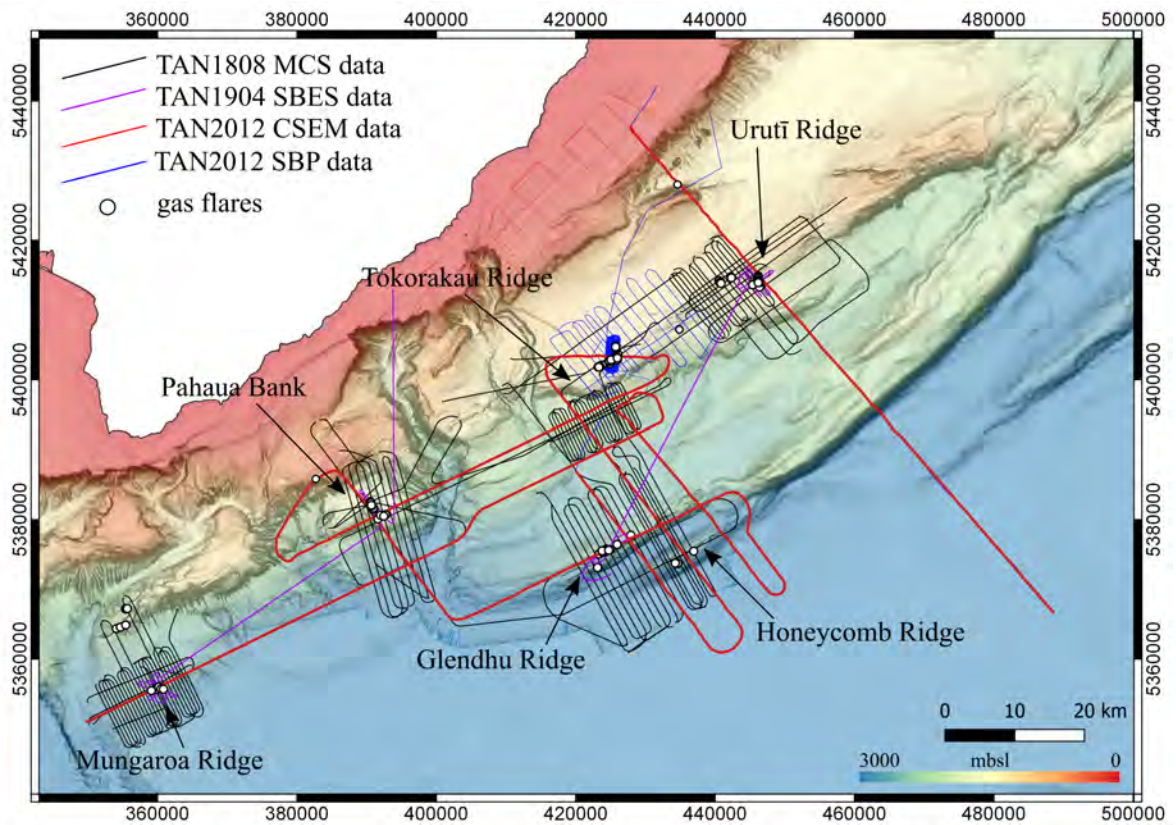


**Figure 1.8:** Southern Wairarapa: map of HYDEE I (TAN1808), HYDEE II (TAN1904) and HYDEE III (TAN2012) voyages. MCS: multi-channel seismic; CSEM: controlled source electromagnetic; SBES: single beam echo-sounder; SBP: sub-bottom profiler. Map coordinates are in UTM Zone 60S (WGS84 datum).



# Chapter 2

## Geophysical methods for the study of gas hydrate systems

The methods applied in this thesis are based on multi-channel seismic reflection data, bathymetric and hydroacoustic data and theoretical rock-physics and acoustic backscatter models. This chapter introduces an overview of these methods and theoretical models, while the applications are presented in following chapters.

### 2.1 Seismic imaging of gas hydrate systems

The presence of gas hydrates within sediment pore spaces significantly affects the bulk physical properties of marine sediments (Sloan, 1998). For this reason, indirect geophysical methods provide the most effective means for identifying large-scale offshore gas hydrate deposits. Seismic reflection methods have been broadly used for the study of offshore gas hydrates systems (e.g., Gorman *et al.*, 2002; Katz, 1981; Minshull *et al.*, 1994; Rodrigo *et al.*, 2009; Shipley *et al.*, 1979).

Seismic waves are sensitive to changes in seismic impedance  $Z$ , which is the product of seismic velocity and density. When the physical properties of the medium through which the wave is travelling change, seismic energy is partly transmitted and partly reflected across the boundary, following Snell's Law. These contrasts in impedance can be caused by changes in lithologies or in petrophysical properties such as porosity and fluid saturation between the sedimentary units. The typical indicators of gas hydrates in seismic data are the presence of bottom simulating reflections (BSRs) (Figure 2.1). BSRs are caused by an impedance contrast at the base of the gas hydrate stability

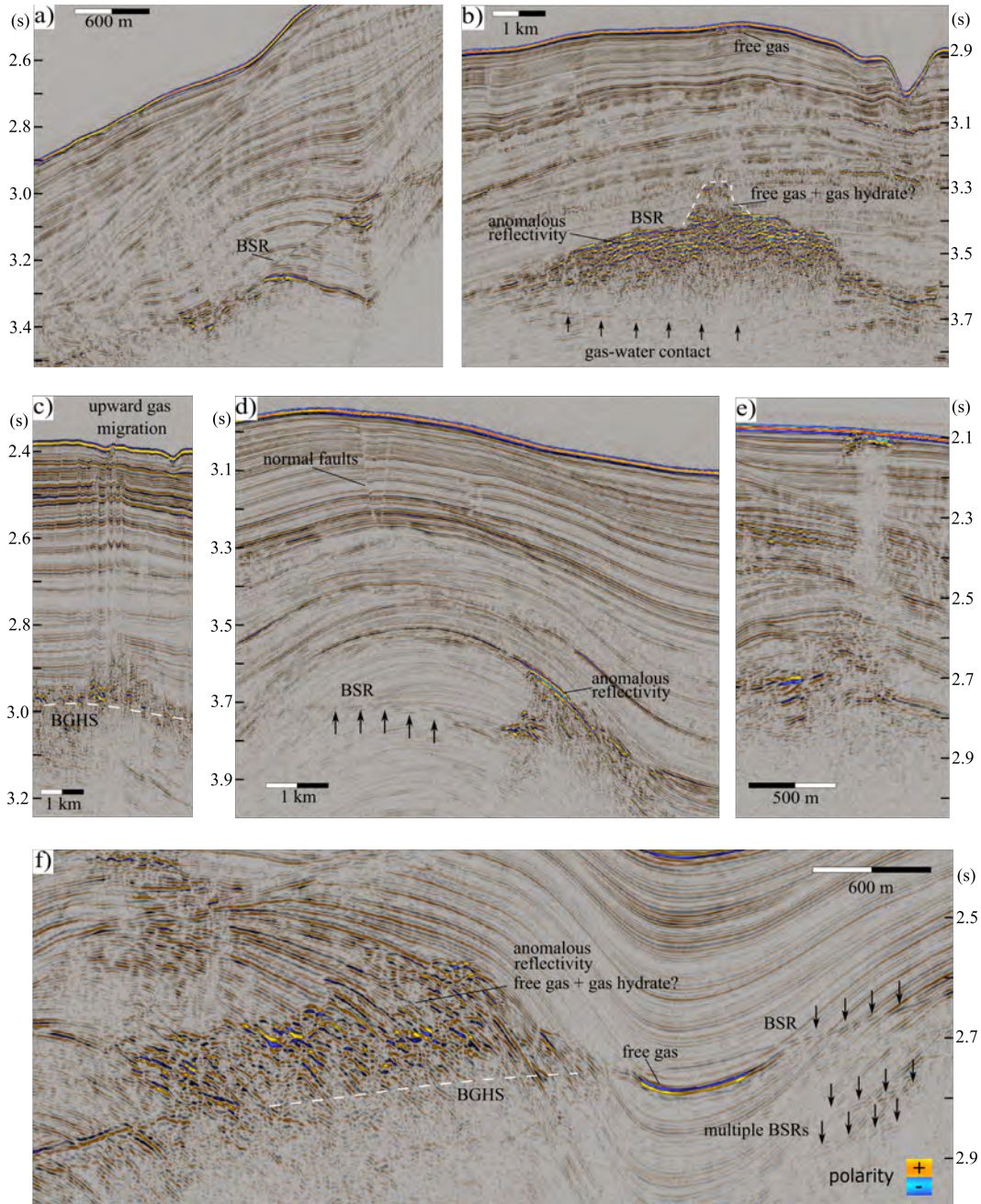


**Figure 2.1:** Examples of evidence of gas hydrates and free gas in seismic data. a), e) and f) are examples from Pahaua Bank (Lines TAN1808-46 in a) and f), and TAN1808-42 in e)); b) and d) from Mungaroa Ridge (Lines TAN1808-112 and TAN1808-108, respectively); c) is located at Tokorakau Ridge (Line TAN1808-56) . See Fig. 1.7 for locations.

zone (GHSZ), that arises from relatively higher velocities in the overlying gas hydrate-bearing sediments with respect to the free-gas bearing sediments below it. Pure gas

hydrate has a P-wave velocity ( $V_P$ ) of ca. 3300 m/s (Sloan, 1998), more than double that of seawater (ca. 1500 m/s). Because BSRs define a change in physical conditions and not a lithological boundary, they often cross-cut the stratigraphy (Figure 2.1a). The presence of multiple BSRs has been documented on the Hikurangi Margin and elsewhere (e.g., Auguy *et al.*, 2017; Barnes *et al.*, 2010; Crutchley *et al.*, 2019; Foucher *et al.*, 2002; Geletti and Buseti, 2011; Zander *et al.*, 2017) and it can be related to the migration of the base of the methane hydrate stability zone over time. There are different processes that could cause a shift of the BGHS on subduction margins: sea bottom warming, changes in sea level, sedimentation and erosion, tectonic uplift or advection of warm fluids from depth. Figure 2.1f shows an example from the southern Hikurangi Margin, while Han *et al.* (2021) extensively document and synthesise the occurrence of multiple BSRs on the northern Hikurangi Margin.

Other typical features observed in seismic data associated with gas hydrate systems are shown in Figure 2.1. Regions of anomalous high reflectivity are often observed at the base of the GHSZ (Figure 2.1b, 2.1d and 2.1f), which are caused by significant differences in acoustic impedance in porous strata hosting free gas and gas hydrates in high saturation (Colin *et al.*, 2020; Paganoni *et al.*, 2016; Qin *et al.*, 2020). The BGHS is typically imaged in the subsurface as having a negative polarity phase, as the deeper gas-bearing units are characterised by lower acoustic impedance with respect to water- or hydrate-bearing ones. Figure 2.1e and 2.1f show two examples of free-gas bearing strata. The example in Figure 2.1e appears to be contained by the decrease of permeability caused by the presence of gas hydrates in the pore space above the BSR. Figure 2.1f shows a manifestation of shallow free gas-charged sediments in the immediate vicinity of an active gas seep. Fluid migration features such as chimneys (Fig. 2.1c) are often associated with gas hydrate systems, indicating that overpressured fluids can form pathways through the GHSZ upwards towards the seafloor. Vigorous venting systems on the seafloor are often associated with wide regions of reduced amplitude (blanking) in the subsurface (Fig. 2.1e).

Despite the broad use of seismic methods for identifying natural gas hydrate occurrences since the 1960s (Makogon, 1966), quantitative resource assessments of gas hydrate reservoir formations are only available for a small number of locations worldwide, where accurate estimates of petrophysical properties are constrained by in-situ measurements such as wireline logging, logging-while drilling (LWD) or core data (e.g.,

Bellefleur *et al.*, 2012; Boswell *et al.*, 2017; Haines *et al.*, 2017; Shukla *et al.*, 2019; Taladay *et al.*, 2017). Challenges to quantifying the total amount of gas stored and released in these systems arise mainly from the difficulty to accurately constrain petrophysical properties such as porosity, gas hydrate morphology and saturation at the regional scale. Understanding the spatial distribution of these properties is the basis for any attempt of resource assessment of gas hydrates.

## 2.2 Seismic velocities

Important information that seismic data can give us about the subsurface physical properties is the speed at which sound waves travel through the media. The seismic velocity of a rock is mostly determined by its mineral composition and structure, but it is strongly influenced by properties like in situ confining stresses, pore pressure, fluid saturation, type of fluids, temperature and porosity. Therefore, the ability to retrieve velocity information from seismic data is a key step for any further physical characterisation of the Earth’s interior. There are different methods to estimate the subsurface distribution of seismic velocities from seismic data: semblance-based velocity analysis, traveltimes tomography and full-waveform inversion are the methods used and described in this thesis.

### 2.2.1 Semblance-based velocity analysis

Multi-channel seismic reflection data acquisition ensures the multifold coverage of a specific common mid point (CMP) location with non-zero offset seismic traces, thus allowing retrieval of the velocity structure of the subsurface. Under the assumption of horizontally stratified media, reflection traveltimes are described by hyperbolae governed by the traveltimes equation:

$$t^2(x) = t^2(0) + \frac{x^2}{V_{NMO}^2}, \quad (2.1)$$

where  $x$  is the offset (distance between source and receiver),  $V_{NMO}$  is the average velocity of the media above the reflecting interface and  $t$  is the traveltimes (Yilmaz, 2001). The normal move-out (NMO) describes the effect of the distance between the source and the receivers, located at different offsets;  $V_{NMO}$  is derived by Eq. 2.1 assuming a small-spread assumption (offsets are small compared to the target depth). The stacking velocity ( $V_{stk}$ ), on the other hand, is the velocity that yields the best

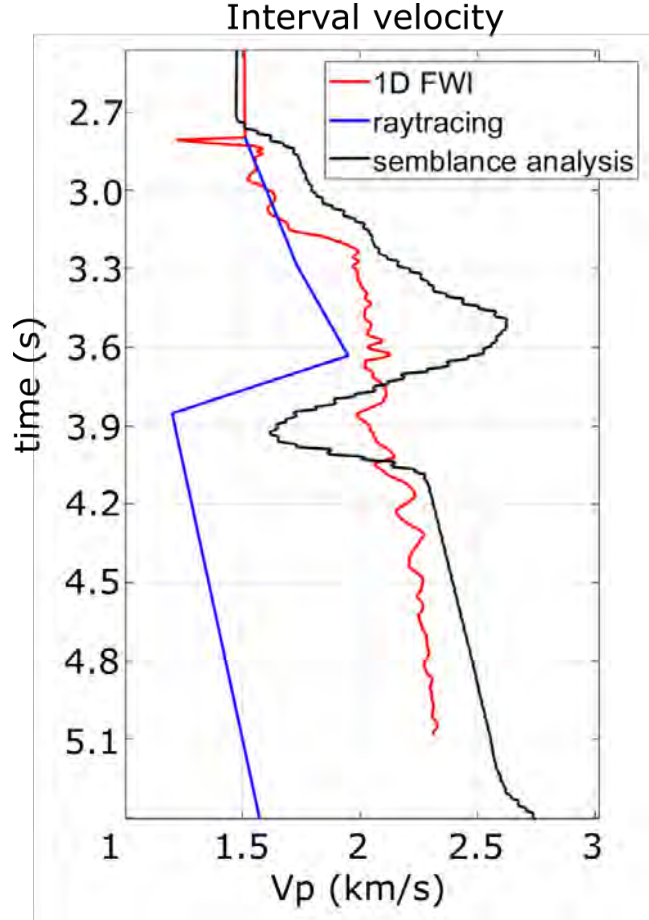


**Figure 2.2:** Comparison between profiles of interval velocities for CDP 5031 of Line APB13-21 estimated using different methodologies and converted to the time domain: semblance analysis, raytracing and 1D full-waveform inversion. The velocity values below the BSR ( $\sim 3.9$  s) are poorly constrained in all models by the lack of distinct seismic reflections in the data.

fit of traveltimes to a hyperbola within the entire spread length of the CMP gather (i.e. considering all offsets). In practice, these two velocities are often treated as being identical.

Semblance-based velocity analysis of reflection seismic data is performed on CMP gathers: the output is a velocity spectrum, that is a measure semblance along the hyperbolic trajectories of seismic events governed by velocity, offset, and traveltime. The 1D velocity profiles resulting from the velocity analysis represent the root-mean square velocity ( $V_{RMS}$ , Eq. 2.2), that is the velocity of a wave passing through layers of different interval velocity, and is equal to the stacking velocity when source-receiver

offset approaches zero and layers are horizontal and isotropic. The  $V_{RMS}$  at the reflector on which the depth point is situated is given by:

$$V_{RMS}^2 = \frac{1}{t(0)} \sum_{i=1}^N V_{INT,i}^2 \Delta t_i(0), \quad (2.2)$$

where  $\Delta t_i(0)$  is the vertical two-way-traveltime (TWT) of the  $i$ th layer, and  $t(0)$  is the total TWT from the surface to that layer. To calculate the interval velocity of a layer bounded by two reflectors ( $V_{INT}$ ), the Dix conversion formula is used:

$$V_{INT} = \sqrt{\frac{t_2 V_{RMS2}^2 - t_1 V_{RMS1}^2}{t_2 - t_1}}, \quad (2.3)$$

where  $t_2$ ,  $t_1$ ,  $V_{RMS2}$  and  $V_{RMS1}$  are the traveltimes and the RMS velocities of the deeper and the shallower reflectors, respectively. Semblance-based velocity analysis stands as a basis for the quantitative characterisation of the GHSZ (Chapters 3 and 4). Because conventional velocity analysis is based on the hyperbolic assumption, this method often fails to provide accurate velocities in areas with complex structures, dipping strata and sharp lateral changes in the subsurface physical properties.

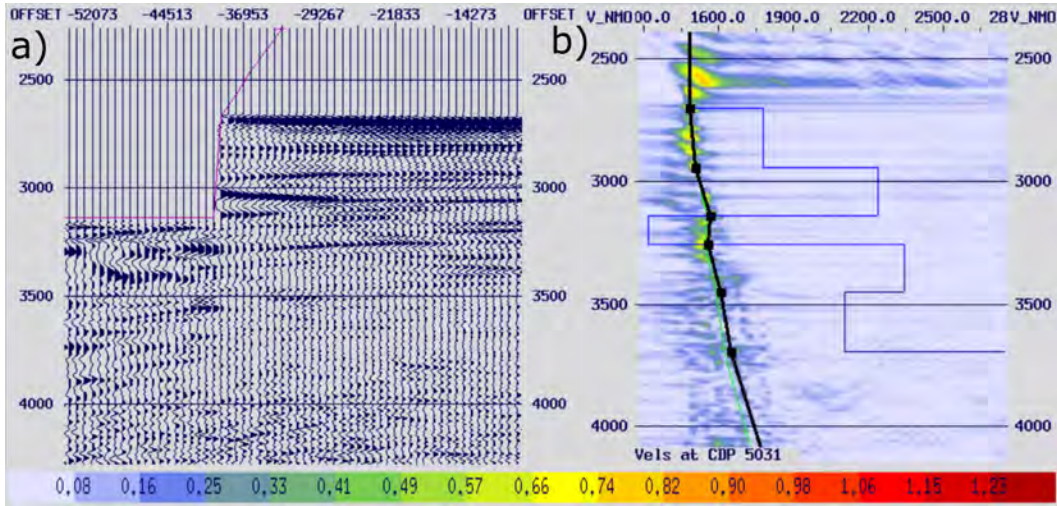


**Figure 2.3:** Example of the semblance spectrum of CDP 5031 of line APB13-21 (b) and the corresponding NMO-corrected CDP gather (a). The interval velocity profile is shown in Figure 2.2.

## 2.2.2 Traveltime tomography

The term tomography in seismology refers to the mathematical inverse method used for estimating the Earth's physical parameters through the back projection of seismic data along a raypath that connects sources and the receivers (Dziewonski and Anderson, 1984). The goal of traveltime tomography is to update the Earth model, in terms of seismic velocities, so that differences between the traveltime arrival of seismic waves in the observed data and that in the synthetic data are minimized. The reflection traveltime of a seismic wave from the source located at the surface to a reflection point in the subsurface and back to a receiver at the surface is given by an integral of the different traveltime segments along the raypath, which in turn depend on the seismic velocity at each point along the path. The inversion of traveltimes is by nature a non-linear problem, which can be formally linearized by a ray-theoretical approximation of the scalar wave equation, called the eikonal equation (Eq. 2.4), which gives the traveltime value  $T(x, y, z)$  for a ray passing through a point  $(x, y, z)$  in a medium with velocity  $v(x, y, z)$ :

$$\left(\frac{\delta T}{\delta x}\right)^2 + \left(\frac{\delta T}{\delta y}\right)^2 + \left(\frac{\delta T}{\delta z}\right)^2 = \frac{1}{v^2(x, y, z)}, \quad (2.4)$$

where the terms on the left represent the partial derivatives of the 3D traveltime surface  $T(x, y, z)$ , and the term on the right is the squared slowness. Kinematically, the solution to the eikonal equation is also a solution to the wave equation, and it represents the wavefront in three dimensions at a given instant of time. When this approximation is valid, small changes in the Earth's model parameters are linearly related to small changes in reflection traveltimes. Like all deterministic inversion methods, traveltime tomography can be used to update an existing initial model of the Earth's properties. During ray tracing, the partial derivatives of travel time with respect to the model velocities and the vertical position of layers' boundaries are calculated analytically. The traveltime residuals with respect to the observed data are also computed. The partial derivatives and traveltime residuals are used to update the model parameters in the optimization step by applying, for example, a method of damped least-squares to the linearized inverse problem (Zelt and Smith, 1992).



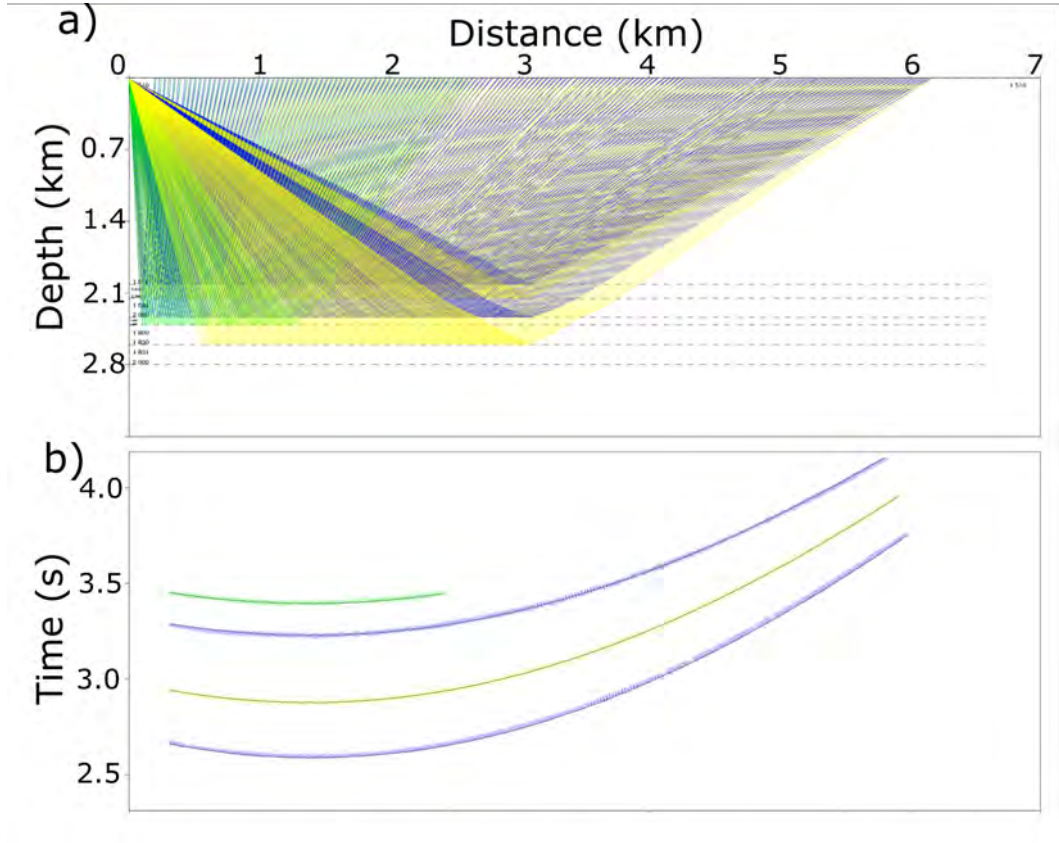


**Figure 2.4:** Results of 1D raytracing for CDP 5031 of Line APB13-21: a) shows the 1D model and the ray paths associated to the reflections picked in the seismic data displayed in (b). b) shows the results of the traveltimes inversion: the picks are displayed in a domain of time versus offset. The length of the picks represents the approximate error in picking reflections, whereas the black lines represent the best-fit move-out modelled by the raytracing algorithm. The inverted  $V_P$  model is shown in Figure 2.2.

### 2.2.3 Full-waveform inversion

The full-waveform inversion (FWI) methodology is capable of imaging the complex heterogeneous P-wave velocity field of the subsurface with high accuracy and resolution. Similarly to traveltime tomography, FWI is formulated as an ill-posed nonlinear optimization problem, with non-unique solutions, which seeks to minimize the difference between observed and forward modelled seismic data, updating the Earth model iteratively. However, contrary to traveltime tomography, which is a ray-based approach where sound is assumed to act as a ray, FWI is a wave-based method that relies on the numerical solution of the wave-equation (shown in its 3D scalar formulation in Eq.



2.5, where  $P(x, y, z)$  represents a compressional plane wave).

$$\nabla^2 P = \frac{\delta^2 P}{\delta x^2} + \frac{\delta^2 P}{\delta y^2} + \frac{\delta^2 P}{\delta z^2} = \frac{1}{v^2(x, y, z)} \frac{\delta^2 P}{\delta t^2}. \quad (2.5)$$

Therefore, the misfit function to be minimized is calculated considering not only the traveltimes, but also the phase and amplitude information of the seismic events. Chapter 5 provides further details into the method used in this thesis, which consist of a 1D full-waveform inversion code presented by Kormendi and Dietrich (1991) and extensively applied to gas hydrate studies worldwide (e.g., Crutchley *et al.*, 2011; Gorman *et al.*, 2002; Korenaga *et al.*, 1997; Pecher *et al.*, 1996; Singh and Minshull, 1994). In this method, synthetic seismograms are forward modelled using the generalised reflection-transmission matrix method (Kennett and Kerry, 1979), and the misfits with the observed data are calculated in the frequency-slowness ( $\omega - p$ ) domain following the objective function:

$$S(m) = \frac{\|d - d_{obs}\|_D^2 + \|m - m_0\|_M^2}{2}, \quad (2.6)$$

where  $d_{obs}$  is the observed data,  $d = f(m)$  is the synthetic data,  $f$  is the operator that maps the Earth model  $m$  from the model space  $M$  to the data domain  $D$ ,  $m_0$  is the initial model and  $\|$  is the  $L_2$ -norm. The search for the minimum of the objective function starts in the vicinity of the starting model, and the model update at each iteration can be written as a perturbation of the model parameters  $\Delta m$ . Applying a second order Taylor expansion of the objective function and taking the partial derivative with respect to the Earth model parameters gives the Frechet derivative (Eq. 2.7), which allows relating changes in the objective function to changes in the model.

$$\frac{\delta S(m + \Delta m)}{\delta m} = \frac{\delta S(m)}{\delta m} + \frac{\delta^2 S(m)}{\delta m^2} \Delta m, \quad (2.7)$$

This derivative will become zero when the inversion converges on the correct model, in other words when  $m = m_0 + \Delta m$ , with  $\Delta m$  being the optimal model perturbation. By setting Eq. 2.7 equal to zero and, by rearranging, the expression of the model perturbation is obtained:

$$\Delta m = -\frac{\delta S(m)}{\delta m} \left( \frac{\delta^2 S(m)}{\delta m^2} \right)^{-1}, \quad (2.8)$$

where the term  $\frac{\delta S(m)}{\Delta m}$  is referred to as the gradient, and the term  $\frac{\delta^2 S(m)}{\delta m^2}$  is referred to as the Hessian. The gradient represents the direction of model update along which the optimal step length can be found through linear search methods such as the conjugate-gradient method (Shewchuk *et al.*, 1994).

As for traveltime tomography, FWI is used to update an existing starting model of the subsurface. Therefore, it requires an accurate starting velocity model (long-wavelength velocity variation) based on, for example, a prior traveltime inversion or semblance-based velocity analysis, in order to estimate the fine-scale, short-wavelength velocity structure (Dietrich and Kormendi, 1990; Kormendi and Dietrich, 1991).

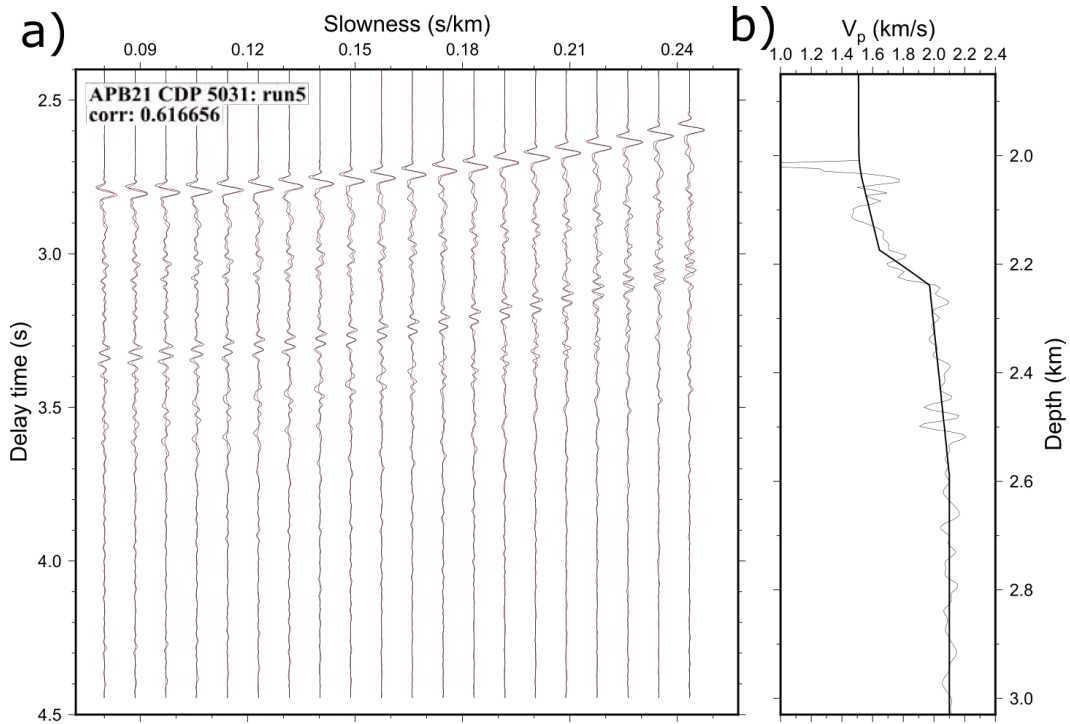


**Figure 2.5:** 1D full-waveform inversion results for CDP 5031 of Line APB13-21: a) shows the comparison between synthetic and real  $\tau$ - $p$  seismograms after 5 successive runs. The correlation coefficient is displayed. b) shows the starting (bold black line) and inverted (grey line)  $V_P$  models.

## 2.3 Rock physics modelling

To be able to estimate the petrophysical properties of the subsurface, such as porosity, mineralogy and fluid or hydrate saturations, they need to be related to the elastic

properties of a porous rock. Rock physics models provide the link between these properties (Dvorkin *et al.*, 2014; Mavko *et al.*, 2020). Different types of rock physics models for hydrate-bearing sediments have been proposed in the literature, and they can be classified in two major groups: 1) empirical models, where rock physics equations are derived based on empirical relations between the physical properties of interest measured in laboratory (Lee *et al.*, 2010, 1996; Wood, 1946; Wyllie *et al.*, 1958) and 2) analytical models, where physics-based equations are derived (Dvorkin *et al.*, 2000; Helgerud *et al.*, 2000; Minshull *et al.*, 1994; Tinivella, 1999).

The first class of models have been successfully applied to the study of gas hydrate reservoirs worldwide, although they cannot be easily extended to general applications because of their dependence on site-specific conditions. For example, Lee *et al.* (1996) apply a weighted equation (Eq. 2.9) based on the three-phase time-average (Wyllie *et al.*, 1958) and the Wood (1941) equations to relate the  $V_P$  and the hydrate saturation of unconsolidated hydrate bearing sediments:

$$\frac{1}{V_P} = \frac{W_\phi(1 - S_H)^n}{V_{P,Wood}} + \frac{1 - W_\phi(1 - S_H)^n}{W_{P,TA}} \quad (2.9)$$

where  $V_{P,wood}$  is the expected P-wave velocity calculated with the Wood equation,  $V_{P,TA}$  is the P-wave velocity calculated with the three-phase time-average equations,  $W$  is a weighting factor of the contribution of the time average and the Wood equations, and  $n$  is a constant simulating the rate of lithification with hydrate concentration. The second type of models are considered predictive, as they are based on first physical principles and do not depend on site-specific parameters. In the next section, I will describe one of the most commonly used models for unconsolidated sediments bearing gas hydrates.

### 2.3.1 Effective medium theory

Helgerud *et al.* (2000) proposed a physics-based effective-medium model for sediments containing gas hydrate to quantify gas hydrate saturation from elastic properties. Effective medium models for sediments containing gas hydrate, as developed by Dvorkin *et al.* (2000), rely on the concept of critical porosity  $\phi_0$ , i.e., the porosity value that marks the transition between the elastic behaviour of a suspension and that of a grain-supported rock. This value is typically about 0.4 for sedimentary rocks (Mavko

*et al.*, 2020). In the models proposed by Dvorkin *et al.* (2000), the sediments containing gas hydrate are modelled by averaging the elastic properties of the material at the critical porosity and the pure solid phase material at zero porosity. The models use the effective moduli of a dense random packing of identical spheres.

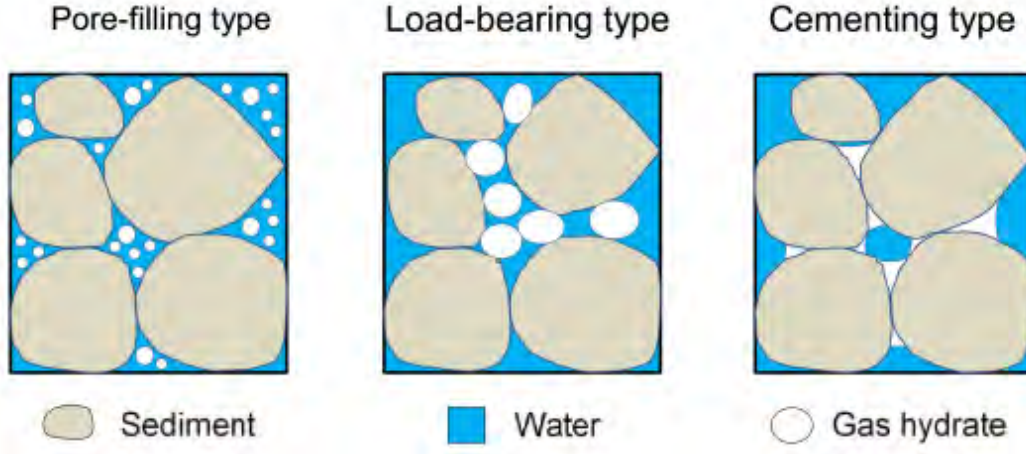


**Figure 2.6:** Different types of hydrate morphologies, after Fang *et al.* (2020)

The hydrate fraction is modelled as part of the matrix phase as an effective medium in which the elastic moduli, i.e., the matrix bulk modulus  $K_{mat}$  and the matrix shear modulus  $G_{mat}$ , are computed by averaging the elastic moduli of the mineral component and that of the hydrate weighted by their fractions, using Hill's average (Helgerud *et al.*, 2000):

$$K_{mat} = \frac{1}{2} \sum_{i=1}^N \left( f_i K_i + \frac{f_i}{K_i} \right), \quad (2.10)$$

$$G_{mat} = \frac{1}{2} \sum_{i=1}^N \left( f_i G_i + \frac{f_i}{G_i} \right), \quad (2.11)$$

where  $f_i$  is the weight fraction of the solid phase (quartz, clay, hydrate) and  $K_i$  and  $G_i$  are their bulk and shear moduli, respectively. The volume of hydrate is:

$$v_{hyd} = \phi S_H, \quad (2.12)$$

where  $\phi$  is the original porosity and  $S_H$  the hydrate saturation. Since the hydrate is considered part of the solid frame, the reduced effective porosity is given by:

$$\phi_{eff} = \phi(1 - S_H), \quad (2.13)$$

and volumetric fractions of the solid phases are:

$$f_i = \frac{v_i}{1 - \phi_{eff}}, \quad (2.14)$$

where  $v_i$  are the volumes of each constituent of the matrix. The fractions are normalized such that their sum equals 1 in order to compute the elastic moduli of the whole solid. At the critical porosity  $\phi_0$ , the values of the bulk modulus  $K_{HM}$  and shear modulus  $G_{HM}$  of the dry rock are computed using Hertz-Mindlin equations:

$$K_{HM} = \sqrt[3]{\frac{P_e[n(1 - \phi_0)G_{mat}]^2}{18[\pi(1 - \nu)]^2}}, \quad (2.15)$$

$$G_{HM} = \frac{5 - 4\nu}{5(2 - \nu)} \sqrt[3]{\frac{3P_e[n(1 - \phi_0)G_{mat}]^2}{2[\pi(1 - \nu)]^2}}, \quad (2.16)$$

where  $P_e$  is the effective pressure in gigaPascals,  $n$  is the average number of contacts per grain and  $\nu$  is the Poisson's ratio of the solid matrix phase. For porosity values below the critical porosity  $\phi_0$ , the bulk modulus  $K_{dry}$  and shear modulus  $G_{dry}$  of the dry rock are computed using the modified Hashin-Shtrikman lower bounds (Mavko *et al.*, 2020):

$$K_{dry} = \left( \frac{\frac{\phi}{\phi_0}}{K_{HM} + \frac{4}{3}G_{HM}} + \frac{1 - \frac{\phi}{\phi_0}}{K_{mat} + \frac{4}{3}G_{HM}} \right)^{-1} - \frac{4}{3}G_{HM}, \quad (2.17)$$

$$G_{dry} = \left( \frac{\frac{\phi}{\phi_0}}{G_{HM} + \zeta} + \frac{1 - \frac{\phi}{\phi_0}}{G_{mat} + \zeta} \right)^{-1} - \zeta, \quad (2.18)$$

where

$$\zeta = \left( \frac{G_{HM}}{6} \right) \frac{9K_{HM} + 8G_{HM}}{K_{HM} + 2G_{HM}}. \quad (2.19)$$

Similarly, for porosity values above the critical porosity  $\phi_0$ , the bulk modulus  $K_{dry}$  and shear modulus  $G_{dry}$  are computed using the Reuss (1929) average. Gassmann's equations (Mavko *et al.*, 2020) are then applied to include the water effect and to compute elastic moduli of the water-saturated rock:

$$K_{sat} = K_{dry} + \frac{\left(1 - \frac{K_{dry}}{K_{mat}}\right)^2}{\frac{\phi}{K_w} + \frac{1-\phi}{K_{mat}} - \frac{K_{dry}}{K_{mat}^2}}, \quad (2.20)$$

$$G_{sat} = G_{dry}, \quad (2.21)$$

where  $K_w$  is the bulk modulus of water. P-wave and S-wave velocity are computed as:

$$V_P = \sqrt{\frac{K_{sat} + \frac{4}{3}G_{sat}}{\rho}}, \quad (2.22)$$

$$V_S = \sqrt{\frac{G_{sat}}{\rho}}, \quad (2.23)$$

where  $\rho$  represents density. The density of the saturated rock is given by:

$$\rho = (1 - \phi)\rho_{mat} + \phi\rho, \quad (2.24)$$

where  $\rho_{mat}$  is the density of the matrix, computed as a linear average of densities of the minerals and hydrate, and  $\rho_w$  is the density of water (see Table 2.3.1 for details).

The elastic properties of hydrate-bearing sediments are affected by the microscopic distribution of the hydrate within the pore space, as well as by the amount of gas hydrate present (e.g., Lee and Collett, 2001). Generally, because of the solid state of methane hydrate, the bulk and shear moduli are greater in rocks that contain gas hydrates. Therefore, compressional and shear wave velocities are higher in hydrate-bearing sediments when compared to water-saturated rocks, even though the bulk density slightly decreases (Dai *et al.*, 2004b). The various types of hydrate occurrence will affect the elastic properties of the sediment in different ways. Several rock physics models exist in the literature that quantify the effect of hydrate concentrations and

type of occurrence on elastic properties (Chand *et al.*, 2004; Dvorkin *et al.*, 2000; Sava and Hardage, 2006; Xu *et al.*, 2004).

Phase	Bulk modulus K (GPa)	Shear modulus G (GPa)	Density $\rho$ (g/cm <sup>3</sup> )	Reference
Quartz	36.6	45	2.65	Helgerud et al. (1999)
Clay	21	7	2.58	Mavko et al. (2009)
Hydrate	8.4	3.5	0.91	Helgerud et al. (2009)
Water	2.3	0	1.035	Helgerud et al. (1999)

**Table 2.1:** Examples of rock physics model parameters.

## 2.4 Hydroacoustic characterisation of gas seeps

On subduction margins, fluids are released both from the subducting plate and from the accretionary wedge, due to dewatering of the subducting sediments and porosity reduction within the wedge caused by tectonic compression (Barnes *et al.*, 2010), as shown in Figure 2.7.

Fluid migration is mostly dependent on the existence of permeable pathways such as fracture zones, faults or permeable strata (Hillman *et al.*, 2020, Crutchley *et al.* 2021), that allow the fluids to migrate upwards towards the seafloor. On the seafloor, gas seeps are the most common manifestations of ongoing subsurface fluid flow (Judd and Hovland, 2009). The gases that are expelled from cold seeps on continental margins are primarily composed of methane, leaving major questions open on how much methane reaches the ocean surface (McGinnis *et al.*, 2006; Shakhova *et al.*, 2010), how the seeps are connected to deep hydrocarbon systems and what role gas hydrate dissociation plays (Reagan *et al.*, 2011), how the gas flow rates change with time and whether or not there is a relationship between fluid flow and seismicity (Bassett *et al.*, 2014; Bonini, 2019; Legrand *et al.*, 2021).

Estimating the temporal variability of the gas flow rate at seep sites and quantifying gas volumes escaping from the seafloor has recently become a challenge that can be addressed by acoustic monitoring of the water column.

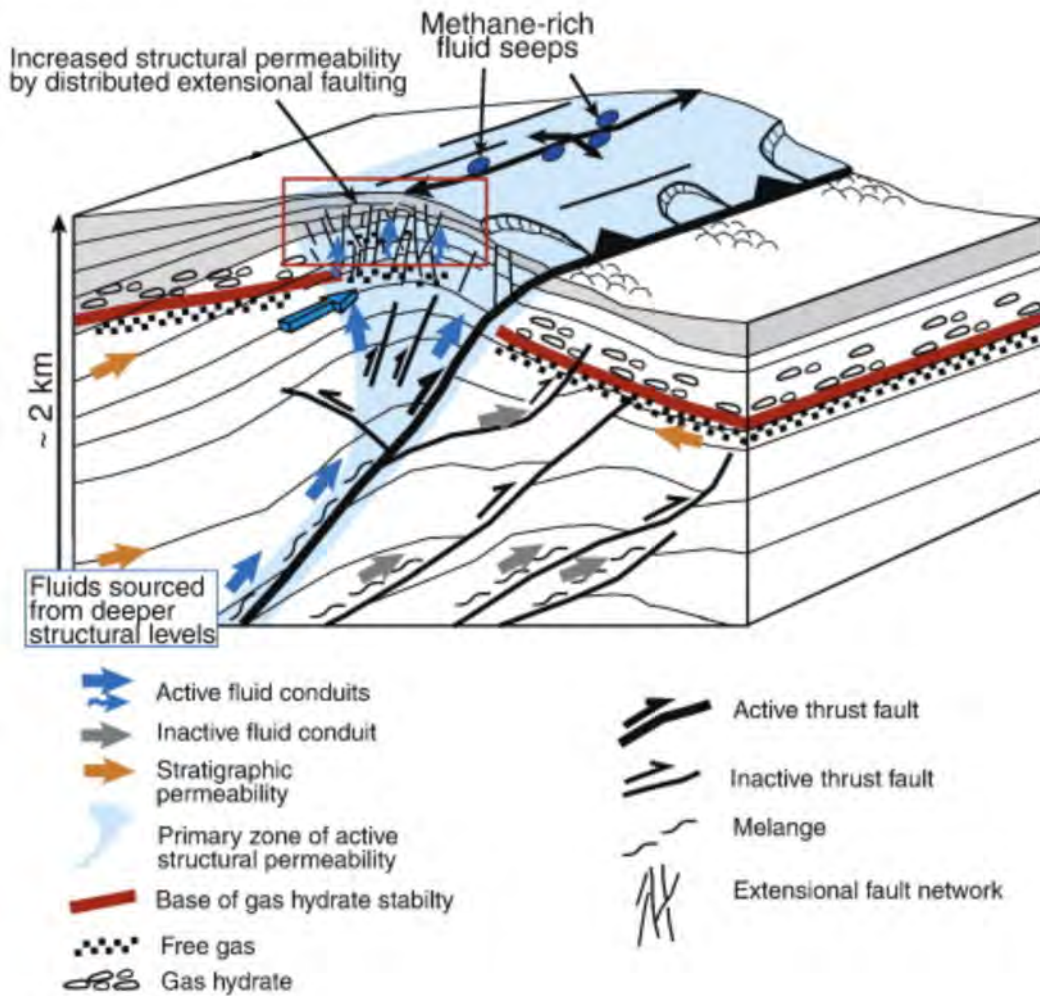


**Figure 2.7:** Conceptual model of the structural and stratigraphic permeability beneath active gas seeps located at the thrust ridges on the southern Hikurangi Margin. Image after Barnes *et al.* (2010).

### 2.4.1 Acoustic imaging of gas flares

Active hydroacoustic systems are efficient tools for detecting and imaging free gas seepage in marine environments. Gas bubbles rising in the water are excellent acoustic targets due to their strong contrast in acoustic impedance with respect to the surrounding medium, and can be detected in sonar systems. Bubble clouds arising from cold vents are typically referred to as "flares" in acoustic water column data (i.e. echograms from single-beam echosounders), because of the typical shape they produce when ensonified (Fig. 2.8). Acoustic surveys using multi-beam, single-beam or split-beam echosounders have been used as a standard method for studies of gas emissions in marine settings, for example, in the Black Sea (Greinert *et al.*, 2010), in the North



Sea (Böttner *et al.*, 2020; von Deimling *et al.*, 2011), in the Sea of Marmara (Dupré *et al.*, 2015), as well as in coastal lagoon environments (Duarte *et al.*, 2007) and in lakes (Granin *et al.*, 2010).

## **Multibeam**

Multi-beam echosounders systems (MBES) ensonify a swath below the hull of the ship, providing swath bathymetric data, as well as acoustic images of the water column (Fig. 2.8b). Although these systems are typically used for bathymetric surveys, they have increasingly been applied to oceanographic studies in recent decades (Colbo *et al.*, 2014). The advantage of MBES systems is the ability to acoustically image large areas of the ocean, providing high temporal and spatial resolution data. The data analysed and presented in this thesis were acquired using a hull-mounted Kongsberg Simrad EM302 onboard R/V Tangaroa during several scientific surveys (see Chapters 1 and 6). This echo-sounder operates at a frequency of 30 kHz, with an angular sector of 140°, providing across track coverage of about 3 to 5 times the water depth (depending on depth and mode) and a maximum ping rate of 10 Hz.

## **Singlebeam**

Active hydroacoustic systems are efficient tools for detecting and imaging free gas seepage in marine environments. Gas bubbles rising in the water are excellent acoustic targets due to their strong contrast in acoustic impedance with respect to the surrounding medium, and can be detected in sonar systems. Bubble clouds arising from cold vents are typically referred as "flares" in acoustic water column data (i.e. echograms from single-beam echosounders), because of the typical shape they produce when ensonified (Fig. 2.8). Acoustic surveys using multi-beam, single-beam or split-beam echosounders have been used as a standard method for studies of gas emissions in marine settings, for example, in the Black Sea (Greinert *et al.*, 2010), in the North Sea (Böttner *et al.*, 2020; von Deimling *et al.*, 2011), in the Sea of Marmara (Dupré *et al.*, 2015), as well as in coastal lagoon environments (Duarte *et al.*, 2007) and in lakes (Granin *et al.*, 2010).

## **Multibeam**

Multi-beam echosounders systems (MBES) ensonify a swath below the hull of the ship, providing swath bathymetric data, as well as acoustic images of the water column

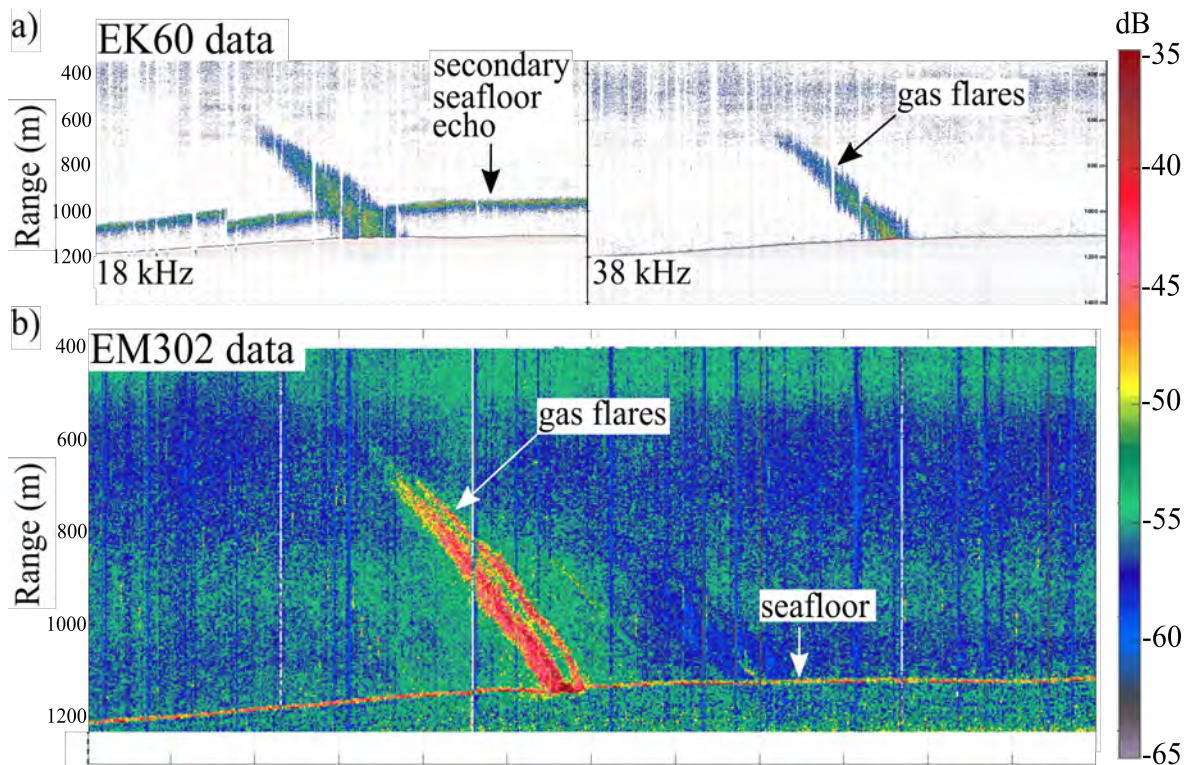


**Figure 2.8:** Example of the use of hydroacoustic data to image water column features such as gas flares (TAN2012 dataset). a) Split-beam echo sounder  $S_v$  data (EK60) representing the 18 kHz and 38 kHz channels; b) range-stacked view of the same flare as in a) in the multibeam EM302 data.

(Fig. 2.8b). Although these systems are typically used for bathymetric surveys, they have increasingly been applied to oceanographic studies in recent decades (Colbo *et al.*, 2014). The advantage of MBES systems is the ability to acoustically image large areas of the ocean, providing high temporal and spatial resolution data. The data analysed and presented in this thesis were acquired using a hull-mounted Kongsberg Simrad EM302 onboard R/V Tangaroa during several scientific surveys (see Chapters 1 and 6). This echo-sounder operates at a frequency of 30 kHz, with an angular sector of 140°, providing across track coverage of about 3 to 5 times the water depth (depending on depth and mode) and a maximum ping rate of 10 Hz.

## 2.4.2 Bubble backscatter theory and modelling

In this section, I present a theoretical model to estimate the relationship between the backscattering strength in the acoustic data and the quantity of gas bubbles present in the water column (Leblond *et al.*, 2014; MacLennan *et al.*, 2002). The energy reflected (or backscattered) by a single bubble of radius  $a$  in the water is often modeled as an equivalent surface referred to as acoustic backscattering cross-section ( $\sigma_{bs}$ ), expressed in  $\text{m}^2$  (Ainslie and Leighton, 2009; MacLennan *et al.*, 2002).

$$\sigma_{bs} = \frac{4\pi a^2}{\left(\frac{\omega_1}{\omega} - 1\right)^2 + \delta^2}, \quad (2.25)$$

where  $\omega$  is the frequency of the active source of the acoustic signal,  $\omega_1$  is the resonance frequency of the bubble and  $\delta$  is a dimensionless frequency-dependant damping constant (Ainslie and Leighton, 2009). For a bubble cloud, the total backscattering volume coefficient ( $s_v$ , in  $\text{m}^{-1}$ ) is given by the contribution of all single targets:

$$s_v = \int \sigma_{bs} n(a) da, \quad (2.26)$$

where  $n(a)$  is the concentration of bubbles in  $\text{m}^{-3}$ , per classes of size (radii)

$$n(a) = \frac{n^\circ \text{ of bubbles of radius } a}{\text{volume}}. \quad (2.27)$$

When the bubble size distribution is unknown (e.g. when no quantitative optical measurements of the bubble cloud are available), multi-frequency acoustic measurements are an efficient tool to estimate  $n(a)$ , as explained in detail in Chapter 6.

Equation 2.26 states that the volume backscattering coefficient is controlled by the bubble size distribution (BSD) and by the single bubble backscattering cross-section  $\sigma_{bs}$  (Eq. 2.25). In decibels, the backscattering cross-section of a single bubble is expressed as the target strength:

$$TS = 10 \log_{10}(\sigma_{bs}), \quad (2.28)$$

and the volume backscattering coefficient of multiple discrete bubbles is then expressed as the volume backscattering strength:

$$S_v = 10 \log_{10}(s_v), \quad (2.29)$$

both in dB relative to 1 m<sup>2</sup>. In the literature, theoretical models to predict the acoustic backscattering cross-section of underwater bubbles differ in terms of parameters such the bubble size, its morphology, the frequency range of the acoustic signal and the environment characteristics. For the scope of this thesis, the model proposed by Ainslie and Leighton (2009) is used (Eq. 2.25).

## 2.5 Controlled-source electromagnetic methods

Another effective tool for the detection of gas hydrates is electromagnetic surveying. Like all hydrocarbons, hydrate-bearing sediments are electrically more resistive than the surrounding sediments saturated with seawater. Controlled-source electromagnetic methods (CSEM) are sensitive to changes in the bulk resistivity of the subsurface, and are commonly used for hydrocarbon exploration (Liu *et al.*, 2020). Offshore CSEM surveys consist in deep-towing a series of electromagnetic receivers and an electric dipole transmitter around 50 m above the seafloor (Figure 2.9). The analysis and inversion of resistivity data is useful to constrain the amount of hydrocarbon contained in the sediments, although it doesn't allow to distinguish between free-gas and gas hydrate. Often, the joint analysis and inversion of elastic and electromagnetic data is carried out to achieve a more detailed characterisation of gas hydrate systems (Berndt *et al.*, 2019; Kannberg and Constable, 2020).

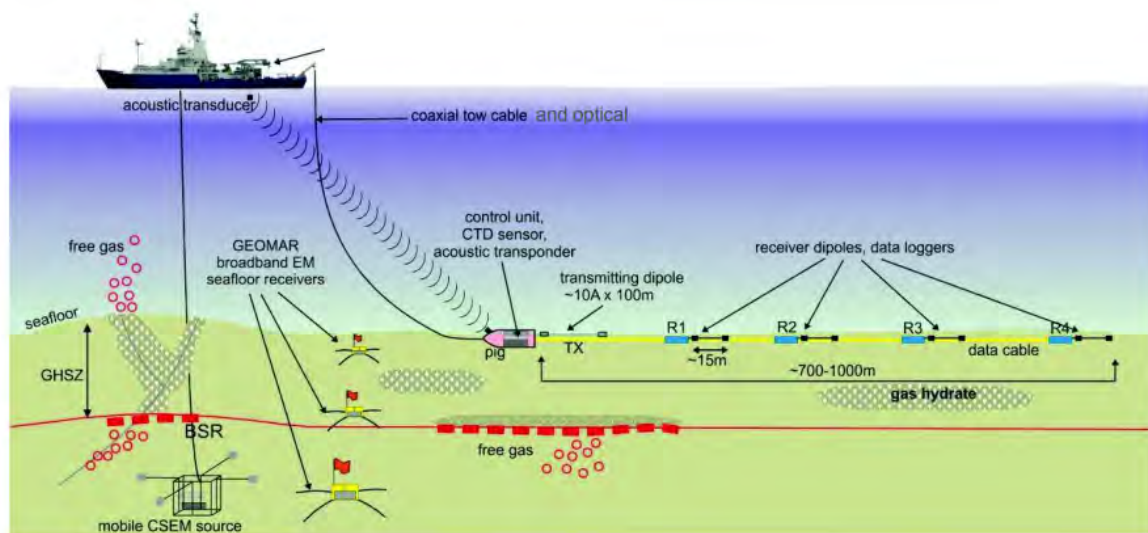


**Figure 2.9:** Example of two marine CSEM experiments (Schwalenberg *et al.*, 2016)

## Chapter 3

# Seismic velocity and reflectivity analysis of concentrated gas hydrate deposits on the southern Hikurangi Margin

This chapter presents a detailed analysis of two concentrated gas hydrate accumulations at Glendhu and Honeycomb ridges, and a first attempt to quantify the gas hydrate saturation at discreet selected locations, based on a combined reflectivity and velocity analysis of seismic data. This work has been published as *Seismic velocity and reflectivity analysis of concentrated gas hydrate deposits on the southern Hikurangi Margin (New Zealand)* by Turco F., Crutchley G.J., Gorman A.R., Mountjoy J.J., Hillman J.I.T. and Woelz S. in the journal *Marine and Petroleum Geology*;

### **CRedit: authors' contribution**

Turco F.: Conceptualisation, Software, Formal analysis, Investigation, Data Curation, Writing - Original Draft.

Crutchley G.J.: Conceptualisation, Methodology, Software, Validation, Resources, Supervision, Writing - Review and Editing.

Gorman A.R.: Supervision, Methodology, Writing - Review and Editing, Resources, Validation.

Mountjoy J.J.: Writing - Review and Editing, Data Curation.

Hillman J.I.T.: Data Curation.

Woelz S.: Data Curation.

## 3.1 Introduction

As explained in Section 2.3, the seismic response of hydrate-bearing sediments varies significantly according to the nature and stratigraphic architecture of sedimentary units, as well as the degree of saturation, as described in detail by Boswell *et al.* (2016a). For instance, consider a sand unit of low seismic impedance buried between two consolidated (high impedance) mud units. With low levels of gas hydrate saturation in the sand unit, the impedance of that layer will begin to increase and approach the impedance of the neighbouring mud units, which could theoretically result in a suppression of reflectivity from the mud-sand interface (Boswell *et al.*, 2016a; Dillon *et al.*, 1991; Lee and Dillon, 2001; Yoo *et al.*, 2013). As saturations increase to higher levels (e.g. above 40%), the presence of hydrate in the pore space can lead to significantly higher impedance in the sand unit than that of the surrounding mud units (Boswell *et al.*, 2016a). In this case, strong positive polarity reflections from the hydrate-bearing layer are to be expected. It is also possible that the background (“hydrate free”) impedance of a gas hydrate reservoir layer is higher than surrounding layers, meaning that the reflection marking the reservoir layer is a peak rather than a trough. In such a case, any increase in hydrate saturation within the reservoir layer will simply increase its impedance and thereby increase the amplitude of the positive polarity reflection. In general, high amplitude reflections within the GHSZ, with similar polarity to that of the seafloor are expected to indicate highly concentrated gas hydrate accumulations (several tens %, Bellefleur *et al.*, 2006; Boswell *et al.*, 2016a; Nouzé *et al.*, 2004). If a coherent reflection can be traced from beneath the BSR to above the BSR, a clear change in polarity is often identifiable, marking the change from gas-charged strata (negative polarity) below, to gas hydrate-charged strata (positive polarity) above. Within the GHSZ, anomalous reflectivity corresponding to gas hydrate-bearing sediments should reveal positive polarity events, i.e. the same polarity as the seafloor and opposite polarity to the BSR. However, in geological settings where the sediment layers’ thicknesses are below the vertical seismic resolution, tuning effects often occur, and the identification of hydrate-bearing strata may no longer be possible based only on polarity observations.

Glendhu and Honeycomb ridges are thrust ridges that lie at the toe of the Hikurangi accretionary wedge in water depths ranging from 2100 to 2800 m (Fig. 3.1). A recent synthesis of 2D industry seismic surveys allowed the identification and mapping of highly reflective features within the GHSZ on the southern Hikurangi Margin (Crutch-

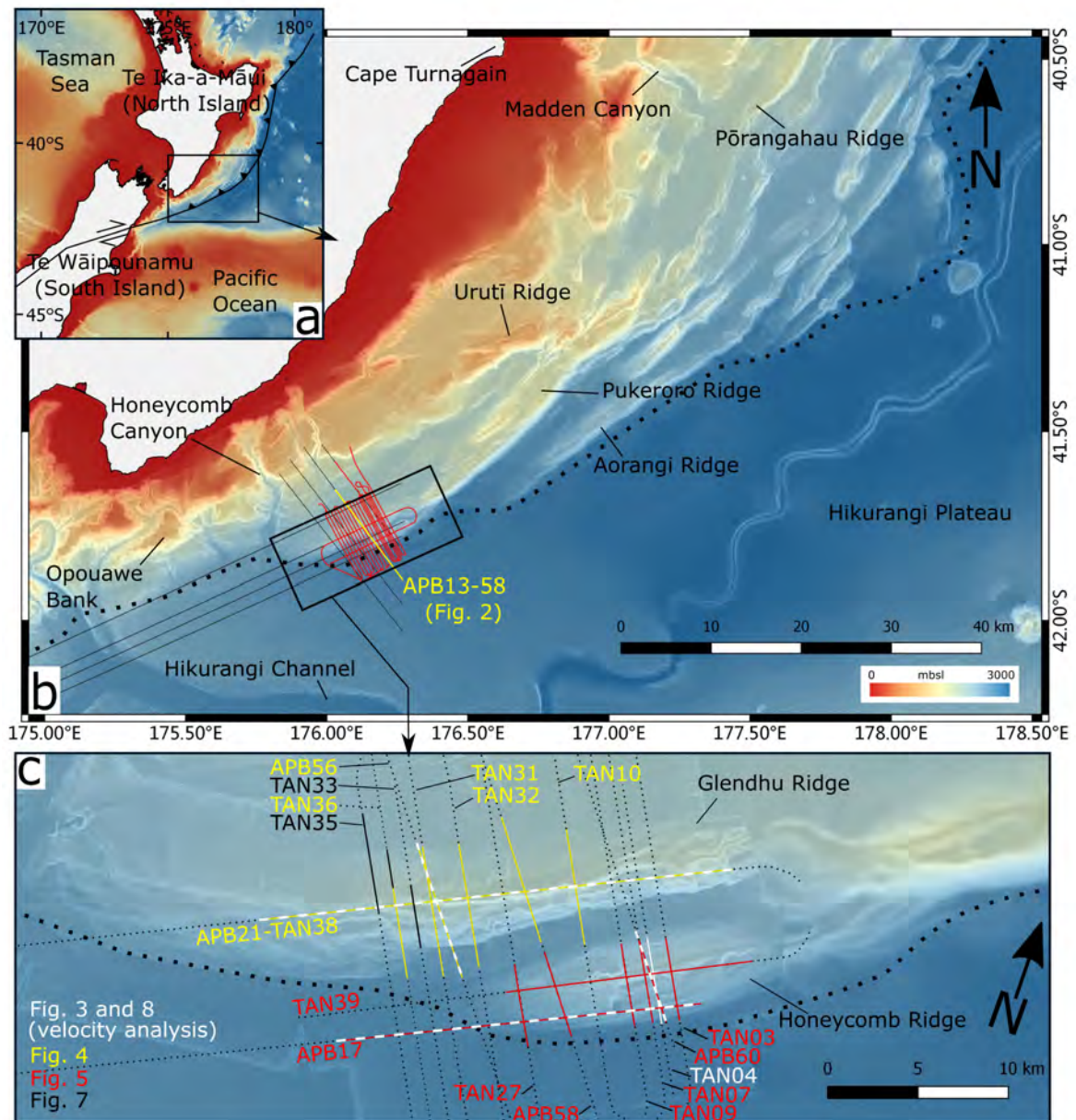


**Figure 3.1:** a) Overview of the geographic and tectonic setting of the Hikurangi Margin in New Zealand; b) Setting of the southern Hikurangi Margin and the available seismic reflection profiles: red lines correspond to the TAN1808 data set, black lines to the APB13 data set. The dotted black line represents the approximate seafloor location of the deformation front. In yellow is the seismic section APB13-58 shown in Fig. 1.7. c) Enlargement of the study area of Glendhu and Honeycomb ridges: the bold dotted line is the deformation front; the fainter dotted black lines are the seismic profiles presented in this paper. The lines coloured white, red, yellow and black correspond to the portions of seismic profiles shown in Figures 3.2, 3.3, 3.4 and 3.6, respectively.



ley *et al.*, 2019). These data reveal both positive and negative seismic polarity features that have been interpreted as concentrated gas hydrate and free gas accumulations, respectively, within layers that are interpreted as relatively high-permeability units.

In this chapter, regions of anomalously high reflectivity above the BSR are identified as accumulations of concentrated gas hydrate, following the approach set out, for example, in Boswell *et al.* (2016a). The over-arching objective of this chapter is to provide a detailed characterisation of the gas hydrate system at Glendhu and Honeycomb ridges on the southern Hikurangi Margin. Moreover, the identification of anomalous positive polarity events is enhanced by quantifying the amount of gas hydrate present in the pore space of selected sedimentary layers at the top of the concentrated hydrate zones (CHZ). To this end, a relationship between the seismic velocity and reflectivity of these seismic events and the gas hydrate saturation ( $S_H$ ) is established through rock physics models for hydrate-bearing sediments (Dvorkin *et al.*, 2000; Lee *et al.*, 1996). Following this approach, I make first-order local estimations of gas hydrate saturation within the concentrated hydrate zones. The effective medium model for gas hydrate-bearing sediments (Dvorkin *et al.*, 2000) systematically predicts higher gas hydrate saturations than the three-phase weighted equation (Lee *et al.*, 1996), which probably underestimates the amount of gas hydrate present in the pore space. The results presented in this chapter confirm that high gas hydrate saturations ( $>40\%$ , Yun *et al.*, 2005) can cause significant seismic amplitude anomalies within the GHSZ. Moreover, I show that the combined analysis of seismic velocity and reflectivity is a reliable method to locally estimate gas hydrate saturation based on multi-channel seismic (MCS) data.

## 3.2 Seismic data processing

This study is based on multi-channel seismic reflection profiles from two datasets: APB13 (R/V Duke, 2013) and TAN1808 (M/V Tangaroa, 2018). The acquisition parameters are described in Table 3.2. The two datasets provide a complementary basis for characterising gas hydrate systems. The long-streamer low frequency (35 Hz) APB13 industry data enable to image large-scale features, obtain P-wave velocity models from seismic velocity analysis, and calculate the seafloor reflection coefficient at each CDP. In contrast, the short-streamer higher frequency (95 Hz) TAN1808 data allow imaging high-amplitude anomalies at higher resolution and carry out more detailed reflectivity analysis on selected seismic events.

Survey	APB13	TAN1808
<b>Energy source (total capacity)</b>	Airgun (3610 cu. in)	GI gun (45/105 cu. in)
<b>Record length</b>	10500 ms	5000-6000 ms
<b>Shot spacing</b>	37.5 m	12.5 m
<b>Streamer length</b>	8100 m	600 m
<b>No. channels</b>	648	48
<b>Group interval</b>	12.5 m	12.5 m
<b>Dominant frequency</b>	35 Hz	95 Hz
<b>Vertical seismic resolution (1500-2000 m/s)</b>	10 - 14 m	4 - 5 m

**Table 3.1:** Seismic acquisition parameters.

I reprocessed the APB13 data to preserve true relative amplitudes of seismic events. The processing flow consisted of geometry application and CDP sorting, Butterworth filtering with corner frequencies of 7, 14, 90, 120 Hz, spherical divergence correction applied with a velocity field modelled from seismic velocity analysis, iterative pre-stack Kirchhoff time migration, and final stack of offsets up to 3000 m. For near offset reflectivity analysis, I extracted only the nearest four traces prior to stacking, which corresponded to a maximum incidence angle of  $\sim 2^\circ$ . The TAN1808 data were acquired aboard R/V Tangaroa to obtain high-resolution seismic imaging of interpreted concentrated methane hydrates throughout the southern Hikurangi Margin. The processing of TAN1808 data included shot-domain quality control to remove noisy traces, marine “crooked line” geometry application, a bandpass frequency filter with corner frequencies of 7, 14, 150, 200 Hz, FK filtering to remove constant high-dip noise, a spherical divergence correction with water velocity, CDP sorting and NMO correction with water velocity, final stack of all offsets, and post-stack Kirchhoff time migration with water velocity. For near offset reflectivity analysis, I extracted only the first two traces of each CDP gather, corresponding to a maximum offset of 192 m and maximum incidence angle of  $\sim 3^\circ$ . I carried out the depth conversion using a velocity function of 1500 m/s above the seafloor reflection, and a constant increase of 330 m/s below the seafloor.

The depth converted seismic profiles were interpreted with the Markit IHS Kingdom seismic interpretation software package. A BSR could be mapped through most of the seismic sections and, where it was not present, I inferred the depth of the BGHS by interpolating from observations either side. The top of the concentrated hydrate zone (CHZ) was picked as the top of the zone of anomalously high seismic amplitudes and interpolated between the densely spaced lines.

### 3.3 Reflectivity and velocity analysis

The purpose of the reflectivity analysis is to estimate the gas hydrate saturation of a host layer at a specific location within the GHSZ, assuming that there is a relationship between the reflectivity of such a layer and the amount of gas hydrate hosted within the sediment pore space. The basis of these interpretations is that concentrated gas hydrates will lead to strong seismic reflections directly above the BGHS, extending upward towards the seafloor. If a coherent reflection can be traced from beneath the BSR to above the BSR, a clear change in polarity is often identifiable, marking the change from gas-charged strata (low impedance) below, to gas hydrate-charged strata (high impedance) above. Within the GHSZ, anomalous reflectivity corresponding to gas hydrate-bearing sediments should reveal positive polarity events, i.e. the same polarity as the seafloor and opposite polarity to the BSR. In several gas hydrate provinces, highly concentrated gas hydrate accumulations occur in sedimentary sequences characterised by thin alternating layers of permeable coarse-grained and less permeable fine-grained sediments. Geophysical and borehole studies at Adaini-Atsumi Knoll in the Nankai Trough (Fujii *et al.*, 2015), in the Gulf of Mexico (Boswell *et al.*, 2012, 2016a), in the Ulleung Basin offshore South Korea (Ryu *et al.*, 2013), Borneo (Paganoni *et al.*, 2016) and offshore SW Taiwan (Berndt *et al.*, 2019; Klaucke *et al.*, 2016) reveal that the top of concentrated hydrate deposits is commonly represented by a positive polarity high-amplitude reflection, indicating an increase in acoustic impedance.

To estimate gas hydrate saturation, I selected specific seismic events that could be continuously traced both within the CHZ region and outside of the interpreted upper boundary of the CHZ in the pre-stack time migrated seismic sections. High-amplitude seismic events with the same polarity as the seafloor were picked (at their maximum peak) both within and beyond the CHZ. I assume that the part of the event that lies outside the CHZ corresponds to a host layer and has negligible gas hydrate saturation

( $S_H \approx 0$ ). This assumption should be conservative, since I made a point of tracing the events beyond the CHZ, but still within the GHSZ – i.e. it is possible that the reflection represents a layer that has some low level of gas hydrate saturation. I used the reflection coefficient beyond the CHZ, together with the background velocity and density models, to estimate the gas hydrate saturation of the layer within the CHZ, applying and comparing two different rock physics models for hydrate-bearing marine sediments: 1) an empirical method described by Lee *et al.* (1996), and 2) an effective medium model presented by Dvorkin *et al.* (2000).

The effects of seismic attenuation were considered negligible in this study. Because the “hydrare-free” properties of the layers on which we carried out the reflectivity analysis were estimated at the same depth of the CHZ, if seismic amplitudes were corrected for seismic attenuation, the selected horizons would show a decrease in reflection coefficient both outside and within the CHZ, having a negligible impact on the hydrate saturation estimation.

### 3.3.1 Three-phase weighted equation

In the first approach, the relationship between  $S_H$  and compressional wave velocity is derived through a weighted equation (Eq. 3.5 Lee *et al.*, 1996) based on the three-phase time-average (Wyllie *et al.*, 1958) and the Wood (1941) equations. The workflow for the  $S_H$  calculation consists of the following steps:

1. Estimate the seismic background velocities from velocity analysis.
2. Estimate the layer’s density ( $\rho_{layer}$ ) from the trend calculated from the measured density values at the sites U1517 and U1518 of IODP Expedition 372 on the northern Hikurangi Margin (Pecher *et al.*, 2018; Wallace *et al.*, 2019).
3. Calculate the reflection coefficient at the seafloor  $R_{sf}$  for each seismic trace by dividing the amplitude of the first seafloor multiple  $A_m$  by that of the water-bottom reflection  $A_{sf}$ , after correction for spherical divergence (Hyndman and Spence, 1992; Pecher *et al.*, 1998; Warner, 1990):

$$R_{sf} = -\frac{A_m}{A_{sf}} = \frac{Z_{sf} - Z_w}{Z_{sf} + Z_w}, \quad (3.1)$$

where  $R_{sf}$  is the seafloor reflection coefficient,  $A_m$  is the amplitude of the first seafloor multiple,  $A_{sf}$  is the amplitude of the seafloor reflection,  $Z_{sf}$  is

the acoustic impedance of the seafloor, and  $Z_w$  is the acoustic impedance of the seawater above the seafloor.

4. Calculate the reflection coefficient of the picked seismic event  $R_e$  by scaling its amplitude  $A_e$  to that of the seafloor in the same trace:

$$R_e = \frac{R_{sf}A_e}{A_{sf}}, \quad (3.2)$$

5. Estimate the host layer's P-wave velocity ( $V_{P,layer}$ ) and porosity ( $\phi_{layer}$ ) through:

$$R_{e,S=0} = \frac{V_{P,layer}\rho_{layer} - V_{P,bkg}\rho_{bkg}}{V_{P,layer}\rho_{layer} + V_{P,bkg}\rho_{bkg}}, \quad (3.3)$$

$$\phi_{layer} = \frac{\rho_m - \rho_{layer}}{\rho_m - \rho_w}, \quad (3.4)$$

where  $V_{P,bkg}$  and  $\rho_{bkg}$  are the background P-wave velocity and density calculated in step 1,  $\rho_m$  is the density of the matrix, assumed to be 2.62 g/cm<sup>3</sup> for marine sediments (Dvorkin *et al.*, 2000),  $\rho_w$  is the density of water, assumed to be 1.035 g/cm<sup>3</sup> and  $R(e, S = 0)$  is the mean reflection coefficient of the “hydrate free” part of the picked seismic event (outside the CHZ).

6. Calculate the hydrate saturation required to generate the observed reflection coefficients for the remaining part of the picked seismic event (within the CHZ):

$$\frac{1}{V_P} = \frac{W\phi(1 - S_H)^n}{V_{P,Wood}} + \frac{1 - W\phi(1 - S_H)^n}{V_{P,TA}}, \quad (3.5)$$

where  $V_{P,wood}$  is the expected P-wave velocity calculated with the Wood equation,  $V_{P,TA}$  is the P-wave velocity calculated with the three-phase time-average equations,  $W$  is a weighting factor of the contribution of the time average and the Wood equations, and  $n$  is a constant simulating the rate of lithification with hydrate concentration. Because of the lack of logging data to constrain  $W$  and  $n$ , I calibrated the value of  $W$  for the hydrate free part of the reflection, assuming  $n = 1$  as used by Lee *et al.* (1996).

### 3.3.2 Effective medium model

The second approach is based on an analytical model presented by Dvorkin *et al.* (2000) which relates SH to the elastic properties of gas hydrate-bearing sediments. For the different types of hydrate morphology, I applied the pore-filling model for  $S_H$  below 0.4, and the load-bearing model for higher saturations, based on a number of laboratory and field studies (Cook and Waite, 2018; Lee *et al.*, 2010; Yun *et al.*, 2005). Dvorkin’s analytical models relate the elastic properties of hydrate-bearing sediment to the hydrate saturation, according to the geometrical configuration of the hydrate present in the pore space. The pore-filling model assumes that gas hydrate forms away from sediment grains and does not affect the bulk modulus of the solid frame. In the load-bearing model, gas hydrate acts as a component of the solid sediment frame, thus altering the elastic moduli of the rock and reducing its porosity. By assuming a constant effective pressure of 5 MPa, and a critical porosity of 40% (Nur *et al.*, 1998), I iteratively calculated the elastic response of the hydrate-bearing sediments at increasing  $S_H$ , to minimize the difference between the calculated and the observed reflection coefficient at each trace location.

A detailed presentation of this specific rock physics model, as well as the analytical expression of the petro-elastic properties are described in Section 2.3.

## 3.4 Results

### 3.4.1 Concentrated hydrate zones (CHZ)

The most typical indicator of the broad gas hydrate system at Glendhu and Honeycomb ridges is a discontinuous BSR that can be mapped across the entire study area. Its amplitude is highly variable, showing stronger reflectivity below the anticline structures and becoming weaker within the syncline between the two ridges (Fig. 1.7c). I obtained velocity models for the APB13 data by iteratively applying Kirchhoff pre-stack time migration and updating the velocity models for each iteration. Figure 3.2 shows the final pre-stack time migrated sections, with the respective seismic velocity fields overlaid. All profiles show a broad region above the BSR characterised by high P-wave velocity values (1900-2500 m/s), and a region of variable thickness below the BSR of lower P-wave velocities (1500–1700 m/s).

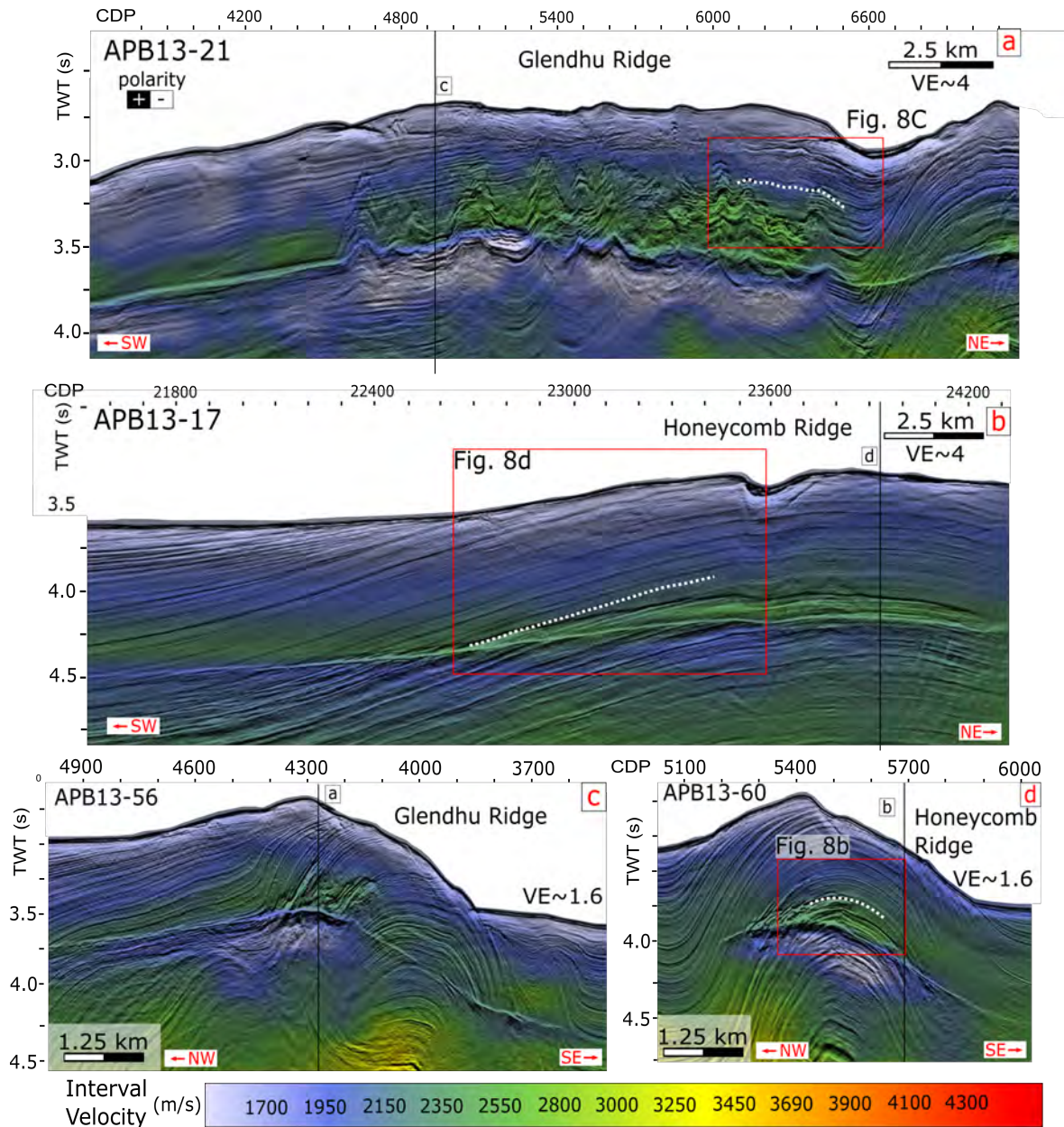


**Figure 3.2:** P-wave interval velocities at Glendhu and Honeycomb ridges, overlying the pre-stack time migrated seismic sections; (a) and (c) show the P-wave velocity variations at Glendhu Ridge along strike and along dip, respectively; (b) and (d) show the velocity variations at Honeycomb Ridge along strike and along dip, respectively. The red rectangles are the locations of the insets shown in Fig. 3.7, and the white dotted lines represent the seismic reflections analysed in terms of reflectivity. See Fig. 3.1 for profile locations. VE: vertical exaggeration at the seafloor.

The high velocities above the BSR probably correlate to gas hydrate bearing sediments, whereas the low velocities beneath the BSR are representative of free gas within

the pore space (e.g., Crutchley *et al.*, 2015; Fraser *et al.*, 2016; Pecher, 2011). Concentrated hydrate zones (CHZ) beneath the ridges can be identified in both the APB13 (lower frequency) and the TAN1808 (higher frequency) datasets from anomalously high amplitudes between the BSR and the seafloor (Figs 3.3 and 3.4). The spatial variability of the CHZs throughout the region is well exemplified by the strike lines (parallel to the ridges; Figs 3.3a and 3.4a, b) and representative segments of dip lines (perpendicular to the ridges; Figs 3.3c-j and 3.4c-h). The CHZ beneath both ridges correlates with the broad zones of high interval velocities determined from semblance analysis of the long-offset data (Fig. 3.2). The volume of the CHZs at Glendhu and Honeycomb ridges is  $9.4 \times 10^6 \text{ m}^3$  and  $4.1 \times 10^6 \text{ m}^3$ , respectively.

At Glendhu Ridge (Fig. 3.3), the high-amplitude reflections develop on the landward NW-dipping strata of the anticline, extending from the BSR upwards towards the seafloor. On the strike lines (Fig. 3.3a, c, d), the anomalies show high lateral variability from SW to NE, and the BSR is patchy and uplifted in some locations (Fig. 3.3a, 4h, 4j). Figure 3.3a also shows the location of active seafloor gas seepage, projected onto the seismic line (locations after Watson *et al.*, 2020). In Figure 3.3i and 3.3j, flat spots beneath the crest of Glendhu Ridge have been interpreted as gas-water contacts (Crutchley *et al.*, 2019).

Figure 3.4 illustrates the high-amplitude anomalies at Honeycomb Ridge. Unlike Glendhu Ridge, where the only available strike lines are coincident (APB13-21 and TAN1808-38), the presence of two seismic sections trending NE-SW (TAN1808-39 and APB13-17) provides a better understanding of the three-dimensional geometry of the high-amplitude anomalies. Active gas seepage out of the seafloor has also been observed on the crest of Honeycomb Ridge (Watson *et al.*, 2020); the locations are shown in Fig. 3.3a and b. Where the stratigraphy crosses the BSR, polarity reversal can be noted (Fig. 3.4c and d), showing the transition from hydrate-bearing (above) to free gas-bearing sediments (below). Strong reflections below the BSR are observed at Honeycomb Ridge, displaying typical negative polarity in the TAN1808 data (Fig. 3.4c) and, curiously, positive polarity in the APB13 data (Fig. 3.4d).

The densely-spaced 2D seismic lines have enabled us to map both the BGHS and the top of the CHZ. At both ridges, I interpreted the top of the CHZ by considering the occurrence of anomalously high-amplitude reflections with the same polarity as the seafloor (positive polarity), corresponding to an increase in P-wave velocities. This



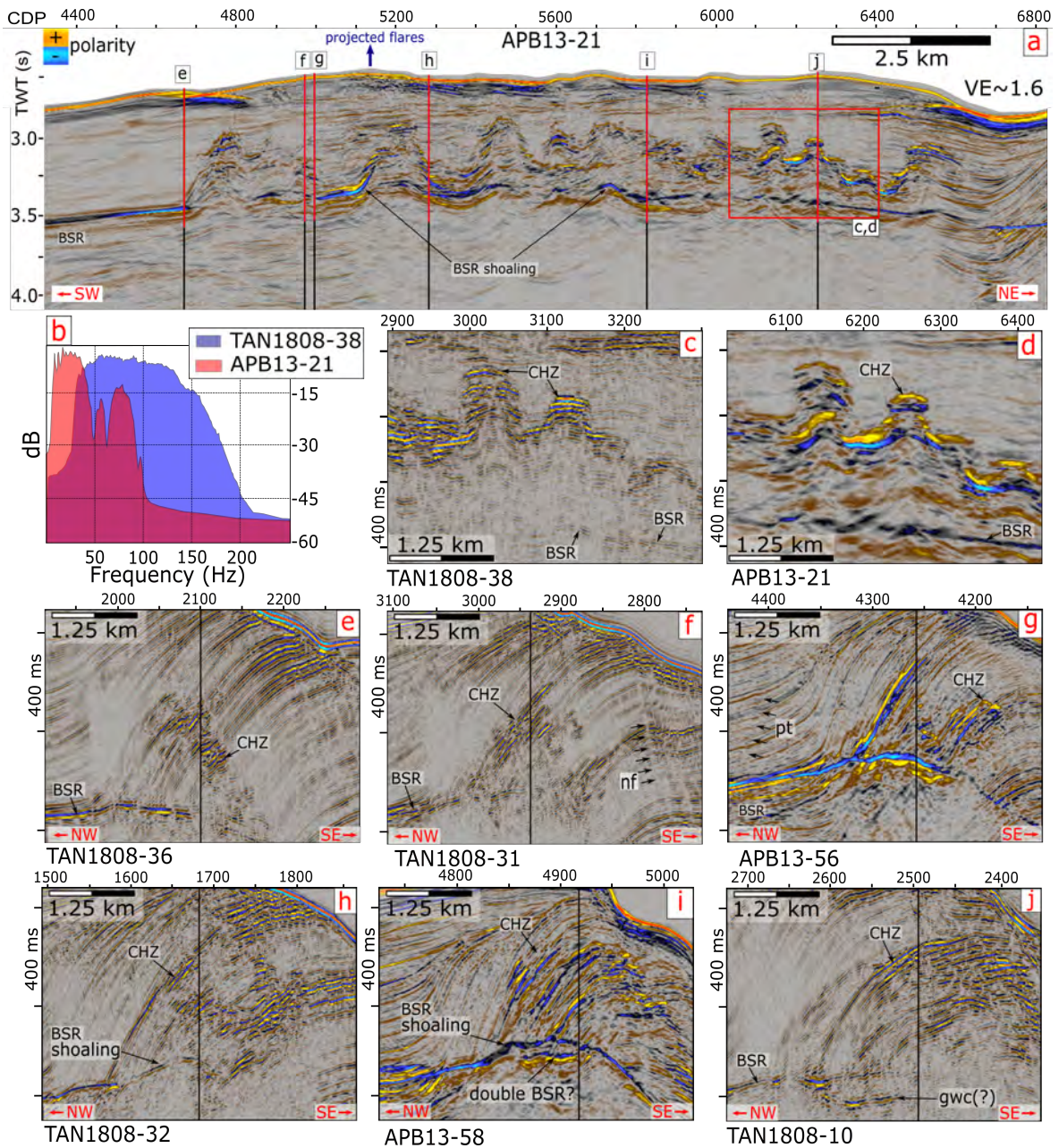


**Figure 3.3:** Glendhu Ridge overview (see Fig. 3.1c for profile locations): along strike seismic section (a), showing the location of the sections along dip (panels c-l); (b) frequency content of the two reprocessed data sets: TAN1808 (c) and APB13 (d); (c) and (d) are enlargements of the red rectangle in (a) in the TAN1808 and APB13 data, respectively; (e-j) panels showing the NW-SE trending sections intercepting line APB13-21 and TAN1808-38; CHZ: concentrated hydrate zone; BSR: bottom simulating reflection; gwc: gas-water contact; nf: normal faults; pt: prototrusts. “Projected flares” are locations of active gas seepage (Watson *et al.*, 2020, acoustic flares) projected onto these profiles. VE: vertical exaggeration at the seafloor.



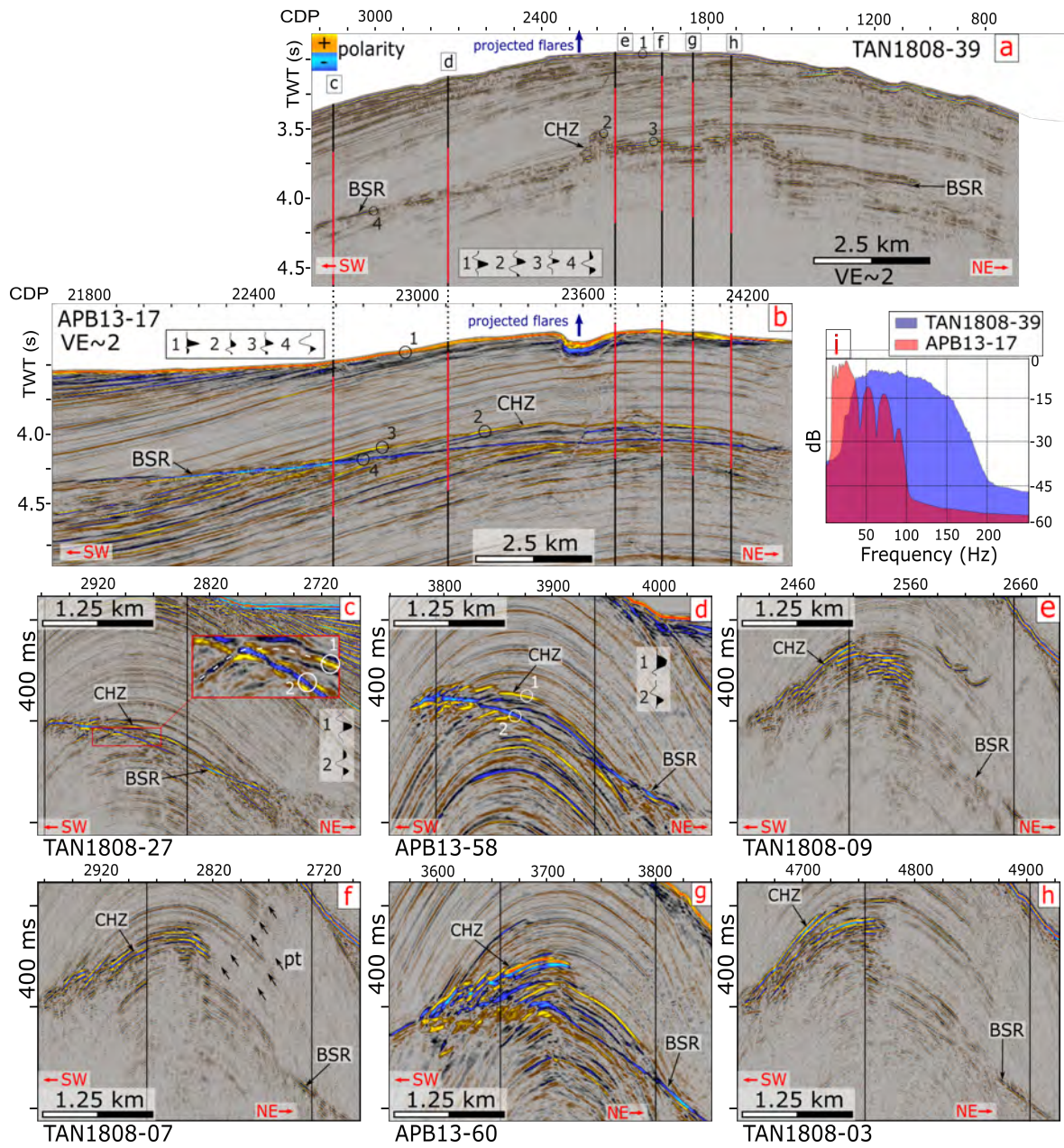


**Figure 3.4:** Honeycomb Ridge overview (see Fig. 3.1c for profile locations): along strike seismic sections TAN1808-39 (a) and APB13-17 (b), showing the location of the sections along dip (c-h panels); (c-h) panels show the NW-SE trending sections intercepting line APB13-17 and TAN1808-39; (i) frequency content of the two reprocessed data sets TAN1808 (a) and APB13 (b); insets in a), b), c) and d) show waveforms of the indicated locations 1-4; CHZ: concentrated hydrate zone; BSR: bottom simulating reflection; pt: protothrusts. “Projected flares” are locations of active gas seepage (Watson *et al.*, 2020, acoustic flares) projected onto these profiles. VE: vertical exaggeration at the seafloor.

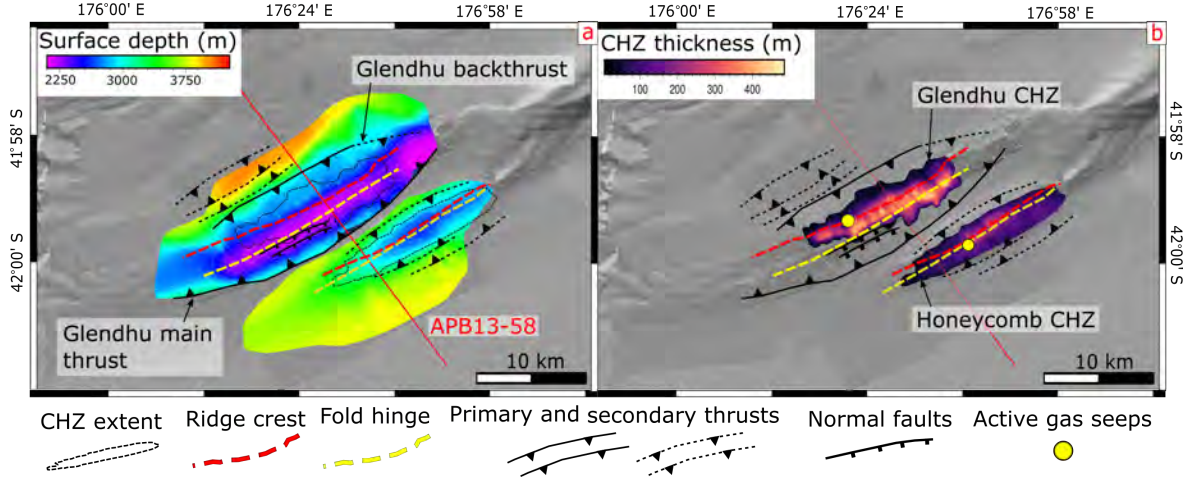


**Figure 3.5:** (a) Structural map of the geology underlying Glendhu and Honeycomb ridges (arbitrary surfaces and main faults shown in section APB13-58 in Fig. 1.7c); (b) thickness and extent of the CHZ and its relation to the geological structures from (a).

type of reflection has been interpreted as the top of CHZs in other studies in offshore Chile (Rodrigo *et al.*, 2009), Taiwan (Berndt *et al.*, 2019; Klaucke *et al.*, 2016) and Japan (Fujii *et al.*, 2015; Taladay *et al.*, 2017), among others. Using a mean seismic interval velocity of 2000 m/s, consistent with the seismic velocities in the CHZ intervals (Fig. 3.2), I have converted these horizons to depth to estimate the thickness of the CHZ beneath both Glendhu Ridge and Honeycomb Ridge (Fig. 3.5). The distribution of the CHZ beneath each ridge (Fig. 3.5b) correlates with stratigraphic closures (Fig. 3.5a) that I have characterised by mapping out the arbitrary reflections highlighted in yellow and orange in Fig. 1.7c.

### 3.4.2 Structural analysis of Glendhu and Honeycomb ridges

The joint interpretation of seismic profiles of different frequency content and resolution provides a more detailed understanding of the structural framework of the two ridges than was previously possible (Crutchley *et al.*, 2019), as well as allowing the identification of finer scale features. NE-SW oriented proto-thrusts can be observed on the seaward side of Honeycomb Ridge (e.g. Fig. 3.4f), and a developing back-thrust is clearly visible on its landward side (Fig. 1.7c). Glendhu Ridge is also underlain by proto-thrusts, but in this case occurring on the landward side of the ridge. The distribution of landward-verging and seaward-verging thrusts surrounding both ridges is shown in Figure 3.5a, in relation to the locations of the ridge crests and the broad folding of selected arbitrary reflections. The longitudinal hinge lines of both anticlines



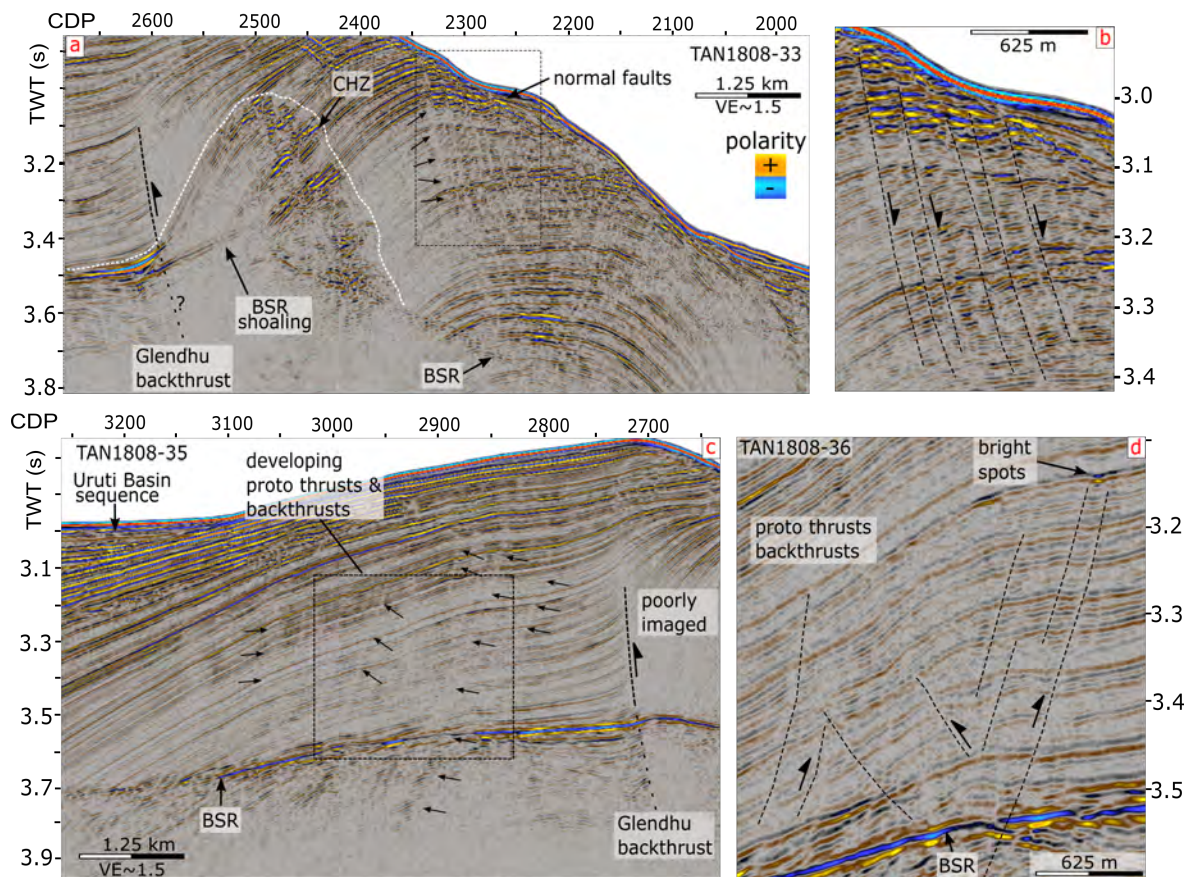


**Figure 3.6:** Deformation processes at Glendhu Ridge: (a) Glendhu anticline affected by collapse normal faulting on the slope (b); (c) proto-thrusts (indicated by black arrows) developing NW of the ridge crest, deforming the sedimentary sequence; (d) enlargement from an adjacent seismic profile (TAN1808-36) showing proto-thrusts. The projected location of this panel is shown on Line TAN1808-35 in (c). VE: vertical exaggeration at the seafloor.

are not coincident with the bathymetric crest of the ridges; instead, they intercept the seafloor on their seaward slope. At the Glendhu site, the offset between the hinge of the anticline and the bathymetric crest of the ridge is greater than at the Honeycomb site (Fig. 3.5). NW of Glendhu Ridge, the Urutī Basin sequence is characterised by a thick sedimentary cover of mostly undeformed sediments that thins towards the crest of the ridge (Figs 1.7c and 3.6c), as they have been deposited contemporaneously with its uplift (Barnes *et al.*, 2010).

Figure 3.6 highlights the diversity of compressional and extensional structures characterising Glendhu Ridge. The seaward slope of the ridge is cored by a series of closely-spaced seaward-dipping normal faults (Fig. 3.6a and b), whereas the landward-dipping sediments on the landward side of the ridge host a series of proto-thrusts (Fig. 3.6c and d). The normal faults extend very close to the seafloor and cut through the central region of the anticline, extending almost as deep as the BSR. The proto-thrusts appear to cut through the clear BSR and deform the overlying sedimentary sequence to a shallower depth, only a few tens of metres below the seabed. In some cases, bright spots are associated with the faults (Fig. 3.6d).

### 3.4.3 Reflectivity analysis and hydrate saturation

In the absence of direct measurements from well log data, first order estimates of the gas hydrate saturation in the CHZs can be made based on seismic velocity and near incidence reflectivity analysis. I carried out reflectivity analysis on selected reflections that cross the CHZ, intercepting the BSR and the top of CHZ (Fig. 3.7). These reflections could be continuously picked within and beyond the CHZ, which is assumed to be hydrate-free, as explained in Section 3.3. Using the empirical model by Lee *et al.* (1996), and assuming zero background gas hydrate saturation for the part of the layer that is beyond the limit of the CHZ (yellow segment in Fig. 3.7), I estimate methane hydrate saturations between 0.05% and 40% within the Honeycomb CHZ, and ~14% at the Glendhu CHZ. The values of hydrate saturation at the same horizons estimated using Dvorkin *et al.* (2000) models are also shown in Fig. 3.7. Hydrate saturations estimated from the higher frequency near-incidence data reach values of over 90% in the NW dipping side of the Honeycomb anticlinal structure, close to the apex of the fold (Fig. 3.7a and b) whereas those estimated from the lower frequency data at the same location are lower, around 40-65%. Saturations range from ~18% to ~25% at the Honeycomb CHZ (Fig. 3.7d), although a peak of ~40% is observed just above the

BSR. Values of  $\sim 20\%$  to  $\sim 38\%$  are estimated at the Glendhu Ridge CHZ (Fig. 3.7c).

## 3.5 Discussion

### 3.5.1 Evolution of thrust ridges at the deformation front

The analysis of seismic profiles along Glendhu and Honeycomb ridges allows us to study the interactions between tectonic, sedimentary and erosive processes at the toe of the southern Hikurangi deformation wedge. These processes play an important role in the fluid flow system and the way gas hydrate forms and accumulates. Honeycomb Ridge, right at the deformation front of the wedge, is a young thrust ridge, whereas Glendhu Ridge is interpreted as a more developed structure that has undergone tectonic deformation for a longer time, assuming in-sequence fault propagation at the advancing deformation front. A schematic representation of the evolution of these ridges based on representative seismic sections from the analysed dataset is shown in Figure 3.8, from the initial development of the deformation front to later stage faulting, folding, sedimentation and erosion. Initially, the stratified sedimentary layers are folded very gently (limb angles  $< 1^\circ$ ) as strain is transferred into the trench fill sequence in front of the accretionary wedge. The developing stratigraphic trap geometry is sufficient to focus free gas accumulation to the apex of the fold (Fig. 3.8a). Moreover, the decreased seafloor gradient causes a reduction in the transport of larger-grained sediments across the incipient ridge, hence increasing the deposition of coarse-grained sediments on the landward side of the ridge. Deformation continues, resulting in tighter folds and the appearance of a clear fold geomorphology at the seafloor defining the location of the deformation front (Fig. 3.8b). As folding progresses and the ridges become more mature, a pronounced asymmetry develops as a result of sedimentation landward of the ridge crests, which form baffles to sediment transfer from the shelf-break to the Hikurangi Trench. Erosion of the seaward flanks means that the ridge crest steps landward of the fold apex. As the ridges develop, there is often a seaward rotation of the hinge of the anticline reflecting asymmetric folding with thrust fault propagation (Fig. 3.8d). Backthrusts may develop on the landward side of the ridge to accommodate the increasing degree of deformation in the more mature ridges. Stratigraphically-controlled upward gas migration continues along the steeply-dipping strata, above the thick free gas zone, promoting the accumulation of concentrated gas hydrates beneath the ridge crest (Fig. 3.8d).

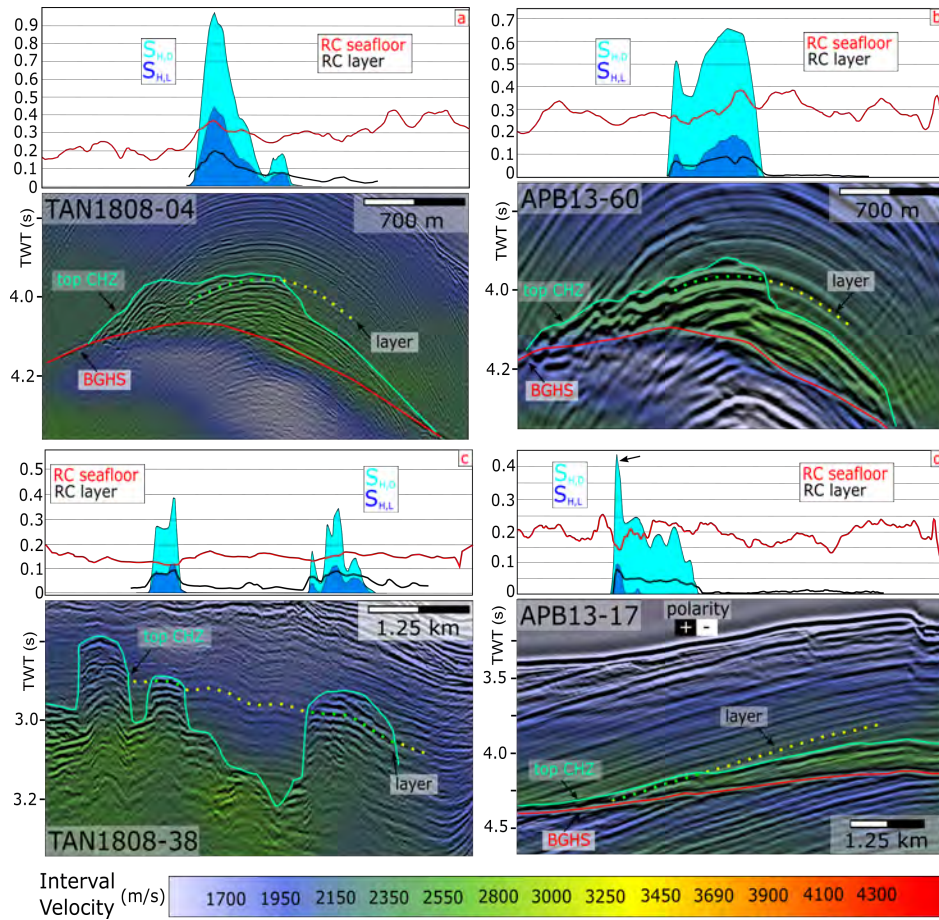


**Figure 3.7:** Reflectivity analysis and gas hydrate saturation estimates for selected seismic reflections (see Figs 1c and 3 for profile locations). The selected reflections are shown by the dotted lines (green dotted lines within the CHZ; yellow dotted lines beyond the CHZ). Seismic velocities are overlain on the seismic data. a) Along-dip seismic section TAN1808-04, which is nearly coincident to the section shown in b), therefore the seismic velocities estimated from APB13-60 data are shown; b) Along-dip reprocessed seismic section APB13-60; c) Along-strike seismic section TAN1808-38 showing Glendhu Ridge CHZ; d) Along-strike reprocessed seismic section APB13-17 showing Honeycomb Ridge. The panels on the top of the seismic profiles represent the reflection coefficient measured at the seafloor and at the selected layer (red and black lines, respectively), and the estimated gas hydrate saturation using Lee *et al.* (1996) empirical model (dark-blue curve,  $S_{H,L}$ ) and Dvorkin *et al.* (2000) effective medium theory model (light-blue curve,  $S_{H,D}$ ), based on the background P-wave velocity and reflectivity (see Section 3.3). The top and base of the CHZ are represented by the green and red lines, respectively; BGHS: base of gas hydrate stability. The small black arrow in d) is pointing at a hydrate saturation peak occurring just above the BSR. This could be an artefact in the gas hydrate saturation estimate due to the abrupt reduction of the reflection coefficient of the seafloor (red curve) at this location.

### 3.5.2 Stratigraphic versus structural control on fluid flow

An important aspect in the characterisation of gas hydrate systems is understanding the factors that control the supply of gas for hydrate formation. Several gas migration mechanisms have been proposed to explain the occurrence of concentrated gas hydrate accumulations in marine sediments, spanning diffusive “short range” migration of methane in solution, to advective “long range” migration of free gas from beneath the BGHS (Boswell *et al.*, 2012; Cook and Malinverno, 2013; Crutchley *et al.*, 2015; Hillman *et al.*, 2017; Malinverno, 2010; Nole *et al.*, 2016; VanderBeek and Rempel, 2018). In this study, I have used high-amplitude seismic anomalies congruent to an increase in P-wave velocity as the main proxy to identify the extent of the CHZs (e.g., Berndt *et al.*, 2019). From our data, the relative contributions of diffusion-driven dissolved methane migration (Malinverno, 2010) and advective gas migration into the GHSZ are difficult to separate. However, based on the occurrence of low-velocity zones beneath the CHZs of both Glendhu and Honeycomb ridges (Fig. 3.2c and d), the most likely mechanism for hydrate formation in these ridges is advective gas migration into the GHSZ from below the BSR. Gas hydrate recycling within these ridges is a mechanism that probably leads to ongoing gas and gas hydrate accumulation with time (Crutchley *et al.*, 2019). Diffusion-driven methane migration within the GHSZ is likely to supplement the long-range gas migration.

The CHZs mostly follow the stratigraphy of the sedimentary layers within the GHSZ (Figs 3.3 and 3.4), and are not observed extending along the faults identified in the seismic data (Fig. 3.6). The bright spot observed in Fig. 3.6d could be evidence of fluid flow focusing toward the tips of secondary thrusts, but neither the amplitude nor the extent of this bright spot are comparable to the highly reflective features characterising the CHZs directly above the BGHS (e.g. Fig. 3.4). The general absence of high-amplitude anomalies along secondary thrusts and normal faults seems to indicate that focused fluid flow into the hydrate system of these ridges is primarily driven by the stratigraphy rather than by structural elements. It is worth noting that there is pronounced lateral (along strike) variation in the CHZ evident in the strike lines on Glendhu Ridge (Figures 3.2 and 3.3). This lateral variation may represent significant lateral (along-strike) heterogeneity in terms of reservoir quality and/or along strike variations in gas flux into the key reservoir layers.



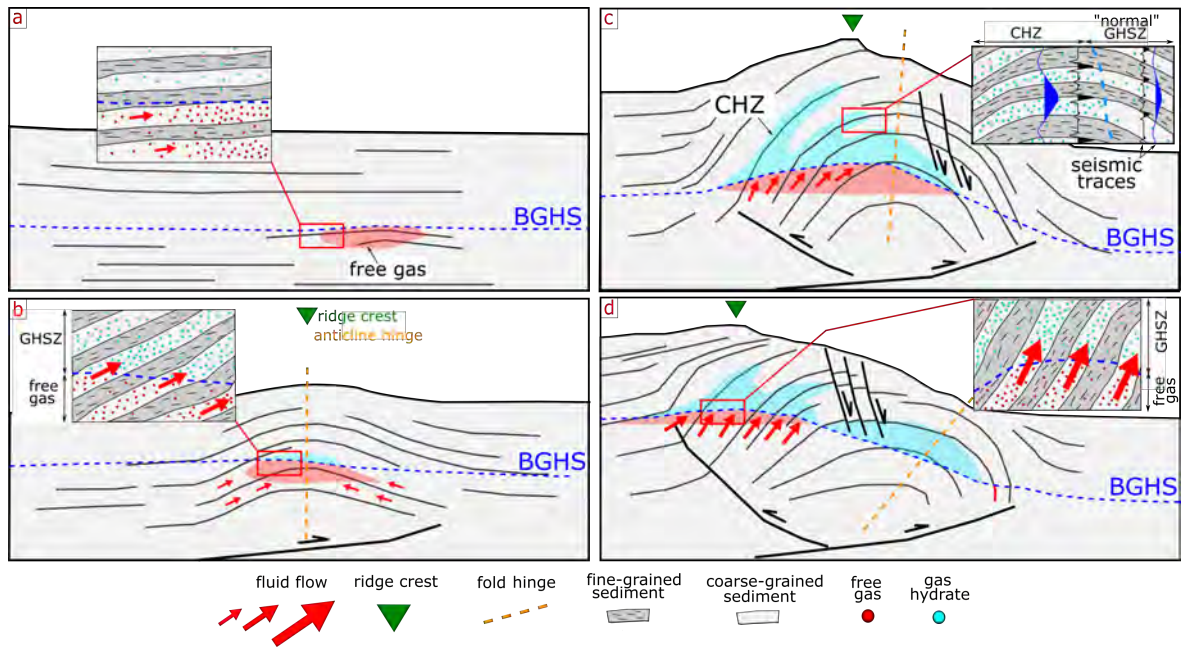


**Figure 3.8:** Schematic representation of the evolution, progressing from (a) to (d) of a CHZ in a thrust ridge at the southern Hikurangi Margin; GHSZ: gas hydrate stability zone; BGHS: base of gas hydrate stability; CHZ: concentrated hydrate zone; Z: acoustic impedance. The right inset in (a) shows the seismic response of sub-seismic scale units and the possible tuning effects occurring both above and below the BSR. Although not to scale, panel (c) is representative of the current geometry of Honeycomb Ridge and panel (d) is representative of the more mature Glendhu Ridge. The inset in panel (c) shows the seismograms of the low- and high-resolution seismic data (blue and black seismic traces, respectively).

The fact that CHZs are observed mainly in the landward-dipping strata of anticlines has been described by Crutchley *et al.* (2019), who suggested that higher sedimentation rates on the landward sides of thrust ridges lead to preferential gas hydrate recycling, free gas injection and gas hydrate formation within permeable coarse-grained layers. In addition, the presence of growing structures impacts directly the sedimentation, favouring the deposition of coarser-grained deposits landward of the ridge crests, from density flows coming from nearby canyons or from the landward slopes. Our estimates of gas saturation from both landward-dipping and seaward-dipping strata within a given anticline (Honeycomb Ridge) tend to support this interpretation, as the extent and average saturation of concentrated gas hydrate estimated from the reflectivity analysis on a seaward-dipping reflection (Fig. 3.7d) is lower than that of a landward-dipping layer (Fig. 3.7a and 3.7b).

A key point for reservoir characterization is understanding the nature of the CHZs. Some seismic horizons, like the ones shown in Figure 3.7, are characterized by an abrupt decrease of amplitude at the edge of the CHZ. The amplitude damping could be explained either by a lateral decrease in hydrate saturation within a relatively homogeneous sedimentary unit (Tamaki *et al.*, 2017) or by a lateral decrease in reservoir continuity/quality (Boswell *et al.*, 2012). From 2D seismic data alone it is not clear what the cause of amplitude damping at the margins of the CHZs might be. Further quantitative investigations comparing landward- to seaward-dipping strata would be needed to provide a more robust assessment of differences in hydrate saturation across the ridges. Ultimately, drilling would be required to determine the relative importance of reservoir quality deterioration versus hydrate saturation reduction as the primary control on the margins of the CHZs.

### 3.5.3 Comparison of Glendhu and Honeycomb ridges

The proximity of these two ridges and the fact that they record increasing tectonic deformation means they provide a valuable comparison in terms of how gas hydrate systems respond to progressive deformation. Assuming a major stratigraphic control of fluid migration and gas accumulation, the role of the angle at which the strata cross the BGHS has been argued to be a significant factor in hydrate formation and accumulation (Chatterjee *et al.*, 2014; Crutchley *et al.*, 2019). Our analysis of Glendhu and Honeycomb ridges suggests that the vertical extent of a CHZ is a function of the steepness of the strata crossing the BGHS (calculated in Crutchley *et al.* (2019)), which in

turn is dependent on the structural maturity of the ridges. For all of the seismic data analysed, strata-to-BGHS angles (following the nomenclature of Crutchley *et al.*, 2019) at the Glendhu CHZ are greater than strata-to-BGHS angles at the Honeycomb CHZ:  $0-37^\circ$  ( $\pm 5^\circ$ ) at Glendhu Ridge and  $0-25^\circ$  ( $\pm 4^\circ$ ) at Honeycomb Ridge (Fig. 1.7c). The more steeply dipping strata are interpreted to enhance gas migration upward along-strata into the GHSZ, resulting in CHZs that are more vertically extensive (i.e. they extend further from the BGHS towards the seafloor). Our analysis of the depositional and erosional processes during the evolution of the ridges shows that the steepness relationship I see is related to the maturity of the ridge. On the more mature Glendhu Ridge, the CHZ has moved landward of the anticline core with ridge evolution and is now located within the backlimb of the anticline where stratigraphic dip is greater. This observation may indicate that more significant CHZs will be found in more mature structures as a function of ridge evolution rather than simply a longer period for gas accumulation and hydrate formation. However, the potential source rock volume drained by each structure also plays an important role in the formation of CHZs: the Glendhu anticline has drained a larger volume of sediments for a longer period than the Honeycomb anticline.

Interestingly, the BSR at Glendhu Ridge shows localised shoaling in some seismic sections (Fig. 3.3a, h, j). It is possible that BSR shoaling can be an artefact of viewing data in the time domain when anomalously high seismic velocities above the BSR have not been accounted for (i.e. a velocity “pull-up” effect). However, this is unlikely since I only observe the shoaling in particular locations beneath the CHZ, despite the BSR being well-imaged beneath the broad CHZ (Fig. 3.3a). A more probable explanation for the BSR shoaling is that it is caused by focused upward fluid flow associated with pronounced advective heat flow, resulting in an upward deflection of the BGHS (c.f. Crutchley *et al.*, 2014; Pecher *et al.*, 2010; Shedd *et al.*, 2012). The BSR shoaling occurs in proximity to the apex of Glendhu Ridge, which is where flexural extension develops that may produce significant secondary permeability (Barnes *et al.*, 2010; Wang *et al.*, 2017a). However, since I see little evidence for focused fluid flow along flexural normal faults (Section 3.4), it is more likely that localised anomalous advective heat flow beneath Glendhu Ridge is primarily a function of steeper stratigraphic dips than those observed at Honeycomb Ridge, where I do not observe BSR shoaling. That said, sub-seismic scale structures (faults and fractures) cannot be ruled out as contributing to increased vertical fluid flow.

### 3.5.4 Seismic resolution and tuning effects

The increase in acoustic impedance due to the presence of gas hydrate in the pore space should result in a reflection with a similar polarity to that of the seafloor (Boswell *et al.*, 2016a); on the other hand, free-gas bearing units should be characterized by an opposite seismic response (i.e. decreasing acoustic impedance). However, if the thickness of the units is below the vertical seismic resolution, tuning effects might occur (Waite *et al.*, 2019). Two strong negative polarity responses may interfere constructively and generate a strong positive phase with small negative lobes, and vice versa. The general threshold for vertical seismic resolution is usually  $\frac{1}{4}$  of the dominant wavelength, which in turn is dependent on the data dominant frequency and the seismic velocities (Yilmaz, 2001). For seismic velocities ranging from 1500 to 2000m/s, the APB13 and the TAN1808 data have a vertical resolution of 10-14 and 4-5 m, respectively. An example of constructive interference can be seen at Honeycomb Ridge, where strong reflections below the BSR display negative polarity in the higher frequency data (Fig. 3.4c), but positive polarity in the lower frequency APB13 data (Fig. 3.4d). I suggest that the positive polarity events beneath the BSR in Figure 3.4d are caused by thin gas charged strata that cause a tuning effect in the lower frequency data.

### 3.5.5 Sensitivity of hydrate saturation estimates

The gas hydrate saturations estimated through the empirical rock physics model (Lee *et al.*, 1996) are systematically lower than the saturations obtained applying the effective medium theory model (Dvorkin *et al.*, 2000). The analytical Dvorkin's model better describes the occurrence of the high amplitude seismic anomalies, which are commonly caused by high hydrate saturations (>30-40%, Lee *et al.*, 2010; Yun *et al.*, 2005). In general, the reflectivity analysis method for local estimates of hydrate saturation relies on a set of assumptions. Firstly, because it is possible to assess only the P-wave background velocity from the seismic data, the bulk density is estimated based on the density logs measured at the sites of IODP Expedition 372 in the northern Hikurangi Margin (Pecher *et al.*, 2018). Despite the drill sites' location, 400 km northeast of the study area, the averaged trend is compiled from density logs that are characteristic of sediments from the mid-lower slope and from the subduction trench, so they are assumed to be representative of the conditions in the area of the Glendhu and Honeycomb ridges. Secondly, I assume that the seismic reflections corresponding to the host layers beyond the CHZ have a positive polarity (Fig. 3.7); this choice is

relatively arbitrary, since it is not possible to directly relate acoustic impedance values to changes in lithology from our data. Nevertheless, by assuming that the “hydrate-free” layer has a positive polarity reflection, the hydrate saturation of that layer within the CHZ are possibly being underestimated. Finally, because our approach is based on seismic reflectivity, the results are dependent on the vertical resolution of the seismic data, which is 14 m for the reprocessed APB13 data and 5 m for the TAN1808 data, considering dominant frequencies of 35 and 95 Hz, respectively (Fig. 3.3b and 3.4i), and an average seismic velocity of 2000 m/s within the CHZs.

The reflection coefficients of the selected seismic events are related to the peak amplitude of that event at each CDP location. The gas hydrate saturation estimated at the Honeycomb Ridge CHZ from the higher resolution data (Fig. 8a) is higher than the gas hydrate saturation estimated from the medium resolution data on the same ridge (Fig. 3.7b), even though the selected seismic reflection is likely to represent the same geological horizon in both sections. The observed seismic response is representative of a vertical interval equal to the seismic resolution, as shown in Figure 3.8c (inset). Therefore, both the elastic properties estimated from the seismic data (P-wave velocity and density) and the derived gas hydrate saturation values, are averaged over such thicknesses.

The comparison of the reflectivity analysis results between the two datasets at the same location clearly show the higher frequency data allow us to resolve thinner layers and presumably higher local gas hydrate saturations. Because of the higher resolution, I expect the reflection coefficients estimated from the TAN1808 data to be more accurate than those estimated from the lower resolution APB13 data. Sub-metre sedimentary units have been documented in similar geological settings, dominated by a turbiditic sedimentary pattern (Fujii *et al.*, 2015), and are likely to be present in this area. Therefore, it is also likely that there are occurrences of thinner coarse-grained layers bearing gas hydrate at higher concentrations, interbedded with hydrate free fine-grained layers, typical of turbiditic deposits that are common along continental margins. Studies from the first offshore production tests in the Nankai Trough off Japan, for example, report the occurrence of thin turbidite assemblages with highly concentrated (50%-80%) gas hydrate present in tens to hundreds of centimetres thick sandy intervals (Fujii *et al.*, 2015). Logging-while-drilling data from the Gulf of Mexico Boswell *et al.* (2012); Lee *et al.* (2012) and in the Krishna-Godavari Basin (Joshi *et al.*, 2019; Pandey *et al.*, 2019;

Yadav *et al.*, 2019) show similar patterns of thin, high hydrate saturation (>50%) sands interbedded with fine grained, low hydrate saturation muds.

## 3.6 Conclusions

This chapter presents a detailed structural characterisation and combined seismic velocity and reflectivity analysis of Glendhu and Honeycomb ridges at the deformation front of the southern Hikurangi Margin. Two concentrated hydrate zones (CHZs), characterised in seismic data by high-amplitude reflections congruent with high seismic velocities, are identified beneath the two ridges. The CHZs occur in the cores of two four-way closure systems, and lie above a discontinuous BSR that indicates free gas-bearing strata below. The results suggest that the extent of the accumulations is a function of the steepness of the strata crossing the BSR, and that the main driving mechanism for concentrated hydrate accumulation in the study area is along-strata gas migration. A comparison of the two ridges provides insight into the evolution of thrust related anticlines at the toe of the accretionary wedge, suggesting that older structures situated further landward of the deformation front are more likely to host more extensive CHZs than the deeper and younger ridges located at the deformation front. This reflects the interplay of deposition and erosion driving the location of the CHZs away from the gentle stratigraphic dips in the core of the anticline into the steeper dips in the (landward) backlimb of the more structurally mature anticlines. Moreover, older structures are likely to have drained a larger region of potential source rocks for a longer time. The estimated gas hydrate saturations at selected locations within the CHZs vary widely, depending on the rock physics model that is used. The effective medium theory model is likely to be more accurate than the empirical three-phase weighted equation, and predicts saturation values mostly ranging between  $\sim 30\%$  and  $\sim 60\%$ , but exceeding  $\sim 90\%$  on a very reflective seismic horizon in the axial region of Honeycomb Ridge. In general, the gas hydrate saturation estimates are considered to be averaged values over vertical zones with thicknesses on the order of the seismic data resolution (5 – 14 m). Due to the limited vertical resolution of the seismic data, I cannot rule out the presence of higher hydrate saturations at a smaller scale. Further studies are required to better constrain the physical properties of the reservoir lithology and to better characterise the hydrate accumulations at this site in terms of pore space gas hydrate saturations, reservoir connectivity and permeability.

# Chapter 4

## Characterisation of gas hydrates systems through geostatistical seismic and petrophysical inversion

This chapter is focused on the quantitative characterisation of the Glendhu and Honeycomb concentrated hydrate deposits, described in detail in Chapter 3, based on the inversion of long-offset seismic data for petrophysical properties. This work has been published under the title *Characterisation of gas hydrate systems on the Hikurangi Margin (New Zealand) through geostatistical seismic and petrophysical inversion* by Turco F., Azevedo L., Grana D., Crutchley G.J., Gorman A.R., in the journal *GEOPHYSICS*.

### **CRedit: authors' contribution**

Turco F.: Conceptualisation, Software, Formal analysis, Investigation, Data Curation, Writing - Original Draft.

Azevedo L.: Methodology, Software, Validation, Resources, Supervision, Writing - Review and Editing.

Grana D.: Supervision, Software, Methodology, Writing - Review and Editing, Validation.

Crutchley G.: Supervision, Visualization, Project administration, Funding acquisition, Data Curation.

Gorman A.: Supervision, Project administration, Funding acquisition, Data Curation.

## 4.1 Introduction

The presence of gas hydrates within sediment pore spaces significantly affects the bulk physical properties of marine sediments (Sloan Jr and Koh, 2007). For this reason, indirect geophysical methods such as multi-channel seismic methods (MCS) provide the most effective means for identifying large offshore gas hydrate deposits. However, despite the broad use of these methods for identifying natural gas hydrate occurrences since the 1960s (Makogon, 1966), quantitative resource assessments of gas hydrate reservoir formations are only available for a small number of locations worldwide, where accurate estimates of petrophysical properties are constrained by in-situ measurements such as wireline logging, logging-while drilling (LWD) or core data (e.g., Bellefleur *et al.*, 2012; Boswell *et al.*, 2012; Haines *et al.*, 2017; Shukla *et al.*, 2019; Taladay *et al.*, 2017). In unexplored sedimentary basins with no wells, seismic data are often the only information available for quantitative studies of rock properties such as seismic velocities, density and attenuation. Seismic inversion provides a means to characterize these sub-surface properties at high resolution – i.e., vertical resolution on the order of the wavelength of the seismic signal being inverted. In a traditional petroleum exploration workflow, seismic reflection data are first inverted for elastic properties such as compressional and shear velocities ( $V_P$  and  $V_S$ , respectively) and density (Tarantola, 2005), then the elastic properties are converted into petrophysical parameters through inverse methods (e.g., Dai *et al.*, 2008; Doyen, 2007; Grana, 2016; Grana and Della Rossa, 2010; Mukerji *et al.*, 2001). A variety of probabilistically based seismic inversion methods have been trialled that generally depend on assumptions, a priori information, and global optimisation methods (e.g., Buland and Omre, 2003; Doyen, 1988). Doyen (2007), Bosch *et al.* (2010) and Azevedo and Soares (2017) provide detailed reviews of seismic inversion methods that incorporate rock physics information for quantitative seismic reservoir characterisation.

Over the last 20 years, both deterministic and probabilistic seismic inversion techniques have been applied successfully for gas hydrate characterisation. Some studies have focused on the investigation of the nature of the BSR (Pecher *et al.*, 1998; Tinivella and Accaino, 2000), others have unraveled the physical properties of the entire gas hydrate stability zone in terms of seismic attenuation (Singhroha *et al.*, 2016), velocities (Gassner *et al.*, 2019; Gorman *et al.*, 2002; Minshull *et al.*, 1994), resistivity (Gehrmann *et al.*, 2016; Kannberg and Constable, 2020) or a combination of these (Berndt *et al.*, 2019), through analysis and inversion of controlled source seismic and electromagnetic



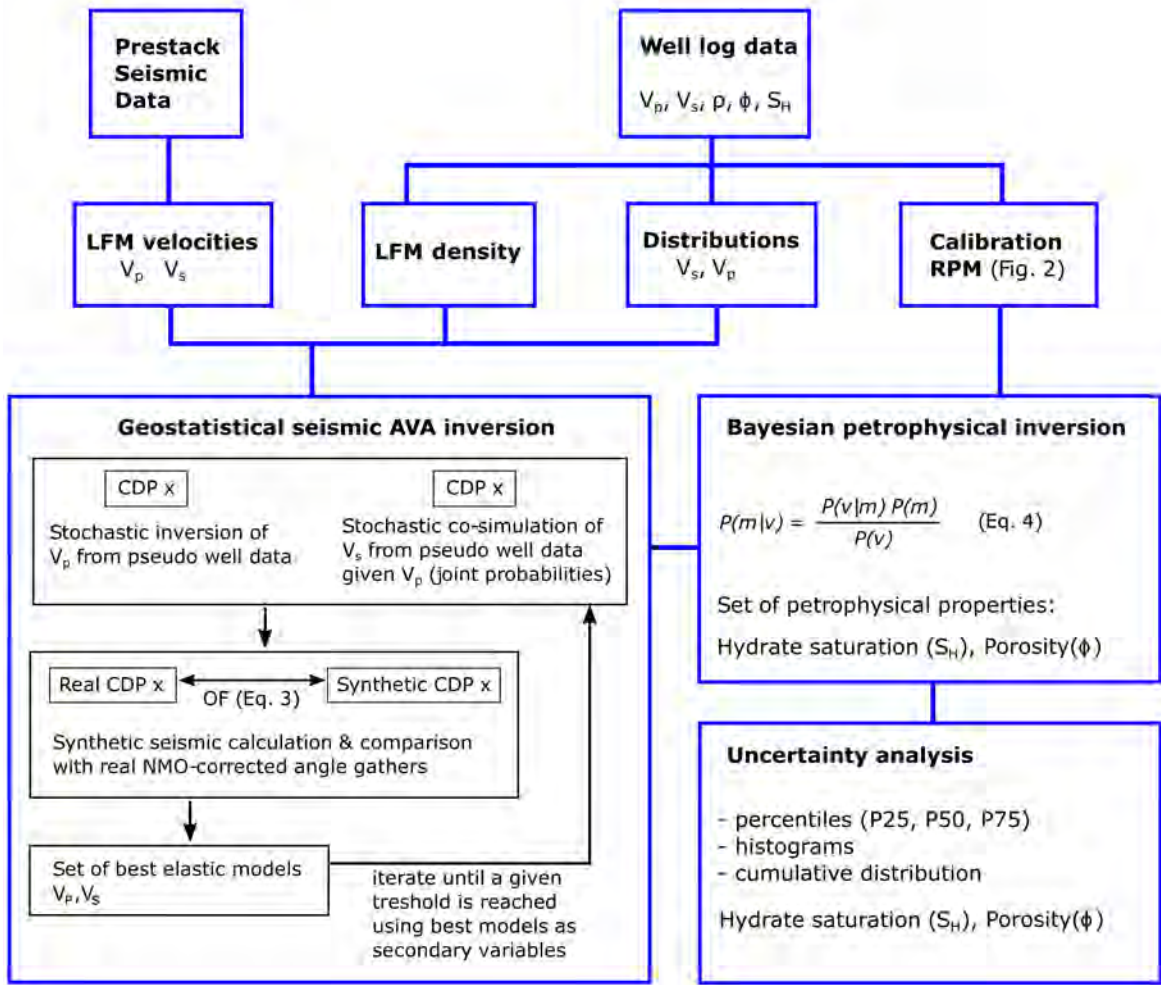


**Figure 4.1:** Flow chart representation of the geological modelling workflow used to predict the spatial distribution of gas hydrate saturation and porosity. The following shorthand terms are used:  $V_P$  = P-wave velocity,  $V_S$  = S-wave velocity,  $\rho$  = density,  $\phi$  = porosity,  $S_H$  = gas hydrate saturation, CDP = common depth point, OF = objective function, NMO = normal move-out, AVA = amplitude versus angle, LFM = low frequency model, RPM = rock physics model.

data. Theoretical rock physics models relate petrophysical properties such as hydrate saturation ( $S_H$ ) and porosity to elastic properties and seismic amplitudes (Dvorkin *et al.*, 2000; Helgerud *et al.*, 2000; Minshull *et al.*, 1994; Tinivella, 1999), and could be integrated in the inversion process for the prediction of the spatial distribution of subsurface petrophysical properties (e.g., Dai *et al.*, 2004b; Dubreuil-Boisclair *et al.*, 2012; Fohrmann and Pecher, 2012; Liu *et al.*, 2017; Tinivella *et al.*, 2002; Wang *et al.*, 2018). However, these methods are still affected by high uncertainty, especially when the inversion cannot be constrained by in-situ information (Dai *et al.*, 2008). In these

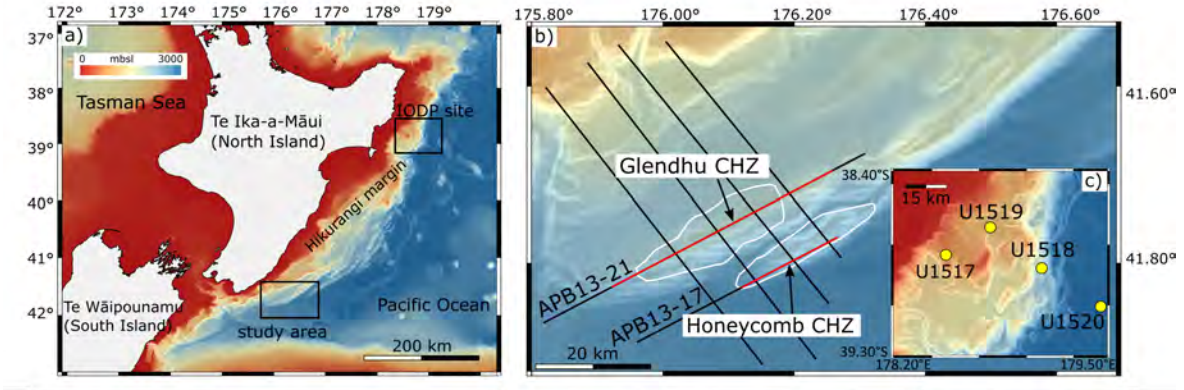


**Figure 4.2:** a) Location of the Hikurangi Margin of New Zealand. Southern black box (study area) is enlarged in (b). Northern black box is enlarged in (c). b) Enlarged bathymetric map of the study area showing the areal extents of concentrated gas hydrate accumulations: the Glendhu Concentrated Hydrate Zone (CHZ) and the Honeycomb CHZ (white polygons, after Turco *et al.*, 2020). Long-offset seismic profiles from the APB13 survey are shown by black lines. The lines used for the inversion are marked in red. c) locations of IODP Expedition 372 drill holes further north on the margin, Pecher *et al.* (2018). Map coordinates are in latitude/longitude (WGS84 datum).

cases, the application of stochastic inversion approaches is essential to quantify the uncertainty related to the predictions (Senger *et al.*, 2010; Shelander *et al.*, 2010).

In this chapter, I propose a sequential geological modelling workflow that combines statistically based seismic and rock physics inversions to characterise two submarine ridges hosting concentrated hydrate deposits on the southern Hikurangi Margin east of New Zealand. The advantage of combining geostatistical seismic amplitude-versus-angle (AVA) inversion with a Bayesian rock physics inversion is the potential to predict and simulate the spatial distribution of elastic and petrophysical properties at small-scale variability (i.e., down to the scale of seismic resolution). The workflow is illustrated by its application to two seismic profiles that cross the area of interest. The study area is a primary target of current research into the economic potential of New Zealand’s gas hydrate deposits, and the environmental implications of extracting energy from them. This work builds upon previous investigations that identified concentrated gas hydrate accumulations in the region (Crutchley *et al.*, 2015, 2019; Fraser *et al.*, 2016). Preliminary analysis based on the reflectivity of discrete seismic events provided localized estimates of gas hydrate saturations (Turco *et al.*, 2020, Chapter 3); this current study extends that initial research into a detailed geophysical characteri-

sation of the entire gas hydrate stability zone (GHSZ) in the area, and the assessment of the related uncertainty. The proposed workflow can be applied to other gas hydrate settings globally where high quality long-offset MCS data exist.

## 4.2 Two step inversion

In this section, I first describe the rock physics model (RPM) parametrisation adopted in this work for gas hydrate-bearing sediments (Dvorkin *et al.*, 2000; Helgerud *et al.*, 2000), then I illustrate the workflow used to model the spatial distribution of porosity and gas hydrate saturation. This workflow can be divided into two main steps (Figure 4.1): (1) an iterative geostatistical seismic AVA inversion to obtain 2D elastic models of P- and S-wave velocity (Azevedo *et al.*, 2018), and (2) a Bayesian petrophysical inversion based on the calibrated rock physics model to predict gas hydrate saturations and porosity using the inverted elastic models (Grana and Della Rossa, 2010).

### 4.2.1 Rock physics model calibration

A rock physics model links petrophysical properties, such as porosity, mineralogy and hydrate and water saturations, to the elastic properties of a porous rock, such as P-wave and S-wave velocities and density (Dvorkin *et al.*, 2014; Mavko *et al.*, 2020). Effective medium models for sediments containing gas hydrate, as developed by Dvorkin *et al.* (2000), rely on the concept of critical porosity, i.e., the porosity value that marks the transition between the elastic behaviour of a suspension and that of a grain-supported rock. This value is typically about 0.4 for sedimentary rocks (Mavko *et al.*, 2020).

In the models proposed by Dvorkin *et al.* (2000), the sediments containing gas hydrate are modeled by averaging the elastic properties of the material at the critical porosity and the pure solid phase material at zero porosity. The models use the effective moduli of a dense random packing of identical spheres (see Chapter 2.3). The elastic properties of hydrate-bearing sediments are affected by the microscopic distribution of the hydrate with respect to the matrix grains and the pore space, as well as by the amount of gas hydrate present (e.g., Lee and Collett, 2005). Generally, because of the solid state of methane hydrate, the bulk and shear moduli are larger in rocks that contain gas hydrates. Therefore,  $V_P$  and  $V_S$  are higher in hydrate-bearing sediments when compared to water-saturated rocks, even though the bulk density slightly decreases (Dai *et al.*, 2004b).

The various types of hydrate occurrence will affect the elastic properties of the sediment in different ways. Several rock physics models exist in the literature that quantify the effect of hydrate concentrations and type of occurrence on elastic properties (Chand *et al.*, 2004; Dvorkin *et al.*, 2000; Sava and Hardage, 2006; Xu *et al.*, 2004). I use a model that treats gas hydrate as a component of the load-bearing matrix of the sediment, in line with laboratory and field studies (e.g., Cook and Waite, 2018; Lee *et al.*, 2010; Yun *et al.*, 2005), which show that highly concentrated gas hydrates deposits in coarse-grained sediments act as a “load-bearing” part of the matrix.

A detailed description of the rock physics model adopted in this work is presented in Chapter 2.3. The calibration of the rock physics model was performed by tuning the parameters of effective pressure, mineral content, and coordination number until a satisfactory fit between the observed and predicted porosities and hydrate saturations was achieved (Figure 4.3). Fine tuning of the RPM input parameters is essential to ensure that the model accurately represents the well log dataset. Even though quantitative calibration methods provide the best validation of the rock physics models, especially in cases where collocated wells exist within the study area and intercept the target formation or a reservoir (e.g., Bachrach and Avseth, 2008; Dvorkin and Wollner, 2017; Moyano *et al.*, 2011), I deem the qualitative analysis of the cross-plots shown in Figure 4.3 satisfactory for the objective of this work. The value of critical porosity was set to 0.4 (Dvorkin and Nur, 2002), and the coordination number was fixed at 6. The choice of the clay/quartz ratio was made assuming that interbedded mudstone and sandstone layers are typical of this geological setting (Pecher *et al.*, 2018). The clay content was set to 60% (i.e. 40% quartz). Finally, the effective pressure parameter was set as a linear trend increasing from 0 to 5 MPa at the BSR depth.

## 4.2.2 Geostatistical seismic AVA inversion

The aim of seismic inversion is to predict the spatial distribution of the subsurface elastic properties  $v$  (e.g., impedances, P-wave and S-wave velocities) from a set of observed data ( $d_{obs}$  - i.e., the recorded seismic data). The link between the model and data domains may be summarized by:

$$d_{obs} = F(v) + e, \quad (4.1)$$

where  $F$  is the forward operator, which allows computation of the synthetic data from a given model  $v$ ;  $e$  represents the noise in the data and physical model assumptions.  $F$  represents the convolution between a given wavelet and the subsurface reflection coefficients computed from  $v$ . The goal of seismic inversion is to find the best set of model parameters describing the spatial distribution of elastic properties in the subsurface, such that the synthetic data generated by a forward model are as similar as possible to the observed data. However, solving a seismic inverse problem can be challenging as they are nonlinear, ill-posed problems with non-unique solutions. Such problems can be solved under a deterministic or probabilistic framework (Bosch *et al.*, 2010; Tarantola, 2005).

To predict the spatial distribution of subsurface elastic properties I use iterative geostatistical seismic AVA inversion (Azevedo *et al.*, 2018; Azevedo and Soares, 2017). In this inversion method, the model parameter space is represented by a 2D grid with x and z dimensions equal to, respectively, number of traces and number of time samples, and cell width equal to the trace spacing, or bin length (12 m). The  $V_P$  model (4.4) is generated and perturbed using stochastic direct sequential simulation (DSS, Soares, 2001), whereas the  $V_S$  model is co-simulated using the joint probability distribution between  $V_P$  and  $V_S$  retrieved from regional IODP well logs data, described in the next section (co-DSS, Deutsch and Journel, 1994; Horta and Soares, 2010). The well log data (described in the next section) provide the range of values for each property to be simulated, as well as the target marginal and joint distributions to be reproduced by the geostatistical simulation algorithm. Stochastic sequential simulations and co-simulation methods ensure that the relationship between  $V_P$  and  $V_S$  as observed in the well log data is honoured at any given pair of models simulated during the iterative process. The synthetic angle-gathers are computed solving the full Zoeppritz equations (Avseth *et al.*, 2010), and compared with the real gathers according to the following similarity metric:

$$S = \frac{2 \sum_{s=1}^N (d_{obs,s}, d_{syn,s})}{\sum_{s=1}^N (d_{obs,s})^2 + \sum_{s=1}^N (d_{syn,s})^2}, \quad (4.2)$$

where  $d_{obs}$  and  $d_{syn}$  are, respectively, the real and the synthetic seismic traces, with  $N$  seismic samples.  $S$  measures the similarity between seismic traces and, as Pearson's correlation coefficient, is bounded between -1 and 1.  $S$  is simultaneously sensitive to both the seismic waveform and amplitudes.

The use of a priori low-frequency models (LFM) of  $V_P$  and  $V_S$  allows exploiting existing knowledge about the subsurface geology in the inversion process. Following the approach presented by Pereira *et al.* (2019), the LFM are incorporated in a two-term objective function:

$$OF = w_1 S + w_2 \left( 1 - \frac{|m_{sim} + m_{LFM}|}{max(m_{sim})} \right), \quad (4.3)$$

where  $m_{LFM}$  and  $m_{sim}$  are the a priori and the simulated models, respectively, and  $w_1$  and  $w_2$  are user defined weighting factors controlling the importance of each term of the equation and must sum to unity. Qualitatively, these weights can be determined according to the quality of the seismic data and to the reliability of the  $m_{LFM}$ . In this work, after running several tests, the parametrisation was set to 0.25 and 0.75 for  $w_1$  and  $w_2$ , respectively. The a priori model of  $V_P$  is obtained from the iterative pre-stack time migration during the seismic processing, and the  $V_S$  low-frequency model is obtained through a  $V_P - V_S$  relationship given by the rock physics models (Chapter 2.3). The minimization of OF drives the iterative procedure ensuring the convergence of the method. The geostatistical seismic AVA inversion is summarized below.

1. Stochastic sequential simulations:

- (a) Generate an ensemble of  $N_s$   $V_P$  velocity models using direct sequential simulations (Soares, 2001)
- (b) Generate an ensemble of  $N_s$   $V_S$  velocity models with direct sequential co-simulation with joint probability distributions (Horta and Soares, 2010) using the  $V_P$  velocity models generated in a) as auxiliary variables

2. Seismic data comparison:

- (a) Compute synthetic seismic angle gathers: for each set of realizations generated in step 1, compute angle-dependent reflection coefficient volumes using the simulated  $V_P$  and  $V_S$  models and the background density model, and convolve them with the estimated wavelets
- (b) Compute  $OF$  (Eq. 4.3) for each CDP location: the first term is given by computing  $S$  (Eq. 4.2) from the synthetic and the real angle gathers; the second term is calculated between the simulated  $V_P$  and  $V_S$  vertical profiles and the respective low-frequency model at that particular CDP location

3. For each CDP location, select and store the vertical profiles of  $V_P$  and  $V_S$  that produce the highest values of  $OF$  from the  $Ns$  ensembles of models generated in 1a-b), along with the corresponding  $OF$  value associated with each CDP; the resulting models are called  $V_P^*$ ,  $V_S^*$  and  $OF^*$  models
4. Use the best local models from 3) ( $V_P^*$  and  $V_S^*$ ) and the corresponding similarity values ( $OF^*$ ) as secondary variables in the stochastic sequential co-simulation of a new set of  $V_P$  and  $V_S$  models following the sequential procedure described in 1)
5. Return to 2) and iterate until a pre-defined stopping criterion is reached.

After six iterations, with  $Ns$  set to 32, the inversion results were considered satisfactory. Conditioned stochastic sequential simulation and co-simulation generally require the availability of well-log data for each property of interest. As no boreholes have ever been drilled in the immediate vicinity of the study area, I use well-log data from IODP Expedition 372 (Pecher *et al.*, 2018), on the northern Hikurangi Margin, to infer the conditioning probability distribution of the elastic properties of interest to be used in the stochastic sequential simulation and co-simulation steps (e.g., Dai *et al.*, 2008; Shelandar *et al.*, 2010). Collected over 300 km to the north-east on the same continental margin, these log data characterize marine sediments from the mid and lower slope of the accretionary wedge and the Hikurangi subduction trench. As such, they are considered to be broadly representative of the geological environment of the study area. In this work, I assume a bulk density trend variation with depth at Honeycomb and Glendhu ridges compiled and averaged from the IODP data from the northern Hikurangi Margin and assume that changes in elastic impedance are mainly caused by changes in  $V_P$  and  $V_S$ . All models generated with stochastic sequential simulation and co-simulation during the inversion procedure ensure the reproduction of the marginal and joint probability distributions of each elastic property. The probability distributions, in turn, are inferred from the well logs and given spatial continuity patterns as revealed and imposed by a variogram model (Azevedo *et al.*, 2018).

### 4.2.3 Bayesian petrophysical inversion

The goals of petrophysical inversion are to predict the spatial distribution of petrophysical properties, in this case hydrate saturation and porosity, from inverted elastic properties, and to quantify their uncertainty. The inversion is performed under a Bayesian framework where the prior distribution of the petrophysical properties is a

linear combination of Gaussian distributions, referred to as a Gaussian mixture model (Grana and Della Rossa, 2010). In particular, I aim to predict the probability of the petrophysical properties given the elastic properties  $P(m|v)$  as:

$$P(m|v) = kP(v|m)P(m), \quad (4.4)$$

where  $k = 1/\int P(v|m)P(m)dm$ . The probability  $P(m)$  is the prior distribution of the petrophysical properties. The probability  $P(v|m)$  is the likelihood model of the elastic properties for each possible value of the petrophysical properties. The likelihood model is built using a training dataset constructed using the rock physics model.

I assume that the prior distribution of the porosity and hydrate saturation is a bivariate Gaussian mixture distribution:

$$P(m) = \sum_{k=1}^N \lambda_k N(\mu_{m|k}, \Sigma_{m|k}), \quad (4.5)$$

with prior weights  $\lambda_k$ , prior mean  $\mu_{m|k}$ , and prior covariance matrices  $\Sigma_{m|k}$ . I also assume that the likelihood model  $P(v|m)$  is Gaussian with  $P(m) = N(f(m), \Sigma_v)$ , with the mean equal to the rock physics model predictions  $f(m)$  for the petrophysical properties  $m$  and covariance matrix  $\Sigma_v$ . Then, the posterior distribution  $P(m|v)$  of the petrophysical properties conditioned by the elastic properties is a Gaussian mixture model (Grana, 2016):

$$P(m|v) = \sum_{k=1}^N \omega_k N(\mu_{m|v,k}, \Sigma_{m|v,k}), \quad (4.6)$$

with conditional weights  $\omega_k$ , conditional mean  $\mu_{m|v,k}$ , and conditional covariance matrices  $\Sigma_{m|v,k}$ . The analytical expressions of the conditional parameters are given by:

$$\omega_k = \frac{\lambda_k N(\mu_{v|k}, \Sigma_{v|k})}{\sum_{h=1}^N \lambda_h N(\mu_{v|h}, \Sigma_{v|h})}, \quad (4.7)$$

$$\mu_{m|v,k} = \mu_{m|k} + \Sigma_{(m,v),k} (\Sigma_{v|k})^{-1} (v - \mu_{v|k}), \quad (4.8)$$

$$\Sigma_{m|v,k} = \Sigma_{m|k} - \Sigma_{(m,v),k} (\Sigma_{v|k})^{-1} \Sigma_{(v,m),k}, \quad (4.9)$$



where  $\Sigma_{(m,v),k}$  is the cross-covariance of the petrophysical and elastic properties.

The analytical expressions of the rock physics model (described in Section 2.3) allow building a template, or training dataset, for the entire range of properties by forward modelling elastic properties through the load-bearing model using all possible combinations of porosity and hydrate saturation values. This step allows us to retrieve the relationships among P-wave velocity, S-wave velocity, density, porosity and gas hydrate saturation. The Bayesian inversion is then applied sample by sample, and at each point the maximum of the posterior distribution  $P(m|v)$  is the most likely value at that location.

### 4.3 Geophysical data

The seismic data used in this study comprise a set of 2D MCS profiles from the publicly available APB13 dataset. The main acquisition parameters for these data are summarised in Table 3.2.

I reprocessed the APB13 data to preserve the true relative amplitude of the traces. The processing consisted of these steps: application of crooked line geometry, CDP sorting, resampling at 2 ms, Butterworth filtering with corner frequencies of 2, 4, 60, 90 Hz, correction for spherical divergence applied with the velocity field obtained from semblance-based velocity analysis, iterative pre-stack Kirchhoff time migration, conversion from offset to angle domain and muting above the seafloor. In this chapter, I apply the workflow to two key seismic profiles that cross the two ridges (Lines APB13-21 and APB13-17 – Figure 4.2).

The calibration of the rock physics model and the conditioning distributions of the stochastic sequential simulations used in the geostatistical seismic AVA inversion are based on the data from IODP sites U1517 and U1518 of Expeditions 372A (Pecher *et al.*, 2018) and 372B/375 (Saffer *et al.*, 2018) from the northern Hikurangi Margin. The available well-log data consist of logging while drilling (LWD) measurements of neutron porosity, P- and S-wave velocities, neutron density and resistivity. Estimations of gas hydrate saturations at these locations are based on pore water chlorinity and resistivity logs (Pecher *et al.*, 2019). Although these IODP sites are several hundred kilometres from our study area (Figure 4.2), they are the only drilling-based measurements for

these parameters that exist on the margin. I opt to use these data over global empirical models (e.g., Tenzer and Gladkikh, 2014) because they come from the same regional geological setting, and because the dataset includes a broad range of parameter values over the depth range of interest for this study.

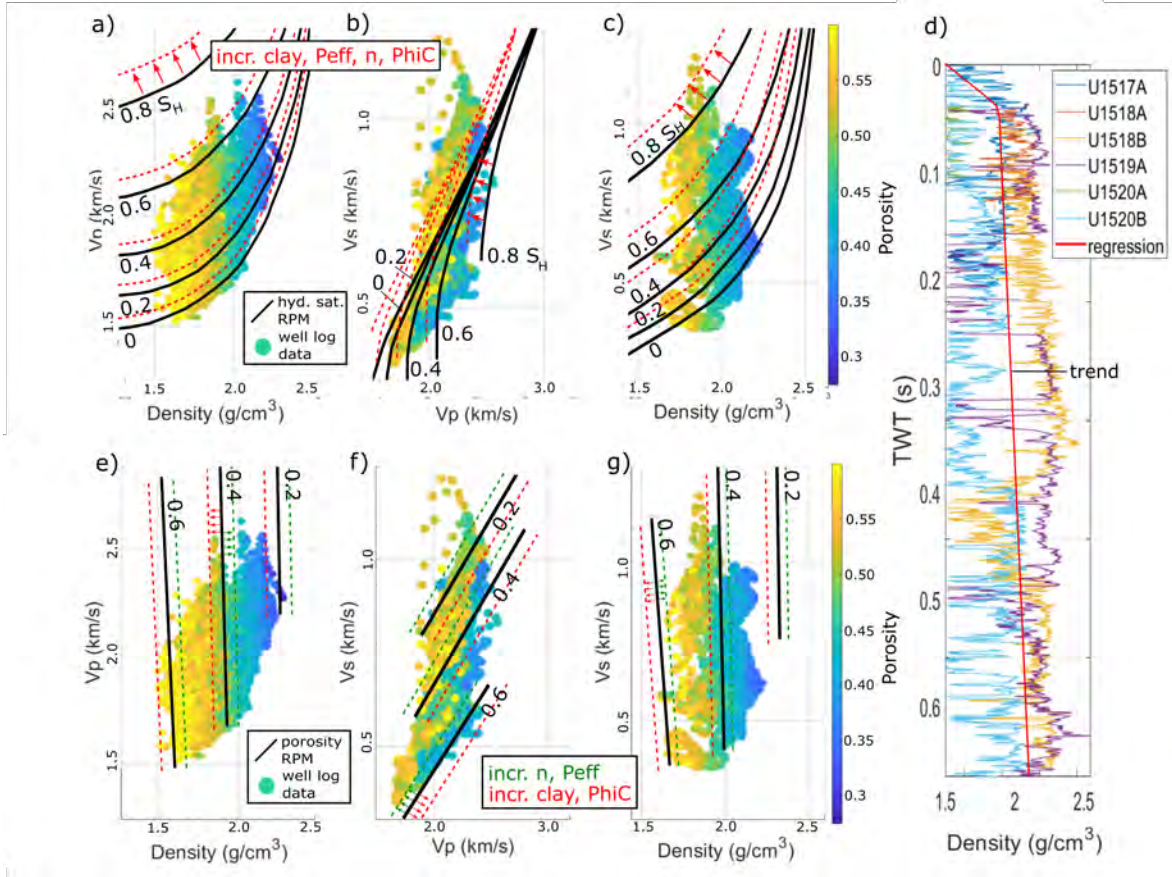


**Figure 4.3:** (a) – (c): Rock physics model (RPM, bold and dashed lines) overlain on the available IODP data from sites U1517A and U1518B (circles). The panels (a)-(c) show the relations between the elastic properties and gas hydrate saturations (shown in %). The panels (e)-(g) show the relations between elastic properties and porosity estimated through the calibrated rock physics model. The IODP data are colour-coded according to porosity in all panels. The dashed red and green lines represent the changes in the petrophysical properties caused by a change (increase) in the RPM input parameters:  $n$ : coordination number;  $P_{eff}$ : effective pressure; clay: clay content;  $\Phi_{iC}$ : critical porosity. (d) the density trend with depth used for the inversion (red line), calculated from all available IODP data from the northern Hikurangi Margin and used in the geostatistical seismic AVA inversion, which is carried out in the time domain (TWT: two-way travel-time below seafloor at each site).

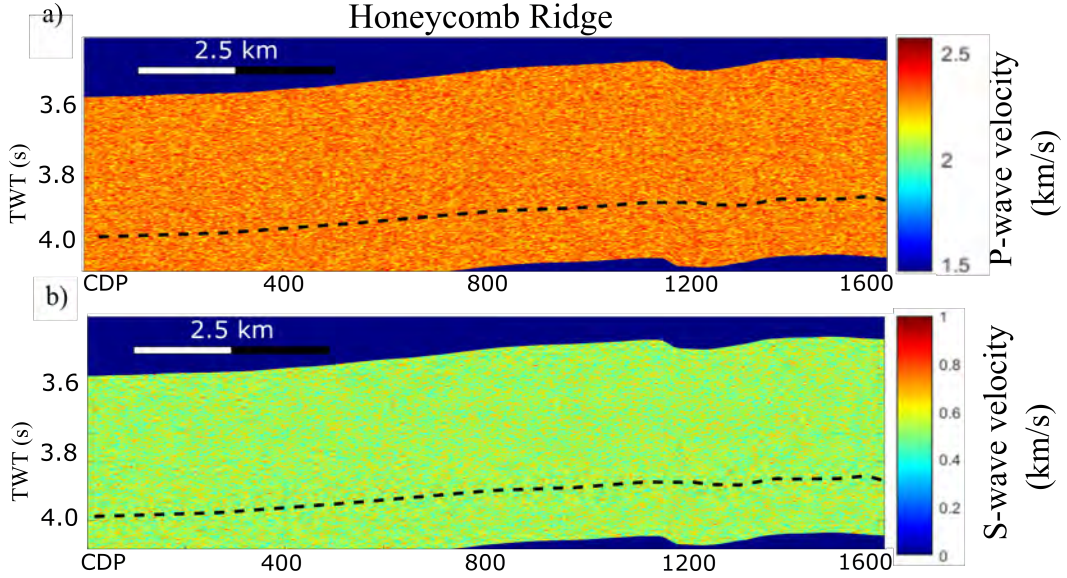


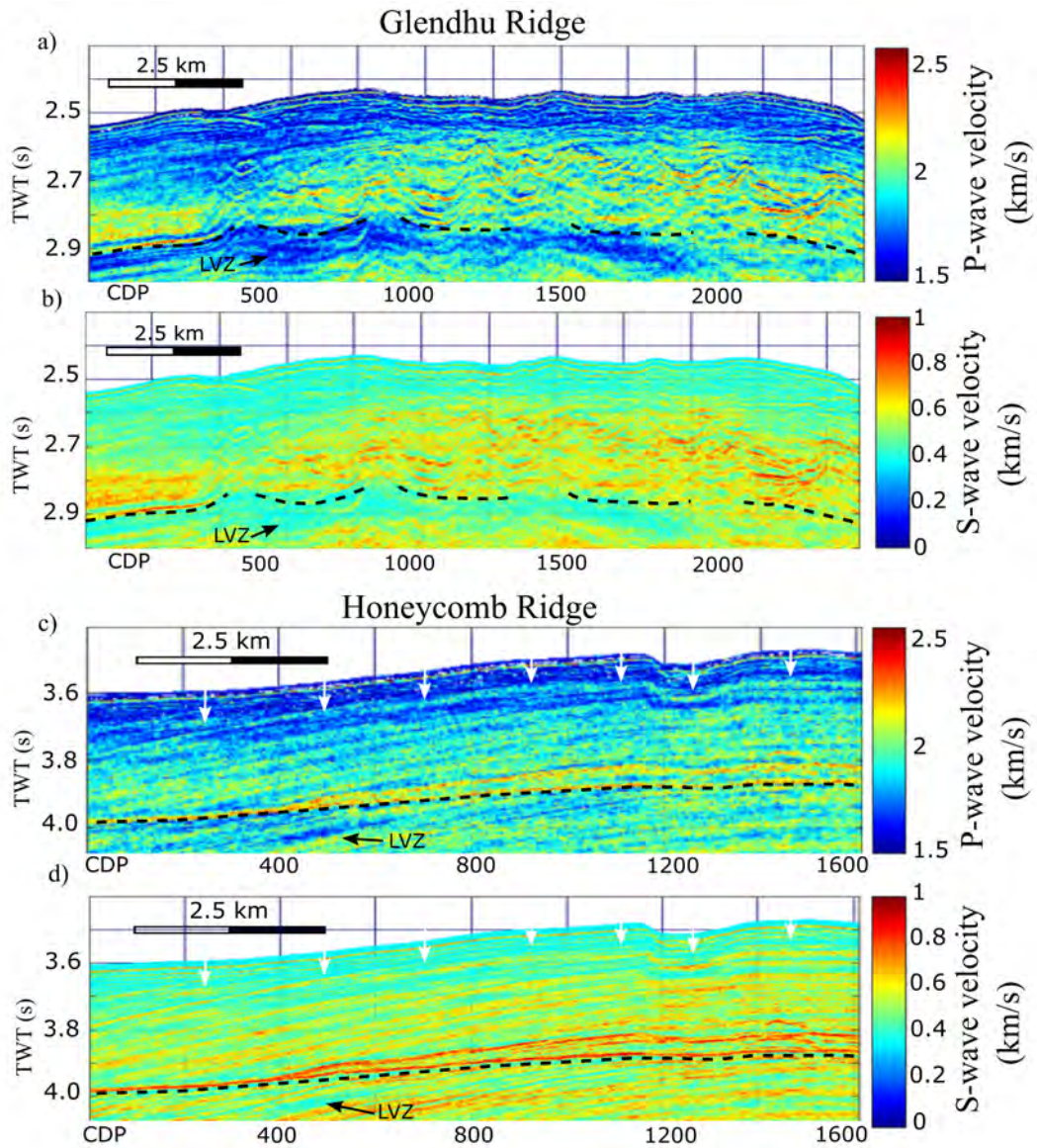
**Figure 4.4:** Examples of starting models of  $V_P$  and  $V_S$  for Line APB13-17 (Honeycomb Ridge).

## 4.4 Results

### 4.4.1 Prediction of elastic properties

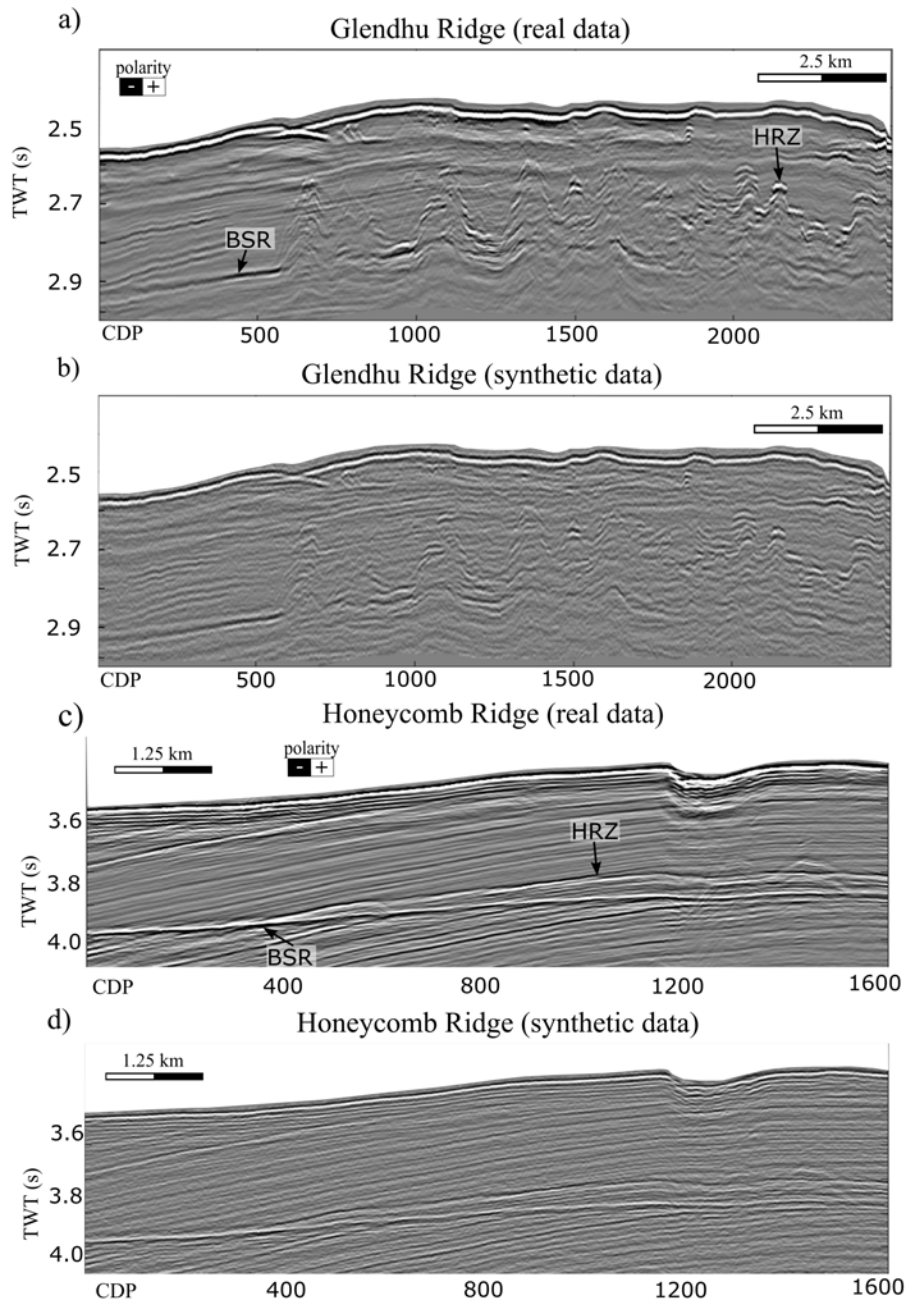
The iterative geostatistical seismic AVA inversion technique ran with six iterations and 32 realizations of  $V_P$  and  $V_S$  per iteration. The input data for the inversion consisted of the elastic logs used to build the conditioning distributions, and a low frequency trend for each elastic property, which I derived from the conventional seismic velocity (i.e.,  $V_P$ ) analysis and included in the objective function as proposed by Pereira *et al.* (2019). I set the weight of the low-frequency trend component in the objective function to 75%, and its signature can be observed in the inverted velocity models as a background trend that increases with depth within the GHSZ, and slightly decreases below the BSR (Figure 4.5). I selected this weighting during the parametrisation stage of the inversion method. Angle-dependent wavelets, ranging from  $2^\circ$  to  $55^\circ$ , were estimated from the pre-stack seismic gathers by averaging the seafloor reflection of adjacent traces corresponding to a region of flat bathymetry. The inversion was carried out in the pre-stack domain.

Figure 4.5 shows the mean model for  $V_P$  and  $V_S$  of the set of realizations generated during the last iteration of the inversion. Broad regions of high  $V_P$  and  $V_S$  above the BSR correspond to regions of high reflectivity in the seismic data (Figure 4.6). These



**Figure 4.5:** Mean model of the elastic realizations generated at the last iteration of the geostatistical inversion for Glendhu (APB13-21 profile) and Honeycomb (APB13-17 profile) ridges: (a), (c)  $V_P$ ; (b), (d)  $V_S$ . LVZ: low-velocity zones. The dashed black line represents the BSR location as interpreted in the original seismic data. The white arrows in (c) and (d) indicate an inversion artefact corresponding to the bubble pulse effect in the wavelet.





**Figure 4.6:** Near-stack sections (up to 300 m offset) of APB13-21 (a) and APB13-17 (c) at Glendhu and Honeycomb ridges a), c) show the real seismic data and b) and d) the synthetic data calculated from the mean elastic models shown in Figure 4.6. Correlation coefficient between the two sections is 0.78 for Glendhu Ridge and 0.79 for Honeycomb Ridge; BSR: bottom simulating reflection; HRZ: high reflectivity zone.

regions correspond to the concentrated hydrate deposits that have been investigated regionally (Chapter 3). At both ridges, the base of the GHSZ is clearly manifested in both  $V_P$  and  $V_S$  models by a velocity reduction. In terms of  $V_P$ , this is due to a transition from gas hydrate and water within the GHSZ to free gas and water beneath the GHSZ. In terms of  $V_S$ , the contrast is due to the transition from gas hydrate bearing sediments above (that increase the shear modulus) to sediments free of gas hydrates below. A decrease in  $V_P$  and  $V_S$  can be observed within the GHSZ at Glendhu Ridge between CDPs 500 and 700 (low-velocity zone LVZ, Figure 4.5), directly below a region of local BSR shoaling observed in the seismic data (LVZ, Figure 4.5). A band of high velocities that mimics the seafloor can be observed in all panels in Figure 4.5 at about 0.1 s below the seafloor; this is an inversion artefact corresponding to a bubble pulse effect in the wavelet. To preserve the true seismic amplitudes, deconvolution was not applied to the data - as such, the reverberation of the seafloor results in an artificial increase in impedance in the inversion process.

The synthetic near-stack seismic data computed from the mean  $V_P$ ,  $V_S$  and density models are able to capture the most significant seismic events, especially the high amplitude reflections observed at Glendhu Ridge at CDPs 800-1000 and 2000-2200 (Figure 4.6a and 4.6b), as well as the BSR and the top of concentrated hydrate accumulation at Honeycomb Ridge (Figure 4.6c and 4.6d). The synthetic seismic data computed from the predicted elastic models have a correlation coefficient of 0.78 compared to the real data for the Glendhu Ridge seismic line, and of 0.79 for the Honeycomb Ridge line ( $S$  in equation 4.2). Some high-frequency noise is introduced in the synthetic data by the stochastic small-scale perturbation of the models, that is performed at the sample scale (2 ms). Nevertheless, the quality of the synthetic section is satisfactory, as the main seismic events of interest are reproduced in terms of spatial location, amplitude and phase (i.e., BSR, high amplitude reflections). The slightly suppressed amplitude range in the synthetic data comes from the fact that they are based on the mean inverted elastic parameters, which will be slightly smoothed compared to the (unknown) real elastic parameters.

#### 4.4.2 Prediction of petrophysical properties

Based on the set of inverted elastic models, the next step was to proceed with the petrophysical inversion. Because the GHSZ is our target and I am applying a rock physics model for gas hydrate-bearing sediments, only the interval between the

seafloor and the BSR is considered. In locations where no clear BSR is present, it is interpolated from adjacent observations. The inversion is performed trace-by-trace.

The spatial distribution of petrophysical properties computed from average models of  $V_P$ ,  $V_S$  and density is shown in Figure 4.7. Porosity along Glendhu Ridge ranges from 0.35 to 0.6, generally decreasing with depth. The hydrate saturation distribution, expressed as fraction of pore space, appears “patchy”, especially within the regions where anomalous reflectivity indicates the existence of concentrated hydrate zones (CHZ), as interpreted in Chapter 3. The extent of the CHZs in both lines corresponds to the regions beneath the dashed white lines in Figure 4.7. The CHZ region beneath Glendhu Ridge is characterized by estimated saturations that locally exceed 0.4 (Figure 4.7a). At Honeycomb Ridge, the same porosity trend is observed. The gas hydrate saturations reach values of  $>0.6$  at the top of the CHZ beneath Honeycomb Ridge (Figure 4.7c). Figure 4.8 shows the relation among petrophysical and elastic properties of the inverted models and compares the distribution with the theoretical rock physics model discussed above. The good match between the observed inverted values and the theoretical model is indicative of the accuracy of the Bayesian inversion for porosity and gas hydrate saturation.

To describe the variability of the resulting models, the set of 32 pairs of  $V_P$  and  $V_S$  realizations produced during the last (6<sup>th</sup>) iteration were inverted for  $S_H$  and porosity, and the 25% and 75% percentiles were computed from the sets of models for each property. Figure 4.8 shows a summary of the initial analysis that was qualitatively performed after the inversion: for a given CDP location, the 32  $V_P$ ,  $V_S$ ,  $S_H$  and porosity realizations from the last iteration are plotted (Figure 4.8a). The mean of the realizations is shown by the bold black line and is used to compute the synthetic seismic angle traces shown in Figure 4.8e (near, mid and far angles). Figures 4.8f - 4.8m show the relationship between the petrophysical and elastic properties of the mean of the realizations superimposed on the calibrated rock physics model.

Figure 4.9 shows the two seismic profiles displayed in terms of percentiles for  $V_P$ ,  $V_S$ ,  $S_H$  and porosity. As expected, porosity displays little variability (Fig. 4.9m-4.9p), because it is strongly dependent on the density model, which was not updated throughout the iterations. The high amplitude reflections within the GHSZ at both ridges are characterized by consistently increased seismic velocities (Fig. 4.9a-4.9h), and high hydrate saturation (Fig. 4.9i-4.9l).

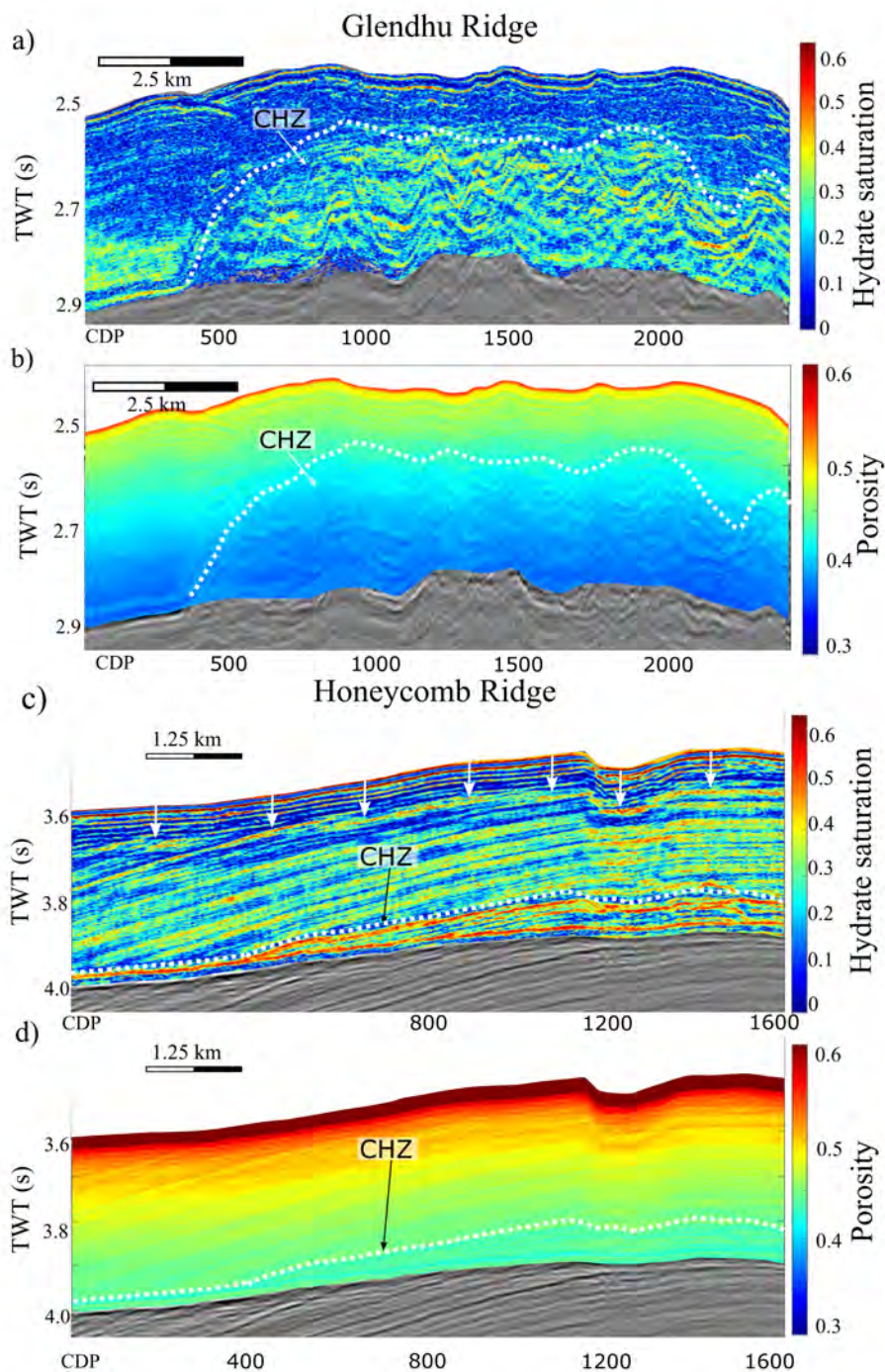


**Figure 4.7:** Inverted models of hydrate saturation (a) and porosity (b) for profile APB13-21 at Glendhu Ridge, and (c), (d) for profile APB13-17 at Honeycomb Ridge, calculated from the mean models shown in Figure 4.5, overlain on the original seismic section. CHZ: concentrated hydrate zone. The white arrows in (c) indicate an inversion artefact corresponding to the bubble effect in the wavelet.



### 4.4.3 Local gas hydrate volume assessment

After predicting the spatial distribution of elastic and petrophysical properties in the study area, I can make a first order estimate of the amount of gas hydrate. 3D spatial constraints of the interpreted CHZs at the two ridges are provided by the interpretation of a closely spaced 2D seismic reflection dataset, which allows the thickness of the reservoirs to be mapped (Chapter 3). The CHZs at Glendhu and Honeycomb ridges have volumes of  $9.4 \times 10^6 \text{ m}^3$  and  $4.1 \times 10^6 \text{ m}^3$ , respectively, covering a total combined surface area of  $110 \text{ km}^2$ . These reservoirs are considered regions of sediments where the gas hydrate can be present in a rather laterally heterogeneous distribution. However, highly concentrated gas hydrate regions appear to be following the stratigraphy at the top and within these highly reflective regions, suggesting that the Glendhu and Honeycomb CHZs could be systems of different prospects, rather than single accumulations of concentrated gas hydrate.

Because of the lack of geological data to better constrain the reservoirs, it is best to calculate the total gas hydrate volume following a bulk approach, considering the entire regions of high seismic reflectivity (CHZs in Figure 4.2 and Figure 4.7). The set of estimated porosity and gas hydrate saturation models, calculated from the 32 realizations of  $V_P$  and  $V_S$  from the last iteration of the seismic inversion step, are used to compute the 25%, the 50% and the 75% percentiles of all the seismic trace samples lying within the CHZs shown in Figure 4.7. These values are then used to calculate pessimistic, most likely and optimistic scenarios for the regional gas hydrate volume assuming an average value of porosity and  $S_H$  for the entire CHZ.

The gas hydrates volume ( $G$ ) is:

$$G = \phi S_H V, \quad (4.10)$$

where  $\phi$  is the total porosity,  $S_H$  is the gas hydrate saturation and  $V$  is the bulk sediment volume of the reservoir. The total volumes of gas hydrate estimated assuming a bulk mean porosity and mean hydrate saturations for the Glendhu and Honeycomb CHZs (Table 4.4.3)) range from  $2.45 \times 10^5 \text{ m}^3$  to  $1.72 \times 10^6 \text{ m}^3$ , with the best estimate at  $9.68 \times 10^5 \text{ m}^3$ .

	<b>Bulk porosity</b> ( $\phi$ )	<b>Bulk hydrate saturation</b> ( $S_H$ )	<b>Hydrate volume in</b> $\text{m}^3$
<b>P25</b>	0.36	0.04	$2.45 \times 10^5$
<b>P50</b>	0.38	0.20	$9.68 \times 10^5$
<b>P75</b>	0.39	0.34	$1.72 \times 10^6$

**Table 4.1:** Low (P25), best (P50) and high (P75) estimates of petrophysical properties for the two reservoirs and total gas hydrate volume assessment.

## 4.5 Discussion

The processes that led to the development of concentrated gas hydrate accumulations at the base of the GHSZ along the Hikurangi Margin have been considered widely (e.g., Barnes *et al.*, 2010; Crutchley *et al.*, 2019; Fohrmann and Pecher, 2012; Wang *et al.*, 2017a). Upward gas migration often seems to be facilitated by moderately-steeply dipping permeable strata. Gas migrating across the base of the GHSZ presumably leads to the accumulation of highly saturated hydrate deposits in these permeable (probably sand-rich) layers. Such deposits manifest themselves as highly reflective regions in seismic data, congruent with high elastic velocities. They are typically observed in the cores of anticlinal ridges and in other continental margins and deep-sea basins around the world (e.g., Berndt *et al.*, 2019; Fujii *et al.*, 2015; Portnov *et al.*, 2019; Rodrigo *et al.*, 2009; Shankar and Riedel, 2011; Yoo *et al.*, 2013).

### 4.5.1 Comparison with previous studies

This work builds on a detailed study of the Honeycomb and Glendhu hydrate systems (Chapter 3), which made initial quantifications of the gas hydrate saturation at specific locations within the CHZs, based on normal incidence seismic reflectivity. The great advance made by the two-step seismic inversion approach presented in this study is the ability to retrieve the 2D spatial distribution of elastic properties and gas hydrate saturation, without relying on the limitation of tracking continuous seismic events within the CHZ. Furthermore, the geostatistical seismic AVA inversion allowed us to estimate the  $V_S$  distribution within the GHSZ. The shear wave velocity of hydrate-bearing sediments may or may not increase with respect to the hydrate-free sediment velocity, depending on the hydrate morphology and saturation (Chand *et al.*, 2004;

Dvorkin *et al.*, 2000; Pan *et al.*, 2019). Therefore, the jointly inverted compressional and shear wave velocity models, together with the background density trend, can provide a more reliable estimation of gas hydrate saturation (Riedel *et al.*, 2014), under the assumption that the hydrate interacts with the matrix (load-bearing model).

Comparing gas hydrate saturations estimated in this work with the values estimated by the normal incidence reflectivity method is not straightforward, because the methods rely on different assumptions and approximations. For instance, in Chapter 3 I made conservative estimates assuming that the GHSZ outside of the CHZ was hydrate-free, whereas the Bayesian inversion carried out in this chapter is based on a rock physics template that contains all possible combinations of elastic and petrophysical properties (as shown in Figures 4.1 and 4.8), rather than on assumptions of the background properties. The hydrate saturations estimated in Chapter 3 from selected high amplitude seismic reflections are systematically lower than the saturations predicted in this study. For example, saturations of  $\sim 20\text{-}40\%$  were estimated from the APB13-17 profile across Honeycomb Ridge, whereas the results in this study suggest saturations of  $\sim 40\text{-}60\%$  in the same region. Similarly, the predicted hydrate saturations along a highly reflective horizon at Glendhu Ridge are higher ( $\sim 40\text{-}50\%$ ) than the previous estimates ( $\sim 25\text{-}30\%$ ). I suggest that this systematic difference is due to the conservative nature of the approach employed in Chapter 3, as described above.

A wide range of approaches have been undertaken globally to estimate regional or local in-place gas hydrate saturations, using different types of geophysical data. Approaches have included the analysis of MCS data (e.g., Fohrmann and Pecher, 2012), ocean bottom cable data (Bünz and Mienert, 2004), LWD and core data integrated with seismic data (e.g., Frye *et al.*, 2012b; Haines *et al.*, 2017; Lee *et al.*, 2013; Shankar and Riedel, 2011), controlled-source electromagnetic (CSEM) data (e.g., Kannberg and Constable, 2020), and combined analyses of seismic and CSEM data (e.g., Berndt *et al.*, 2019). Gas hydrate saturations within specific hydrate provinces vary as a function of gas supply and reservoir quality (e.g., Boswell *et al.*, 2012). All attempts to estimate hydrate saturations have inherent uncertainties that depend on the data type and quality, as well as the rock physics methods used to invert for hydrate saturation. In general, the gas hydrate saturations that have been estimated in this study are in good agreement with other studies of concentrated hydrate-bearing sediments, which suggest that significant amplitude anomalies attributed to gas hydrate within the GHSZ are

probably caused by saturations above 40% (Boswell *et al.*, 2016b; Cook and Waite, 2018; Lee *et al.*, 2010; Yun *et al.*, 2005).

#### 4.5.2 Limitations of the method

The estimated gas hydrate saturations presented in this paper are based on several assumptions. The most fundamental assumption is that gas hydrate is part of the solid frame of the sediment, often referred to as a matrix-supporting or load-bearing hydrate morphology (Cook and Waite, 2018; Dai *et al.*, 2008; Dvorkin *et al.*, 2000; Pan *et al.*, 2019; Xu *et al.*, 2004). Although some methods have been presented to identify the type of hydrate morphology based on indirect measurements such as P-wave velocity and density (Liu and Liu, 2018), the lack of borehole and geological data in our study area does not allow us to assess the dominant type of hydrate occurrence. The choice of a matrix supporting model is motivated by field and laboratory studies from other authors, which suggest that the saturation of highly concentrated gas hydrate deposits in coarse-grained sediments tends to be best approximated by the “load-bearing” model (Cook and Waite, 2018; Lee *et al.*, 2010; Yun *et al.*, 2005). Because quantitative characterisation of gas hydrate reservoirs in the southern Hikurangi Margin is still at an early stage, I suggest that the use of a load-bearing model yields a good first-order estimate of the amount of gas hydrate in place.

Another important assumption in this work is that sediment density varies linearly with depth. However, density has a strong correlation with porosity (Figure 4.8f), which means that errors in density lead to significantly biased predictions of porosity, which in turn result in erroneous estimates of gas hydrate saturation. In most seismic inversion methods, density is the most poorly defined property (Biswas *et al.*, 2019; Quijada and Stewart, 2007) because it is not directly dependent on lithology; rather it is a function of the mineral composition, porosity, fluid type and degree of saturation. Often, in the absence of well log data, additional constraints on density are required to stabilize the inversion, typically by using a density-velocity relation (Korenaga *et al.*, 1997; Wang, 1999), or density-depth trend (Shelander *et al.*, 2010). Because lithologies are poorly constrained in this region, I aimed to avoid introducing biased density values into the geostatistical seismic AVA inversion step by using the same smooth density model throughout the six iterations (Figure 4.1). It therefore follows that changes in acoustic and elastic impedances in the CHZs are caused only by variations in  $V_P$  and  $V_S$ . This assumption is based on the reliable interpretation that highly reflective regions

above the BSR (i.e., the CHZs, as defined in Chapter 3) are caused by anomalous gas hydrate saturations (e.g., Boswell *et al.*, 2016b), and not by localized increases in density. Because gas hydrate is only slightly less dense than seawater, high variability of bulk density along the same sedimentary layers is unlikely. This assumption results in the small variability of the set of optimized porosity models observed in 4.8d and 4.9. Because of the strong dependence of porosity on density, unconstrained high density values would only cause a reduction in the porosity estimates and not significantly affect the gas hydrate saturation prediction (Cook and Tost, 2014).

Predicting gas hydrate saturation from geophysical data has inherently high uncertainties. Downhole measurements provide the most accurate estimates of gas hydrate saturation (Lee and Collett, 2001; Sava and Hardage, 2006), although errors in resistivity measurements have been shown to approximately double the systematic errors in the saturation calculation (Hyndman and Spence, 1992). At a reservoir scale, the uncertainty related to the estimation of gas hydrate saturation varies widely depending on the method used to calculate it. In this study, I present a qualitative description of the variability of the set of optimized models (Figures 4.8 and 4.9). From the petrophysical models, the 25%, 50% and 75% percentiles are computed and considered to be the pessimistic, best, and optimistic predictions, respectively, for the CHZs shown in Figure 6. Because the workflow combines frequency-based optimization and Bayesian-framed inversion methods, a rigorous uncertainty analysis has not been undertaken, which would be beyond of the scope of this chapter.

The variability analysis does not account for the uncertainty in the rock physics model, since the uncertainty associated with the petrophysical inversion (expressed by the posterior covariance matrix in Eq. 4.9) has not been added to the results, which just represent the most likely petrophysical value at each seismic sample.

Structural information about the reservoir volumes is a key aspect for the derivation of the total in-place gas hydrate volumes. In this work, the spatial extent of the reservoirs calculated based on depth converted seismic profiles (Chapter 3) are used, but no detailed analysis of the structural uncertainty is undertaken. Uncertainty is inherent in each step of the subsurface seismic imaging process and derives mostly from the inexact subsurface velocity models that are used to migrate and depth convert the data (Messud *et al.*, 2017; Osypov *et al.*, 2013). Although different methods are available in the literature to quantify and propagate such uncertainties in the seismic

images (Ely *et al.*, 2018; Zhu and Gibson, 2018), a detailed analysis of this source of uncertainty has not been undertaken for this chapter. The analysis presented here, that does not include structural uncertainty, suggests that the probable total volume of gas hydrates in place in the Glendhu and Honeycomb concentrated hydrate deposits lies between  $2.45 \times 10^5 \text{ m}^3$  and  $1.72 \times 10^6 \text{ m}^3$ , with the best estimate at  $9.68 \times 10^5 \text{ m}^3$ . However, if we consider the average interval velocities within the CHZs to be between 1900 m/s and 2200 m/s, the volume estimation variability is in the order of  $\sim 14\%$ , which suggests that the most likely scenario lies between  $8.38 \times 10^5$  and  $1.13 \times 10^6 \text{ m}^3$  of total gas hydrate in place.

## 4.6 Conclusions

I have estimated the spatial distribution of porosity and gas hydrate saturation along two deep sea ridges on the southern Hikurangi Margin of New Zealand. The approach used for this assessment is based on a two-step probabilistic inversion of 2D marine seismic data, supported by regional well log information. This study has provided pessimistic, most likely and optimistic scenarios for total in-place gas hydrate volume assessments. The total gas hydrate volume in place in the reservoirs at Glendhu and Honeycomb ridges is estimated to be between  $2.45 \times 10^5 \text{ m}^3$  and  $1.72 \times 10^6 \text{ m}^3$ , with the best estimate at  $9.68 \times 10^5 \text{ m}^3$ . These estimates should be considered as preliminary, as detailed prospect analysis would require a better geological understanding of the reservoirs, but they are comparable to concentrated gas hydrate deposits found in other continental margins. These first-order predictions of total gas hydrate in place, accompanied by the analysis of the variability of the estimations, provide a good basis for ongoing gas hydrate studies in the region. Future research in this large gas hydrate province would benefit from the acquisition of controlled-source electromagnetic data and, ultimately, drilling, to better characterise the reservoir. The methods I have presented in this study highlight the effectiveness of probabilistic seismic inversions in characterising concentrated gas hydrate reservoirs, even in the absence of drilling data within the target reservoirs. The approach can be applied to other gas hydrate settings globally where high quality long-offset seismic data exist.

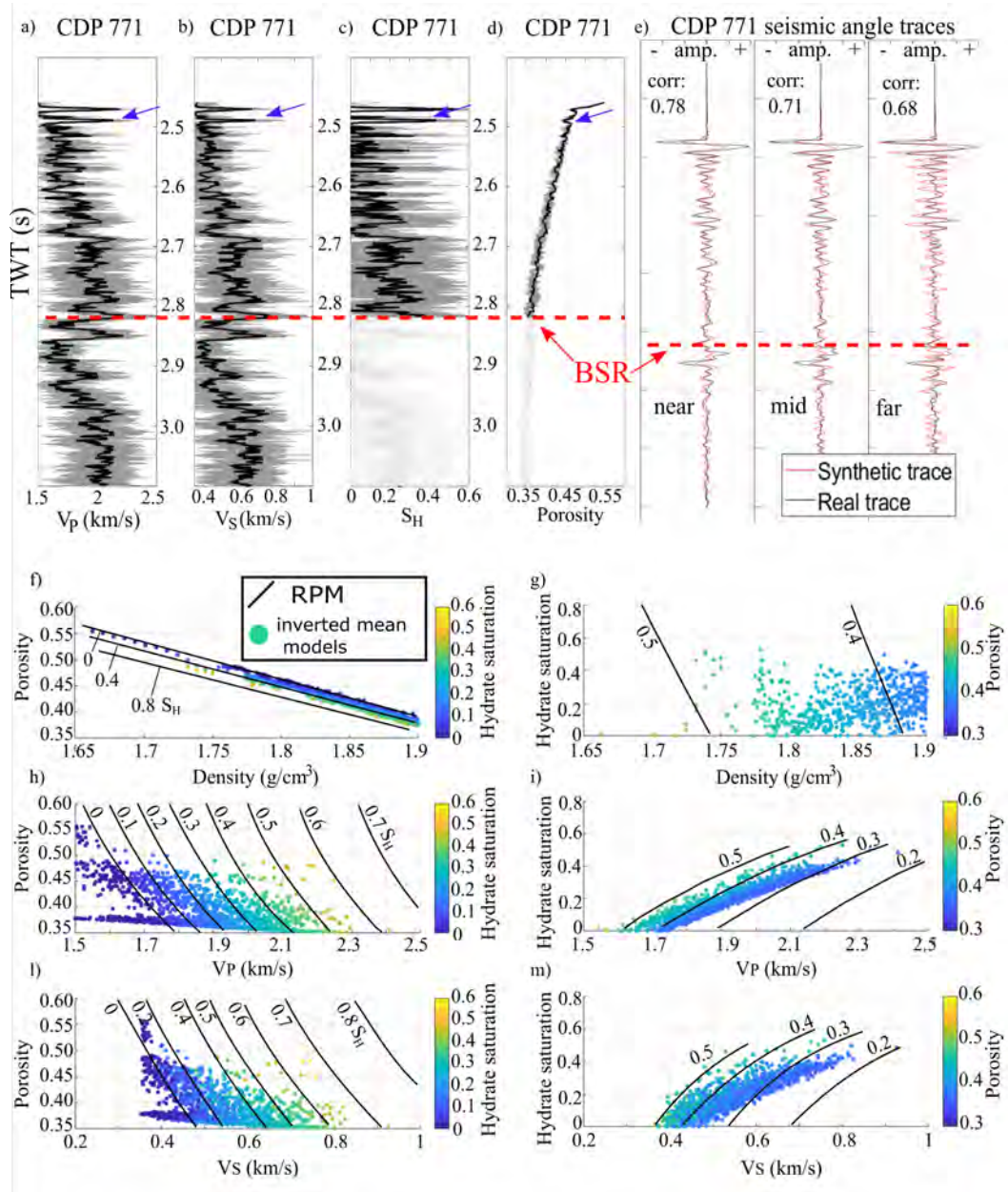


**Figure 4.8:** (a)-(d) Vertical profiles located at CDP 771 of the APB13-21 line of the elastic and petrophysical models of  $V_P$ ,  $V_S$ ,  $S_H$  and porosity; the grey lines show the 32 realisations of the last iteration of the inversion, and the bold black line is the mean; the purple arrows point to the bubble pulse effect described in the text; (e) comparison between the synthetic (red) and the real (black) seismic traces from the angle gather at CDP 771: near, mid and far angle traces are shown, together with the corresponding correlation coefficient values; (f)-(m): scatterplots showing the distribution of petrophysical and elastic properties of selected traces from the mean of the inverted models (bold black line in (a)-(d)) compared with the rock physics template, shown by the black lines. RPM: rock physics model;  $S_H$ : hydrate saturation.

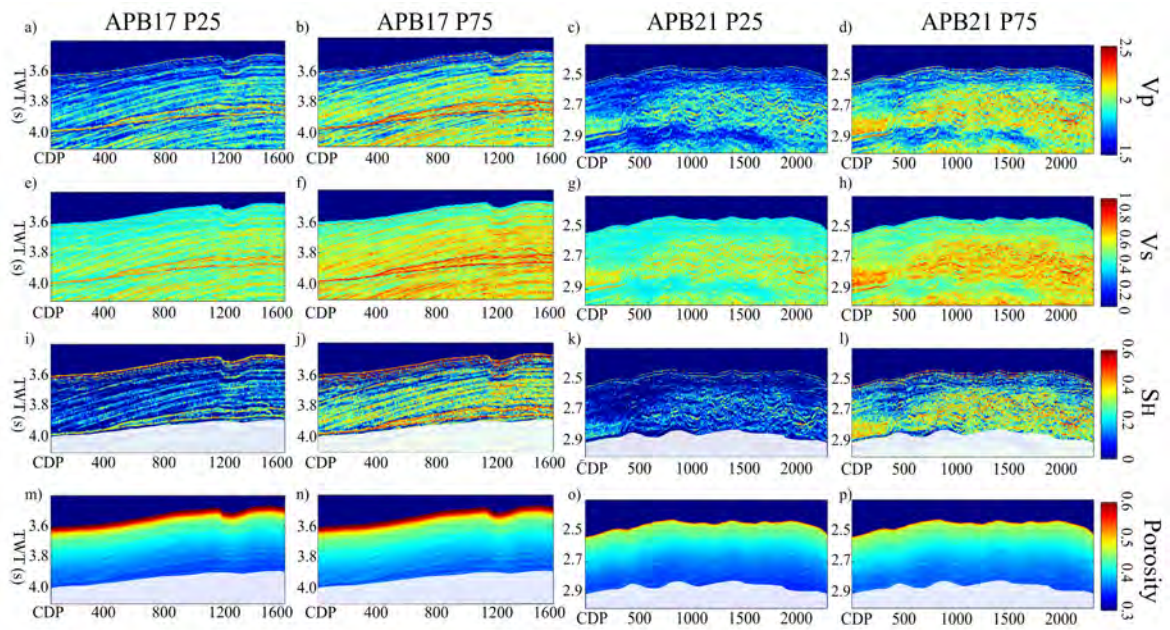


**Figure 4.9:** Percentiles (P25 and P75) sections of all predicted petro-elastic properties. The white areas in i)-p) represent the region below the GHSZ, for which the calibrated rock physics model is not representative.



# Chapter 5

## 1D full-waveform inversion studies of the gas hydrate stability zone

The theoretical principles of full-waveform inversion are outlined in Section 2.2, Chapter 2. The method consists of several steps, from the pre-processing of seismic data to the final inverted 1D fine-scale velocity model. In this chapter, I provide insight into the separate stages of the inversion process, and present the results of the application of 1D full-waveform inversion to selected locations along 2D seismic profiles that cross concentrated hydrate deposits in the southern Hikurangi Margin.

### 5.1 Motivation

Enhanced seismic reflections within or immediately below the base of the GHSZ are features typically associated with the presence of concentrated gas hydrates and free-gas in the sediments (e.g., Berndt *et al.*, 2019; Crutchley *et al.*, 2019; Pecher *et al.*, 2010; Wang *et al.*, 2018). The anomalously high seismic reflections that characterise some of the gas hydrate systems on the southern Hikurangi Margin have been associated with high gas hydrate saturation (>40%, Chapter 3 and Chapter 4). However, the underlying assumption made in these studies neglects the possible presence of free-gas within the GHSZ. In recent years, evidence supporting the coexistence of free-gas and gas hydrate around the base of the GHSZ has been reported in several field studies (e.g., Colin *et al.*, 2020; Paganoni *et al.*, 2016; Qian *et al.*, 2018; Qin *et al.*, 2020; Singhroha *et al.*, 2019). Such studies suggest that the interaction between free-gas migration, gas hydrate formation and the geological context (in terms of the structural and stratigraphical framework of the hosting sequence) is much more complex than previously

thought. The formation of hydrate does not only depend on the pressure-temperature conditions, but also on the availability of pore-water and on the supply of free gas. When these conditions are not met, free gas can be present even within the GHSZ (Qin *et al.*, 2020). On the other hand, hydrates can also be found below the BGHS (e.g., Han *et al.*, 2021; Paganoni *et al.*, 2016). This can be due to the slow response of gas hydrates to changes in the GHSZ caused by tectonic uplift, rapid sedimentation or heat advection due to fluid migration, which can remain in a transient state of on-going dissociation for thousands of years (Pecher *et al.*, 2018). Hence, investigating the detailed distribution of physical properties of the subsurface is valuable, in order to characterise gas hydrate systems in detail.

In this chapter, the fine-scale velocity structure of the GHSZ is investigated at selected target sites at Glendhu and Honeycomb ridges, where concentrated accumulations of gas hydrate and pronounced fluid flow through the GHSZ are inferred. The detailed velocity profiles estimated through 1D full-waveform inversion contribute quantitatively to the study of enhanced fluid flux and both free-gas and gas hydrate distribution.

## 5.2 Methodology

The inversion technique of Kormendi and Dietrich (1991) is applicable to MCS data sorted by CDP gathers. Synthetic seismograms are calculated using the generalised reflection transmission matrix method (Kennett and Kerry, 1979), and the misfits are computed in the frequency-slowness ( $\omega - p$ ) domain. The subsurface property to be inverted is compressional velocity  $V_P$ . Similar to most deterministic inversion techniques, a low-frequency initial model of  $V_P$  in the subsurface is required to stabilise the inversion process and ensure its convergence towards a global minimum of the misfit function (Tarantola, 2005). The process can be divided into four different stages: pre-processing of the seismic data, estimation of the seismic wavelet, building a good starting  $V_P$  model and running the inversion (e.g., Crutchley *et al.*, 2011; Gorman *et al.*, 2002; Minshull *et al.*, 1994).

### 5.2.1 Seismic processing

Waveform inversion methods rely on the preservation of the relative seismic amplitudes (e.g., Causse *et al.*, 1999; Cichostępski *et al.*, 2019). The processing applied to

the seismic data ensures the relative amplitude preservation. Seismic data sorted by CDP domain (e.g., Figure 5.1) represent the wave-field sampled at the selected location (after pre-stack time migration), and are used as the input to the 1D inversion routine. The long-offset APB13 data comprise offsets ranging from 100 to 8000 m. Geometry and navigation were applied to the data before sorting from shot to CDP domain, with a CDP bin size of 6.25 m along the direction of seismic recording. The average fold for the central portion of the seismic profiles is 110 traces per CDP gather. The raw data were broad band-pass filtered with corner frequencies of 2, 4, 40 and 60 Hz, then they were corrected for spherical divergence using the pre-stack time migration velocities (Chapter 3), and finally migrated using an iterative Kirchhoff pre-stack time migration algorithm. This processing sequence was applied to improve the signal-to-noise ratio while preserving the true relative amplitude of the traces. The choice of using pre-stack time migrated data as opposed to unmigrated CDP-sorted data as an input is motivated by the presence of steeply dipping reflections in the subsurface, that invalidate the assumption of one dimensionality in the non-migrated traces. A  $\tau - p$  transform followed by a Fourier transform was then applied to selected common image point gathers (CIG), to obtain the input data for the inversion in the  $\omega - p$  domain.

## 5.2.2 Wavelet estimation

To extract a wavelet that is representative of the seismic data, I selected a region of relatively flat bathymetry and windowed the pre-stacked traces of the  $\tau - p$  transformed CDP gather of interest to extract the seafloor reflection. I have also carried out several inversion tests using the wavelet estimated from the CDP gather traces in the  $t - x$  domain, and averaging the primary seafloor reflection with the negative of the first seafloor multiple, as suggested by Warner (1990). However, the best convergence of the inversion procedure is achieved by using the wavelet estimated from the image gather in the  $\tau - p$  domain (Figure 5.2).

## 5.2.3 Definition of the background Earth model

The low-frequency (or background) Earth models of the selected locations consist of a succession of 5 m thick layers extending from sea level to a defined depth in the subsurface. It is important to point out that the main factor contributing to the vertical resolution in the inversion procedure is not the choice of the interval between the layers of the model, but rather the resolution of the seismic data, which is estimated to be

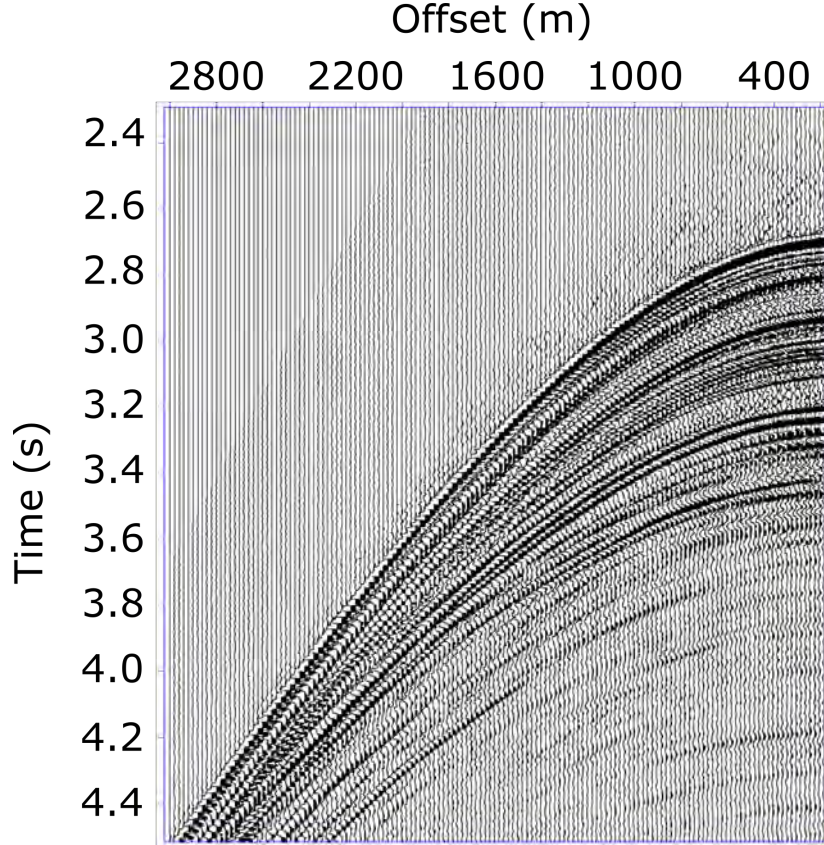


**Figure 5.1:** Examples of pre-stack time migrated gather (CDP 5031, line APB13-21). NMO corrections were removed prior to  $\tau$ - $p$  transformation.

between 10 and 14 m, considering a dominant frequency of about 35 Hz and seismic velocities of 1500 and 2000 m/s, respectively. The models consist of five parameters: P-wave velocity ( $V_P$ ), S-wave velocity ( $V_S$ ), density ( $\rho$ ), P-wave attenuation ( $Q_P$ ) and S-wave attenuation ( $Q_S$ ). The initial  $V_P$  profiles were defined through a combination of 1D ray tracing and semblance-based velocity analysis. For each image gather, at least three conspicuous reflections were selected (the top one being the seafloor, the deepest one being the BSR and a third one being a clear reflection within the GHSZ). From these events the observed travel time arrivals were picked over offsets ranging between 100 and 6500 m. The misfit between the observed and the modelled travel times was minimised to obtain an initial velocity model defined from ray-tracing travel time damped-least-squares inversion (Section 2.2; Zelt and Smith, 1992). These models were manually refined according to the interval velocities calculated from pre-stack time migration stacking velocity models ( $V_{RMS}$ ). The  $V_P$  decreases, corresponding to the BGHS observed in the stacking velocity models, were ignored, and the velocity values below the BSR were kept constant. This step ensured the smoothness of the

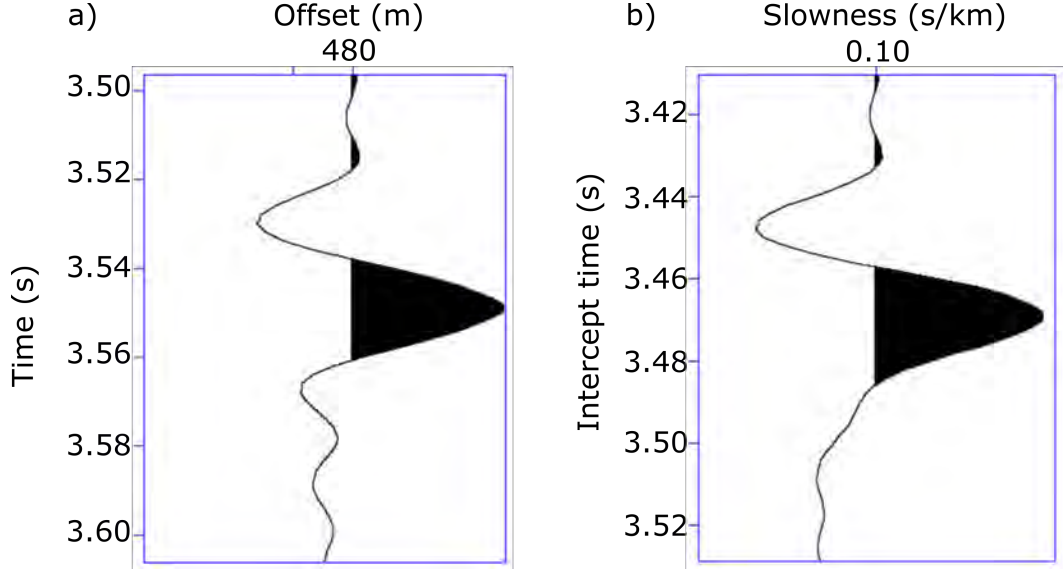


**Figure 5.2:** Example of seafloor reflection for wavelet estimation: a) seafloor reflection of the trace corresponding to an offset of 480 m in the pre-stack time migrated gather of CDP 5031, line APB13-21; b) the same seafloor reflection in the trace corresponding to a  $p$  value of 0.1 s/km in the  $\tau$ - $p$  transform of the same CDP gather.

starting model (Kormendi and Dietrich, 1991). The  $V_S$  profile was created by assuming an empirical relationship with  $V_P$  for marine sediments (Castagna *et al.*, 1985). The  $\rho$  profile was defined using Hamilton (1978) empirical relationship to  $V_P$  below the seafloor, and by assuming seawater density to be 1.035 g/cm<sup>3</sup>.  $Q_P$  was set to 10,000 in the water column, to reproduce negligible attenuation, to 300 for the GHSZ and to 200 below the BGHS (e.g., Dvorkin and Uden, 2004).  $Q_S$  was set to 100 everywhere below the seafloor.

#### 5.2.4 Inversion procedure

The 1D inversion is performed in the frequency-slowness ( $\omega$ - $p$ ) domain, and the results were inverse-Fourier transformed in the intercept time-slowness domain ( $\tau$ - $p$ ) to assess the quality of the inverted seismograms. The full-waveform inversion method employed is well documented in Kormendi and Dietrich (1991), Minshull *et al.* (1994) and Korenaga *et al.* (1997). The partial derivatives with respect to the model parameters are computed from the analytical solution of the Frechet derivatives presented by Dietrich and Kormendi (1990) to construct the conjugate gradients. Although the Earth model consists of five parameters ( $V_P$ ,  $V_S$ ,  $\rho$ ,  $Q_P$  and  $Q_S$ ), only  $V_P$  is updated by the conjugate gradient search, while the remaining elastic parameters are kept fixed

during the inversion process. While a multi-parameter inversion is theoretically possible (Kormendi and Dietrich, 1991), the lack of a reliable background model for density and  $V_S$  could cause the inversion to get stuck in a local minimum.

The inversion procedure was applied to 20 traces corresponding to values of slowness between 0.08 and 0.25 s/km. Six successive runs were performed, characterised by increasing time intervals for the data and by increasing depth intervals for the models. The goal of the first run was to optimize the fit between the real and synthetic seafloor reflections: this often translates into extremely large and unrealistic velocity changes in the first few model layers below the seafloor, which is an artefact caused by small differences between the source wavelet and the seafloor reflection. However, because the target of the study are the high amplitude reflections above the BSR, the presence of such artefacts in the shallow subsurface does not affect the interpretation of the results. In fact, the seafloor reflection is the biggest contributor to the misfit function, because of the higher amplitudes contained in the  $\tau$ - $p$  traces with respect to deeper seismic events. Therefore, a good fit of this reflection ensures a quicker convergence of the inversion in the following five runs. In runs 2-6, the first 10 model layers below the seafloor were held constant, and the depth and time interval were progressively increased to include the entire model and data, to increase the likelihood of convergence to the global minimum of the misfit function. Each run consisted of a maximum of 8 iterations. Because the data contain relatively low frequencies (2-60 Hz), the frequency range was kept constant throughout all 6 runs.

### 5.3 Seismic observations and inversion results

Seven CDP locations were chosen on two key seismic profiles that cross Glendhu and Honeycomb ridges. The 1D full-waveform inversion studies target specific reflections observed within the GHSZ, as well as the character of the BSR. The results are presented and discussed in the following paragraphs. The results were analysed by computing the correlation coefficient between the real and the synthetic traces in the  $\tau - p$  domain. The correlation was calculated excluding the seafloor reflection, which generally accounts for around 70% of the seismic energy of the whole gather. The fit of the synthetic data was evaluated by plotting the synthetic seismograms over the recorded data, and the resulting inverted  $V_P$  model was compared with the starting model. The fine-scale  $V_P$  inverted profiles of the targeted CDP are overlain on the

near-trace migrated data in Figures 5.3 and 5.4. The velocity profiles are plotted as the differences between the inverted models (after 5 inversion runs) and the starting models, or  $\Delta V_P$ .

### 5.3.1 APB13-21 - Glendhu Ridge

#### CDP 4272

This site lies on the SW flank of the Glendhu Ridge four-way closure. In this region, the BSR is a distinct negative polarity reflection. During the processing of the seismic data described in Chapter 3, I identified consistent high-frequency seismic events (visible between 3.3 and 3.5 s in the low  $p$  traces, Figure 5.5a) that could not be flattened by NMO correction nor by the pre-stack Kirchhoff time migration using stacking velocities. The fact that these events can not be flattened through seismic processing suggests that they may not represent primary reflections. These events are also not well reproduced in the synthetic seismograms generated during the inversion routine (Figure 5.5a), despite the use of an appropriate starting  $V_P$  model. Consequently, the inverted velocity profile shows a region of almost zero  $\Delta V_P$  between 3.3 and 3.5 s. This suggests that these events might represent strong out-of-plane reflections that cannot be imaged using 1D inversion of 2D seismic data. The BSR is characterised by a discrete negative polarity synthetic reflection (Figure 5.5a), which corresponds to a 150 m/s decrease from the starting velocity model (Figure 5.3c).

#### CDP 4675

The targeted reflection of this CDP is the BSR - a distinct negative polarity reflection (Figure 5.3b). The inversion of CDP 4675 reveals a 100 m/s  $V_P$  decrease associated with the BSR reflection at 3.5 s (Figure 5.3d). Smaller  $V_P$  perturbations within the GHSZ are also on the order of +/- 100 m/s, and correspond to the alternation of peaks and troughs of moderate amplitude in the seismic data.

#### CDP 5052

CDP 5052 intercepts a region of anomalously high seismic amplitudes at  $\sim 3.2$  s. The peaks and troughs in the seismic data correspond to increases and decreases of  $V_P$  in the inverted profile. It is noteworthy that the high and low velocity bulges that appear between the seafloor and 3.05 s are probably artefacts caused by the bubble pulse effect, visible in the near-trace migrated seismic section (Figure 5.3b) and in the

$\tau$ - $p$  gather (Figure 5.5b). Although no distinct BSR is visible in the data, as opposed to CDP 4765 and CDP 4272, a clear velocity reduction of about 100 m/s is resolved by the inversion at the BGHS.

### **CDPs 6038 and 6145**

These locations correspond to regions of localised enhanced reflectivity. The highest seismic amplitudes are observed at the top of two column-shaped vertical structures that extend upwards from the BGHS. These strong reflections were interpreted as sediments bearing gas hydrate in high saturation (Chapters 3 and 4). The alternation of positive and negative polarity reflections at CDP 6038 is mirrored in the inverted  $V_P$  profile by  $\Delta V_P$  values between +150 m/s and -100 m/s. The reflectivity analysis shown in Figure 3.7 indicates that the reflection coefficient of the seismic peak at 3.1 s of CDP 6145 is almost as high as that of the seafloor. This reflection correspond to the most conspicuous  $V_P$  increase of more than 400 m/s in the inverted model. A thick area of  $\Delta V_P$  of -250 and -150 m/s is observed between 3.35 and 3.65 s at CDP 6145.

### **5.3.2 APB13-58 - Honeycomb Ridge**

The target of these inversions is the Honeycomb Ridge CHZ, which is delimited by a positive polarity reflection at the top and by the BSR at the bottom (Figure 5.4a and 5.4b). The seismic character of the CHZ's top boundary is discontinuous and appears to follow the stratigraphy of the Honeycomb anticline. The BSR is characterised by a discontinuous negative polarity reflection that cross-cuts through the strata.

### **CDPs 5827 and 5691**

I selected two CDPs that intercept the Honeycomb CHZ. At CDP 5827, the top of the CHZ is resolved by an increase of 200 m/s in the inverted  $V_P$  model; the BSR is a distinct negative reflection that correspond to a marked  $V_P$  decrease of more than 250 m/s (Figure 5.4c). At CDP 5691, a  $V_P$  increase of  $\sim 180$  m/s defines the top boundary of the interpreted CHZ, while the BGHS is characterised by a decrease in  $V_P$  of  $\sim 100$  m/s (Figure 5.4d). The difference in velocity reduction in the inverted models at the BGHS between the two sites reflects the contrast in seismic amplitudes of the BSR: CDP 5691 corresponds to a gap where the BSR's amplitude is weaker than in the adjacent traces, whereas at CDP 5827 the seismic amplitude of the BSR is higher.



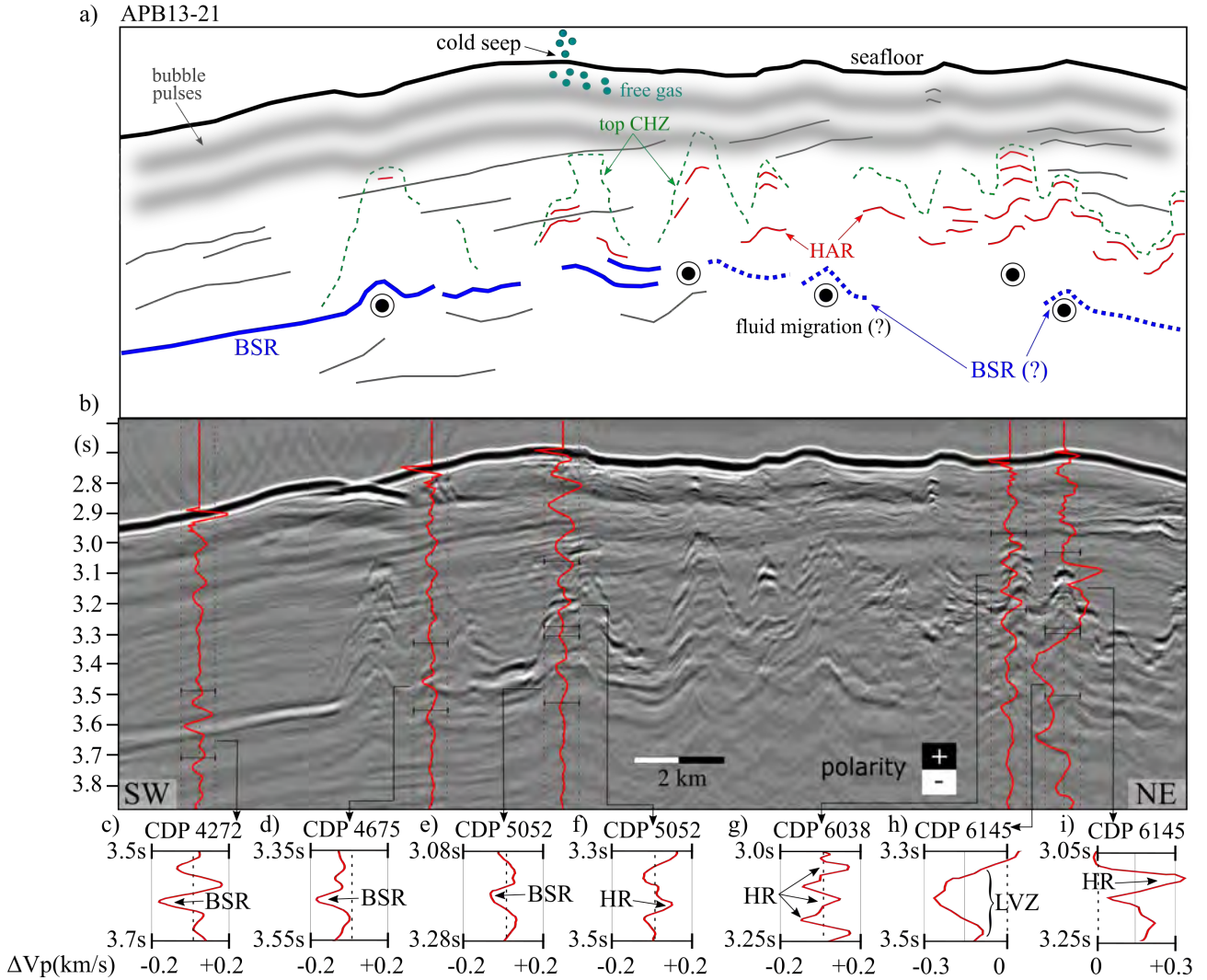


**Figure 5.3:** a) Interpretation of key features observed in the seismic section. The black circles (arrows pointing out of the plane of the page) represent the interpreted direction of fluid migration. The location of cold seeps is also shown (see Chapter 6). HAR: high amplitude reflection; CHZ: concentrated hydrate zone. b) Near-trace (up to 700 m offset), pre-stack time migrated data of line APB13-21, spanning longitudinally across Glendhu Ridge with fine-scale  $V_P$  inversion results overlain in red. c)-i) Enlarged displays of the inverted  $V_P$  profiles showing different portions of the five selected CDP locations for this profile. The dashed lines represent zero deviation from the starting model (i.e.  $\Delta V_P = 0$ ). BSR: bottom-simulating reflection; HR: high reflectivity; LVZ: low velocity zone.

## 5.4 Discussion and conclusions

The 1D full-waveform inversion results presented in this chapter allow retrieval of the fine-scale velocity structure of the Glendhu and Honeycomb CHZs. The inverted

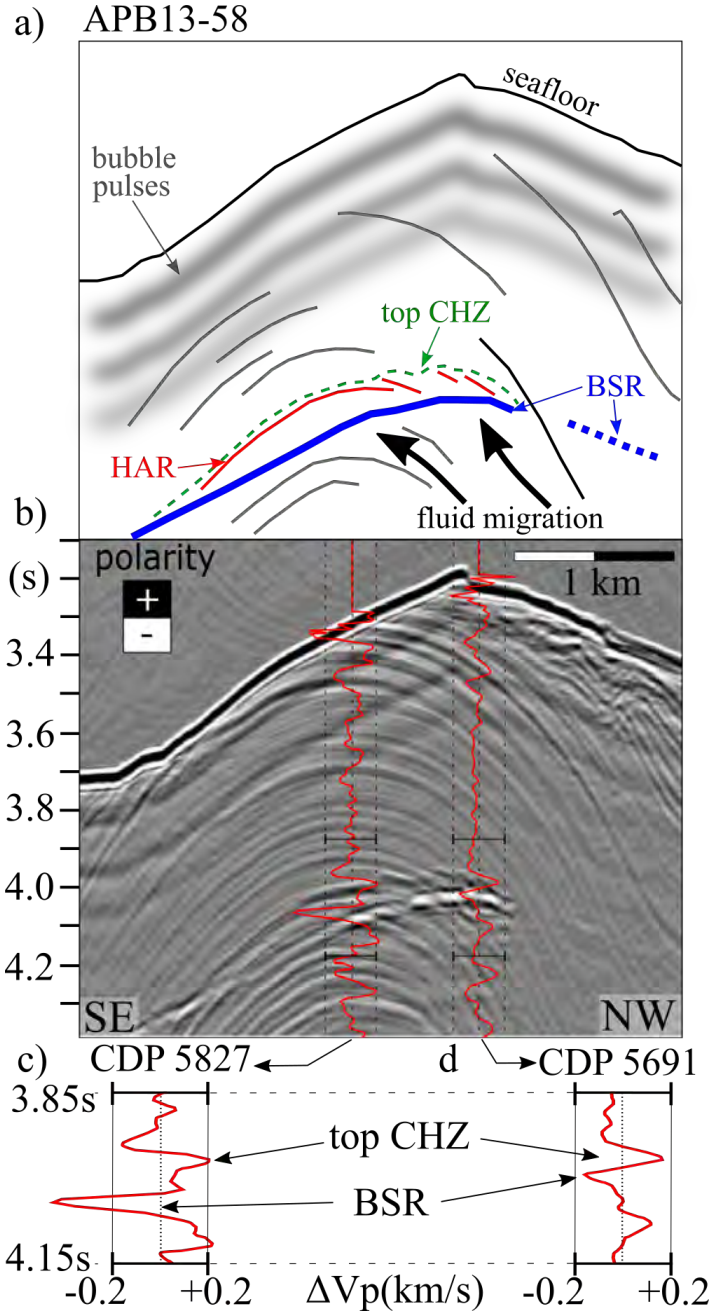


**Figure 5.4:** a) Interpretation of key features observed in the seismic section APB13-58. The black arrows represent the interpreted direction of fluid migration. HAR: high amplitude reflection; CHZ: concentrated hydrate zone. b) Near-trace (up to 700 m offset), pre-stack time migrated data of line APB13-58 crossing Honeycomb Ridge with fine-scale  $V_P$  inversion results overlain in red. c)-d) Enlarged displays of the inverted  $V_P$  profiles showing the CHZ at the two selected CDPs. CHZ: concentrated hydrate zone; BSR: bottom-simulating reflection.

velocity profiles provide a means to characterise with more detail specific structures observed in the seismic data within the GHSZ.

At Glendhu Ridge, the BGHS does not mimic the seafloor, rather there are several areas where it shoals towards the seafloor (Figure 5.3a and 5.3b). In terms of seismic amplitudes, the BSR is not always imaged as a distinct negative polarity reflection (such as at CDP 4272), but it is sometimes characterised by a low-amplitude trough (see CDP 4765 and CDP 5052), and in other areas it is not imaged at all (CDP 6038 and CDP 6145; Figure 5.3b). Decreases of  $\Delta V_P$  in the inverted velocity profiles are observed at the BGHS even when no distinct BSR is present in the seismic data (i.e. Figure 5.3e, 5.3h). Moreover, the chimney-like structure corresponding to the thick low-velocity zone between 3.3 and 3.6 s at CDP 6145 (Figure 5.3b) suggests the presence of free gas injection within the GHSZ, which might be facilitated by dipping porous strata, as discussed in Chapter 3.

The targeted high-amplitude reflections within the GHSZ at Glendhu Ridge correspond to the alternation of high and low  $V_P$  in the inverted velocity profiles (e.g., Figure 5.3f, 5.3g, 5.3i and 5.4c). These features have been interpreted to be caused by porous sediments bearing gas hydrate in high concentration interbedded with fine-grained, less porous strata (Chapter 3). At Honeycomb Ridge, the positive polarity reflection interpreted as the top of the CHZ is characterised by a perturbation of +200 m/s (Figure 5.4b). The strong impedance contrast marks the transition from sediments containing gas hydrate in low concentration above to the CHZ below. Similar to other seismic methods presented in the previous chapters, the results of the 1D full-waveform inversion are dependent on the vertical resolution of the seismic data, which ranges from 10 to 15 m for the APB13 dataset (Table 3.2). This resolution could be at least an order of magnitude larger than the thickness of interbedded sandy and silty layers of typical lower wedge sedimentary units (e.g., Konno *et al.*, 2017). The chimney-like features and the BSR shoaling observed in the seismic data suggest that warm, probably gas-charged fluids are present in the GHSZ. The coexistence of free gas and gas hydrate has been inferred and documented in similar geological settings (e.g., Crutchley *et al.*, 2019; Liu and Flemings, 2006; Pecher *et al.*, 2010, 2018; Qin *et al.*, 2020, Crutchley *et al.*, 2021). Therefore, it cannot be ruled out that the presence of patchy free gas within gas hydrate bearing units thinner than the vertical seismic resolution contributes to the impedance contrasts that manifest themselves as anomalously high

seismic amplitudes. The implementation of the methods presented in this chapter for inversion of other elastic parameters such as  $V_S$  would be required for a further and more detailed characterisation of the GHSZ, especially for distinguishing hydrate- and free gas-bearing units.

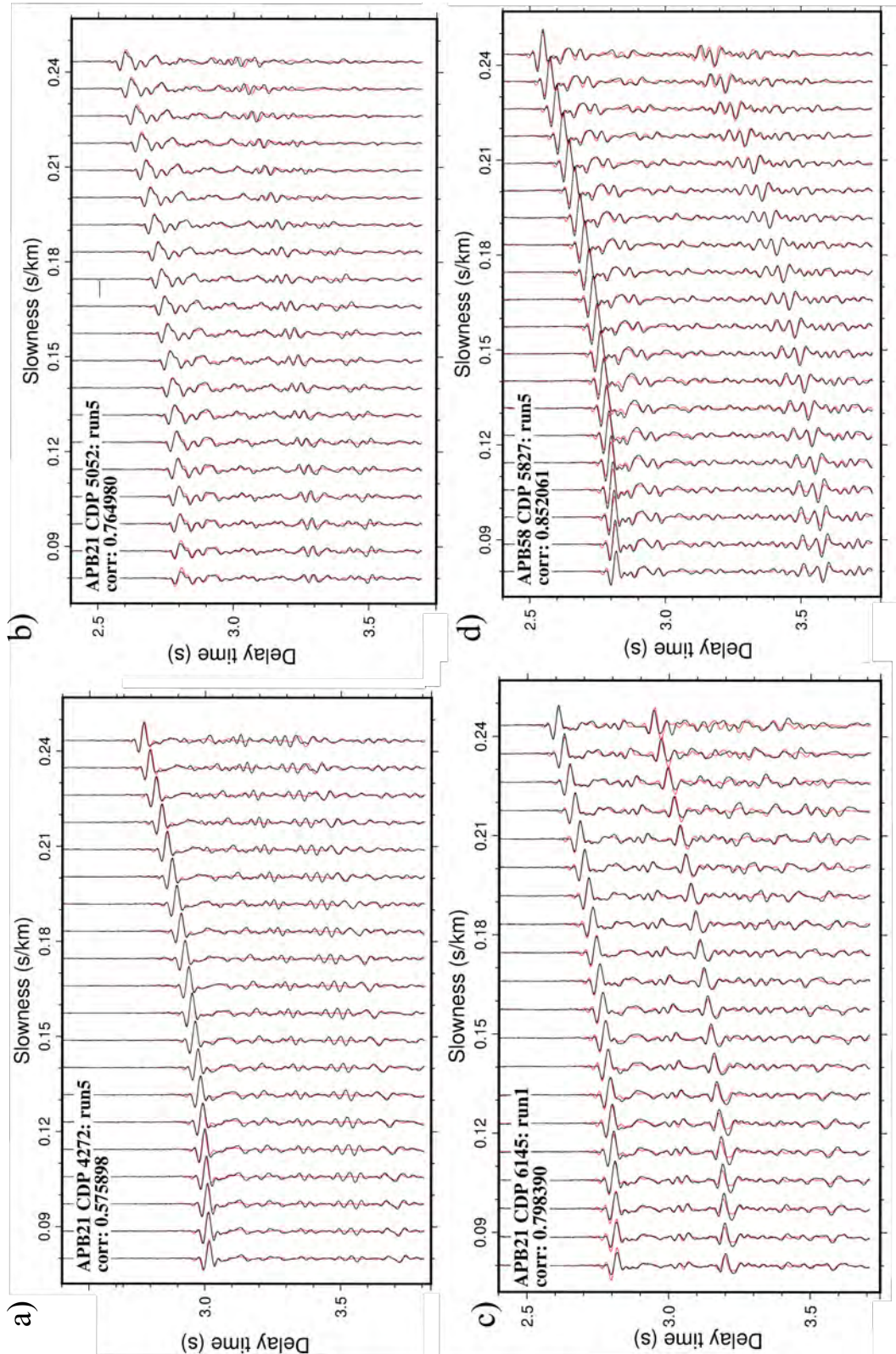


**Figure 5.5:** Examples of wiggle plots of inverted waveforms displayed in the  $\tau$ - $p$  domain (red lines), overlying the real  $\tau$ - $p$  seismograms (black lines). CDPs 4272, 5052 and 6135 of the APB13-21 data are shown in a), b), c), respectively, while CDP 5827 of line APB13-58 is displayed in d). corr: correlation coefficient.

# Chapter 6

## Quantitative analysis of gas seeps and methane fluxes

### 6.1 Introduction

Methane forms in marine sediments that are rich in organic matter through either microbial methanogenesis or thermogenic processes (Schoell, 1988). Methane formation occurs at different depths in the subsurface but, because of the buoyancy of the gas, these fluids migrate upwards across the sediment layers through migration pathways that include permeable carrier sedimentary units, faults or densely fractured regions (Cook and Malinverno, 2013; Crutchley *et al.*, 2015; Hillman *et al.*, 2017; Hoffmann *et al.*, 2019; Nole *et al.*, 2016). When these pathways connect to the surface, methane gas bubbles escape the seafloor as gas seeps, which can range from sporadic and localized emanations of bubbles to widespread vigorous gas flares, and that occur in different geological contexts, from the coastal environment to deep ocean regions (Duarte *et al.*, 2007; Judd, 2004; Watson *et al.*, 2020). In shallow waters, the gas bubbles can reach the sea surface and release greenhouse gases into the atmosphere (Schmale *et al.*, 2005), having direct implications for climate. In deeper seas, however, most of all of the gas that is released at the seabed dissolves into the ocean without reaching the sea surface, causing localized methane-induced seawater acidification over long time scales (Biastrach *et al.*, 2011; Garcia-Tigreros *et al.*, 2021).

Seismic and acoustic methods are useful tools to identify, map and characterize free gas accumulations in the subsurface (e.g., Kim *et al.*, 2020), evidence for past and present seepage at the seafloor (e.g., Stott *et al.*, 2019) and acoustic imaging of gas flares

in the water column (e.g., Böttner *et al.*, 2020; Colbo *et al.*, 2014). In the subsurface, the presence of gas in the pore-space significantly affects the elastic properties of the bulk sediment, primarily by reducing the bulk seismic velocities and generating a contrast in acoustic impedance. The detection, mapping and characterisation of subsurface gas reservoirs are parts of the traditional hydrocarbon exploration workflow (Yilmaz, 2001). Low seismic velocities, often associated with fluid migration through geological structures such as chimneys, conduits and faults, can be an indicator of free gas in the sediments.

In the ocean, columns of rising gas bubbles (also called flares for the typical shape they assume in hydroacoustic imaging) are less dense than seawater and thus represent strong acoustic reflectors, as they generate sharp localized changes in the acoustic impedance of the water column. Calculating methane fluxes at a seep site is challenging, as it requires ground-truth information about bubble size distribution, chemical composition, density, coating and ascending speed (Leblond *et al.*, 2014). Typically, gas bubbles released at the seafloor tend to have a radius in the range of 1 to 15 mm (Veloso *et al.*, 2015), resonating at frequencies from a few hundred Hz to  $\sim 12$  kHz, depending on the depth and size (Weidner *et al.*, 2019). Single-frequency sonar systems have been successfully used for the identification of the location of seep sites and for water column imaging for decades (e.g., Hornafius *et al.*, 1999; Merewether *et al.*, 1985; Nikolovska *et al.*, 2008). However, these instruments cannot be used to determine the size distribution of the bubble population.

A common approach for the estimation of gas fluxes is coupling acoustic imaging of the gas flares with optical point-source measurements like deep towed imaging systems (DTIS Higgs *et al.*, 2019), remotely operated vehicles (ROV Naudts *et al.*, 2010), bubble observation modules (Bayrakci *et al.*, 2014) or bubble traps (Römer *et al.*, 2012). Although these point-source measurements provide the most accurate observation of bubble parameters, they require long deployment durations and a restricted field of view of less than  $\sim 15$  m. Moreover, they are also limited to measurements at the seafloor, and cannot provide a way to track the changes in bubble size distribution as they rise through the water column. Broadband hydroacoustic methods provide a more efficient tool to directly estimate bubble parameters by insonifying large areas of the oceans using a range of frequencies (e.g., Colbo *et al.*, 2014; Dupré *et al.*, 2015; Veloso *et al.*, 2015; von Deimling *et al.*, 2011).



The highest concentration of cold seep sites worldwide has been observed along convergent margins, where fluid migration through the sedimentary sequence is enhanced by the tectonic deformation and successive dewatering of marine sediments (Saffer and Tobin, 2011; Suess, 2020). In these regions, gas flares observed at the seabed and other shallow gas migration features are often connected to subsurface methane reservoirs through gas conduits (e.g., Crutchley *et al.*, 2021; Krabbenhoeft *et al.*, 2013; Meldahl *et al.*, 2001; Petersen *et al.*, 2010). The southern Hikurangi Margin, off the North Island of New Zealand, reveals evidence of widespread methane seepage (Barnes *et al.*, 2010; Greinert *et al.*, 2010; Watson *et al.*, 2020). The accretionary wedge here consists of a series of thrust-related ridges striking NE-SW, made of compressed and deformed sediments, probably turbidites and ancient trench-fill deposits (Kroeger *et al.*, 2015; Lewis *et al.*, 1998). Seismic data show evidence of concentrated gas hydrate accumulations in the core regions of many thrust ridges in this region, indicating the preferential migration of free gas along permeable strata towards the core of anticlinal structures (Crutchley *et al.*, 2019; Schwalenberg *et al.*, 2010; Turco *et al.*, 2020; Wang *et al.*, 2017a). Estimation of gas fluxes at cold seep locations on the Hikurangi Margin has so far relied on in situ optical measurements of gas bubble using DTIS (Higgs *et al.*, 2019) and ROVs (Naudts *et al.*, 2010).

In this chapter, I use a combination of seismic and acoustic data to characterise five known sites of active cold venting on the southern Hikurangi Margin. The interpretation of seismic amplitudes provides a means to identify regions of free gas accumulations within the sediments. Qualitative analysis of multibeam data collected over three years allows the spatial extent of the region of active venting at the seafloor to be mapped, while also imaging the acoustic flares in the water column and analysing their variability over time. Split-beam echo sounder data are used to extract important parameters for the quantification of gas bubbles in the water from the backscattered acoustic energy; this step is essential for the estimation of active gas fluxes at the cold seep locations.

## **6.2 Data and methods**

### **6.2.1 Acoustic data processing**

The identification and mapping of cold seeps in deep waters was achieved through the analysis of acoustic data. Bathymetric and acoustic data were acquired during three



scientific voyages onboard the R/V Tangaroa: TAN1808 (September-October 2018), TAN1904 (July 2019) and TAN2012 (November 2020).

Swath bathymetry and acoustic backscatter of mid-water reflectors were collected with a hull-mounted Kongsberg EM302 multibeam echo-sounder during the three voyages. The EM302 echo sounder operates at a frequency of 30 kHz and with a swath of 120°. The use of the multibeam data was twofold: 1) to accurately locate gas seeps on the seafloor and 2) to calculate the area of seepage at the seafloor. For the former objective, the data were processed using the NIWA custom-built software *Espresso* with the following steps: seafloor detection filtering, removal of the outermost noisy beams ( $>45^\circ$ ), removal of bad pings, filtering side lobe artefacts and muting the first 5 m of data above the automatically picked seafloor, to avoid misinterpreting the smearing of the beams at the seafloor as gas bubbles (Schimel *et al.*, 2020). The correct pinpoint (as well as could be determined) of seepage at the seafloor was facilitated by the fan visualization of MBES data (Figure 6.3c). In order to calculate the total area of gas seepage in proximity of the seafloor, the processed data were vertically summed over a window between 5 m and 20 m above the seabed - a process known as echo integration (MacLennan *et al.*, 2002). The output of this process is a georeferenced image of volume backscatter intensity with a horizontal spatial resolution of 15 m x 15 m, that allowed mapping the spatial extent of the acoustic anomaly in the water column (Figure 6.1).

A suite of 5 Simrad EK60 echo sounders were used to obtain calibrated acoustic measurement of the water column during TAN1904 and TAN2012 voyages. The data were acquired over the five targeted areas based on existing multibeam coverage. These split-beam systems were calibrated using a standard 38.1 mm tungsten sphere hung under the vessel, following standard procedures (Demer *et al.*, 2015). Given the relatively great water depth of most targeted flares ( $>1000$  mbsl), only the 18 and the 38 kHz echo sounders had sufficient range to penetrate through the water column and image the gas bubbles. The two-way beam angle of the EK60 echo sounder is  $7^\circ$  for the 18 kHz system and  $11^\circ$  for the 38 kHz one. I extracted and processed the data recorded for the targeted gas flares using the open-source software package ESP3 (Ladroit *et al.*, 2020). The data were processed to only extract the acoustic signal associated with gas venting. The processing included seafloor echo detection and removal, bad ping removal and de-noising (De Robertis and Higginbottom, 2007). Once acoustic flares

were identified and extracted, I carried out frequency analysis on the pre-processed split-beam data, and compared the frequency response to theoretical bubble backscatter models to estimate the bubble size distribution (BSD) of the entire flare (Figure 6.1). Finally, I echo integrated the processed 18 kHz data using cells 25 m high and 10 m wide, in order to retrieve a mean  $S_v$  response for each cell.

### 6.2.2 Estimation of gas fluxes

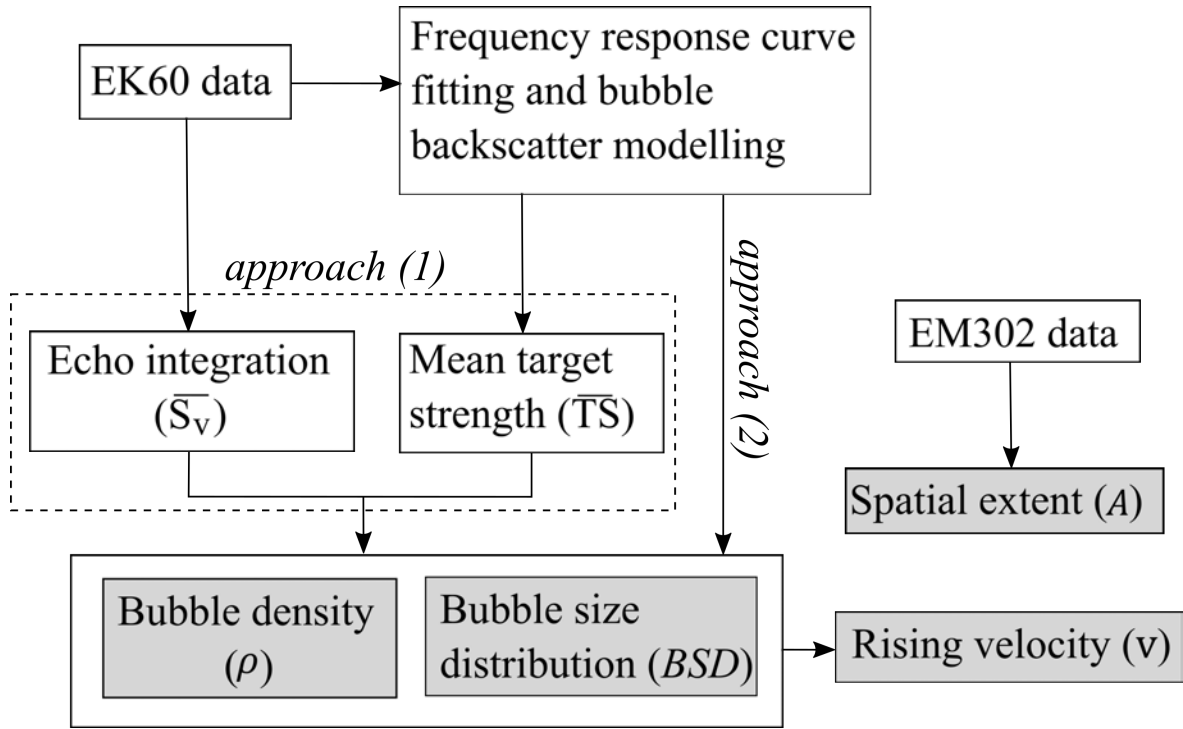


**Figure 6.1:** Illustration of the workflow to estimate gas fluxes from MBES (EM302) and single-beam (EK60) backscatter data

The workflow to estimate gas fluxes at the seep locations is illustrated in Figure 6.1. To estimate the bubble size distribution and density, I followed two approaches, one based on the normalised frequency response of the 18 and 38 kHz channels of the EK60 data, and one based on the non-normalised frequency response.

In the first approach, gas flares were isolated using the 18 kHz data, and they were echo integrated using a variable cell size ranging from 25 - 50 m in height and 5 - 10 m in width. The echo integration process yields a mean  $S_v$  for each cell of the acoustic flare.

The frequency analysis of the gas plume from both the 18 and 38 kHz channels, normalised relatively to the 38 kHz  $S_v$  values, provides frequency-dependant  $S_v$  values that the theoretical backscatter model curves aim to match. The curve-matching procedure was achieved through manual tuning of the following parameters: mean bubble radius, bubble size distribution and water depth. When the match is considered satisfactory, i.e., when the residuals between the observed  $S_v$  and the theoretical  $S_v$  are below a chosen threshold for each water depth, the resulting BSD is considered representative of the entire flare, and the mean target strength ( $\bar{TS}$ ) is computed following:

$$\bar{TS} = \frac{\int_0^{a_{max}} BSD(a)TS(a)da}{\int_0^{a_{max}} BSD(a)da}, \quad (6.1)$$

where  $TS$  is the same as in Eq. 2.28,  $BSD$  is the bubble size distribution and  $a$  the bubble radius.  $BSD$  is parametrised by a mean bubble radius and a standard deviation for the log-norm distribution, and by a mean bubble radius and a shape of the PDF for the Weibull distribution. To retrieve the density of bubbles per volume unit (in  $m^3$ ), the mean volume backscattering strength  $\bar{S}_v$  value of each cell of the echo integrated flare is compared to the representative  $\bar{TS}$  value of the whole flare following:

$$\rho = \frac{\bar{S}_v}{\bar{\sigma}_{bs}}. \quad (6.2)$$

Equation 6.2 relates the mean backscattering cross-section representative of the entire flare  $\bar{\sigma}_{bs}$  ( $m^{-1}$ , or expressed in decibels by  $\bar{TS}$ ) to the mean volume backscattering coefficient of a given cell of the echogram  $\bar{s}_v$  ( $m^2$ , or  $\bar{S}_v$  in decibels).

Then,  $\rho$  is averaged across cells located at the same water depth, hence a mean density of bubbles is estimated for each horizontal slice of the gas plume ( $\bar{\rho}$ ).

The second approach to retrieve  $BSD$  and  $\bar{\rho}$  for each flare consists of a linear inversion technique that aims to minimise the difference between the modelled and the observed non-normalised volume scattering strengths at each depth of the acoustic flare. The forward modelled data are computed following the theoretical backscatter model by Ainslie and Leighton (2009) described in Section 2.4.2, and the optimisation is achieved through a conjugate gradient technique. The model parameters that are inverted are bubble size, bubble size distribution and density of bubbles per volume unit. These parameters are initialised using the results from the first approach, and updated

iteratively during the inversion. 100 iterations were performed on each flare, and the inversion was carried out twice, once assuming a Weibull bubble size distribution, and once assuming a log-normal type distribution.

Once the BSD and  $\bar{\rho}$  are known, the gas flux is estimated for the entire flare (which could represent a field of seeps) following Eq. 6.3:

$$flux = A\bar{\rho} \int_0^{a_{max}} \frac{4}{3}\pi a^3 BSD(a)v(a) da \quad (6.3)$$

where  $A$  is the spatial extent of the acoustic anomaly in the proximity of the seafloor as interpreted from the processed MBES data,  $\bar{\rho}$  is the mean density of bubbles in the water in  $m^{-3}$ ,  $v(a)$  is the mean rising velocity of the gas bubbles, BSD is the bubble size distribution and  $a$  is the bubble radius. The bubble rise velocity values are based on the work by Leifer and Patro (2002), and consider the two end-members clean and "dirty" bubbles, where the latter model represent gas bubbles which are coated with oil or hydrate. In the next section, the estimated gas fluxes are presented as ranges of values. The major source of variability in the flux estimations comes from the use of coated versus clean bubbles models: because clean bubbles rise faster than coated bubbles, changes in  $v$  have a linear effect on the fluxes (Eq. 6.3). The secondary source of uncertainty in the estimations is related to the approach used for the calculation of the BSD and density (Figure 6.1). These parameters impact both the mean rising velocity - which depends on the bubble size, and the volume of gas calculated at the seafloor, as discussed in the following sections.

## 6.3 Results

### 6.3.1 Identification of gas seeps

Gas venting sites are identified in the multibeam data by anomalous high acoustic backscatter in the water column with respect to the surrounding region. High backscatter values in the water could also indicate the presence of schools of fish, thermo-haline layering or artefacts. Given the ambiguity in interpreting vertically-summed (echo integrated) backscatter intensity maps, I analysed horizontally-stacked sections and fan-view images of backscatter intensity (Figure 6.3b and c, respectively) in the vicinity of the acoustic anomalies, to confidently interpret gas flares where regions of high backscatter intensity propagate from the seafloor upwards, as expected from a rising

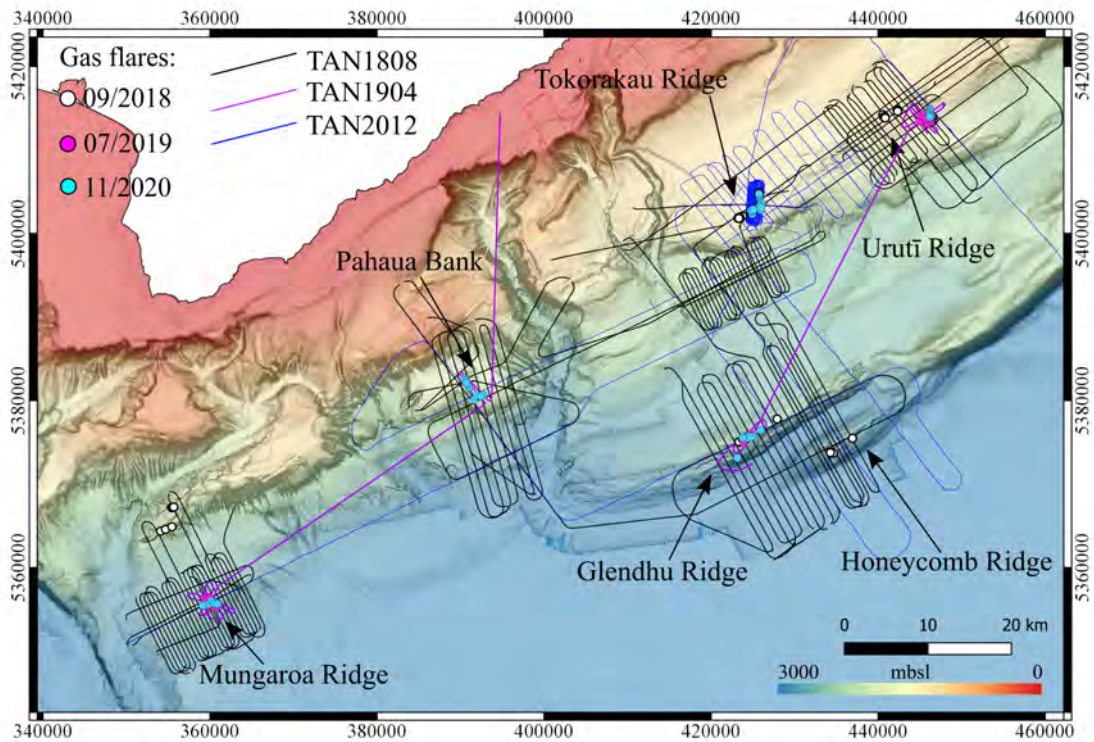


**Figure 6.2:** Southern Hikurangi Margin: gas flares identified from the MBES data from the three HYDEE voyages (see Section 1.2.2s). The five target areas are mentioned in the text. Lines are ship tracks from each of the voyages; dots are gas flares. Map coordinates are in UTM Zone 60S (WGS84 datum).

aggregate of gas bubbles. I analysed three datasets from different voyages that surveyed the same target areas (see Chapter 1). This approach ensures that I accurately pinpoint the location of gas venting at the seafloor. In the study area, I identified a total of 129 individual gas flares: 43 from TAN1808, 33 from TAN1904 and 53 from TAN2012 datasets. Most of these cold seeps are located approximately at the same point on the seafloor in the three datasets; however, the difference in data quality and acquisition parameters doesn't allow a more detailed comparison between the three datasets. It is important to point out that the flares observed in the acoustic data are presumably formed by multiple jets sited in an area that is smaller than the insonified seabed area. The lateral resolution of the MBES data at the seafloor depends on the beam-width and the water depth. The five regions of focused gas seepage are: Uruti Ridge, Tokorakau Ridge, Pahaua Bank, Glendhu and Honeycomb ridges and Mungaroo Ridge (Figure 6.2). The shallowest seeps occur at Tokorakau Ridge at  $\sim 1100$  mbsl,

while the deepest one is the Honeycomb Ridge seep, located in  $\sim 2400$  m water depth. There is no acoustic evidence that any of the analysed gas flares reaches the sea surface in the study area.

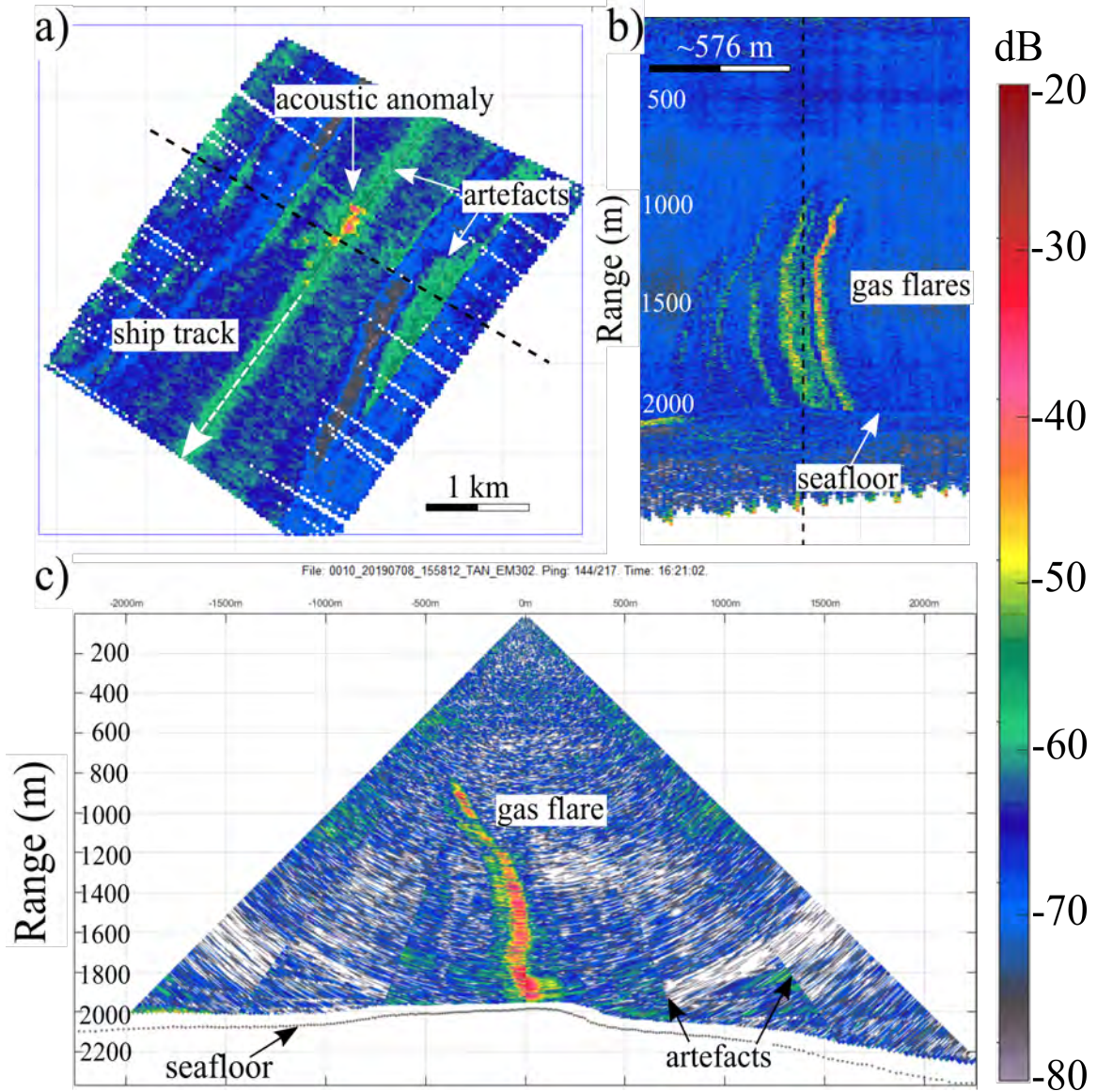


**Figure 6.3:** Backscatter intensity images of the Glendhu seep field (see Fig. 6.2 for location) from multibeam data. a) echo integrated map (resolution 20x20 m); b) range stacked view along the profile shown in a); c) fan view at the location indicated by the dashed black line.



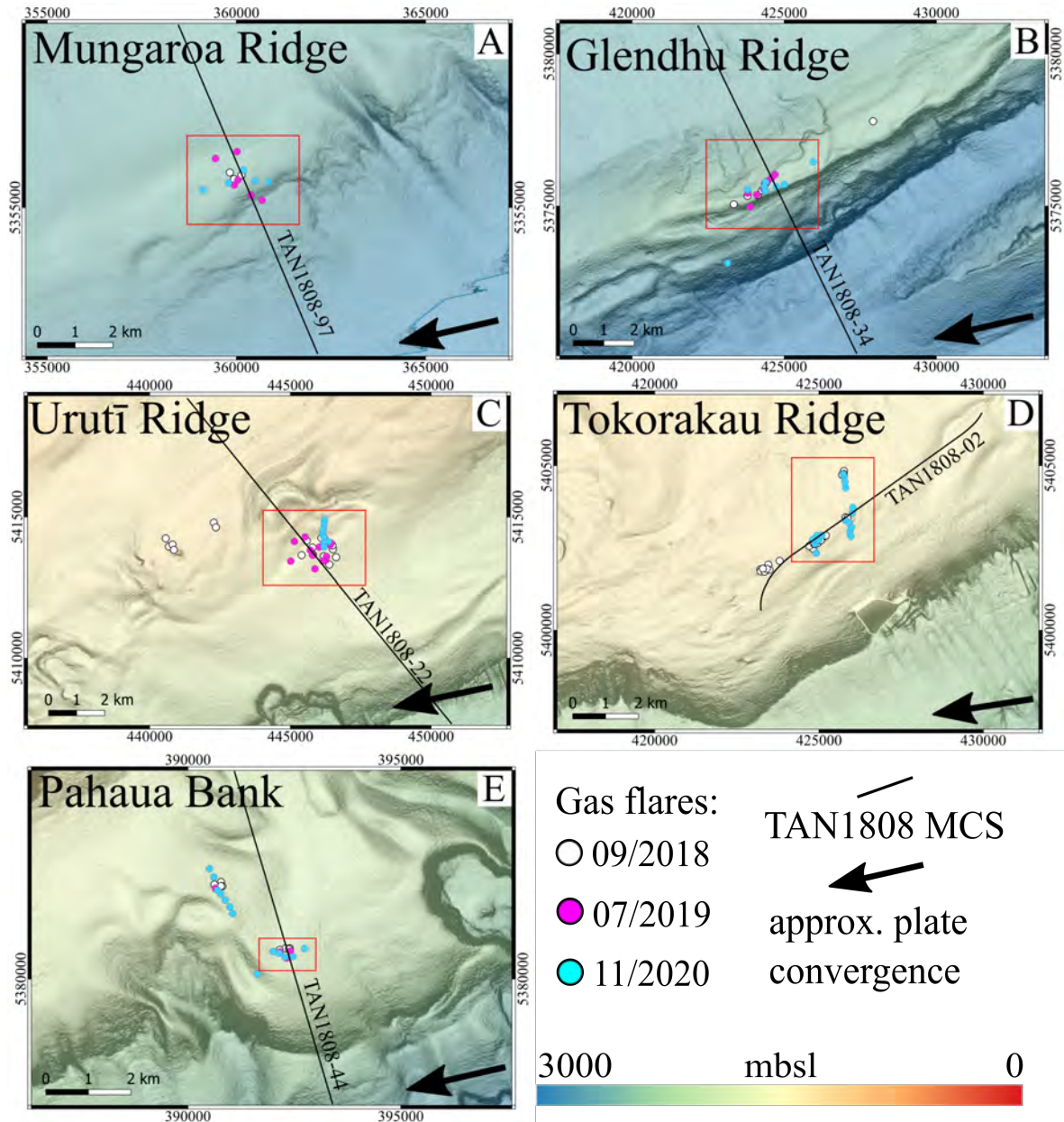


**Figure 6.4:** Distribution of the acoustic seeps identified in the five target areas: (a) Mungaroa Ridge; (b) Glendhu Ridge; (c) Urutī Ridge; (d) Tokorakau Ridge; (e) Pahaua Bank. The approximate direction of plate convergence are extracted from the MORVEL online tool (Argus *et al.*, 2011). MCS: multi-channel seismic data

### 6.3.2 Gas fluxes and seismic observations

In this section, I present the results of gas flux estimations for the five target areas and analyse the local geological structure of these sites. The details of the parametrization of gas flares for each of the target sites, along with the estimated fluxes is given in

Table 6.3.2. The average thickness of the GHSZ varies according to the water depth and the geological context, from  $\sim 360$  m at Urutī Ridge (1200 mbsl) to  $\sim 630$  m at Mungaroo Ridge (2100 mbsl). Despite being visible throughout the five study areas, BSRs associated with gas hydrate occurrence are discontinuous, and cannot be observed directly below the locations of gas seepage.

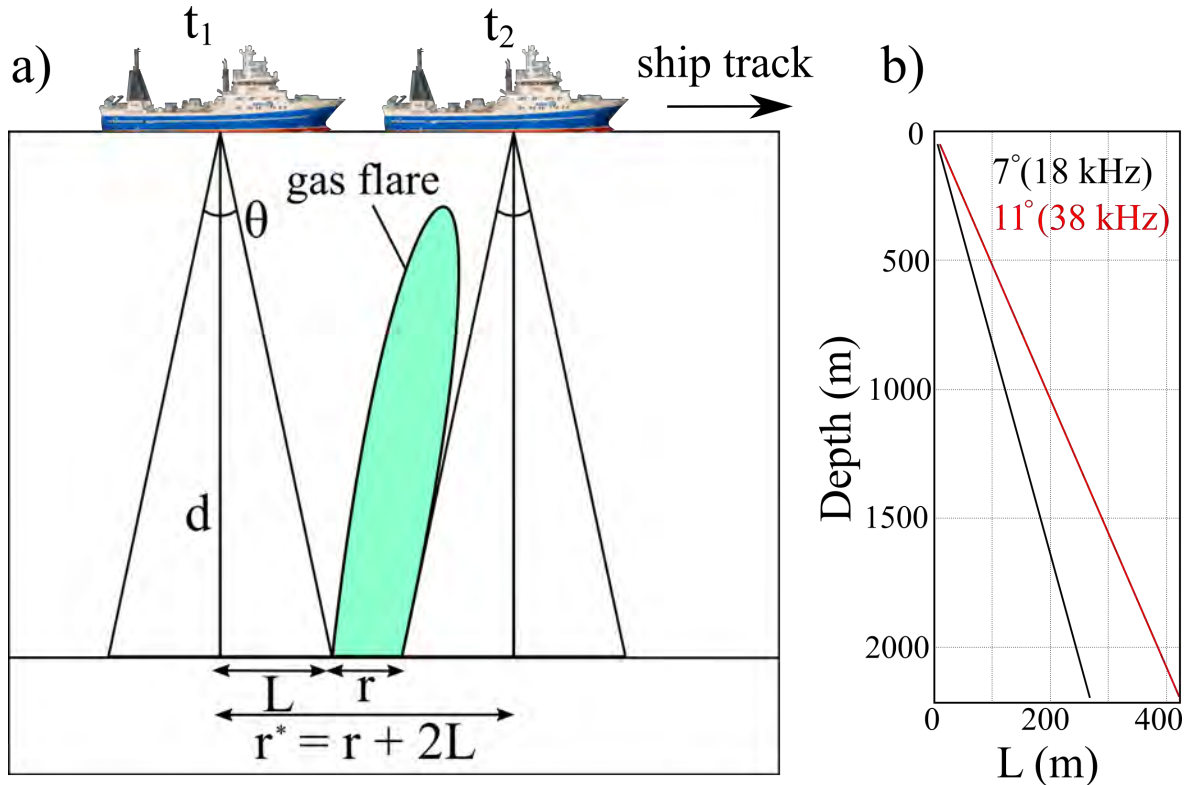


**Figure 6.5:** a) Graphical illustration of the lateral resolution of the acoustic images of the single-beam (EK60) data. b) Plot showing the dependence of the lateral resolution ( $L$ ) on water depth and beam angle.

### Urutī Ridge

The main Urutī Ridge seep field is located slightly seaward of the bathymetric high of the anticlinal ridge. The field of seep activity measures  $\sim 4$  km<sup>2</sup> at the seafloor, in water depths from 1175 m to 1300 m, and tens of flares can be identified from the acoustic data (10 flares identified in the 2018 datasets, 14 flares in the 2019 one and 8 in 2020). Most acoustic flares reach  $\sim 700$  m water depth, and the total area of high acoustic anomaly at 20 m above the seafloor measures 0.43 km<sup>2</sup>. The easternmost flares imaged in the TAN2012 dataset seem to be aligned roughly NS, which is sub-perpendicular to the direction of plate convergence in this part of the margin. Four flares were selected



from the many active plumes of this region for extracting the density of bubbles per cubic metre. Gas flux estimates for the entire seep field at Urutī Ridge range between 0.45 and  $7.1 \times 10^6$  kg/year. The seismic profile shown in Figure 6.6 runs perpendicular to the strike of the main anticlinal structure, and it crosses the seabed location of two major gas flares used for flux estimations, imaged in the EK60 data. A broad region of  $\sim 1$  km of the shallow subsurface shows high-amplitude negative polarity reflections that reveal the presence of free gas in the sediments. The sedimentary sequence below this region is characterised by a general decrease in seismic amplitudes (seismic blanking) and disrupted reflections. The blanking zone in the overlying stratigraphic sequence is bounded in depth by a seismic unconformity that marks the top of a highly reflective unit of steeply dipping strata that form the seaward limb of the Urutī Ridge anticline. The amplitude of the BSR is higher to the NW and to the SE of the flares site, it fades out in the core region of the anticline, and it is not observed in the region of enhanced reflectivity on the seaward limb of the anticline.

### **Glendhu Ridge**

Glendhu Ridge is a thrust-related elongated structural feature with four-way closure that lies close to the present-day deformation front. The anticlinal structure of the ridge is imaged in the seismic profiles that cross the location of the seeps (Figure 6.7). On the landward side of the anticline, the Glendhu backthrust cuts through the sedimentary sequence. The seismic blanking observed to the SE of the backthrust is likely an imaging artefact caused by the steep angle of the strata. The BSR is clearly imaged in the seismic data, and phase reversal can be observed in a high amplitude reflection crossing it, indicating the presence of free gas in the sediments below (Figure 6.7D). There is no BSR below the seep location at the top of the ridge, similar to what is observed at Urutī Ridge (Figure 6.6). The seismic image of the shallow sediments below the crest of the ridge shows a pattern of disrupted reflections, typically caused by scattering of seismic energy due to the presence of gas. Interestingly, the normal faults that cut through the core region of the anticline to the SE of the ridge crest do not seem to act as fluid pathways and are not linked to fluid expulsion features on the seafloor. The main gas venting field is located right on the bathymetric crest of the ridge, at a water depth of about 2000 m, where 6 - 8 main acoustic flares can be identified from the multibeam data. The seeps are roughly aligned ENE-WSW, parallel to the long-axis of the four-way closure and sub-parallel to the vector of plate convergence (Figure 6.4b). For the parametrization of this gas seep field, we used the

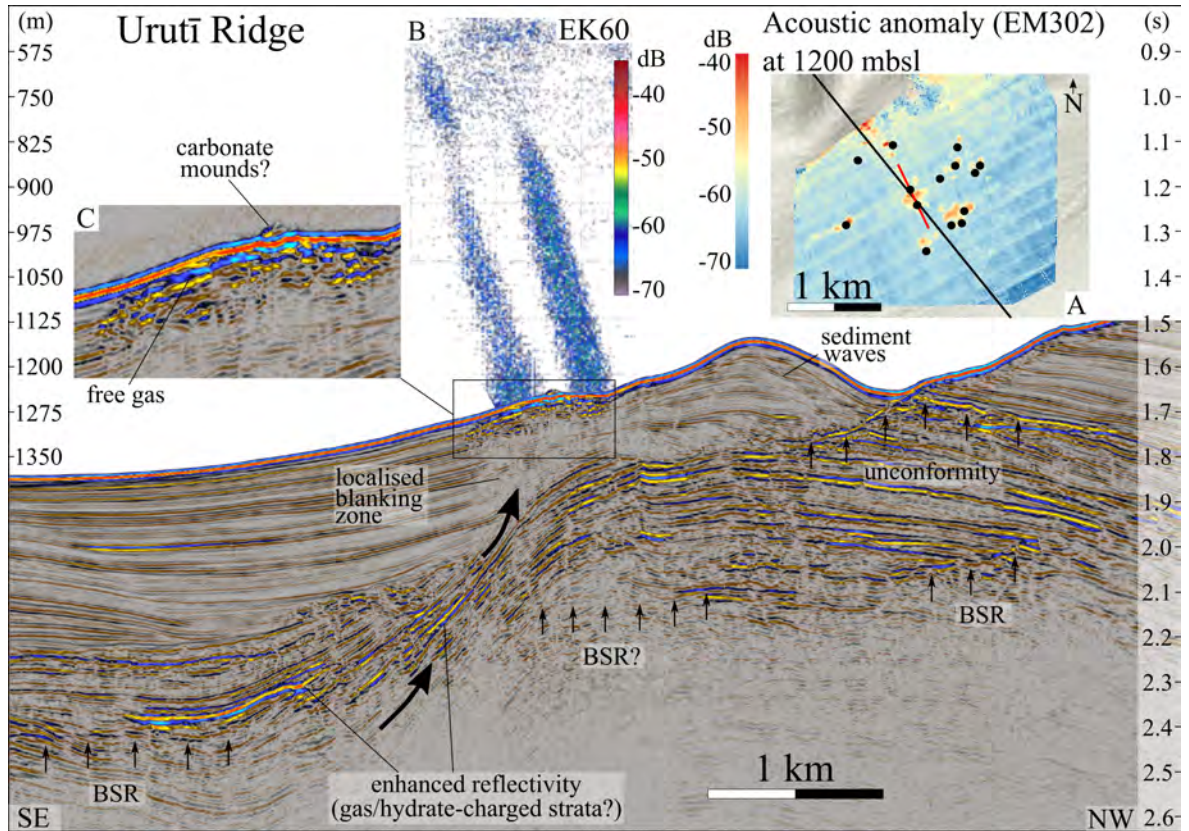


**Figure 6.6:** Overview of the Urutī Ridge seep site: the interpreted TAN1808-22 seismic profile is shown in the main panel. The bold black arrows represent the direction of fluid flow as interpreted from the seismic data and explained in the text. BSR: bottom simulating reflection. A) Map view of the Urutī Ridge seeps (red box in Figure 6.4c), showing the acoustic backscatter anomaly in the echo integrated MBES (EM302) data in proximity of the seafloor. The location of the TAN1808-22 seismic line and of the single-beam data (EK60) are indicated by the black and the red lines, respectively. The black dots represent the location of the main gas flares. The hydroacoustic data were collected during the TAN1904 voyage. B) Echogram of two gas flares as imaged by the 18 kHz channel in the single-beam data. The horizontal scale is the same of the seismic panel. C) Expanded view of the seismic data showing the shallow region beneath the cold seeps.

main acoustic flare visible in Figure 6.7, which rises from the seafloor for roughly 1200 m reaching a depth of  $\sim 780$  m. The area of acoustic anomaly at this site is  $0.17 \text{ km}^2$ , yielding total gas fluxes of  $1.32$  and  $4.1 \times 10^6 \text{ kg/year}$ , considering coated and clean bubbles, respectively.

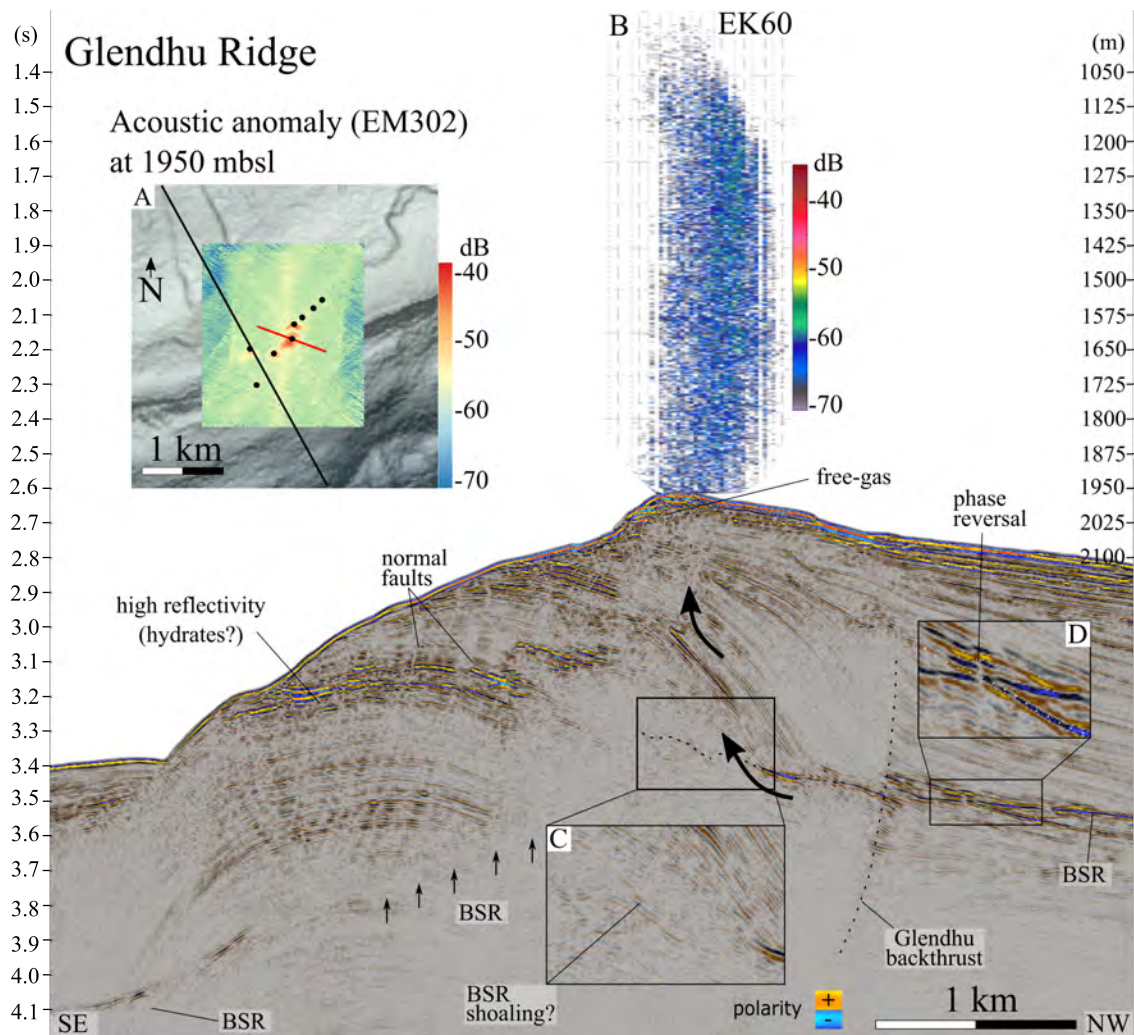


**Figure 6.7:** Overview of the Glendhu Ridge seep site: the interpreted TAN1808-34 seismic profile is shown in the main panel. The bold black arrows represent the direction of fluid flow as interpreted from the seismic data and explained in the text. BSR: bottom simulating reflection. A) Map view of the Glendhu Ridge seeps (red box in Figure 6.4b), showing the acoustic backscatter anomaly in the echo integrated MBES (EM302) data in proximity of the seafloor. The location of the TAN1808-34 seismic line and of the single-beam data (EK60) are indicated by the black and the red lines, respectively. The black dots show the locations of the main gas flares. The hydroacoustic data were collected during the TAN1904 voyage. B) Echogram of the gas flare as imaged by the 18 kHz channel in the single-beam data. The horizontal scale is the same of the seismic panel. C) Expanded view of the seismic data showing the possible shoaling of the BSR beneath the crest of the ridge. D) Expanded view of the seismic data showing the polarity reversal of a reflection crossing the BSR.

## **Pahaua Bank**

Pahaua Bank is a submarine ridge located on the mid-slope portion of the accretionary wedge, roughly half-way between the continental shelf break and the subduction trench, at water depths of 1450 - 1570 m. There are two regions of concentrated gas seepage at the seafloor: the northernmost group of gas seeps includes at least seven distinct flares aligned NNW-SSE, perpendicular to the direction of plate convergence. The southernmost group consists of at least six flares rising from 1560 m. In both groups, the acoustic signature of the rising bubbles reaches the depth of  $\sim 750$  mbsl. The total area of acoustic anomaly close to the seafloor measures  $0.21 \text{ km}^2$ . One flare from the southernmost group was used for bubble size and density parametrization, yielding gas flux estimates between  $1.43$  and  $6.22 \times 10^6 \text{ kg/year}$  for this site. The seismic data reveal a  $\sim 400$  m long strong reflection with negative polarity right below the seabed at the location of gas seepage, indicative of widespread free gas in the shallow sediments (Figure 6.8). Below the free gas accumulation, a column-shaped region of localised seismic blanking extends downwards towards the base of the GHSZ, in a region of disrupted reflections in the vicinity of an apparent BSR shoaling.

## **Tokorakau Ridge**

This is the shallowest of the analysed seep fields, and it lies in a region of relatively flat bathymetry at  $\sim 1140$  m water depth. Tokorakau Ridge is a SW-NE trending anticline that represents the southern extension of Urutī Ridge. The seismic profile shown in Figure 6.9 runs parallel to the strike of the anticline, and crosses two areas of gas seepage. The sedimentary sequence is characterised by relatively flat and parallel strata. The thickness of the GHSZ at Tokorakau Ridge is  $\sim 0.5$  s, or  $\sim 450$  m using an estimated seismic velocity of  $1800 \text{ m/s}$ . While the BSR appears as a distinct negative polarity reflection adjacent to the seep locations, it is characterised by a series of lower amplitude reflections in the central part of the seismic profile, and it is not imaged beneath the regions of gas expulsion. High amplitude reflections with the same polarity as the seafloor indicate the presence of concentrated gas hydrates in the shallow sediments, while column-shaped regions of seismic blanking suggest upward fluid migration from the BGHS towards the cold seeps. Similar to the Urutī Ridge eastern flares and to the Pahaua Bank northern flares, the acoustic gas plumes at Tokorakau Ridge are aligned roughly perpendicularly to the direction of plate convergence. The 23 imaged flares can be grouped into four clusters (Figure 6.4d), and they rise for  $\sim 500$



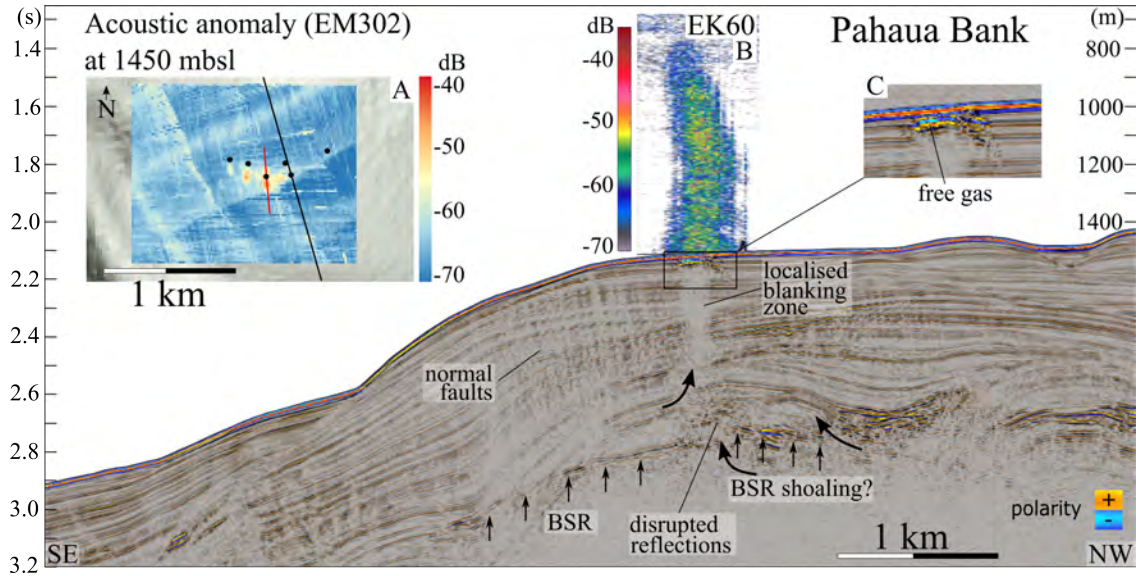


**Figure 6.8:** Overview of the Pahaua Bank seep site: the interpreted TAN1808-44 seismic profile is shown in the main panel. The bold black arrows represent the direction of fluid flow as interpreted from the seismic data and explained in the text. BSR: bottom simulating reflection. A) Map view of the Pahaua Bank seeps (red box in Figure 6.4e), showing the acoustic backscatter anomaly in the echo integrated MBES (EM302) data in proximity of the seafloor. The location of the TAN1808-44 seismic line and of the single-beam data (EK60) are indicated by the black and the red lines, respectively. The black dots show the locations of the main gas flares. The hydroacoustic data were collected during the TAN1904 voyage. B) Echogram of a gas flare as imaged by the 18 kHz channel in the single-beam data. The horizontal scale is the same of the seismic panel. C) Expanded view of the seismic data showing the shallow region beneath the cold seeps, where free gas accumulation is inferred by the negative polarity reflection.

m from the seafloor. One flare was selected to estimate bubble parameters (see Table 6.3.2). With a total area  $\sim 0.45 \text{ km}^2$  of acoustic anomaly, the gas flux estimates for the Tokorakau venting field lie between  $0.87$  to  $4.42 \times 10^6 \text{ kg/year}$ .

### Mungaroo Ridge

The Mungaroo seep field (Figure 6.10) is the deepest analysed in this study, with its main gas flare located at 2080 mbsl at the top of Mungaroo Ridge, a thrust-related four-way closure that lies at the toe of the accretionary wedge (Crutchley et al., 2021). The gas-water contact visible in the seismic data suggests the presence of a thick free-gas column accumulation beneath the BGHS. High amplitude reflections are observed

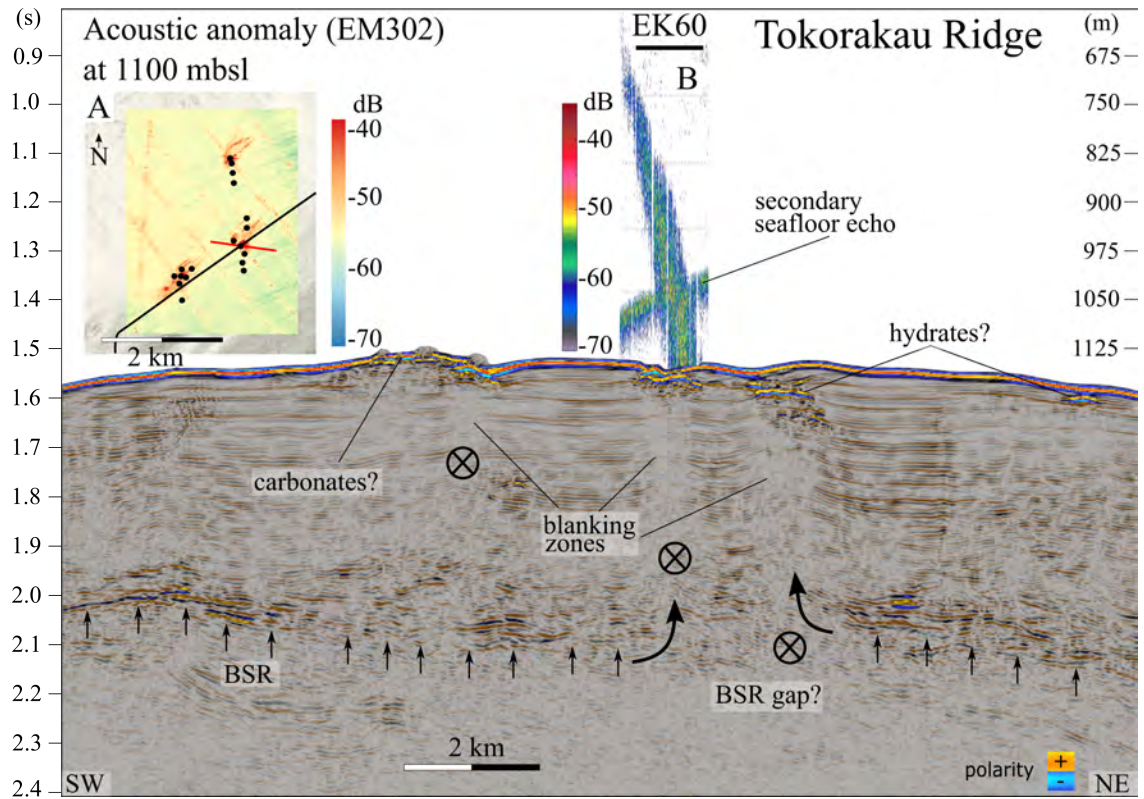


**Figure 6.9:** Overview of the Tokorakau Ridge seep site: the interpreted TAN1808-02 seismic profile is shown in the main panel. The black arrows show the direction of fluid flow as interpreted from the seismic data and explained in the text. BSR: bottom simulating reflection. A) Map view of the Tokorakau Ridge seeps (red box in Figure 6.4d), showing the acoustic backscatter anomaly in the echo integrated MBES (EM302) data in proximity of the seafloor. The location of the TAN1808-02 seismic line and of the single-beam data (EK60) are indicated by the black and the red lines, respectively. The black dots show the locations of the main gas flares. The hydroacoustic data were collected during the TAN2012 voyage. B) Echogram of a gas flare as imaged by the 38 kHz channel in the single-beam data. The horizontal scale is the same of the seismic panel.

in the core region of the anticline, where a network of normal faults cuts through the sedimentary sequence. From the top of the highly reflective region, a vertical chimney structure connects the gas reservoir to the seafloor location of the gas flare. The main flares observed on the seafloor lie in the vicinity of the chimney, suggesting that fluids are flowing along this fracture. The site was surveyed during the three HYDEE voyages, and six flares are observed in the acoustic data, rising from the seabed up to roughly 600 mbsl, making them the highest flares observed in the region (~1400 m high). The

estimated methane fluxes at this site range from 0.79 to  $8.35 \times 10^6$  kg/year.

Seep	Mean bubble radius in mm (1)-(2)-(3)	Density of bubbles in $\text{m}^{-3}$ (1)-(2)-(3)	Mean flux in kg/year (clean - coated)	Seafloor depth in m
Mungaroa Ridge	2.18 - 1.38 - 1.57	0.316 - 0.288 - 0.189	$5.52 - 1.88 \times 10^6$	2060
Glendhu Ridge	1.90 - 1.35 - 1.87	0.288 - 0.232 - 0.268	$4.26 - 1.51 \times 10^6$	1950
Pahaua Bank	1.56 - 1.35 - 1.87	0.450 - 0.244 - 0.374	$6.02 - 1.77 \times 10^6$	1550
Tokorakau Ridge	1.60 - 1.15 - 2.67	0.25 - 0.190 - 0.129	$8.34 - 3.20 \times 10^6$	1110
Urutī Ridge	1.67 - 1.08 - 2.25	0.039 - 0.042 - 0.128	$3.38 - 1.14 \times 10^6$	1240

**Table 6.1:** Bubble size parameters and fluxes. (1): linear inversion with Weibull distribution; (2): linear inversion with log-normal distribution; (3): manual curve fitting with Weibull distribution. All values are calculated at the seafloor.

## 6.4 Discussion

The quantitative study of the water column combined with observations of subsurface geological structures has allowed a detailed characterisation of the five targeted cold seep areas on the southern Hikurangi Margin. In this section, we discuss the key findings of this study and highlight their main implications.

### 6.4.1 Acoustic data resolution

Figures 6.6 - 6.10 show seismic profiles crossing the targeted seep fields, overlain on the acoustic backscatter image ( $S_v$ ) of the water column from the 18 kHz channel of the EK60 split-beam echo sounder. While the horizontal and vertical scale of the two images match, the acoustic image of the water column shows the apparent resolution of the EK60 data: the true horizontal resolution depends on the beam-width and varies with depth following:

$$r = r^* - 2d(\tan \frac{\theta}{2}), \quad (6.4)$$

where  $r$  is the horizontal resolution,  $r^*$  is the apparent resolution measured in the echograms,  $d$  is the water depth and  $\theta$  is the beam aperture angle ( $11^\circ$  for the 18 kHz channel, Figure 6.5).

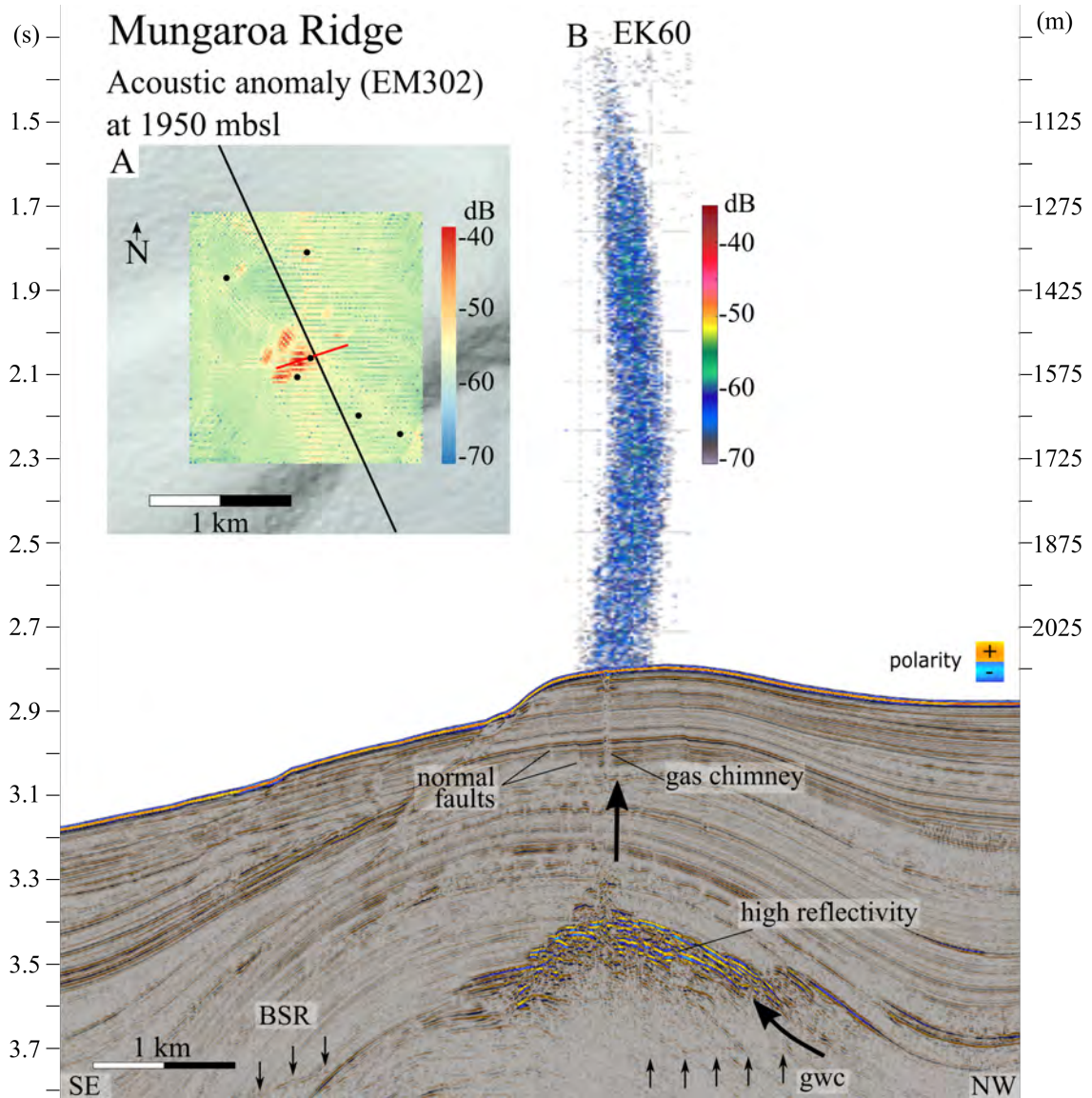


**Figure 6.10:** Overview of the Mungaroo Ridge seep site: the interpreted TAN1808-97 seismic profile is shown in the main panel. The black arrows show the direction of fluid flow as interpreted from the seismic data and explained in the text. BSR: bottom simulating reflection; gwc: gas-water contact. A) Map view of the Mungaroo Ridge seeps (red box in Figure 6.4a), showing the acoustic backscatter anomaly in the echo integrated MBES (EM302) data in proximity of the seafloor. The location of the TAN1808-97 seismic line and of the single-beam data (EK60) are indicated by the black and the red lines, respectively. The black dots represent the locations of the main gas flares. The hydroacoustic data were collected during the TAN2012 voyage. B) Echogram of a gas flare as imaged by the 38 kHz channel in the single-beam data.



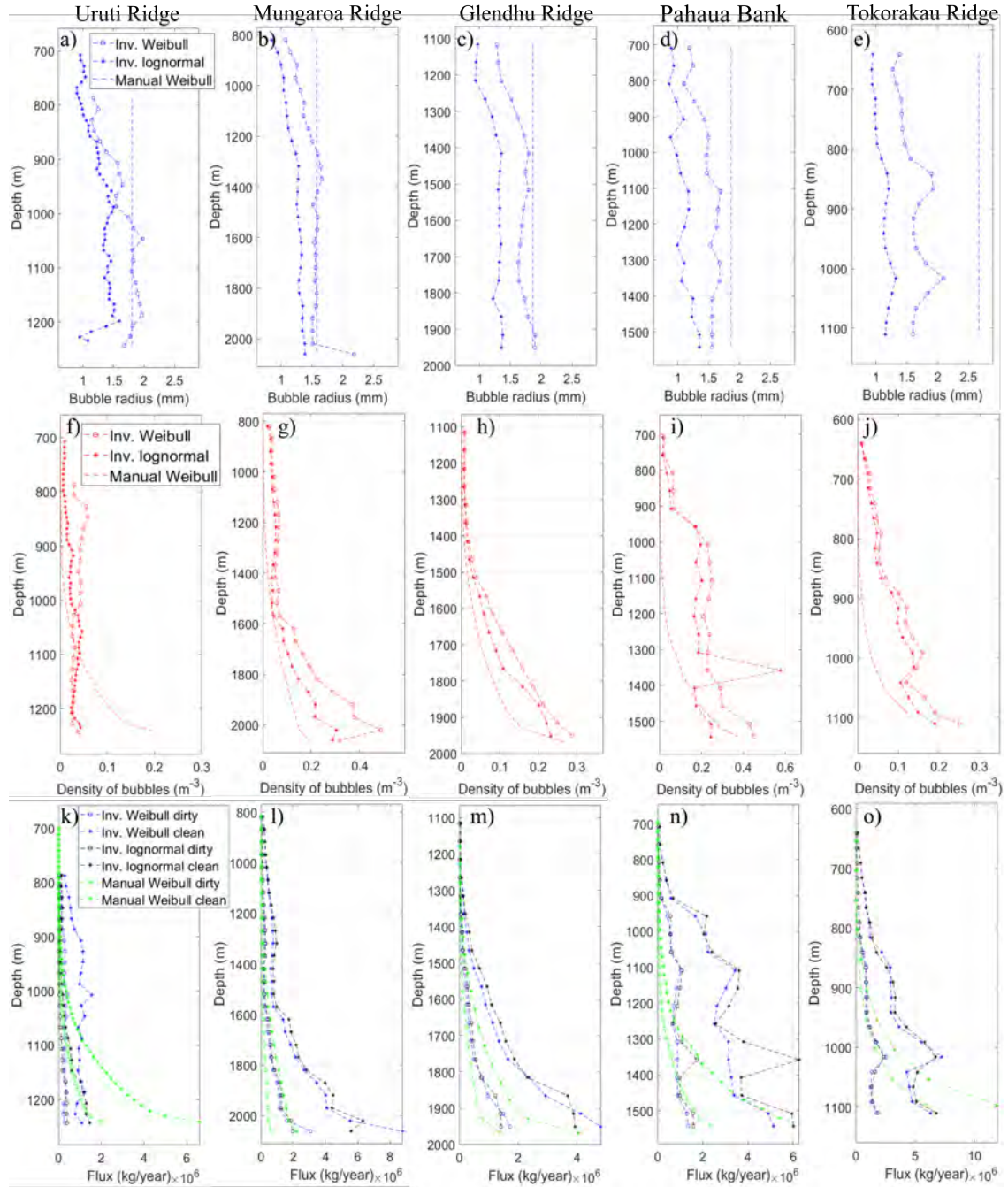


**Figure 6.11:** Results of methane flux estimations for the five seep locations. a)-e) show the variations of the mean bubble radius versus depth; f)-j) show the mean density of bubbles and k)-o) show the mean methane fluxes calculated at depth with the clean and coated (dirty) ascending velocity models.

## 6.4.2 Constraints on bubble size distributions

Quantification of gas flux is generally dependent on observations of bubble parameters. Ideally, optical measurements such as video observation, bubble size measuring,

and sampling of the seep fluids provide the most accurate measures of the bubble size distribution function, their rising velocity and the chemical gas composition, enabling the determination of realistic values of gas flow rates (e.g., Higgs *et al.*, 2019; von Deimling *et al.*, 2011; Wang *et al.*, 2016; Weber *et al.*, 2014).

Due to the lack of optical observations of the seeps analysed in this study, no measurements of BSD are available, and we adopt a variation of the method proposed by Veloso *et al.* (2015) to estimate the BSD from the split-beam EK60 data. To test the validity of the results, we analyse the dependance of the estimated methane fluxes on different BSD functions: we first parametrise the BSD by assuming log-normal and Weibull probability density functions (PDF), and then compare the inverted results (Figure 6.12). The choice of these PDFs was made based on published seep studies, which have suggested several distribution functions to describe bubble size data including normal (Römer *et al.*, 2012), log-normal (Wang *et al.*, 2016), and Weibull (Li *et al.*, 2020).

The modelled  $S_v$  depends on both the BSD and the density of bubbles (Eq. 2.26). If the BSD parameters are over corrected during the curve matching procedure, the density of bubbles will be underestimated, so that the final impact on the calculation of gas fluxes is minimal. This can be observed, for example, in the inversion results for Mungaroo Ridge flare at 2060 mbsl (Figure 6.10), where the mean bubble radius of the BSD modelled assuming a Weibull distribution increases above 2 mm, the density of bubbles for the corresponding depth shows a sharp decrease.

ROV footage of the Glendhu Ridge seep was acquired during a recent voyage onboard R/V Tangaroa, and qualitative observations seem to indicate that there is a narrow range of bubble sizes emitted at the seafloor (Sarah Seabrook, personal communication, 2021). The number of bubbles smaller than 0.5 mm is probably overestimated by the Weibull PDF, and the log-normal curves are more likely to represent the real BSD at these seep sites. Nevertheless, our analysis shows that the overall impact of the BSD on the methane flux estimates is small. The fluxes estimated assuming a constant BSD for the entire flare and based on the normalised  $S_v$  response (manual curve fitting method) show a general smooth trend with depth. The mean volume backscattering strength ( $\bar{S}_v$  in equation 6.2), which is related to the density of bubbles, also increases with depth. This trend can be explained by the fact that in this approach a mean  $S_v$  is calculated by averaging the echo integrated backscatter volume strength of the

cells located at the same depth. The fluxes calculated through the linear inversion method (both assuming Weibull and log-normal distributions) show more variability in the calculated density of bubbles and fluxes, despite a general increase with depth (e.g., Fig. 6.8).

There are two sources of variability in the resulting estimations of gas fluxes at the seafloor: one related to the uncertainty in bubble parameters (such as mean radius, bubble density and bubble size distribution), and one related to the model used to estimate the bubble rising velocity (assuming either clean bubbles or coated ones). Considering the flux values calculated at the deepest point of the flares (i.e., close to the seafloor), the largest difference related to the first type of uncertainty is observed at the Pahaua Bank site for the clean bubble model, and is about  $6.3 \times 10^6$  kg/year. The bubble parameters shown in Figures 6.6 - 6.10 are summarized in Table 6.3.2.

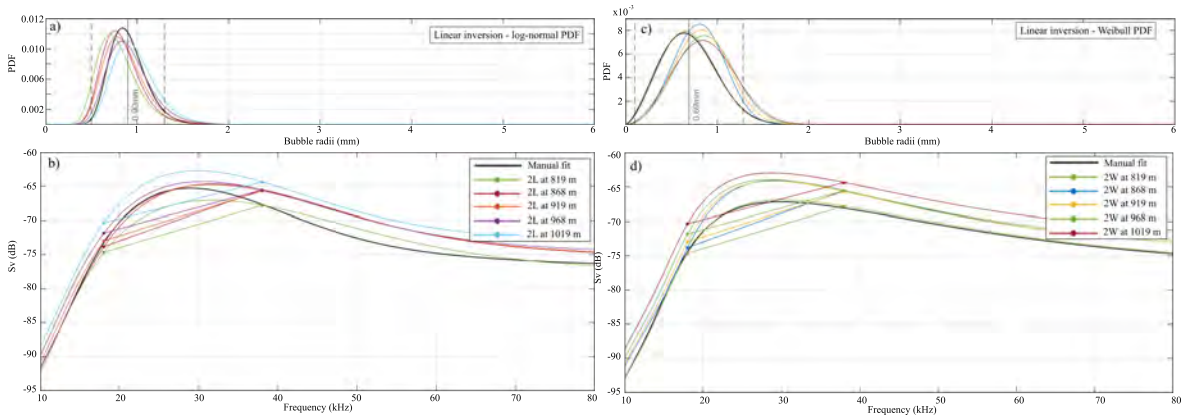


**Figure 6.12:** Bubble size distributions estimated from linear inversion of the split-beam data at the Mungaroa Ridge gas flare, imposing log-normal (a) and Weibull (c) distributions. Each curve is representative of a 50 m high horizontal slice of the gas flare, and is color coded according to the water depth. b) and d) show the theoretical frequency response curves at each horizontal slice of the gas flare, and the dots represent the observed Sv at the same water depth for the 18 and the 38 kHz channels.

### 6.4.3 Source of gas and seismic manifestation of fluid flow

The southern Hikurangi Margin is a well-established province of gas hydrate occurrence, fluid migration and gas seepage (e.g., Barnes *et al.*, 2010; Crutchley *et al.*, 2011; Kroeger *et al.*, 2019; Watson *et al.*, 2020). Consistent with the majority of subduction

margins, the analysis of gases emitted at the seafloor suggests a predominantly microbial origin of methane over a thermogenic origin (Faure *et al.*, 2010; Greinert *et al.*, 2010). At all the flare sites observed in this study, we found evidence of gas migrating from the base of the GHSZ to the seafloor. In the case of Mungaroo Ridge, a large free gas reservoir in the core region of the anticline is the source that supplies gas to the main seep observed at the seafloor. Here, the overpressured gas caused hydraulic fracturing of the overlying sediments leading to the formation of the vertical gas chimney imaged in the seismic data (Figure 6.10; Crutchley *et al.*, 2021). The presence of such large and interconnected free gas accumulations is not observed at any of the other target sites. However, highly reflective strata are imaged at Urutī and Glendhu ridges, crossing the base of the GHSZ at steeply dipping angles. The enhanced reflectivity may be caused by the strong impedance contrast between fine-grained impermeable layers and sandy gas-charged sedimentary units. Stratigraphically-driven fluid migration along permeable dipping strata has been suggested to be the main mechanism for upward fluid flow in many anticline-related ridges on the Hikurangi Margin (e.g., Barnes *et al.*, 2010; Crutchley *et al.*, 2019; Turco *et al.*, 2020; Wang *et al.*, 2017a).

The seismic data beneath the flares show different manifestations of fluid migration in the sediments including blanking zones, bright spots, chimney-like structures, disturbed stratification and shoaling of the base of the GHSZ. Fluid migration through the GHSZ is identified by areas of decreased amplitude (seismic blanking) and disrupted stratifications in the sediments below the seeps, as at Tokorakau Ridge, Pahaua Bank and Urutī Ridge, or by localised vertical chimney-like structures, such as at Mungaroo and Glendhu ridges. The disruption of sedimentary strata can be due to the scattering of seismic energy caused by the presence of gas (Judd and Hovland, 1992).

The fact that broad regions of reduced amplitudes are not observed below the seeps at the ridges closer to the deformation front (Mungaroo and Glendhu) could be explained by the younger age of these structures. In the initial stages of a gas seep formation, gas supply might come from a deeper reservoir through localised gas chimneys created by hydrofracturing, similarly to the Mungaroo Ridge seep case (Crutchley *et al.*, 2021). Over time, precipitation of authigenic carbonate (e.g., Greinert *et al.*, 2001) or formation of gas hydrate might cause localised barriers which would block the fractures used for fluid migration, causing the overpressured gas to create new fractures disrupting the sediments (e.g., Petersen *et al.*, 2010; Sun *et al.*, 2012). Therefore, the seep sites

that lie closer to the Hikurangi subduction trough are characterised by a narrower zone of sediment disruption (i.e. the vertical chimney-feature at Mungaroa Ridge, Figure 6.10). At the more landward sites, on the other hand, fluids might have been migrating for longer time, creating a net of interconnected pathways that disrupted the geological stratification resulting in the broad blanking regions observed in the seismic data.

#### 6.4.4 Temporal variability of the seeps

There are many mechanisms that control the activity of different types of gas seeps. Consequently, the time scales over which the activity of cold seeps fluctuates can span from minutes to millennia. For example, Feseker *et al.* (2014) document the eruption of a deep-sea mud volcano that triggered large methane and CO<sub>2</sub> emissions over a period of minutes. Pressure changes at the seafloor caused by tides have been shown to impact the flow rate of shallow and deep-sea gas seeps (Boles *et al.*, 2001; Riedel *et al.*, 2018; Römer *et al.*, 2016), while seasonal sea-bottom temperature variations can cause cold seeps to hibernate during the cold months, trapping gas in the sediments that is released in large pulses during warmer months (Ferré *et al.*, 2020). On the other hand, natural seismicity (Franek *et al.*, 2017) and ocean warming (Baumberger *et al.*, 2018; Berndt *et al.*, 2014) are potential triggers for significant release of methane from the sediments, especially in hydrate provinces. This study represents an opportunity to analyse the variability of methane emissions on the southern Hikurangi Margin over a three years period. Although quantitative estimates were calculated only once for each gas flare, from either the 2019 or from the 2020 datasets, the qualitative analysis of multibeam and split-beam data suggests that there is no substantial difference in the activity of the main seeps between 2018 and 2020 (Figure 6.13). The spatial extent of the acoustic anomaly close to the seafloor remains fairly constant for the five target areas in the three datasets, as does the height of the acoustic flares.

In addition to stable gas seepage over a period of three years, it is known from authigenic carbonates (for example on Urutī Ridge) that many of the seep sites have been active for thousands of years (e.g. Jones *et al.*, 2010; Liebetrau *et al.*, 2010). Likewise, there is evidence for stable methane seepage over intermediate time-scales from tube worms (*Lamellibrachia spp.*) up to 2 m long sampled at Mungaroa, Urutī and Glendhu ridges (Sarah Seabrook, pers. comm., 2021). Tube worms of this species require at least 200 years to reach such lengths (Cordes *et al.*, 2007; Fisher *et al.*, 1997).

Understanding and monitoring the temporal variability of a field of cold seeps is relevant to a number of scientific and socio-economic issues. At a national scale, one of the most direct implications is related to regional ecosystem management. Cold seeps are increasingly recognized as centres of local biogeochemical cycling and oases for many animals with recent studies finding that commercially important fisheries species are associated with seep habitats and consume methane derived carbon from chemosynthetic production in seep systems (Grupe *et al.*, 2015; Levin *et al.*, 2016; Seabrook *et al.*, 2019; Turner *et al.*, 2020).

#### 6.4.5 Global implications for ocean acidification

From the acoustic imaging of the water column, no evidence was found that methane bubbles reach the sea surface at any of the analysed gas fares. Considering the depth of the seep sites reported here, two different processes will interact to prevent the CH<sub>4</sub> emitted at the seafloor from reaching the atmosphere: (1) the methane contained in the bubbles will dissolve into the water driven by the low concentration of CH<sub>4</sub> in the ocean (Wiesenburg and Guinasso Jr, 1979), and (2) dissolved CH<sub>4</sub> is converted into CO<sub>2</sub> in the water column by abiotic and biotic forces (McGinnis *et al.*, 2006). Although bubble-stripping and methane oxidation reduce the amount of CH<sub>4</sub> released into the atmosphere, these processes can significantly impact local marine habitats and the global ocean chemistry. At a regional scale, massive emissions of CH<sub>4</sub> can cause localised deoxygenation of waters causing the depletion of species that are important to an ecosystem (Dickens, 2001; Kessler *et al.*, 2011). Moreover, because the oxidation process of the CH<sub>4</sub> emitted at cold seeps occurs in deep waters, which have higher solubility to CO<sub>2</sub> due to higher pressure, methane seeps represent an indirect source of CO<sub>2</sub> that needs to be taken into account in ocean acidification models (Archer *et al.*, 2009; Biastoch *et al.*, 2011).

In order to refine our understanding of the global effect of deepwater acidification, it is important to study the potential implications of hydrate dissociation on a regional scale. To this end, the relevance of margin-wide studies on natural methane seeps has increased in the past decade: Pohlman *et al.* (2011) found that up to 28% of the total dissolved organic carbon derives from fossil methane, while Garcia-Tigreros *et al.* (2021) conclude that aerobic oxidation of CH<sub>4</sub> has a greater influence on ocean chemistry in regions where methane concentrations are locally elevated. Based on the analysis of more than 300 gas seeps, Riedel *et al.* (2018) estimate a combined average in-situ flow

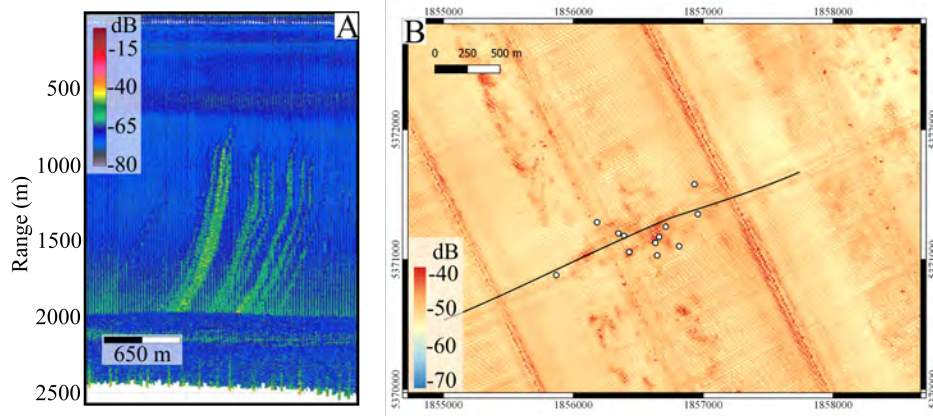
rate of about  $88 \times 10^6$  kg/year for the Cascadia Margin. Complementing this other work, the results of this chapter provide a quantitative assessment of the methane contribution of the southern Hikurangi Margin, which can be considered within the global carbon budget (Saunoi *et al.*, 2020), filling gaps of unknown methane sources and better constraining models of ocean acidification. Moreover, the fluxes presented here can be used as a proxy to monitor changes in the flux rates in the mid- to long term associated with ocean warming.

## 6.5 Conclusions

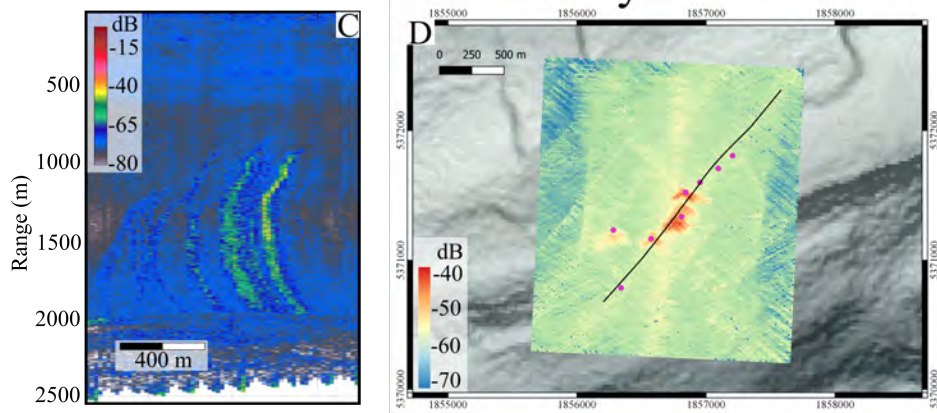
The combination of seismic and hydroacoustic data analysis allowed the characterisation of five cold seep sites on the southern Hikurangi Margin in terms of geological setting and gas flux estimates. The seismic data allowed imaging of the geological structures underlying the seep sites, showing gas hydrate systems through which the gas is flowing, and provided insights into the origin of the gas in the subsurface. Most of the gas comes from below the BGHS and the migration occurs either along steeply dipping strata or through sub-seismic structural fractures that manifest themselves as narrow or wide regions of seismic blanking. Hydroacoustic data collected over three years allowed mapping of the backscatter anomalies near the seafloor at the sites of seepage and pinpointing the location of the main gas flares on the sea bed. A total of 43, 33 and 53 individual flares were identified from the TAN1808, TAN1904 and TAN2012 datasets, respectively. Qualitative analysis of multibeam and split-beam data suggests that there is no substantial difference in the activity of the main seeps between 2018 and 2020.

The use of the multi-frequency split-beam echosounder allowed estimates of the gas flux rates at the five target sites to be made. The cold seeps lie in water depths ranging from 1110 to 2060 m, and emit, combined, between  $9.52$  and  $27.52 \times 10^6$  kg of gas per year. This study provides a quantitative assessment of the greenhouse gas contribution from the southern Hikurangi Margin, and has implications for seafloor biological communities and ocean chemistry.

## TAN1808 - September 2018



## TAN1904 - July 2019



## TAN2012 - November 2020

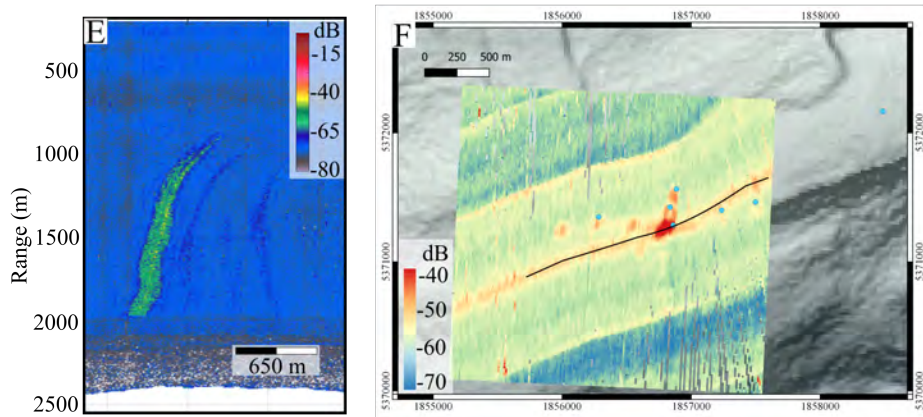


**Figure 6.13:** Evolution of the Glendhu Ridge seep site over the years. The panels on the left (A, C, E) show range stacked views of MBES (EM302) data of the gas flares on the top of Glendhu Ridge from TAN1808, TAN1904 and TAN2012 datasets, respectively. The panels on the right (B, D, and F) show the acoustic backscatter anomaly in the echo integrated MBES data in proximity of the seafloor. The black lines represent the ship track shown in the left panels. The coordinate system is UTM Zone 60S (WGS84 datum).



# Chapter 7

## Conclusions

The southern end of the Hikurangi Margin is a prime location to study the interaction between tectonic processes, focused fluid migration, hydrate formation and seafloor gas seepage. This region provided a prime location to apply different seismic methods to study gas hydrate systems. Comparing the results is often a difficult task, given the different assumptions underlying each method.

The novelty and over-arching objective of this thesis has been to provide a quantitative assessment to estimate: 1) the volumes of gas hydrate stored in concentrated accumulations within the thrust-ridges and 2) the volumes of greenhouse gases emitted at the seafloor at known cold seepage locations. This chapter summarises the key findings of the work presented in Chapters 3, 4, 5 and 6, and provides recommendations for further work.

**Highly concentrated gas hydrate in anticlinal ridges** The southern Hikurangi Margin hosts several accumulations of gas hydrate in high concentration, most of which are found in the core region of thrust related anticlinal ridges. The formation of such accumulations is primarily driven by upward fluid migration along permeable, steeply-dipping strata. These anticlines also act as geological traps for gas-rich fluids that start forming hydrate once they reach the GHSZ.

**Importance of ridge development for hydrate accumulations** The analysis of Glendhu and Honeycomb ridges provides insight into the evolution of anticlinal thrust-related ridges located at the toe of the accretionary wedge: older structures situated further landward of the deformation front are more likely to host more extensive accumulations than the younger ridges located at the deformation front, due to the fact

that they have drained a larger region of potential source rocks for a longer time. The interaction of sedimentation and erosion drives the location of the concentrated hydrate deposits away from the gentle stratigraphic dips in the core of the anticline (i.e. Honeycomb Ridge) into the steeper dips in the backlimb of the more structurally-mature anticlines (i.e. Glendhu Ridge).

**Resolution considerations** In terms of gas hydrate saturation, estimates based on the combined analysis of seismic velocity and reflectivity have to be considered an average over vertical zones with thicknesses on the order of the seismic data resolution (5 – 14 m), and the presence of higher hydrate saturations at a smaller scale cannot be ruled out.

**Estimates of hydrate in place** The probable estimated total volume of gas hydrates in place in the Glendhu and Honeycomb concentrated hydrate deposits lies between  $2.45 \times 10^5 \text{ m}^3$  and  $1.72 \times 10^6 \text{ m}^3$ , with the best estimate at  $9.68 \times 10^5 \text{ m}^3$ . This estimate provides a first-order assessment for further gas hydrate evaluations in the region. The sequential workflow applied to estimate porosity and gas hydrate saturation in the reservoirs highlights the effectiveness of probabilistic seismic inversions in characterising concentrated gas hydrate reservoirs, even in the absence of drilling data within the target reservoirs.

**Fine-scale velocity structure** The application of 1D full-waveform inversion allowed retrieval of the fine-scale  $V_P$  structure of key locations within concentrated hydrate deposits. The BGHS at the targeted sites is characterised by a consistent decrease in  $V_P$  even when no distinct BSR is present in the seismic data. Broad low-velocity regions in the inverted models associated with chimney-like structures in the seismic data are interpreted as evidence of free gas injection into the GHSZ, which might be facilitated by steeply dipping porous strata. The top of the concentrated gas hydrate deposits, marked by high amplitude positive polarity reflections, corresponds to  $\Delta V_P$  values of +200 m/s. The resolution of the seismic data and of the inverted  $V_P$  profiles could be at least an order of magnitude lower than the thickness of the sedimentary layers typical of the lower accretionary wedge. Therefore, the coexistence of free gas and gas hydrate in the pores of units that are thinner than the vertical seismic resolution cannot be ruled out.

**Structures beneath methane seeps** At the five targeted areas of gas seepage, seismic data show that most of the gas emitted at the seafloor comes from below the BGHS and the migration occurs either along steeply dipping strata or through subseismic structural fractures that manifest themselves with narrow or wide regions of seismic blanking.

**Quantitative analysis of gas seeps** A total of 43, 33 and 53 individual flares were identified from the TAN1808, TAN1904 and TAN2012 hydroacoustic datasets, respectively, lying in water depths ranging from 1110 to 2060 m. No substantial difference in the activity of the main seeps between 2018 and 2020 was observed. Gas flux rates were estimated from the split-beam data at the five target site. The analysed seeps emit between 9.52 and  $27.52 \times 10^6$  kg of gas per year collectively. This study provides the most quantitative assessment to date of the methane release at the southern Hikurangi Margin.

## 7.1 Future work

The analyses at Glendhu and Honeycomb ridges, presented in Chapters 3 and 4, suggests that the high amplitude reflections observed in the seismic data correspond to hydrate saturation of up to 60% or higher, probably concentrated along porous layers interbedded with fine-grained silts/mudstones. In contrast, the concentration of free gas is much harder to estimate because the effects of gas on the elastic properties of the sediment depend on its spatial distribution within the pores (i.e. uniform or patchy). The coexistence of free gas and gas hydrate is a key aspect that has to be taken into account in future quantitative studies of total in-place methane. The analysis and inversion of controlled-source electromagnetic data, which have been collected during TAN2012 voyage over some of the hydrate deposits presented in this thesis, is going to provide a complementary interpretation that will better constrain the amount of in-place methane that accumulates in the region.

For a more detailed characterisation of the GHSZ, implementation of the 1D full-waveform inversion adopted in Chapter 5 is needed. In particular, the joint inversion of other elastic parameters, such as  $V_S$ , would allow the distinction of hydrate- and free gas-bearing sediments. Such an analysis would require ocean-bottom seismometer data that could record converted shear waves.

The quantitative analysis of gas hydrate deposits and the estimates of methane flux into the ocean will be crucial for understanding the role that gas hydrate systems play in supporting biological communities at the seafloor and in altering ocean chemistry. In particular, regional oceanographic models will be used to generate methane dispersion models in the ocean to provide a better understanding of the influence of methane seepage on water chemistry at the Hikurangi Margin.

# Participation in data acquisition

As part of my Ph.D., I was involved in two scientific cruises co-funded by the HYDEE research programme. I was part of the MCS data acquisition team during TAN1808, and of the hydroacoustic data acquisition team during TAN2012 (Figures 7.1 and 7.2).



**Figure 7.1:** Crew and scientific party of the TAN1808 research voyage (HYDEE I). Picture taken offshore Kaikōura on a calm and sunny spring day - October 2018.



**Figure 7.2:** Scientific party of the TAN2012 research voyage (HYDEE III). Picture taken offshore Wairarapa - November 2020.

# References

- Ainslie, M. A. and Leighton, T. G. (2009). Near resonant bubble acoustic cross-section corrections, including examples from oceanography, volcanology, and biomedical ultrasound. *The Journal of the Acoustical Society of America*, 126(5), 2163–2175.
- Archer, D., Buffett, B., and Brovkin, V. (2009). Ocean methane hydrates as a slow tipping point in the global carbon cycle. *Proceedings of the National Academy of Sciences*, 106(49), 20596–20601.
- Argus, D. F., Gordon, R. G., and DeMets, C. (2011). Geologically current motion of 56 plates relative to the no-net-rotation reference frame. *Geochemistry, Geophysics, Geosystems*, 12(11).
- Arzhanov, M. M., Malakhova, V. V., and Mokhov, I. I. (2020). Modeling thermal regime and evolution of the methane hydrate stability zone of the Yamal peninsula permafrost. *Permafrost and Periglacial Processes*, 31(4), 487–496.
- Auguy, C., Calvès, G., Calderon, Y., and Brusset, S. (2017). Seismic evidence of gas hydrates, multiple BSRs and fluid flow offshore Tumbes Basin, Peru. *Marine Geophysical Research*, 38(4), 409–423.
- Avseth, P., Mukerji, T., and Mavko, G. (2010). *Quantitative seismic interpretation: Applying rock physics tools to reduce interpretation risk*. Cambridge university press.
- Azevedo, L., Nunes, R., Soares, A., Neto, G. S., and Martins, T. S. (2018). Geostatistical seismic Amplitude-versus-angle inversion. *Geophysical Prospecting*, 66(S1), 116–131.

- Azevedo, L. and Soares, A. (2017). *Geostatistical methods for reservoir geophysics*. Springer.
- Bachrach, R. and Avseth, P. (2008). Rock physics modeling of unconsolidated sands: Accounting for nonuniform contacts and heterogeneous stress fields in the effective media approximation with applications to hydrocarbon exploration. *Geophysics*, 73(6), E197–E209.
- Barnes, P. M., Lamarche, G., Bialas, J., Henrys, S., Pecher, I., Netzeband, G. L., Greinert, J., Mountjoy, J. J., Pedley, K., and Crutchley, G. (2010). Tectonic and geological framework for gas hydrates and cold seeps on the Hikurangi subduction margin, New Zealand. *Marine Geology*, 272(1-4), 26–48.
- Bassett, D., Sutherland, R., and Henrys, S. (2014). Slow wavespeeds and fluid overpressure in a region of shallow geodetic locking and slow slip, Hikurangi subduction margin, New Zealand. *Earth and Planetary Science Letters*, 389, 1–13.
- Baumberger, T., Embley, R. W., Merle, S. G., Lilley, M. D., Raineault, N. A., and Lupton, J. E. (2018). Mantle-derived helium and multiple methane sources in gas bubbles of cold seeps along the Cascadia Continental Margin. *Geochemistry, Geophysics, Geosystems*, 19(11), 4476–4486.
- Bayrakci, G., Scalabrin, C., Dupré, S., Leblond, I., Tary, J.-B., Lanteri, N., Augustin, J.-M., Berger, L., Cros, E., Ogor, A., *et al.* (2014). Acoustic monitoring of gas emissions from the seafloor. Part II: a case study from the Sea of Marmara. *Marine Geophysical Research*, 35(3), 211–229.
- Bellefleur, G., Riedel, M., and Brent, T. (2006). Seismic characterization and continuity analysis of gas-hydrate horizons near Mallik research wells, Mackenzie Delta, Canada. *The Leading Edge*, 25(5), 599–604.
- Bellefleur, M., Riedel, M., Huang, J., Saeki, T., Milkereit, B., Ramachandran, K., and Brent, T. (2012). Seismic characterization of gas hydrate accumulations in permafrost environment: lessons learned from Mallik, NWT, Canada. Geological Survey of Canada.



- Berndt, C., Chi, W.-C., Jegen, M., Lebas, E., Crutchley, G., Muff, S., Hölz, S., Sommer, M., Lin, S., Liu, C.-S., *et al.* (2019). Tectonic controls on gas hydrate distribution off SW Taiwan. *Journal of Geophysical Research: Solid Earth*, *124*(2), 1164–1184.
- Berndt, C., Feseker, T., Treude, T., Krastel, S., Liebetrau, V., Niemann, H., Bertics, V. J., Dumke, I., Dünnbier, K., Ferré, B., *et al.* (2014). Temporal constraints on hydrate-controlled methane seepage off Svalbard. *Science*, *343*(6168), 284–287.
- Biastoch, A., Treude, T., Rüpke, L. H., Riebesell, U., Roth, C., Burwicz, E. B., Park, W., Latif, M., Böning, C. W., Madec, G., *et al.* (2011). Rising Arctic Ocean temperatures cause gas hydrate destabilization and ocean acidification. *Geophysical Research Letters*, *38*(8).
- Biswas, R., Kumar, D., Sen, M., Paul, A., and Packer, K. (2019). Density inversion from seismic using a trans-dimensional approach: A field dataset example. In *SEG Technical Program Expanded Abstracts 2019*, 539–543. Society of Exploration Geophysicists.
- Boles, J., Clark, J., Leifer, I., and Washburn, L. (2001). Temporal variation in natural methane seep rate due to tides, Coal Oil Point area, California. *Journal of Geophysical Research: Oceans*, *106*(C11), 27077–27086.
- Bonini, M. (2019). Seismic loading of fault-controlled fluid seepage systems by great subduction earthquakes. *Scientific reports*, *9*(1), 1–12.
- Bosch, M., Mukerji, T., and Gonzalez, E. F. (2010). Seismic inversion for reservoir properties combining statistical rock physics and geostatistics: A review. *Geophysics*, *75*(5), 75A165–75A176.
- Boswell, R. and Collett, T. S. (2011). Current perspectives on gas hydrate resources. *Energy & environmental science*, *4*(4), 1206–1215.
- Boswell, R., Collett, T. S., Frye, M., Shedd, W., McConnell, D. R., and Shelander, D. (2012). Subsurface gas hydrates in the northern Gulf of Mexico. *Marine and Petroleum Geology*, *34*(1), 4–30.

- Boswell, R., Frye, M., Shelander, D., Shedd, W., McConnell, D. R., and Cook, A. (2012). Architecture of gas-hydrate-bearing sands from Walker Ridge 313, Green canyon 955, and Alaminos canyon 21: northern deepwater Gulf of Mexico. *Marine and Petroleum Geology*, *34*(1), 134–149.
- Boswell, R., Hancock, S., Yamamoto, K., Collett, T., Pratap, M., and Lee, S.-R. (2020). Natural Gas Hydrates: Status of Potential as an Energy Resource. *Future Energy*, 111–131.
- Boswell, R., Schoderbek, D., Collett, T. S., Ohtsuki, S., White, M., and Anderson, B. J. (2017). The Ignik Sikumi field experiment, Alaska north slope: design, operations, and implications for CO<sub>2</sub>–CH<sub>4</sub> exchange in gas hydrate reservoirs. *Energy & Fuels*, *31*(1), 140–153.
- Boswell, R., Shipp, C., Reichel, T., Shelander, D., Saeki, T., Frye, M., Shedd, W., Collett, T. S., and McConnell, D. R. (2016a). Prospecting for marine gas hydrate resources. *Interpretation*, *4*(1), SA13–SA24.
- Boswell, R., Shipp, C., Reichel, T., Shelander, D., Saeki, T., Frye, M., Shedd, W., Collett, T. S., and McConnell, D. R. (2016b). Prospecting for marine gas hydrate resources. *Interpretation*, *4*(1), SA13–SA24.
- Böttner, C., Haeckel, M., Schmidt, M., Berndt, C., Vielstädte, L., Kutsch, J. A., Karstens, J., and Weiß, T. (2020). Greenhouse gas emissions from marine decommissioned hydrocarbon wells: leakage detection, monitoring and mitigation strategies. *International Journal of Greenhouse Gas Control*, *100*, 103119.
- Buffett, B. and Archer, D. (2004). Global inventory of methane clathrate: Sensitivity to changes in the deep ocean. *Earth and Planetary Science Letters*, *227*(3-4), 185–199.
- Buland, A. and Omre, H. (2003). Bayesian linearized AVO inversion. *Geophysics*, *68*(1), 185–198.
- Bünz, S. and Mienert, J. (2004). Acoustic imaging of gas hydrate and free gas at the Storegga Slide. *Journal of Geophysical research: Solid earth*, *109*(B4).

- Castagna, J. P., Batzle, M. L., and Eastwood, R. L. (1985). Relationships between compressional-wave and shear-wave velocities in clastic silicate rocks. *geophysics*, 50(4), 571–581.
- Causse, E., Mittet, R., and Ursin, B. (1999). Preconditioning of full-waveform inversion in viscoacoustic media. *Geophysics*, 64(1), 130–145.
- Chand, S., Minshull, T. A., Gei, D., and Carcione, J. M. (2004). Elastic velocity models for gas-hydrate-bearing sediments—A comparison. *Geophysical Journal International*, 159(2), 573–590.
- Chatterjee, S., Bhatnagar, G., Dugan, B., Dickens, G. R., Chapman, W. G., and Hirasaki, G. J. (2014). The impact of lithologic heterogeneity and focused fluid flow upon gas hydrate distribution in marine sediments. *Journal of Geophysical Research: Solid Earth*, 119(9), 6705–6732.
- Chong, Z. R., Yang, S. H. B., Babu, P., Linga, P., and Li, X.-S. (2016). Review of natural gas hydrates as an energy resource: Prospects and challenges. *Applied energy*, 162, 1633–1652.
- Cichostępski, K., Dec, J., and Kwietniak, A. (2019). Relative amplitude preservation in high-resolution shallow reflection seismic: a case study from Fore-Sudetic Monocline, Poland. *Acta Geophysica*, 67(1), 77–94.
- Colbo, K., Ross, T., Brown, C., and Weber, T. (2014). A review of oceanographic applications of water column data from multibeam echosounders. *Estuarine, coastal and shelf science*, 145, 41–56.
- Colin, F., Ker, S., Riboulot, V., and Sultan, N. (2020). Irregular BSR: evidence of an ongoing reequilibrium of a gas hydrate system. *Geophysical Research Letters*, 47(20), e2020GL089906.
- Collett, T. S., Johnson, A., Knapp, C. C., Boswell, R., *et al.* (2010). *Natural Gas Hydrates: Energy Resource Potential and Associated Geologic Hazards*, AAPG Memoir 89, Volume 89. AAPG.

- Cook, A. E. and Malinverno, A. (2013). Short migration of methane into a gas hydrate-bearing sand layer at Walker Ridge, Gulf of Mexico. *Geochemistry, Geophysics, Geosystems*, *14*(2), 283–291.
- Cook, A. E. and Tost, B. C. (2014). Geophysical signatures for low porosity can mimic natural gas hydrate: An example from Alaminos Canyon, Gulf of Mexico. *Journal of Geophysical Research: Solid Earth*, *119*(10), 7458–7472.
- Cook, A. E. and Waite, W. F. (2018). Archie’s saturation exponent for natural gas hydrate in coarse-grained reservoirs. *Journal of Geophysical Research: Solid Earth*, *123*(3), 2069–2089.
- Cordes, E. E., Bergquist, D. C., Redding, M. L., and Fisher, C. R. (2007). Patterns of growth in cold-seep vestimentiferans including *Seepiophila jonesi*: a second species of long-lived tubeworm. *Marine Ecology*, *28*(1), 160–168.
- Crutchley, G., Fraser, D., Pecher, I., Gorman, A., Maslen, G., and Henrys, S. (2015). Gas migration into gas hydrate-bearing sediments on the southern Hikurangi margin of New Zealand. *Journal of Geophysical Research: Solid Earth*, *120*(2), 725–743.
- Crutchley, G., Gorman, A., Pecher, I., Toulmin, S., and Henrys, S. (2011). Geological controls on focused fluid flow through the gas hydrate stability zone on the southern Hikurangi Margin of New Zealand, evidenced from multi-channel seismic data. *Marine and Petroleum Geology*, *28*(10), 1915–1931.
- Crutchley, G., Mountjoy, J., Davy, B., Hillman, J., Watson, S., Stewart, L., Woelz, S., Kane, T., Gerring, P., Quinn, W., *et al.* (2018). Gas Hydrate Systems of the Southern Hikurangi Margin, Aotearoa, New Zealand. *TAN1808 Voyage Report, RV Tangaroa*.
- Crutchley, G. J., Gorman, A. R., and Fohrmann, M. (2007). Investigation of the role of gas hydrates in continental slope stability west of Fiordland, New Zealand. *New Zealand Journal of Geology and Geophysics*, *50*(4), 357–364.
- Crutchley, G. J., Klaeschen, D., Planert, L., Bialas, J., Berndt, C., Papenberg, C., Hensen, C., Hornbach, M., Krastel, S., and Brückmann, W. (2014). The impact of

- fluid advection on gas hydrate stability: Investigations at sites of methane seepage offshore Costa Rica. *Earth and Planetary Science Letters*, 401, 95–109.
- Crutchley, G. J., Kroeger, K. F., Pecher, I. A., and Gorman, A. R. (2019). How tectonic folding influences gas hydrate formation: New Zealand’s Hikurangi subduction margin. *Geology*, 47(1), 39–42.
- Crutchley, G. J., Mountjoy, J., Hillman, J., Turco, F., Watson, S., Flemings, P., Davy, B., Woelz, S., Gorman, A., and Bialas, J. (2021). Upward-doming zones of gas hydrate and free gas at the bases of gas chimneys, New Zealand’s Hikurangi margin. *Journal of Geophysical Research: Solid Earth*, e2020JB021489.
- Dai, J., Snyder, F., Gillespie, D., Koesoemadinata, A., and Dutta, N. (2008). Exploration for gas hydrates in the deepwater, northern Gulf of Mexico: Part I. A seismic approach based on geologic model, inversion, and rock physics principles. *Marine and Petroleum Geology*, 25(9), 830–844.
- Dai, J., Xu, H., Snyder, F., and Dutta, N. (2004a). Detection and estimation of gas hydrates using rock physics and seismic inversion: Examples from the northern deepwater Gulf of Mexico. *Leading Edge (Tulsa, OK)*, 23(1), 60–66.
- Dai, J., Xu, H., Snyder, F., and Dutta, N. (2004b). Detection and estimation of gas hydrates using rock physics and seismic inversion: Examples from the northern deepwater Gulf of Mexico. *The leading edge*, 23(1), 60–66.
- Dallimore, S. and Collett, T. (2005). Scientific results from the Mallik 2002 gas hydrate production research well program, Mackenzie Delta, Northwest Territories, Canada.
- De Robertis, A. and Higginbottom, I. (2007). A post-processing technique to estimate the signal-to-noise ratio and remove echosounder background noise. *ICES Journal of Marine Science*, 64(6), 1282–1291.
- Demer, D. A., Berger, L., Bernasconi, M., Bethke, E., Boswell, K., Chu, D., Domokos, R., Dunford, A., Fassler, S., Gauthier, S., *et al.* (2015). Calibration of acoustic instruments.

- Deutsch, C. V. and Journel, A. G. (1994). The application of simulated annealing to stochastic reservoir modeling. *SPE Advanced Technology Series*, 2(02), 222–227.
- Dickens, G. (2001). On the fate of past gas: What happens to methane released from a bacterially mediated gas hydrate capacitor? *Geochemistry, Geophysics, Geosystems*, 2(1).
- Dietrich, M. and Kormendi, F. (1990). Perturbation of the plane-wave reflectivity of a depth-dependent elastic medium by weak inhomogeneities. *Geophysical Journal International*, 100(2), 203–214.
- Dillon, W., Booth, J., Paul, C., Felhaber, K., Hutchibson, D., and Swift, B. (1991). Mapping sub-seafloor reservoirs of greenhouse gas: Methane hydrate. In *International symposium on marine positioning, proceedings. Marine Technology Society, Washington, DC*, 545–554.
- Doyen, P. (2007). *Seismic reservoir characterization: An earth modelling perspective*, Volume 2. EAGE publications Houten.
- Doyen, P. M. (1988). Porosity from seismic data: A geostatistical approach. *Geophysics*, 53(10), 1263–1275.
- Duarte, H., Pinheiro, L. M., Teixeira, F. C., and Monteiro, J. H. (2007). High-resolution seismic imaging of gas accumulations and seepage in the sediments of the Ria de Aveiro barrier lagoon (Portugal). *Geo-Marine Letters*, 27(2), 115–126.
- Dubreuil-Boisclair, C., Gloaguen, E., Bellefleur, G., and Marcotte, D. (2012). Non-Gaussian gas hydrate grade simulation at the Mallik site, Mackenzie Delta, Canada. *Marine and Petroleum Geology*, 35(1), 20–27.
- Dupré, S., Scalabrin, C., Grall, C., Augustin, J.-M., Henry, P., Şengör, A. C., Görür, N., Çağatay, M. N., and Géli, L. (2015). Tectonic and sedimentary controls on widespread gas emissions in the Sea of Marmara: Results from systematic, shipborne multibeam echo sounder water column imaging. *Journal of Geophysical Research: Solid Earth*, 120(5), 2891–2912.

- Dvorkin, J., Gutierrez, M. A., and Grana, D. (2014). *Seismic reflections of rock properties*. Cambridge University Press.
- Dvorkin, J., Helgerud, M. B., Waite, W. F., Kirby, S. H., and Nur, A. (2000). Introduction to physical properties and elasticity models. In *Natural Gas Hydrate*, 245–260. Springer.
- Dvorkin, J. and Nur, A. (2002). Critical-porosity models. *Memoirs-American Association of Petroleum Geologists*, 33–42.
- Dvorkin, J. and Uden, R. (2004). Seismic wave attenuation in a methane hydrate reservoir. *The Leading Edge*, 23(8), 730–732.
- Dvorkin, J. and Wollner, U. (2017). Rock-physics transforms and scale of investigation. *Geophysics*, 82(3), MR75–MR88.
- Dziewonski, A. M. and Anderson, D. L. (1984). Seismic Tomography of the Earth’s Interior: The first three-dimensional models of the earth’s structure promise to answer some basic questions of geodynamics and signify a revolution in earth science. *American Scientist*, 72(5), 483–494.
- Ecker, C., Dvorkin, J., and Nur, A. (2005). Estimating the amount of hydrate and free gas from surface seismic. , 65(2), 566–569.
- Ely, G., Malcolm, A., and Poliannikov, O. V. (2018). Assessing uncertainties in velocity models and images with a fast nonlinear uncertainty quantification method. *Geophysics*, 83(2), R63–R75.
- Fang, H., Shi, K., and Yu, Y. (2020). Geomechanical constitutive modelling of gas hydrate-bearing sediments by a state-dependent multishear bounding surface model. *Journal of Natural Gas Science and Engineering*, 75, 103119.
- Farahani, M. V., Hassanpouryouzband, A., Yang, J., and Tohidi, B. (2021). Insights into the climate-driven evolution of gas hydrate-bearing permafrost sediments: implications for prediction of environmental impacts and security of energy in cold regions. *RSC Advances*, 11(24), 14334–14346.

- Faure, K., Greinert, J., von Deimling, J. S., McGinnis, D. F., Kipfer, R., and Linke, P. (2010). Methane seepage along the Hikurangi Margin of New Zealand: Geochemical and physical data from the water column, sea surface and atmosphere. *Marine Geology*, 272(1-4), 170–188.
- Ferré, B., Jansson, P. G., Moser, M., Serov, P., Portnov, A., Graves, C. A., Panieri, G., Gründger, F., Berndt, C., Lehmann, M. F., *et al.* (2020). Reduced methane seepage from Arctic sediments during cold bottom-water conditions. *Nature Geoscience*, 13(2), 144–148.
- Feseker, T., Boetius, A., Wenzhöfer, F., Blandin, J., Olu, K., Yoeger, D., Camilli, R., German, C., and De Beer, D. (2014). Eruption of a deep-sea mud volcano triggers rapid sediment movement, *Nat.*
- Fisher, C., Urcuyo, I., Simpkins, M., and Nix, E. (1997). Life in the slow lane: growth and longevity of cold-seep vestimentiferans. *Marine Ecology*, 18(1), 83–94.
- Fohrmann, M. and Pecher, I. (2012). Analysing sand-dominated channel systems for potential gas-hydrate-reservoirs using an AVO seismic inversion technique on the Southern Hikurangi Margin, New Zealand. *Marine and Petroleum Geology*, 38(1), 19–34.
- Foucher, J.-P., Nouzé, H., and Henry, P. (2002). Observation and tentative interpretation of a double BSR on the Nankai slope. *Marine Geology*, 187(1-2), 161–175.
- Franek, P., Plaza-Faverola, A., Mienert, J., Buenz, S., Ferré, B., and Hubbard, A. (2017). Microseismicity linked to gas migration and leakage on the Western Svalbard Shelf. *Geochemistry, Geophysics, Geosystems*, 18(12), 4623–4645.
- Fraser, D. R., Gorman, A. R., Pecher, I. A., Crutchley, G. J., and Henrys, S. A. (2016). Gas hydrate accumulations related to focused fluid flow in the Pegasus Basin, southern Hikurangi Margin, New Zealand. *Marine and Petroleum Geology*, 77, 399–408.



- Frye, M., Shedd, W., and Boswell, R. (2012a). Gas hydrate resource potential in the Terrebonne Basin, Northern Gulf of Mexico. *Marine and Petroleum Geology*, *34*(1), 150–168.
- Frye, M., Shedd, W., and Boswell, R. (2012b). Gas hydrate resource potential in the Terrebonne Basin, Northern Gulf of Mexico. *Marine and Petroleum geology*, *34*(1), 150–168.
- Fujii, T., Suzuki, K., Takayama, T., Tamaki, M., Komatsu, Y., Konno, Y., Yoneda, J., Yamamoto, K., and Nagao, J. (2015). Geological setting and characterization of a methane hydrate reservoir distributed at the first offshore production test site on the Daini-Atsumi Knoll in the eastern Nankai Trough, Japan. *Marine and Petroleum Geology*, *66*, 310–322.
- Gail, W., Hope, C., and Wadhams, P. (2013). Climate Science: Vast Costs of Arctic Change. *Nature*, *499*(7459), 401–03.
- Garcia-Tigreros, F., Leonte, M., Ruppel, C. D., Ruiz-Angulo, A., Joung, D. J., Young, B., and Kessler, J. D. (2021). Estimating the impact of seep methane oxidation on ocean pH and dissolved inorganic radiocarbon along the US mid-Atlantic Bight. *Journal of Geophysical Research: Biogeosciences*, *126*(1), e2019JG005621.
- Gassner, L., Gerach, T., Hertweck, T., and Bohlen, T. (2019). Seismic characterization of submarine gas-hydrate deposits in the Western Black Sea by acoustic full-waveform inversion of ocean-bottom seismic data. *Geophysics*, *84*(5), B311–B324.
- Gehrmann, R. A. S., Schwalenberg, K., Hölz, S., Zander, T., Dettmer, J., and Bialas, J. (2016). Controlled source electromagnetic data analysis with seismic constraints and rigorous uncertainty estimation in the Black Sea. In *AGU Fall Meeting Abstracts*, Volume 2016, GP42A–06.
- Geletti, R. and Busetti, M. (2011). A double bottom simulating reflector in the western Ross Sea, Antarctica. *Journal of Geophysical Research: Solid Earth*, *116*(B4).

- Gorman, A. R., Holbrook, W. S., Hornbach, M. J., Hackwith, K. L., Lizarralde, D., and Pecher, I. (2002). Migration of methane gas through the hydrate stability zone in a low-flux hydrate province. *Geology*, *30*(4), 327–330.
- Grana, D. (2016). Bayesian linearized rock-physics inversion. *Geophysics*, *81*(6), D625–D641.
- Grana, D. and Della Rossa, E. (2010). Probabilistic petrophysical-properties estimation integrating statistical rock physics with seismic inversion. *Geophysics*, *75*(3), O21–O37.
- Granin, N., Aslamov, I., Kozlov, V., Makarov, M., Kirillin, G., McGinnis, D., Kucher, K., Blinov, V., Ivanov, V., Mizandroutsev, I., *et al.* (2019). Methane hydrate emergence from Lake Baikal: direct observations, modelling, and hydrate footprints in seasonal ice cover. *Scientific reports*, *9*(1), 1–10.
- Granin, N. G., Makarov, M. M., Kucher, K. M., and Gnatovsky, R. Y. (2010). Gas seeps in Lake Baikal—detection, distribution, and implications for water column mixing. *Geo-Marine Letters*, *30*(3-4), 399–409.
- Greinert, J., Bohrmann, G., and Suess, E. (2001). Gas hydrate-associated carbonates and methane-venting at Hydrate Ridge: classification, distribution and origin of authigenic lithologies. *Geophysical Monograph-American Geophysical Union*, *124*, 99–114.
- Greinert, J., Lewis, K., Bialas, J., Pecher, I. A., Rowden, A., Bowden, D., De Batist, M., and Linke, P. (2010). Methane seepage along the Hikurangi Margin, New Zealand: Overview of studies in 2006 and 2007 and new evidence from visual, bathymetric and hydroacoustic investigations. *Marine Geology*, *272*(1-4), 6–25.
- Greinert, J., McGinnis, D. F., Naudts, L., Linke, P., and De Batist, M. (2010). Atmospheric methane flux from bubbling seeps: Spatially extrapolated quantification from a Black Sea shelf area. *Journal of Geophysical Research: Oceans*, *115*(C1).

- Grupe, B. M., Krach, M. L., Pasulka, A. L., Maloney, J. M., Levin, L. A., and Frieder, C. A. (2015). Methane seep ecosystem functions and services from a recently discovered southern California seep. *Marine Ecology*, *36*, 91–108.
- Haines, S. S., Hart, P. E., Collett, T. S., Shedd, W., Frye, M., Weimer, P., and Boswell, R. (2017). High-resolution seismic characterization of the gas and gas hydrate system at Green Canyon 955, Gulf of Mexico, USA. *Marine and Petroleum Geology*, *82*, 220–237.
- Hamilton, E. L. (1978). Sound velocity–density relations in sea-floor sediments and rocks. *The journal of the Acoustical Society of America*, *63*(2), 366–377.
- Han, S., Bangs, N. L., Hornbach, M. J., Pecher, I. A., Tobin, H. J., and Silver, E. A. (2021). The many double BSRs across the northern Hikurangi margin and their implications for subduction processes. *Earth and Planetary Science Letters*, *558*, 116743.
- Helgerud, M. B., Dvorkin, J., and Nur, A. (2000). Rock physics characterization for gas hydrate reservoirs: Elastic properties. *Annals of the New York Academy of Sciences*, *912*(1), 116–125.
- Helgerud, M. B., Dvorkin, J., Nur, A., Sakai, A., and Collett, T. (1999). Elastic-wave velocity in marine sediments with gas hydrates: Effective medium modeling. *Geophysical Research Letters*, *26*(13), 2021–2024.
- Henry, S. A., Ellis, S., and Uruski, C. (2003). Conductive heat flow variations from bottom-simulating reflectors on the Hikurangi margin, New Zealand. *Geophysical Research Letters*, *30*(2).
- Higgs, B., Mountjoy, J., Crutchley, G. J., Townend, J., Ladroit, Y., Greinert, J., and McGovern, C. (2019). Seep-bubble characteristics and gas flow rates from a shallow-water, high-density seep field on the shelf-to-slope transition of the Hikurangi subduction margin. *Marine Geology*, *417*, 105985.

- Hillman, J. I., Cook, A. E., Daigle, H., Nole, M., Malinverno, A., Meazell, K., and Flemings, P. B. (2017). Gas hydrate reservoirs and gas migration mechanisms in the Terrebonne Basin, Gulf of Mexico. *Marine and Petroleum Geology*, *86*, 1357–1373.
- Hillman, J. I., Crutchley, G. J., and Kroeger, K. F. (2020). Investigating the role of faults in fluid migration and gas hydrate formation along the southern Hikurangi Margin, New Zealand. *Marine Geophysical Research*, *41*(1), 1–19.
- Hoffmann, J. J., Gorman, A. R., and Crutchley, G. J. (2019). Seismic evidence for repeated vertical fluid flow through polygonally faulted strata in the Canterbury Basin, New Zealand. *Marine and Petroleum Geology*, *109*, 317–329.
- Holland, M., Schultheiss, P., Roberts, J., and Druce, M. (2008). Observed gas hydrate morphologies in marine sediments. In *6th International Conference on Gas Hydrates, Chevron, Vancouver, BC, Canada*, 6–10.
- Hornafius, J. S., Quigley, D., and Luyendyk, B. P. (1999). The world’s most spectacular marine hydrocarbon seeps (Coal Oil Point, Santa Barbara Channel, California): Quantification of emissions. *Journal of Geophysical Research: Oceans*, *104*(C9), 20703–20711.
- Horta, A. and Soares, A. (2010). Direct sequential co-simulation with joint probability distributions. *Mathematical Geosciences*, *42*(3), 269–292.
- Hyndman, R. and Spence, G. (1992). A seismic study of methane hydrate marine bottom simulating reflectors. *Journal of Geophysical Research: Solid Earth*, *97*(B5), 6683–6698.
- Johnson, A. H. and Max, M. D. (2006). The path to commercial hydrate gas production. *The Leading Edge*, *25*(5), 648–651.
- Johnson, H. P., Miller, U. K., Salmi, M. S., and Solomon, E. A. (2015). Analysis of bubble plume distributions to evaluate methane hydrate decomposition on the continental slope. *Geochemistry, Geophysics, Geosystems*, *16*(11), 3825–3839.

- Jones, A. T., Greinert, J., Bowden, D., Klaucke, I., Petersen, C. J., Netzeband, G., and Weinrebe, W. (2010). Acoustic and visual characterisation of methane-rich seabed seeps at Omakere Ridge on the Hikurangi Margin, New Zealand. *Marine Geology*, 272(1-4), 154–169.
- Joshi, A. K., Sain, K., and Pandey, L. (2019). Gas hydrate saturation and reservoir characterization at sites NGHP-02-17 and NGHP-02-19, Krishna Godavari Basin, eastern margin of India. *Marine and Petroleum Geology*, 108, 595–608.
- Judd, A. and Hovland, M. (1992). The evidence of shallow gas in marine sediments. *Continental Shelf Research*, 12(10), 1081–1095.
- Judd, A. and Hovland, M. (2009). *Seabed fluid flow: the impact on geology, biology and the marine environment*. Cambridge University Press.
- Judd, A. G. (2004). Natural seabed gas seeps as sources of atmospheric methane. *Environmental Geology*, 46(8), 988–996.
- Kannberg, P. and Constable, S. (2020). Characterization and quantification of gas hydrates in the California Borderlands. *Geophysical Research Letters*, 47(6), no–no.
- Katz, H.-R. (1981). Probable gas hydrate in continental slope east of the North Island, New Zealand. *Journal of Petroleum Geology*, 3(3), 315–324.
- Kennett, B. and Kerry, N. (1979). Seismic waves in a stratified half space. *Geophysical Journal International*, 57(3), 557–583.
- Kennett, J. P., Cannariato, K. G., Hendy, I. L., and Behl, R. J. (2003). Methane hydrates in quaternary climate change: The clathrate gun hypothesis. *Methane hydrates in quaternary climate change: the clathrate gun hypothesis*, 54, 1–9.
- Kessler, J. D., Valentine, D. L., Redmond, M. C., Du, M., Chan, E. W., Mendes, S. D., Quiroz, E. W., Villanueva, C. J., Shusta, S. S., Werra, L. M., *et al.* (2011). A persistent oxygen anomaly reveals the fate of spilled methane in the deep Gulf of Mexico. *Science*, 331(6015), 312–315.

- Ketzer, M., Praeg, D., Rodrigues, L. F., Augustin, A., Pivel, M. A., Rahmati-Abkenar, M., Miller, D. J., Viana, A. R., and Cupertino, J. A. (2020). Gas hydrate dissociation linked to contemporary ocean warming in the southern hemisphere. *Nature communications*, *11*(1), 1–9.
- Kim, Y.-J., Cheong, S., Chun, J.-H., Cukur, D., Kim, S.-P., Kim, J.-K., and Kim, B.-Y. (2020). Identification of shallow gas by seismic data and AVO processing: Example from the southwestern continental shelf of the Ulleung Basin, East Sea, Korea. *Marine and Petroleum Geology*, *117*, 104346.
- Klaucke, I., Berndt, C., Crutchley, G., Chi, W.-C., Lin, S., and Muff, S. (2016). Fluid venting and seepage at accretionary ridges: the Four Way Closure Ridge offshore SW Taiwan. *Geo-Marine Letters*, *36*(3), 165–174.
- Konno, Y., Fujii, T., Sato, A., Akamine, K., Naiki, M., Masuda, Y., Yamamoto, K., and Nagao, J. (2017). Key findings of the world’s first offshore methane hydrate production test off the coast of Japan: Toward future commercial production. *Energy & Fuels*, *31*(3), 2607–2616.
- Korenaga, J., Holbrook, W., Singh, S., and Minshull, T. (1997). Natural gas hydrates on the southeast US margin: Constraints from full waveform and travel time inversions of wide-angle seismic data. *Journal of Geophysical Research: Solid Earth*, *102*(B7), 15345–15365.
- Kormendi, F. and Dietrich, M. (1991). Nonlinear waveform inversion of plane-wave seismograms in stratified elastic media. *Geophysics*, *56*(5), 664–674.
- Krabbenhoft, A., Bialas, J., Klaucke, I., Crutchley, G., Papenberg, C., and Netzeband, G. L. (2013). Patterns of subsurface fluid-flow at cold seeps: The Hikurangi Margin, offshore New Zealand. *Marine and Petroleum Geology*, *39*(1), 59–73.
- Kretschmer, K., Biastoch, A., Rüpke, L., and Burwicz, E. (2015). Modeling the fate of methane hydrates under global warming. *Global Biogeochemical Cycles*, *29*(5), 610–625.

- Krey, V., Canadell, J. G., Nakicenovic, N., Abe, Y., Andrulleit, H., Archer, D., Grubler, A., Hamilton, N. T., Johnson, A., Kostov, V., *et al.* (2009). Gas hydrates: entrance to a methane age or climate threat? *Environmental Research Letters*, *4*(3), 034007.
- Kroeger, K., Crutchley, G., Hill, M., and Pecher, I. (2017). Potential for gas hydrate formation at the northwest New Zealand shelf margin—New insights from seismic reflection data and petroleum systems modelling. *Marine and Petroleum Geology*, *83*, 215–230.
- Kroeger, K., Crutchley, G. J., Kellett, R., and Barnes, P. (2019). A 3-D Model of Gas Generation, Migration, and Gas Hydrate Formation at a Young Convergent Margin (Hikurangi Margin, New Zealand). *Geochemistry, Geophysics, Geosystems*, *20*(11), 5126–5147.
- Kroeger, K., Plaza-Faverola, A., Barnes, P., and Pecher, I. (2015). Thermal evolution of the New Zealand Hikurangi subduction margin: Impact on natural gas generation and methane hydrate formation—A model study. *Marine and Petroleum Geology*, *63*, 97–114.
- Kvenvolden, K. A. (1988). Methane hydrates and global climate. *Global biogeochemical cycles*, *2*(3), 221–229.
- Kvenvolden, K. A. (1993). Gas hydrates—geological perspective and global change. *Reviews of geophysics*, *31*(2), 173–187.
- Ladroit, Y., Escobar-Flores, P. C., Schimel, A. C., and O’Driscoll, R. L. (2020). ESP3: An open-source software for the quantitative processing of hydro-acoustic data. *SoftwareX*, *12*, 100581.
- Laurion, I., Vincent, W. F., MacIntyre, S., Retamal, L., Dupont, C., Francus, P., and Pienitz, R. (2010). Variability in greenhouse gas emissions from permafrost thaw ponds. *Limnology and Oceanography*, *55*(1), 115–133.
- Leblond, I., Scalabrin, C., and Berger, L. (2014). Acoustic monitoring of gas emissions from the seafloor. Part I: quantifying the volumetric flow of bubbles. *Marine Geophysical Research*, *35*(3), 191–210.

- Lee, G. H., Bo, Y. Y., Yoo, D. G., Ryu, B. J., and Kim, H. J. (2013). Estimation of the gas-hydrate resource volume in a small area of the Ulleung Basin, East Sea using seismic inversion and multi-attribute transform techniques. *Marine and petroleum geology*, 47, 291–302.
- Lee, J., Francisca, F. M., Santamarina, J. C., and Ruppel, C. (2010). Parametric study of the physical properties of hydrate-bearing sand, silt, and clay sediments: 2. Small-strain mechanical properties. *Journal of Geophysical Research: Solid Earth*, 115(B11).
- Lee, M., Collett, T., and Lewis, K. (2012). Anisotropic models to account for large borehole washouts to estimate gas hydrate saturations in the Gulf of Mexico Gas Hydrate Joint Industry Project Leg II Alaminos Canyon 21 B well. *Marine and Petroleum Geology*, 34(1), 85–95.
- Lee, M., Hutchinson, D., Collett, T., and Dillon, W. P. (1996). Seismic velocities for hydrate-bearing sediments using weighted equation. *Journal of Geophysical Research: Solid Earth*, 101(B9), 20347–20358.
- Lee, M. W. and Collett, T. S. (2001). *Gas hydrate estimation error associated with uncertainties of measurements and parameters*. US Department of the Interior, US Geological Survey.
- Lee, M. W. and Collett, T. S. (2005). *Controls on the physical properties of gas-hydrate-bearing sediments because of the interaction between gas hydrate and porous media*. US Department of the Interior, US Geological Survey.
- Lee, M. W. and Dillon, W. P. (2001). Amplitude blanking related to the pore-filling of gas hydrate in sediments. *Marine Geophysical Researches*, 22(2), 101–109.
- Legrand, D., Iglesias, A., Singh, S., Cruz-Atienza, V., Yoon, C., Dominguez, L., Valenzuela, R., Suárez, G., and Castro-Artola, O. (2021). The influence of fluids in the unusually high-rate seismicity in the Ometepep segment of the Mexican subduction zone. *Geophysical Journal International*, 226(1), 524–535.



- Leifer, I. and Patro, R. K. (2002). The bubble mechanism for methane transport from the shallow sea bed to the surface: A review and sensitivity study. *Continental Shelf Research*, 22(16), 2409–2428.
- Levin, L. A., Baco, A. R., Bowden, D. A., Colaco, A., Cordes, E. E., Cunha, M. R., Demopoulos, A. W., Gobin, J., Grupe, B. M., Le, J., *et al.* (2016). Hydrothermal vents and methane seeps: rethinking the sphere of influence. *Frontiers in Marine Science*, 3, 72.
- Lewis, K. B., Collot, J.-Y., and Lallemand, S. E. (1998). The dammed Hikurangi Trough: a channel-fed trench blocked by subducting seamounts and their wake avalanches (New Zealand–France GeodyNZ Project). *Basin Research*, 10(4), 441–468.
- Li, J., Roche, B., Bull, J. M., White, P. R., Leighton, T. G., Provenzano, G., Dewar, M., and Henstock, T. J. (2020). Broadband acoustic inversion for gas flux quantification—Application to a methane plume at Scanner Pockmark, central North Sea. *Journal of Geophysical Research: Oceans*, 125(9), e2020JC016360.
- Li, J.-f., Ye, J.-l., Qin, X.-w., Qiu, H.-j., Wu, N.-y., Lu, H.-l., Xie, W.-w., Lu, J.-a., Peng, F., Xu, Z.-q., *et al.* (2018). The first offshore natural gas hydrate production test in South China Sea. *China Geology*, 1(1), 5–16.
- Liebetrau, V., Eisenhauer, A., and Linke, P. (2010). Cold seep carbonates and associated cold-water corals at the Hikurangi Margin, New Zealand: new insights into fluid pathways, growth structures and geochronology. *Marine Geology*, 272(1-4), 307–318.
- Liu, J., Zhang, J., Ma, F., Wang, M., and Sun, Y. (2017). Estimation of seismic velocities and gas hydrate concentrations: a case study from the Shenhu area, northern South China Sea. *Marine and Petroleum Geology*, 88, 225–234.
- Liu, T. and Liu, X. (2018). Identifying the morphologies of gas hydrate distribution using P-wave velocity and density: a test from the GMGS2 expedition in the South China Sea. *Journal of Geophysics and Engineering*, 15(3), 1008–1022.

- Liu, T., Liu, X., and Zhu, T. (2020). Joint analysis of P-wave velocity and resistivity for morphology identification and quantification of gas hydrate. *Marine and Petroleum Geology*, *112*, 104036.
- Liu, X. and Flemings, P. B. (2006). Passing gas through the hydrate stability zone at southern Hydrate Ridge, offshore Oregon. *Earth and Planetary Science Letters*, *241*(1-2), 211–226.
- Lu, Z., Zhu, Y., Zhang, Y., Wen, H., Li, Y., and Liu, C. (2011). Gas hydrate occurrences in the Qilian Mountain permafrost, Qinghai province, China. *Cold Regions Science and Technology*, *66*(2-3), 93–104.
- MacLennan, D. N., Fernandes, P. G., and Dalen, J. (2002). A consistent approach to definitions and symbols in fisheries acoustics. *ICES Journal of Marine Science*, *59*(2), 365–369.
- Makogon, Y. (1966). Features of natural gas fields' exploitation in permafrost zone. *Gazovaya Promyshlennost*, *9*, 1–17.
- Makogon, Y. and Omelchenko, R. (2013). Commercial gas production from Messoyakha deposit in hydrate conditions. *Journal of Natural Gas Science and Engineering*, *11*, 1–6.
- Makogon, Y. F., Holditch, S. A., and Makogon, T. Y. (2007). Natural gas-hydrates - A potential energy source for the 21st Century. *Journal of Petroleum Science and Engineering*, *56*(1-3), 14–31.
- Malinverno, A. (2010). Marine gas hydrates in thin sand layers that soak up microbial methane. *Earth and Planetary Science Letters*, *292*(3-4), 399–408.
- Mascarelli, A. (2009). A sleeping giant? *Nature Climate Change*, *1*(904), 46–49.
- Maslin, M., Owen, M., Day, S., and Long, D. (2004). Linking continental-slope failures and climate change: Testing the clathrate gun hypothesis. *Geology*, *32*(1), 53–56.
- Mavko, G., Mukerji, T., and Dvorkin, J. (2020). *The rock physics handbook*. Cambridge university press.

- McGinnis, D. F., Greinert, J., Artemov, Y., Beaubien, S., and Wüest, A. (2006). Fate of rising methane bubbles in stratified waters: How much methane reaches the atmosphere? *Journal of Geophysical Research: Oceans*, *111*(C9).
- Meldahl, P., Heggland, R., Bril, B., and de Groot, P. (2001). Identifying faults and gas chimneys using multiattributes and neural networks. *The leading edge*, *20*(5), 474–482.
- Merewether, R., Olsson, M. S., and Lonsdale, P. (1985). Acoustically detected hydrocarbon plumes rising from 2-km depths in Guaymas Basin, Gulf of California. *Journal of Geophysical Research: Solid Earth*, *90*(B4), 3075–3085.
- Messud, J., Reinier, M., Prigent, H., Guillaume, P., Coléou, T., and Masclet, S. (2017). Extracting seismic uncertainties from tomographic velocity inversion and their use in reservoir risk analysis. *The Leading Edge*, *36*(2), 127–132.
- Mestdagh, T., Poort, J., and De Batist, M. (2017). The sensitivity of gas hydrate reservoirs to climate change: Perspectives from a new combined model for permafrost-related and marine settings. *Earth-science reviews*, *169*, 104–131.
- Mienert, J., Vanneste, M., Bünz, S., Andreassen, K., Hafliðason, H., and Sejrup, H. P. (2005). Ocean warming and gas hydrate stability on the mid-Norwegian margin at the Storegga Slide. *Marine and Petroleum Geology*, *22*(1-2 SPEC. ISS.), 233–244.
- Milkov, A. V. (2004). Global estimates of hydrate-bound gas in marine sediments: how much is really out there? *Earth-science reviews*, *66*(3-4), 183–197.
- Milkov, A. V. (2005). Molecular and stable isotope compositions of natural gas hydrates: A revised global dataset and basic interpretations in the context of geological settings. *Organic geochemistry*, *36*(5), 681–702.
- Minshull, T. A., Singh, S. C., and Westbrook, G. (1994). Seismic velocity structure at a gas hydrate reflector, offshore western Colombia, from full waveform inversion. *Journal of Geophysical Research: Solid Earth*, *99*(B3), 4715–4734.

- Moyano, B., Jensen, E. H., and Johansen, T. A. (2011). Improved quantitative calibration of rock physics models. *Petroleum Geoscience*, 17(4), 345–354.
- Mukerji, T., Avseth, P., Mavko, G., Takahashi, I., and González, E. F. (2001). Statistical rock physics: Combining rock physics, information theory, and geostatistics to reduce uncertainty in seismic reservoir characterization. *The Leading Edge*, 20(3), 313–319.
- Nakicenovic, N., Gritsevskii, A., Grubler, A., and Riahi, K. (2000). Global Natural Gas Perspectives.
- Naudts, L., Greinert, J., Poort, J., Belza, J., Vangampelaere, E., Boone, D., Linke, P., Henriët, J.-P., and De Batist, M. (2010). Active venting sites on the gas-hydrate-bearing Hikurangi Margin, off New Zealand: Diffusive-versus bubble-released methane. *Marine Geology*, 272(1-4), 233–250.
- Nikolovska, A., Sahling, H., and Bohrmann, G. (2008). Hydroacoustic methodology for detection, localization, and quantification of gas bubbles rising from the seafloor at gas seeps from the eastern Black Sea. *Geochemistry, Geophysics, Geosystems*, 9(10).
- Nole, M., Daigle, H., Cook, A. E., and Malinverno, A. (2016). Short-range, overpressure-driven methane migration in coarse-grained gas hydrate reservoirs. *Geophysical Research Letters*, 43(18), 9500–9508.
- Nouzé, H., Henry, P., Noble, M., Martin, V., and Pascal, G. (2004). Large gas hydrate accumulations on the eastern Nankai Trough inferred from new high-resolution 2-D seismic data. *Geophysical Research Letters*, 31(13).
- Nur, A., Mavko, G., Dvorkin, J., and Galmudi, D. (1998). Critical porosity: A key to relating physical properties to porosity in rocks. *The Leading Edge*, 17(3), 357–362.
- O'Connor, F. M., Boucher, O., Gedney, N., Jones, C., Folberth, G., Coppel, R., Friedlingstein, P., Collins, W., Chappellaz, J., Ridley, J., *et al.* (2010). Possible role of wetlands, permafrost, and methane hydrates in the methane cycle under future climate change: A review. *Reviews of Geophysics*, 48(4).

- Osypov, K., Yang, Y., Fournier, A., Ivanova, N., Bachrach, R., Yarman, C. E., You, Y., Nichols, D., and Woodward, M. (2013). Model-uncertainty quantification in seismic tomography: method and applications. *Geophysical Prospecting*, 61(6-Challenges of Seismic Imaging and Inversion Devoted to Goldin), 1114–1134.
- Paganoni, M., Cartwright, J., Foschi, M., Shipp, R., and Van Rensbergen, P. (2016). Structure II gas hydrates found below the bottom-simulating reflector. *Geophysical Research Letters*, 43(11), 5696–5706.
- Pan, H., Li, H., Chen, J., Zhang, Y., Liu, X., Cai, S., and Cao, C. (2019). Evaluation of gas hydrate resources using hydrate morphology-dependent rock physics templates. *Journal of Petroleum Science and Engineering*, 182, 106268.
- Pan, H., Li, H., Grana, D., Zhang, Y., Liu, T., and Geng, C. (2019). Quantitative characterization of gas hydrate bearing sediment using elastic-electrical rock physics models. *Marine and Petroleum Geology*, 105, 273–283.
- Pandey, L., Sain, K., and Joshi, A. K. (2019). Estimate of gas hydrate saturations in the Krishna-Godavari basin, eastern continental margin of India, results of expedition NGHP-02. *Marine and Petroleum Geology*, 108, 581–594.
- Paull, C., Caress, D., Thomas, H., Lundsten, E., Anderson, K., Gwiazda, R., Riedel, M., McGann, M., and Herguera, J. (2015). Seafloor geomorphic manifestations of gas venting and shallow subbottom gas hydrate occurrences. *Geosphere*, 11(2), 491–513.
- Pecher, I., Barnes, P., and LeVay, L. (2019). Creeping gas hydrate slides. *Proceedings of the International Ocean Discovery Program*, 372.
- Pecher, I., Ogebule, O., and Nwanememma, O. (2011). Possible gas hydrates in the Northland and Taranaki Basins, New Zealand-Evidence from seismic data: High-resolution processing and AVO analysis. In *Proc. 7th International Conference on Gas Hydrates, Edinburgh*.
- Pecher, I. A. (2011). GAS HYDRATES IN NEW ZEALAND—A Large RESOURCE FOR A SMALL COUNTRY? *Natural Gas & Oil*, 304, 285–4541.

- Pecher, I. A., Barnes, P. M., LeVay, L. J., Bourlange, S. M., Brunet, M. M., Cardona, S., Clennell, M. B., Cook, A. E., Dugan, B., Elger, J., *et al.* (2018). International ocean discovery program expedition 372 preliminary report: Creeping gas hydrate slides and Hikurangi LWD.
- Pecher, I. A. and Henrys, S. (2003). *Potential gas reserves in gas hydrate sweet spots on the Hikurangi margin, New Zealand*. Institute of Geological & Nuclear Sciences.
- Pecher, I. A., Henrys, S. A., Wood, W. T., Kukowski, N., Crutchley, G. J., Fohrmann, M., Kilner, J., Senger, K., Gorman, A. R., Coffin, R. B., *et al.* (2010). Focussed fluid flow on the Hikurangi Margin, New Zealand—Evidence from possible local upwarping of the base of gas hydrate stability. *Marine Geology*, 272(1-4), 99–113.
- Pecher, I. A., Henrys, S. A., Wood, W. T., Kukowski, N., Crutchley, G. J., Fohrmann, M., Kilner, J., Senger, K., Gorman, A. R., Coffin, R. B., Greinert, J., and Faure, K. (2010). Focussed fluid flow on the Hikurangi Margin, New Zealand — Evidence from possible local upwarping of the base of gas hydrate stability. *Marine Geology*, 272(1), 99–113. Methane seeps at the Hikurangi Margin, New Zealand.
- Pecher, I. A., Minshull, T. A., Singh, S. C., and von Huene, R. (1996). Velocity structure of a bottom simulating reflector offshore Peru: Results from full waveform inversion. *Earth and Planetary Science Letters*, 139(3-4), 459–469.
- Pecher, I. A., Oluwunmi, P., Djeflal, A., Bangs, N. L., Crutchley, G. J., Mountjoy, J. J., Villinger, H. W., Barnes, P., Heeschen, K. U., Dugan, B., *et al.* (2018). Response of Gas Hydrate Systems to Subduction-Zone Processes on the Northern Hikurangi Margin, New Zealand. In *AGU Fall Meeting Abstracts*, Volume 2018, T54C–08.
- Pecher, I. A., Ranero, C. R., Von Huene, R., Minshull, T. A., and Singh, S. C. (1998). The nature and distribution of bottom simulating reflectors at the Costa Rican convergent margin. *Geophysical Journal International*, 133(2), 219–229.
- Pereira, P., Azevedo, L., Nunes, R., and Soares, A. (2019). The impact of a priori elastic models into iterative geostatistical seismic inversion. *Journal of Applied Geophysics*, 170, 103850.

- Petersen, C. J., Bünz, S., Hustoft, S., Mienert, J., and Klaeschen, D. (2010). High-resolution P-Cable 3D seismic imaging of gas chimney structures in gas hydrated sediments of an Arctic sediment drift. *Marine and Petroleum Geology*, *27*(9), 1981–1994.
- Pohlman, J. W., Bauer, J. E., Waite, W. F., Osburn, C. L., and Chapman, N. R. (2011). Methane hydrate-bearing seeps as a source of aged dissolved organic carbon to the oceans. *Nature Geoscience*, *4*(1), 37–41.
- Portnov, A., Cook, A. E., Sawyer, D. E., Yang, C., Hillman, J. I., and Waite, W. F. (2019). Clustered BSRs: Evidence for gas hydrate-bearing turbidite complexes in folded regions, example from the Perdido Fold Belt, northern Gulf of Mexico. *Earth and Planetary Science Letters*, *528*, 115843.
- Qian, J., Wang, X., Collett, T. S., Guo, Y., Kang, D., and Jin, J. (2018). Downhole log evidence for the coexistence of structure II gas hydrate and free gas below the bottom simulating reflector in the South China Sea. *Marine and petroleum geology*, *98*, 662–674.
- Qin, X.-w., Lu, J.-a., Lu, H.-l., Qiu, H.-j., Liang, J.-q., Kang, D.-j., Zhan, L.-s., Lu, H.-f., and Kuang, Z.-g. (2020). Coexistence of natural gas hydrate, free gas and water in the gas hydrate system in the Shenhu Area, South China Sea. *China Geology*, *3*(2), 210–220.
- Quijada, M. F. and Stewart, R. R. (2007). Density estimations using density-velocity relations and seismic inversion. *CREWES Res Rep*, *19*, 1–20.
- Reagan, M. T., Moridis, G. J., Elliott, S. M., and Maltrud, M. (2011). Contribution of oceanic gas hydrate dissociation to the formation of Arctic Ocean methane plumes. *Journal of Geophysical Research: Oceans*, *116*(C9).
- Riboulot, V., Sultan, N., Imbert, P., and Ker, S. (2016). Initiation of gas-hydrate pockmark in deep-water Nigeria: Geo-mechanical analysis and modelling. *Earth and Planetary Science Letters*, *434*, 252–263.

- Riedel, M., Goldberg, D., and Guerin, G. (2014). Compressional and shear-wave velocities from gas hydrate bearing sediments: Examples from the India and Cascadia margins as well as Arctic permafrost regions. *Marine and petroleum geology*, *58*, 292–320.
- Riedel, M., Scherwath, M., Römer, M., Veloso, M., Heesemann, M., and Spence, G. D. (2018). Distributed natural gas venting offshore along the Cascadia margin. *Nature Communications*, *9*(1), 1–14.
- Rivkina, E., Gilichinsky, D. A., McKay, C., and Dallimore, S. (2001). Methane distribution in permafrost: evidence for an inter pore pressure methane hydrate. In *Permafrost Response on Economic Development, Environmental Security and Natural Resources*, 487–496. Springer.
- Rodrigo, C., González-Fernández, A., and Vera, E. (2009). Variability of the bottom-simulating reflector (BSR) and its association with tectonic structures in the Chilean margin between Arauco Gulf (37 S) and Valdivia (40 S). *Marine Geophysical Researches*, *30*(1), 1–19.
- Römer, M., Riedel, M., Scherwath, M., Heesemann, M., and Spence, G. D. (2016). Tidally controlled gas bubble emissions: A comprehensive study using long-term monitoring data from the NEPTUNE cabled observatory offshore Vancouver Island. *Geochemistry, Geophysics, Geosystems*, *17*(9), 3797–3814.
- Römer, M., Sahling, H., Pape, T., Bohrmann, G., and Spieß, V. (2012). Quantification of gas bubble emissions from submarine hydrocarbon seeps at the Makran continental margin (offshore Pakistan). *Journal of Geophysical Research: Oceans*, *117*(C10).
- Ruppel, C. (2015). Permafrost-associated gas hydrate: is it really approximately 1% of the global system? *Journal of Chemical & Engineering Data*, *60*(2), 429–436.
- Ruppel, C. D. and Kessler, J. D. (2017). The interaction of climate change and methane hydrates. *Reviews of Geophysics*, *55*(1), 126–168.



- Ryu, B.-J., Collett, T. S., Riedel, M., Kim, G. Y., Chun, J.-H., Bahk, J.-J., Lee, J. Y., Kim, J.-H., and Yoo, D.-G. (2013). Scientific results of the second gas hydrate drilling expedition in the Ulleung basin (UBGH2). *Marine and Petroleum Geology*, *47*, 1–20.
- Saffer, D., Wallace, L., Petronotis, K., *et al.* (2018). Expedition 375 Preliminary Report: Hikurangi Subduction Margin Coring and Observatories. *International Ocean Discovery Program*.
- Saffer, D. M. and Tobin, H. J. (2011). Hydrogeology and mechanics of subduction zone forearcs: Fluid flow and pore pressure. *Annual Review of Earth and Planetary Sciences*, *39*, 157–186.
- Saunoy, M., Stavert, A. R., Poulter, B., Bousquet, P., Canadell, J. G., Jackson, R. B., Raymond, P. A., Dlugokencky, E. J., Houweling, S., Patra, P. K., *et al.* (2020). The global methane budget 2000–2017. *Earth System Science Data*, *12*(3), 1561–1623.
- Sava, D. and Hardage, B. A. (2006). Rock physics characterization of hydrate-bearing deepwater sediments. *The Leading Edge*, *25*(5), 616–619.
- Schimmel, A. C., Brown, C. J., and Ierodiaconou, D. (2020). Automated filtering of multibeam water-column data to detect relative abundance of giant kelp (*Macrocystis pyrifera*). *Remote Sensing*, *12*(9), 1371.
- Schmale, O., Greinert, J., and Rehder, G. (2005). Methane emission from high-intensity marine gas seeps in the Black Sea into the atmosphere. *Geophysical Research Letters*, *32*(7).
- Schoell, M. (1988). Multiple origins of methane in the Earth. *Chemical geology*, *71*(1-3), 1–10.
- Schwalenberg, K., Haeckel, M., Poort, J., and Jegen, M. (2010). Evaluation of gas hydrate deposits in an active seep area using marine controlled source electromagnetics: Results from Opouawe Bank, Hikurangi Margin, New Zealand. *Marine Geology*, *272*(1-4), 79–88.

- Schwalenberg, K., Rippe, D., Gehrman, R., and Hoelz, S. (2016). Marine CSEM site survey on gas hydrate targets in the Danube delta, western Black Sea. In *26. Schmucker-Weidelt-Kolloquium für Elektromagnetische Tiefenforschung*, 128–137. Deutsche Geophysikalische Gesellschaft e. V.
- Seabrook, S., De Leo, F. C., and Thurber, A. R. (2019). Flipping for food: the use of a methane seep by tanner crabs (*Chionoecetes tanneri*). *Frontiers in Marine Science*, *6*, 43.
- Senger, K., Bünz, S., and Mienert, J. (2010). First-order estimation of in-place gas resources at the Nyegga gas hydrate prospect, Norwegian Sea. *Energies*, *3*(12), 2001–2026.
- Shakhova, N., Semiletov, I., Salyuk, A., Yusupov, V., Kosmach, D., and Gustafsson, Ö. (2010). Extensive methane venting to the atmosphere from sediments of the East Siberian Arctic Shelf. *Science*, *327*(5970), 1246–1250.
- Shankar, U. and Riedel, M. (2011). Gas hydrate saturation in the Krishna–Godavari basin from P-wave velocity and electrical resistivity logs. *Marine and Petroleum Geology*, *28*(10), 1768–1778.
- Shedd, W., Boswell, R., Frye, M., Godfriaux, P., and Kramer, K. (2012). Occurrence and nature of “bottom simulating reflectors” in the northern Gulf of Mexico. *Marine and Petroleum Geology*, *34*(1), 31–40.
- Shelander, D., Dai, J., and Bunge, G. (2010). Predicting saturation of gas hydrates using pre-stack seismic data, Gulf of Mexico. *Marine Geophysical Researches*, *31*(1), 39–57.
- Shewchuk, J. R. *et al.* (1994). An introduction to the conjugate gradient method without the agonizing pain.
- Shipley, T., Houston, M., Buffer, R., Shaub, F., McMillen, K., Ladd, J., and Worzel, J. (1979). Seismic evidence for widespread possible gas hydrates on continental slopes and rises: American Association of Petroleum Geologists Bulletin, v. 63.

- Shukla, K., Collett, T., Kumar, P., Yadav, U., Boswell, R., Frye, M., Riedel, M., Kaur, I., and Vishwanath, K. (2019). National gas hydrate program Expedition 02: Identification of gas hydrate prospects in the Krishna-Godavari Basin, Offshore India. *Marine and Petroleum Geology*, 108, 167–184.
- Singh, S. C. and Minshull, T. A. (1994). Velocity structure of a gas hydrate reflector at Ocean Drilling Program site 889 from a global seismic waveform inversion. *Journal of Geophysical Research: Solid Earth*, 99(B12), 24221–24233.
- Singhroha, S., Bünz, S., Plaza-Faverola, A., and Chand, S. (2016). Gas hydrate and free gas detection using seismic quality factor estimates from high-resolution P-cable 3D seismic data. *Interpretation*, 4(1), SA39–SA54.
- Singhroha, S., Chand, S., and Bünz, S. (2019). Constraints on gas hydrate distribution and morphology in Vestnesa Ridge, western Svalbard margin, using multicomponent ocean-bottom seismic data. *Journal of Geophysical Research: Solid Earth*, 124(5), 4343–4364.
- Skarke, A., Ruppel, C., Kodis, M., Brothers, D., and Lobecker, E. (2014). Widespread methane leakage from the sea floor on the northern US Atlantic margin. *Nature Geoscience*, 7(9), 657–661.
- Sloan, E. D. (1998). Gas hydrates: review of physical/chemical properties. *Energy & fuels*, 12(2), 191–196.
- Sloan Jr, E. D. and Koh, C. A. (2007). *Clathrate hydrates of natural gases*. CRC press.
- Soares, A. (2001). Direct sequential simulation and cosimulation. *Mathematical geology*, 33(8), 911–926.
- Stott, L., Davy, B., Shao, J., Coffin, R., Pecher, I., Neil, H., Rose, P., and Bialas, J. (2019). CO<sub>2</sub> Release from Pockmarks on the Chatham Rise-Bounty Trough at the Glacial Termination. *Paleoceanography and Paleoclimatology*, 34(11), 1726–1743.
- Suess, E. (2020). Marine cold seeps: Background and recent advances. *Hydrocarbons, Oils and Lipids: Diversity, Origin, Chemistry and Fate*, 747–767.

- Sun, Y., Wu, S., Dong, D., Lüdmann, T., and Gong, Y. (2012). Gas hydrates associated with gas chimneys in fine-grained sediments of the northern South China Sea. *Marine Geology*, 311, 32–40.
- Taladay, K., Boston, B., and Moore, G. F. (2017). Gas-in-place estimate for potential gas hydrate concentrated zone in the Kumano Basin, Nankai Trough Forearc, Japan. *Energies*, 10(10), 1552.
- Tamaki, M., Fujii, T., and Suzuki, K. (2017). Characterization and prediction of the gas hydrate reservoir at the second offshore gas production test site in the eastern Nankai Trough, Japan. *Energies*, 10(10), 1678.
- Tarantola, A. (2005). *Inverse problem theory and methods for model parameter estimation*. SIAM.
- Tenzer, R. and Gladkikh, V. (2014). Assessment of density variations of marine sediments with ocean and sediment depths. *The Scientific World Journal*, 2014.
- Tinivella, U. (1999). A method for estimating gas hydrate and free gas concentrations in marine sediments. *Bollettino di Geofisica Teorica ed Applicata*, 40(1), 19–30.
- Tinivella, U. and Accaino, F. (2000). Compressional velocity structure and Poisson's ratio in marine sediments with gas hydrate and free gas by inversion of reflected and refracted seismic data (South Shetland Islands, Antarctica). *Marine Geology*, 164(1-2), 13–27.
- Tinivella, U., Accaino, F., and Camerlenghi, A. (2002). Gas hydrate and free gas distribution from inversion of seismic data on the South Shetland margin (Antarctica). *Marine Geophysical Researches*, 23(2), 109–123.
- Turco, F., Crutchley, G. J., Gorman, A. R., Mountjoy, J. J., Hillman, J. I., and Woelz, S. (2020). Seismic velocity and reflectivity analysis of concentrated gas hydrate deposits on the southern Hikurangi Margin (New Zealand). *Marine and Petroleum Geology*, 120, 104572.

- Turetsky, M. R., Abbott, B. W., Jones, M. C., Anthony, K. W., Olefeldt, D., Schuur, E. A., Koven, C., McGuire, A. D., Grosse, G., Kuhry, P., *et al.* (2019). Permafrost collapse is accelerating carbon release.
- Turner, P. J., Ball, B., Diana, Z., Fariñas-Bermejo, A., Grace, I., McVeigh, D., Powers, M. M., Van Audenhaege, L., Maslakova, S., Young, C. M., *et al.* (2020). Methane seeps on the US Atlantic margin and their potential importance to populations of the commercially valuable deep-sea red crab, *Chaceon quinque-dens*. *Frontiers in Marine Science*, 7, 75.
- Turner, P. J., Thaler, A. D., Freitag, A., and Collins, P. C. (2019). Deep-sea hydrothermal vent ecosystem principles: identification of ecosystem processes, services and communication of value. *Marine Policy*, 101, 118–124.
- VanderBeek, B. P. and Rempel, A. W. (2018). On the importance of advective versus diffusive transport in controlling the distribution of methane hydrate in heterogeneous marine sediments. *Journal of Geophysical Research: Solid Earth*, 123(7), 5394–5411.
- Veloso, M., Greinert, J., Mienert, J., and De Batist, M. (2015). A new methodology for quantifying bubble flow rates in deep water using splitbeam echosounders: Examples from the Arctic offshore NW-S valbard. *Limnology and Oceanography: methods*, 13(6), 267–287.
- Vielstädte, L., Karstens, J., Haeckel, M., Schmidt, M., Linke, P., Reimann, S., Liebetrau, V., McGinnis, D. F., and Wallmann, K. (2015). Quantification of methane emissions at abandoned gas wells in the Central North Sea. *Marine and Petroleum Geology*, 68, 848–860.
- von Deimling, J. S., Rehder, G., Greinert, J., McGinnis, D., Boetius, A., and Linke, P. (2011). Quantification of seep-related methane gas emissions at Tommeliten, North Sea. *Continental Shelf Research*, 31(7-8), 867–878.
- Waite, W. F., Jang, J., Collett, T. S., and Kumar, P. (2019). Downhole physical property-based description of a gas hydrate petroleum system in NGHP-02 Area C:

- A channel, levee, fan complex in the Krishna-Godavari Basin offshore eastern India. *Marine and Petroleum Geology*, 108, 272–295.
- Wallace, L., Barnes, P., Beavan, J., Van Dissen, R., Litchfield, N., Mountjoy, J., Langridge, R., Lamarche, G., and Pondard, N. (2012). The kinematics of a transition from subduction to strike-slip: An example from the central New Zealand plate boundary. *Journal of Geophysical Research: Solid Earth*, 117(B2).
- Wallace, L., Saffer, D., Barnes, P., Pecher, I., Petronotis, K., and LeVay, L. (2019). Hikurangi subduction margin coring, logging, and observatories. *Proceedings of the International Ocean Discovery Program*, 372.
- Wang, B., Socolofsky, S. A., Breier, J. A., and Seewald, J. S. (2016). Observations of bubbles in natural seep flares at MC 118 and GC 600 using in situ quantitative imaging. *Journal of Geophysical Research: Oceans*, 121(4), 2203–2230.
- Wang, H., Crutchley, G., and Stern, T. (2017a). Gas hydrate formation in compressional, extensional and un-faulted structural settings—Examples from New Zealand’s Hikurangi margin. *Marine and Petroleum Geology*, 88, 69–80.
- Wang, H., Crutchley, G. J., and Stern, T. (2017b). Gas hydrate formation in compressional, extensional and un-faulted structural settings – Examples from New Zealand’s Hikurangi margin. *Marine and Petroleum Geology*, 88, 69–80.
- Wang, X., Liu, B., Qian, J., Zhang, X., Guo, Y., Su, P., Liang, J., Jin, J., Luan, Z., Chen, D., *et al.* (2018). Geophysical evidence for gas hydrate accumulation related to methane seepage in the Taixinan Basin, South China Sea. *Journal of Asian Earth Sciences*, 168, 27–37.
- Wang, Y. (1999). Approximations to the Zoeppritz equations and their use in AVO analysis. *Geophysics*, 64(6), 1920–1927.
- Warner, M. (1990). Absolute reflection coefficients from deep seismic reflections. *Tectonophysics*, 173(1-4), 15–23.

- Watson, S. J., Mountjoy, J. J., Barnes, P. M., Crutchley, G. J., Lamarche, G., Higgs, B., Hillman, J., Orpin, A. R., Micallef, A., Neil, H., *et al.* (2020). Focused fluid seepage related to variations in accretionary wedge structure, Hikurangi margin, New Zealand. *Geology*, *48*(1), 56–61.
- Weber, T. C., Mayer, L., Jerram, K., Beaudoin, J., Rzhhanov, Y., and Lovalvo, D. (2014). Acoustic estimates of methane gas flux from the seabed in a 6000 km<sup>2</sup> region in the Northern Gulf of Mexico. *Geochemistry, Geophysics, Geosystems*, *15*(5), 1911–1925.
- Weidner, E., Weber, T. C., Mayer, L., Jakobsson, M., Chernykh, D., and Semiletov, I. (2019). A wideband acoustic method for direct assessment of bubble-mediated methane flux. *Continental Shelf Research*, *173*, 104–115.
- Westbrook, G. K., Thatcher, K. E., Rohling, E. J., Piotrowski, A. M., Pälike, H., Osborne, A. H., Nisbet, E. G., Minshull, T. A., Lanoisellé, M., James, R. H., *et al.* (2009). Escape of methane gas from the seabed along the West Spitsbergen continental margin. *Geophysical Research Letters*, *36*(15).
- Wiesenburg, D. A. and Guinasso Jr, N. L. (1979). Equilibrium solubilities of methane, carbon monoxide, and hydrogen in water and sea water. *Journal of chemical and engineering data*, *24*(4), 356–360.
- Wood, A. B. (1946). *Textbook of sound*. G Bell And Sons, Ltd.
- Wyllie, M., Gregory, A., and Gardner, G. (1958). An experimental investigation of factors affecting elastic wave velocities in porous media. *Geophysics*, *23*(3), 459–493.
- Xu, H., Dai, J., Snyder, F., and Dutta, N. (2004). Seismic detection and quantification of gas hydrates using rock physics and inversion. In *Advances in the study of gas hydrates*, 117–139. Springer.
- Yadav, U., Shukla, K., Ojha, M., Kumar, P., and Shankar, U. (2019). Assessment of gas hydrate accumulations using velocities derived from vertical seismic profiles

- and acoustic log data in Krishna-Godavari Basin, India. *Marine and Petroleum Geology*, 108, 551–561.
- Yilmaz, Ö. (2001). *Seismic data analysis: Processing, inversion, and interpretation of seismic data*. Society of exploration geophysicists.
- Yoneda, J., Oshima, M., Kida, M., Kato, A., Konno, Y., Jin, Y., Jang, J., Waite, W. F., Kumar, P., and Tenma, N. (2019). Pressure core based onshore laboratory analysis on mechanical properties of hydrate-bearing sediments recovered during India's National Gas Hydrate Program Expedition (NGHP) 02. *Marine and Petroleum Geology*, 108, 482–501.
- Yoo, D. G., Kang, N. K., Bo, Y. Y., Kim, G. Y., Ryu, B. J., Lee, K., Lee, G. H., and Riedel, M. (2013). Occurrence and seismic characteristics of gas hydrate in the Ulleung Basin, East Sea. *Marine and Petroleum Geology*, 47, 236–247.
- Yu, T., Guan, G., Abudula, A., Yoshida, A., Wang, D., and Song, Y. (2019). Gas recovery enhancement from methane hydrate reservoir in the Nankai Trough using vertical wells. *Energy*, 166, 834–844.
- Yun, T. S., Francisca, F. M., Santamarina, J. C., and Ruppel, C. (2005). Compressional and shear wave velocities in uncemented sediment containing gas hydrate. *Geophysical Research Letters*, 32(10).
- Zander, T., Haeckel, M., Berndt, C., Chi, W.-C., Klauke, I., Bialas, J., Klaeschen, D., Koch, S., and Atgim, O. (2017). On the origin of multiple BSRs in the Danube deep-sea fan, Black Sea. *Earth and Planetary Science Letters*, 462, 15–25.
- Zelt, C. and Smith, R. (1992). Seismic travelttime inversion for 2-D crustal velocity structure. *Geophysical journal international*, 108(1), 16–34.
- Zhao, J., Liu, Y., Guo, X., Wei, R., Yu, T., Xu, L., Sun, L., and Yang, L. (2020). Gas production behavior from hydrate-bearing fine natural sediments through optimized step-wise depressurization. *Applied Energy*, 260, 114275.



Zhu, D. and Gibson, R. (2018). Seismic inversion and uncertainty quantification using transdimensional Markov chain Monte Carlo method. *Geophysics*, 83(4), R321–R334.